Bellcomm

BELLCOMM, INC.

Washington, D. C.

620-1
TR-70-~~1022-1~~

SOLAR POINTING VARIATIONS IN EARTH ORBIT AND THE IMPACT ON MISSION DESIGN

February 11, 1970

Prepared by:

B. D. Elrod

Work performed for Manned Space Flight, National Aeronautics and Space Administration, under Contract NASW-417.

TABLE OF CONTENTS

ABSTRACT

The solar vector orientation relative to an earth orbit varies with time due to the earth's motion about the sun and motion of the orbital plane due to earth oblateness. In this report a detailed description of this variation is given in terms of two pointing angles: β, the minimum angle between the solar vector and the orbital plane and ψ, the location of orbital noon relative to the ascending node. Typical time variations are shown and various properties of the pointing angles are expressed as a function of orbital parameters for both posigrade and retrograde orbits. Specific results are included for 35° and 50°, 230 NM circular orbits, which have been considered for AAP Workshop missions.

The solar pointing angles help define important spacecraft systems requirements, such as experiment gimbaling and solar array articulation in orbit-oriented modes and spacecraft maneuvers in a solar-inertial mode. They are also significant from a mission design standpoint, since the solar vector orientation is related to factors affecting spacecraft system performance. This includes, for example, the incident thermal energy per orbit on spacecraft and electrical energy output from fixed solar arrays on spacecraft in orbit-oriented modes. Although related to both β and ψ in arbitrary elliptical orbits, performance factors are usually a function only of β in circular and slightly elliptical orbits. A number of factors are considered in this work and the relationship with β is determined. Spacecraft models and attitude modes are chosen to illustrate typical properties and effects of the β variation, as they may affect AAP and future space station missions. All results are given in normalized form to facilitate application to particular spacecraft configurations.

System designs are often based on worst case β conditions. Since these occur only at discrete times in a mission, such designs may impose excessive requirements or may not utilize available performance margins. Consequently mission averages of system performance factors are relevant to mission planning and are developed in this report as a means of assessing the overall impact of the β variation and arbitrary launch time and date.

SOLAR POINTING VARIATIONS IN EARTH ORBIT AND THE IMPACT ON MISSION DESIGN

1.0 INTRODUCTION

Solar pointing is a prime concern in manned spaceflight mission planning because of interrelated requirements for earth and solar viewing experiments, electrical power from solar arrays, and spacecraft thermal control. Specific pointing requirements are governed by the choice of flight attitude. For AAP and future space station missions flight attitudes have been considered[1-4] for holding:

(1) spacecraft including experiments and solar arrays in a "solar-inertial" mode,* or

(2) experiments and solar arrays in a solar orientation and the spacecraft in an orbit-oriented mode such as: LV, LH or POP.**

Of interest in these modes are the solar pointing angles which describe the orientation of the solar vector relative to an earth orbit. These vary with time because of the earth's motion about the sun and continuous motion of the orbital plane due to earth oblateness. The pointing angles are significant since they are related to certain spacecraft system requirements, such as experiment gimbaling and array articulation in orbit-oriented modes and spacecraft maneuvers in a solar-inertial mode. The pointing angles are also useful from a mission design standpoint, since the solar vector orientation is related to various system performance aspects (e.g., the incident thermal energy per orbit on spacecraft and the degradation in electrical energy output from fixed solar arrays in LV, LH and POP modes).

---

*The "solar-inertial" mode is depicted in Fig. (1-1) for the AAP cluster configuration (Saturn-V Workshop: ATM/CSM/OWS). As in the original concept[1], the ATM telescope is pointed at the sun with the CSM/OWS roll axis maintained essentially in the orbital plane and normal to the sun line.

**The attitude modes LV, LH and POP are defined by the orientation of the spacecraft roll axis which is: parallel to the Local Vertical in LV, in the orbital plane and parallel to the Local Horizontal in LH, and Perpendicular-to-the-Orbital-Plane in POP.

The objective of this report is to describe the behavior of solar pointing variations and to examine the effect on pointing requirements as well as the impact on various system performance factors affecting mission design. In the remainder of this section the pointing angles are defined and system performance factors considered in subsequent work are stated.

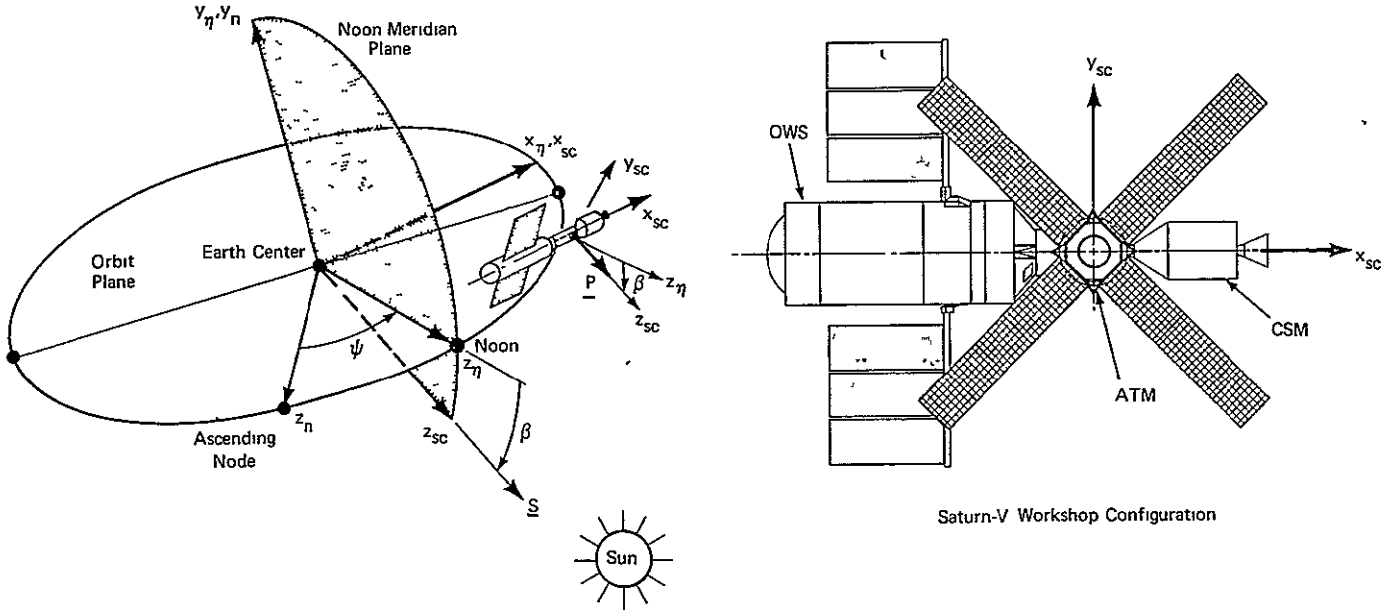

Figure (1-1) - Solar Pointing Geometry in Solar-Inertial Mode

1.1 Solar Pointing Angles (β, ψ)

Pointing in an arbitrary direction is usually achieved by two rotations (pointing angles) about two orthogonal axes. In this report two pointing angles (β, ψ)* are defined relative to the orbital plane, specifically the geocentric coordinate system (x_n, y_n, z_n) shown in Fig.(1-1). In this coordinate system, y_n is normal to the orbital plane, z_n is directed to the orbit ascending node and x_n (not shown) completes the right hand system. The angle ψ is a rotation in the

*The angles β and ψ are synonymous with the pointing angles η_x and η_y used in Reference 5.

orbital plane about y_n and β is a rotation out of the orbital plane about the axis x_n, which lies in the orbital plane, but normal to the sun line. Geometrically, β represents the angle between the orbital plane and the sun line as measured in the noon meridian plane*, whereas ψ represents the angle between the ascending node (z_n) and the noon meridian plane as measured in the orbital plane.

Due to the earth's motion about the sun and motion of the orbit ascending node (z_n) in the earth's equatorial plane, β and ψ vary with time. In subsequent work this variation is examined in detail and various properties of β and ψ are evaluated as a function of orbital parameters. Properties such as $|\beta|_{max}$, $|\dot{\beta}|_{max}$, $\dot{\psi}_{max}$ and $\dot{\psi}_{ave}$ are directly related to spacecraft maneuver requirements in the solar-inertial mode and to experiment gimbaling and array articulation requirements in non-sun-oriented modes.

1.2 System Performance Factors

The solar vector orientation relative to the orbital plane has an effect on the design of many spacecraft systems (attitude control, electrical power, and thermal control) as well as many earth and solar viewing experiments. Specific factors affecting system performance can be related to the solar pointing angles. Significant performance factors include:

(1) Bias gravity gradient torque which contributes to angular momentum dumping requirements for spacecraft controlled by CMGs in a solar-inertial mode,

(2) Duration of an orbital day which affects experiment operations and solar viewing time,

(3) Incident solar energy per orbit which affects the electrical energy available from solar arrays, and

(4) Incident thermal energy per orbit which affects spacecraft thermal control requirements.

---

*The definition of noon is discussed in Appendix A in connection with Fig. (A-1).

For elliptical orbits these particular factors are a function of both β and ψ, although ψ has negligible effect for slightly elliptical orbits* and no effect for circular orbits. In subsequent sections the factors, (1-4) above, are examined in detail for circular orbits and a functional relationship with β is determined. In addition, mission average effects of the β variation and arbitrary mission launch time and date are studied with a view toward assessing certain system requirements and performance margins, as discussed in Section 6. Results are plotted as functions of mission duration and orbital inclination.

*A slightly elliptical orbit is interpreted here as having an eccentricity ≤ 0.01 (e.g., a 260 x 200 NM orbit, which is within launch capability for the Saturn-V Workshop mission).

2.0 DEFINITIONS AND NOTATION

In the following subsections mathematical and geometrical definitions and notational conventions used in deriving pointing angles and in subsequent analysis are given.

2.1 Matrix Transformations

Different coordinate systems are related by transformations of the form

$$\underline{u}_i = \begin{pmatrix} x_i \\ y_i \\ z_i \end{pmatrix} = T \begin{pmatrix} x_j \\ y_j \\ z_j \end{pmatrix} = T\,\underline{u}_j \qquad (2\text{-}1)$$

where T is an orthogonal matrix (i.e., $T^{-1}=T^{\dagger}$)* and $\underline{u}_i$ and $\underline{u}_j$ represent a vector expressed in the i and j systems.** The matrix T is an elementary transformation if two coordinate systems differ by a single Euler angle rotation about a common axis.

The three possible forms are***

$$T_{\xi}^{x} = \begin{bmatrix} 1 & 0 & 0 \\ 0 & c\xi & s\xi \\ 0 & -s\xi & c\xi \end{bmatrix} \qquad (2\text{-}2)$$

$$T_{\xi}^{y} = \begin{bmatrix} c\xi & 0 & -s\xi \\ 0 & 1 & 0 \\ s\xi & 0 & c\xi \end{bmatrix} \qquad (2\text{-}3)$$

$$T_{\xi}^{z} = \begin{bmatrix} c\xi & s\xi & 0 \\ -s\xi & c\xi & 0 \\ 0 & 0 & 1 \end{bmatrix} \qquad (2\text{-}4)$$

---

*The superscripts -1 and † correspond to the matrix inverse and transpose operations.

**Subscripts on a vector denote the system in which it is expressed. Frequently abbreviations are used (e.g., $\underline{u}_{sc}$ for a vector in spacecraft coordinates).

***Superscripts on transformations indicate axis of rotation and subscripts denote the corresponding angles of rotation. For brevity the notation $c\xi$ and $s\xi$ is always used for the trigonometric operations $\cos(\xi)$ and $\sin(\xi)$.

The matrix T may be formed from the product of any number of elementary transformations corresponding to Euler angles μ, η, ξ,.... with the property that

$$T^{\dagger} = (\ldots T^{j}_{\xi}\ T^{k}_{\nu}\ T^{\ell}_{\mu})^{\dagger}$$

$$= (T^{\ell}_{\mu})^{\dagger}\ (T^{k}_{\nu})^{\dagger}\ (T^{j}_{\xi})^{\dagger} \ldots = T_{-\mu}^{\ell}\ T_{-\nu}^{k}\ T_{-\xi}^{j} \ldots \quad (j,k,\ell = x,y \text{ or } z) \tag{2-5}$$

2.2 Definition of Sun Line and Inertial Reference System

To account for the earth's annual rotation about the sun it is convenient to define the sun line with respect to the geocentric inertial reference system $(X_\gamma, Y_\gamma, Z_\gamma)$, henceforth called the equinox system shown in Fig. (2-1). Here Y_γ is positive toward the ecliptic north pole, Z_γ is the direction toward the sun at autumnal equinox and X_γ completes the right-hand system.

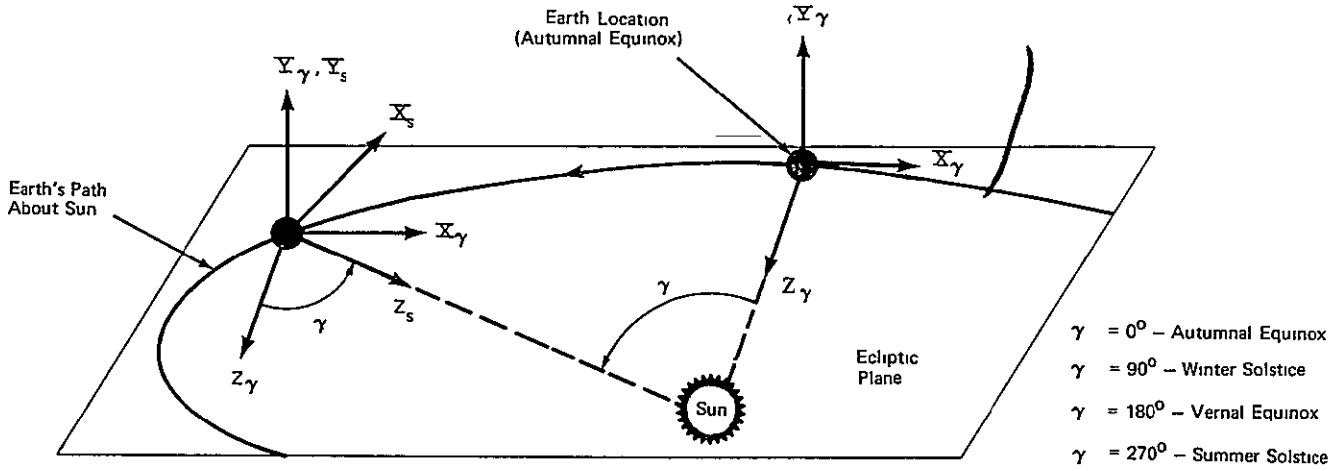

Figure (2 - 1) - Location of Sun Line Relative to Autumnal Equinox

The sun line is defined as the vector $\underline{S}_S = (0,0,1)^{\dagger}$ in the (X_S, Y_S, Z_S) system shown in Fig. (2-1) where Y_S is parallel to Y_γ and Z_S is directed toward the sun. The axes Z_S and Z_γ are displaced by the angle γ which is related to the time of year

with γ=0° corresponding to the autumnal equinox. In the equinox system the sun line is given by

$$\underline{S}_\gamma = T^{Y}_{-\gamma}\,\underline{S}_s = T^{Y}_{-\gamma}\begin{pmatrix}0\\0\\1\end{pmatrix} = \begin{pmatrix}s\gamma\\0\\c\gamma\end{pmatrix} \tag{2-6}$$

Although the earth's orbit about the sun is slightly elliptical, the angle γ is evaluated here on the basis of a circular orbit approximation,*

$$\gamma = \gamma_o + \dot{\gamma}t \tag{2-7}$$

where **

$$\dot{\gamma} = 360/365.26 = 0.9856 \text{ deg/day} \tag{2-8}$$

is the mean sun line rotation rate, t is current time and γ_o is the sun line location at t=0.

---

*The actual sun line location (γ_a) can be determined from the orbit angular velocity equation

$$\dot{\gamma}_a = \dot{\gamma}(1-\varepsilon_s^2)^{3/2}[1 + \varepsilon_s c(\gamma_a-\gamma_{ap})]^2$$

where ε_s=0.016 is the earth's orbital eccentricity and γ_{ap}=282.38° is the earth's perihelion[12] (relative to autumnal equinox). To a first approximation in ε_s it can be shown that

$$\Delta\dot{\gamma}_e \equiv \dot{\gamma}-\dot{\gamma}_a = -2\dot{\gamma}\varepsilon_s c(\gamma_a-\gamma_{ap})$$

$$\Delta\gamma_e = \gamma-\gamma_a = 2\varepsilon_s[1-s(\gamma_a-\gamma_{ap})]$$

Thus, $0 \le |\Delta\dot{\gamma}_e|_{max} < 0.03$ deg/day and $0 \le (\Delta\gamma_e)_{max} < 3.8$ deg with the maximum occurring a few days after vernal equinox (when γ_a=192.38°). For the purposes of this analysis the circular orbit approximation is sufficient.

**The earth's period about the sun is 365.2563835 mean solar days.

2.3 Orientation of Orbital Reference System

The relative orientation of the orbital and equatorial planes and their relationship to the ecliptic plane and sun line is shown in Fig.(2-2) for a particular location of the orbit ascending node (z_n). As previously discussed, the nodal system (x_n, y_n, z_n) is considered as the reference system for determining the solar pointing angles. The Euler angles e, Ω_r and i define the orientation of the nodal system relative to the equinox system ($X_\gamma, Y_\gamma, Z_\gamma$). The angle e is fixed at 23.45° and defines the inclination of the equatorial plane relative to the ecliptic plane. The angle Ω_r defines the location of the orbit ascending node relative to Z_γ. The angle i represents the inclination of the orbital plane relative to the equatorial plane.

As given in Eq.(A-13) of Appendix A, i can be determined from

$$ci = s\alpha_L c\ell \qquad 0 \leq i \leq 180° \qquad (2\text{-}9)$$

where α_L is the launch azimuth measured positively from geographical north and ℓ is the latitude of the launch site. Evaluation of Ω_r is discussed in the next subsection.

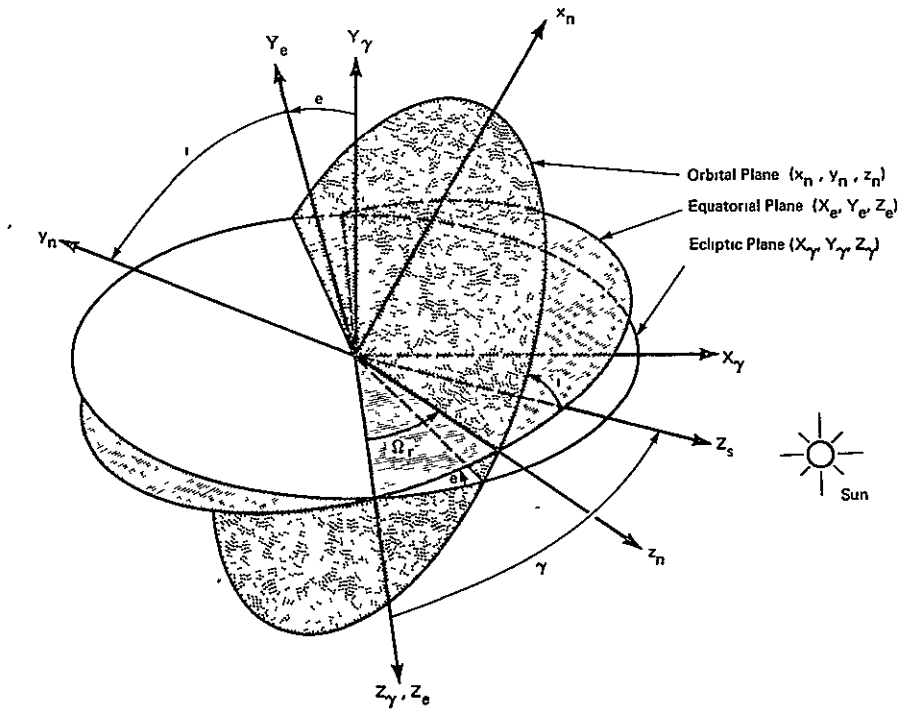

Figure (2 - 2) - Relative Orientation of Orbital, Equatorial and Ecliptic Planes

2.4 Earth Oblateness Effect

Two variations in orbital motion produced by earth oblateness are: 1) rotation of the ascending node about the equatorial plane and 2) rotation of the line-of-apsides in the orbital plane. Motion of the ascending node can be described by*

$$\Omega_r = \Omega_{ro} + \dot{\Omega}_r t \qquad (2\text{-}10)$$

where $\dot{\Omega}_r$ is the rotation rate, t is current time and Ω_{ro} is the ascending node location at t=0. Similarly, motion of the line-of-apsides is described by*

$$\Omega_a = \Omega_{po} + \dot{\Omega}_a t \qquad (2\text{-}11)$$

where $\dot{\Omega}_a$ is the rotation rate and Ω_{po} is the location of perigee relative to the ascending node at t=0 as shown in Fig. (2-3).**

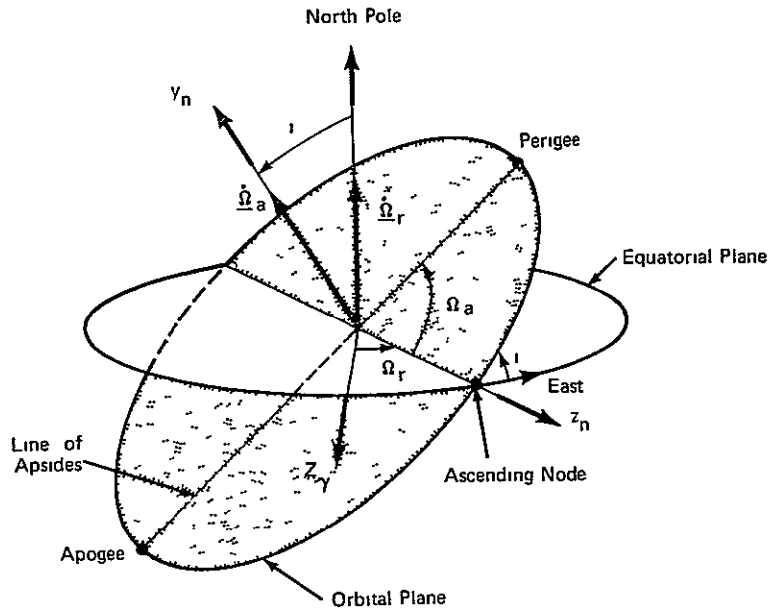

Figure (2 - 3) - Description of Orbital Motion Due to Earth Oblateness

*This model represents the secular variation due to earth oblateness[6]. Periodic variations due to third and higher harmonic terms in the earth's gravitational potential function are small and may be neglected in this work.

**Although the line-of-apsides is undefined in circular orbits, the orbital plane may be viewed as rotating (in-plane) at the rate, $\dot{\Omega}_a$.

The rotation rates $\dot{\Omega}_r$ and $\dot{\Omega}_a$ are given by[6]

$$\dot{\Omega}_r = -\dot{\Omega}_{rm} ci \tag{2-12}$$

and

$$\dot{\Omega}_a = \dot{\Omega}_{rm}\left(\frac{4-5\ s^2 i}{2}\right) \tag{2-13}$$

where

$$\dot{\Omega}_{rm} = \frac{J\mu^{1/2}R^2}{a^{7/2}(1-\varepsilon^2)^2} = 9.996\ \frac{(R/a)^{7/2}}{(1-\varepsilon^2)^2}\ \frac{\text{deg}}{\text{day}} \tag{2-14}$$

and

$J = 1.624 \times 10^{-3}$, dimensionless constant in second harmonic term of oblate spheroid model of earth's gravitational potential function

$\mu = 4.6843 \times 10^{14}$ NM^3/day^2, earth's gravitational constant

$R = 3443.9$ NM, earth radius

ε = orbit eccentricity

a = orbit semi-major axis (NM)

= R+H for circular orbits (ε=0)

H = circular orbit altitude (NM)

Motion of the ascending node is westward (regressive) for $0° \leq i < 90°$ and eastward (progressive) for $90° < i \leq 180°$. Apsidal motion is such that perigee advances relative to the ascending node for $0° \leq i < 63.45°$ or $116.55° < i \leq 180°$ and reverses for $63.45° < i < 116.55°$.

3.0 DERIVATION OF SOLAR POINTING ANGLES

The pointing axis ($\underline{P}$) to be aligned with the sun line can be defined relative to the nodal coordinate system (x_n, y_n, z_n) by the pointing angles (β, ψ) described in Section 1.1. To derive (β, ψ) it is only necessary to equate elements of $\underline{P}$ with corresponding elements of the solar vector $\underline{S}$ also expressed in nodal coordinates.

To determine $\underline{P}_n$ consider the spacecraft coordinate system (x_{sc}, y_{sc}, z_{sc}) shown in Fig. (1-1) which is related to the (x_n, y_n, z_n) system by the transformation

$$\underline{u}_{sc} = T_p \, \underline{u}_n = T_\beta^x \, T_\psi^y \, \underline{u}_n \tag{3-1}$$

Since $\underline{P}_{sc} = (0,0,1)^\dagger$, it follows that

$$\underline{P}_n = \begin{pmatrix} P_1 \\ P_2 \\ P_3 \end{pmatrix} = T_p^\dagger \begin{pmatrix} 0 \\ 0 \\ 1 \end{pmatrix} = \begin{pmatrix} s\psi \; c\beta \\ -s\beta \\ c\psi \; c\beta \end{pmatrix} \tag{3-2}$$

To determine the solar vector $\underline{S}_n$ consider the transformation between the (x_n, y_n, z_n) and $(X_\gamma, Y_\gamma, Z_\gamma)$ coordinate systems shown in Fig. (2-2).

$$\underline{u}_n = T_n \, \underline{u}_\gamma = T_i^z \, T_{\Omega_r}^y \, T_e^z \, \underline{u}_\gamma \tag{3-3}$$

From Eqs. (2-6) and (3-1) it follows that $\underline{S}_n$ is given by

$$\underline{S}_n = \begin{pmatrix} S_1 \\ S_2 \\ S_3 \end{pmatrix} = T_n \, \underline{S}_\gamma = \begin{pmatrix} s\gamma(ci \; ce \; c\Omega_r - si \; se) - ci \; c\gamma \; s\Omega_r \\ -s\gamma(si \; ce \; c\Omega_r + ci \; se) + si \; c\gamma \; s\Omega_r \\ c\gamma \; c\Omega_r + s\gamma \; s\Omega_r \; ce \end{pmatrix} \tag{3-4}$$

Equating $\underline{P}_n$ and $\underline{S}_n$ yields the trigonometric functions specifying the pointing angles (β,ψ).*

$$s\beta = -S_2 = s\gamma(si\ ce\ c\Omega_r + ci\ se) - si\ c\gamma\ s\Omega_r \tag{3-5}$$

$$\tan\psi = \frac{S_1}{S_3} = \frac{s\gamma(ci\ ce\ c\Omega_r - si\ se) - ci\ c\gamma\ s\Omega_r}{c\gamma\ c\Omega_r + s\gamma\ s\Omega_r\ ce} \tag{3-6}$$

or in alternate form

$$s\beta = ci\ se\ s\gamma + si\left[\left(\frac{1+ce}{2}\right)s(\gamma-\Omega_r) - \left(\frac{1-ce}{2}\right)s(\gamma+\Omega_r)\right] \tag{3-7}$$

$$\tan\psi = \frac{-si\ se\ s\gamma + ci\left[\left(\frac{1+ce}{2}\right)s(\gamma-\Omega_r) - \left(\frac{1-ce}{2}\right)s(\gamma+\Omega_r)\right]}{\left[\left(\frac{1+ce}{2}\right)c(\gamma-\Omega_r) + \left(\frac{1-ce}{2}\right)c(\gamma+\Omega_r)\right]} \tag{3-8}$$

As discussed previously, the angles e and i are fixed whereas γ and Ω_r vary with time. The effect of this variation will now be examined.

---

*In general, two solution pairs (β,ψ) exist, one pair corresponding to $-90° \leq \beta \leq 90°$ and the other for $90° \leq \beta \leq 270°$. In subsequent analysis the pair corresponding to $-90° \leq \beta \leq 90°$ is used which implies that β always represents the minimum angle between the sun line and the orbital plane.

4.0 GENERAL CHARACTERISTICS OF β AND ψ

The time variation of β and ψ is affected by the initial values of γ and Ω_r. Derivations for γ_o and Ω_{ro} as a function of launch conditions are given in Appendix A. From Eqs.(A-3) and (A-5) the initial values of γ and Ω_r are*

$$\gamma_o = \dot{\gamma} d_L \tag{4-1}$$

$$\Omega_{ro} = [15(t_L+t_N)-180°] + \Omega_N - \Omega_L \tag{4-2}$$

where

$$d_L = D_L + (t_L-t_{ae})/24$$

$= $ launch time measured from autumnal equinox in days (non-integer)

D_L = number of calendar days (integer) at launch since September 23 (00^h:00 U.T.**)

t_L = launch site Universal Time** at launch ($0 \leq t_L \leq 24.0$ hours)

t_{ae} = launch site Universal Time** at autumnal equinox ($0 \leq t_{ae} \leq 24.0$ hours)

and

---

*The expression for γ_o is based on a circular orbit approximation to the earth's motion about the sun. See Footnote *, p.7. For more accurate results γ_o can be evaluated from ephermeris tables[23], once d_L is determined.

**See Footnote *, Appendix A, p.A-2 for definition of Universal Time (U.T.) at launch site.

t_N = difference between true noon* and apparent (clock) noon at Greenwich ($0 \leq |t_N| < 0.27$ hours)

As illustrated in Fig.(A-1) of Appendix A, Ω_L is the launch site longitude relative to the orbit ascending node and Ω_N is the longitude of the equatorial noon meridian plane* relative to the autumnal equinox. The expressions given in Eqs.(A-9) and (A-15) for obtaining Ω_N and Ω_L are

$$\tan \Omega_N = \tan\gamma_o \, ce \tag{4-3}$$

$$\tan \Omega_L = \tan\alpha_L \, s\ell \tag{4-4}$$

where α_L and ℓ represent the launch azimuth and launch site latitude. The angles Ω_N and Ω_L lie in the same quadrants as γ_o and α_L respectively.

Although these definitions for Ω_{ro} and γ_o are based on instantaneous orbit injection above the launch site, they are also applicable for arbitrary orbit injection points or for previously established orbits. Only appropriate interpretation of parameters is necessary, specifically: α_L is the current heading relative to geographical north; ℓ is the current local latitude; D_L, t_L, t_{ae} and t_N are times (as defined above) corresponding to the current local longitude.

To illustrate the nature of β and ψ as a function of time, the solutions of Eqs.(3-5) and (3-6) for β and ψ are plotted in Fig.(4-1) for a specific set of orbit and launch conditions.** These results are based on a noon launch at autumnal equinox ($\gamma_o = 0°$: $t_L = t_{ae} = 12.0$, $D_L = t_N = 0$). The orbit and launch

---

*See discussion in Appendix A regarding the definition of noon. In this formulation true noon corresponds to $t_L + t_N = 12.0$.

**Expressions for evaluating the initial pointing angles (β_o, ψ_o) for arbitrary launch conditions are given in Appendix A.3.

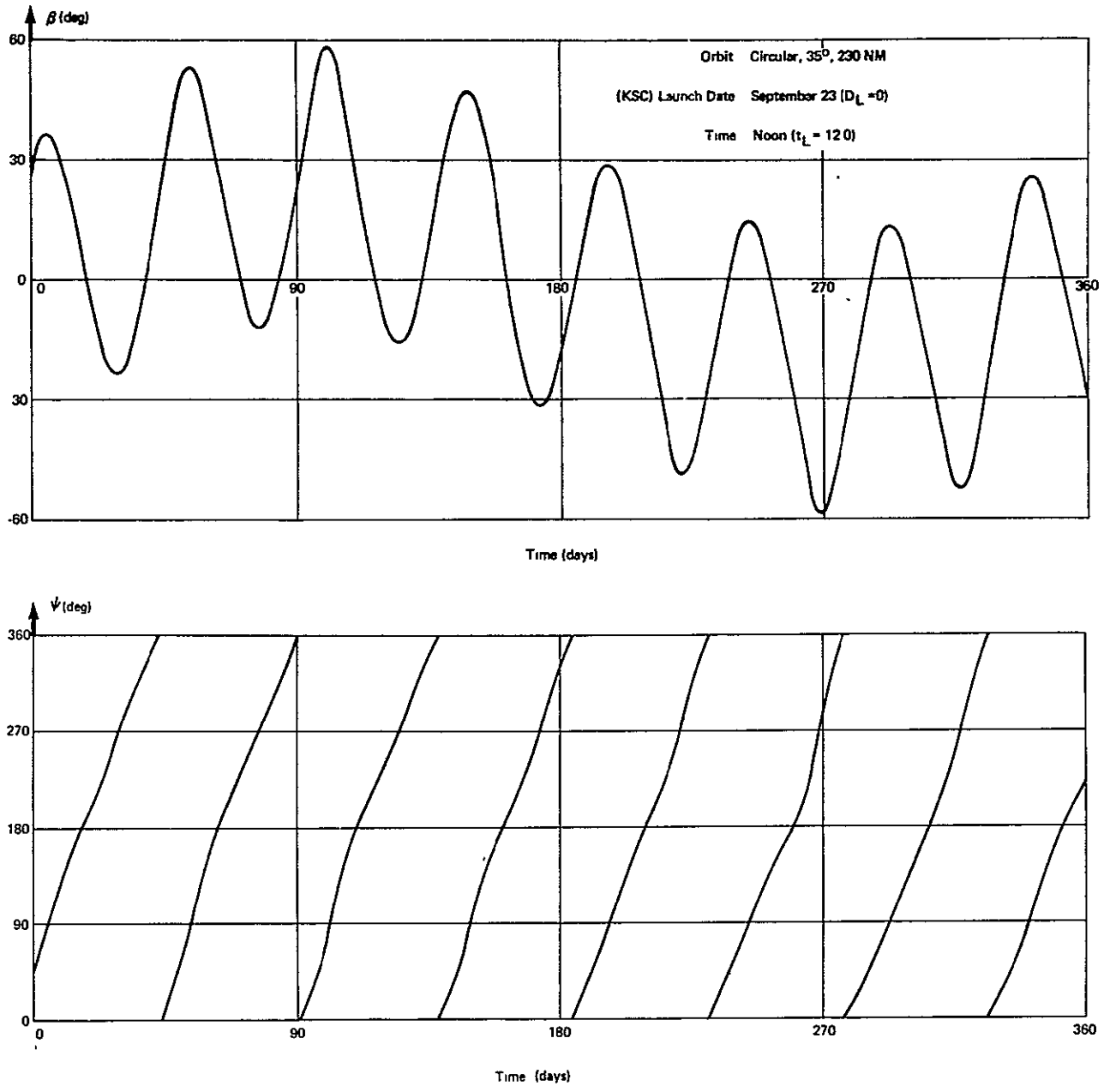

Figure (4 - 1) - Typical Variation in Solar Pointing Angles.

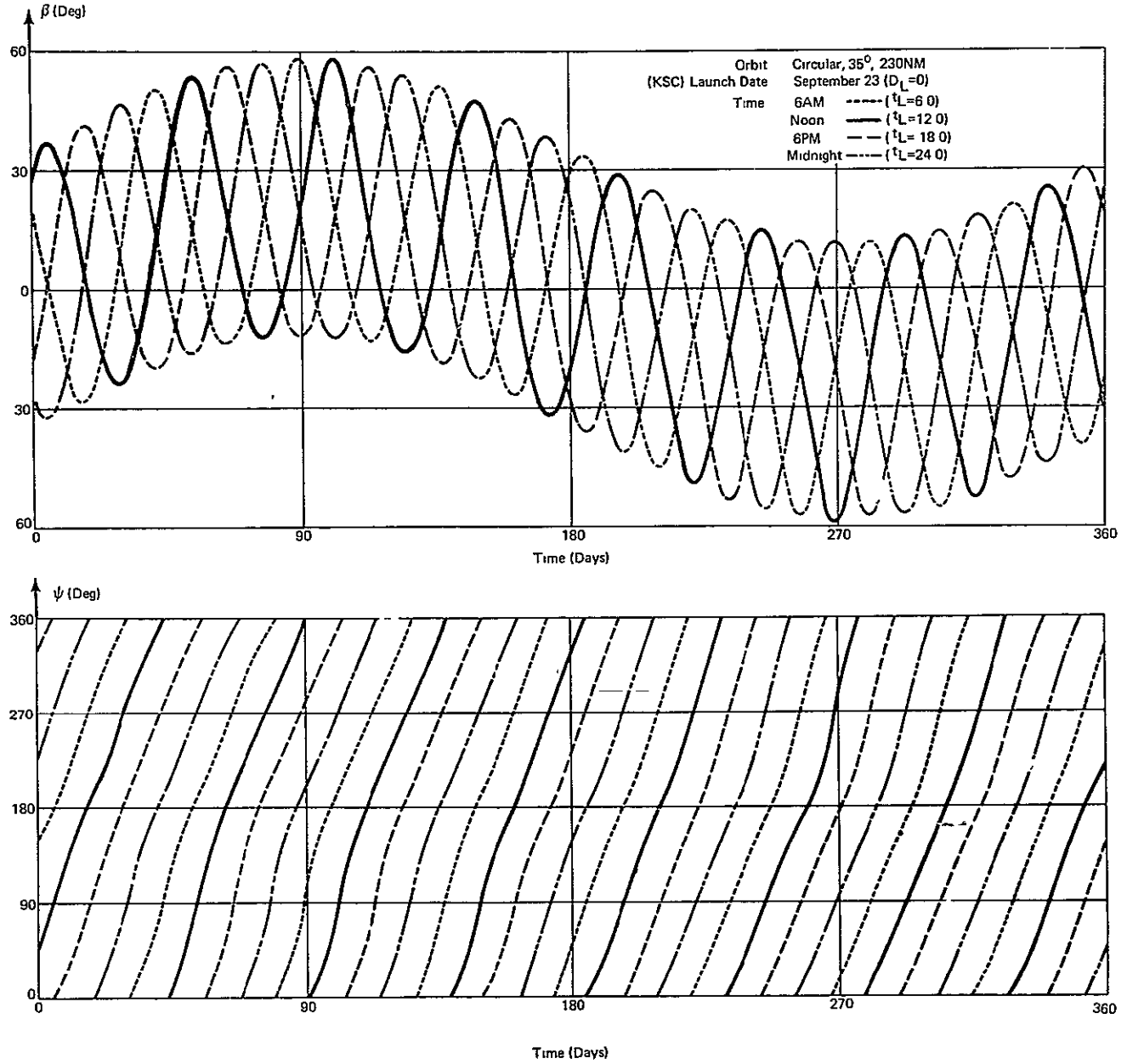

Figure (4 - 2) - Effects of Launch Time on Solar Pointing Angle Variation .

parameters are based on a 35°, 230 NM circular orbit (i=35°, H=230 NM, ε=0) which corresponds to $\dot{\Omega}_r$=-6.51 deg/day. The effect of launch time on β and ψ is shown in Fig.(4-2) where the curves correspond to four different launch times (t_L=6,12,18,24) with the other parameters the same as those used for Fig.(4-1).

The results shown in Figs.(4-1) and (4-2) indicate that ψ increases monotonically with time, in fact, almost linearly. The curves also indicate that β varies harmonically within an envelope whose maximum magnitude occurs at the two solstices (γ_o=90°,270°) with the value $|\beta|_{max}$=(i+e). It is of interest to examine these properties in general. Other characteristics of β and ψ are also of interest, namely $|\dot{\beta}|_{max}$, $|\dot{\psi}|_{ave}$, and $|\dot{\psi}|_{max}$. In the following subsections analytical expressions are obtained which relate these various characteristics to γ, Ω_r and i.

4.1 β Envelope

The β envelope defines the possible extremes of β which may exist at any time of year (γ). At any particular time (γ fixed) extreme values of β can be determined by differentiating $s\beta$ in Eq.(3-5) with respect to Ω_r, since

$$\frac{\partial\, s\beta}{\partial \Omega_r} = \frac{\partial\, s\beta}{\partial \beta} \cdot \frac{\partial \beta}{\partial \Omega_r} = c\beta \frac{\partial \beta}{\partial \Omega_r}$$

Hence, it follows that

$$\frac{\partial\, s\beta}{\partial \Omega_r} = -si(s\gamma\ s\Omega_r\ ce + c\gamma\ c\Omega_r) = 0 \qquad (4\text{-}5)$$

which implies that

$$\tan\Omega_r = -1/(\tan\gamma\ ce) \qquad (4\text{-}6)$$

The two possible solutions for Ω_r give rise to the upper and lower boundaries of the envelope. Using Eq.(4-6) with Eq.(3-5) yields the boundary equations in terms of $s\beta$.

$$s\beta = s\alpha_d\ ci \pm si\ c\alpha_d = s(\alpha_d \pm i) \equiv s\beta_{eb} \qquad (4\text{-}7)$$

where

$$s\alpha_d \equiv s\gamma\ se \tag{4-8}$$

The + and - algebraic signs correspond respectively to the upper and lower envelope boundaries. The angle $-\alpha_d$ can be interpreted physically as the sun declination relative to the equatorial plane.

The time of year (γ) corresponding to the maximum points on the envelope, namely $|\beta|_{max}$, can be determined from

$$\frac{\partial s\beta_{eb}}{\partial \gamma} = \frac{\partial s\beta_{eb}}{\partial \alpha_d} \cdot \frac{\partial \alpha_d}{\partial \gamma} = c(\alpha_d \pm i) \cdot \frac{c\gamma\ se}{c\alpha_d} = 0 \tag{4-9}$$

The solutions for γ obtained from $c(\alpha_d \pm i)=0$ yield

$$s\gamma = \pm\ ci/se = \pm\ ci/c(90°-e) \equiv s\hat{\gamma} \tag{4-10}$$

However, these apply only if $(90°-e) \leq i \leq (90°+e)$. The other solutions for γ follow from $c\gamma=0$ which yields

$$\gamma = 90°, 270° \equiv \hat{\gamma} \tag{4-11}$$

This case applies for $0 \leq i \leq (90°-e)$ and $(90°+e) \leq i \leq 180°$.

The values of $|\beta|_{max}$ and the values $\gamma=\hat{\gamma}$ and $\Omega_r=\hat{\Omega}_r$* yielding $|\beta|_{max}$ are summarized in Table 4-1 for the four applicable ranges of orbital inclination.

TABLE 4-1 — β Envelope Parameters as a Function of Orbital Inclination

Envelope Parameters \ Inclination** Range	(A) $0° \leq i < (90° - e)$	(B) $(90° - e) \leq i \leq 90°$	(C) $90° \leq i \leq (90° + e)$	(D) $(90° + e) < i \leq 180°$
$\lvert\beta\rvert_{max}$	$i + e$	$90°$	$90°$	$180° - i + e$
$\hat{\gamma}$	$90°, 270°$	$\pm \sin^{-1}$ (ci/se)	$\pm \sin^{-1}$ (ci/se)	$90°, 270°$
$\hat{\Omega}_r$***	$0°$	$\tilde{\Omega}_r$	$180° + \tilde{\Omega}_r$	$180°$

*$\hat{\Omega}_r$ is obtained by solving Eq. (4-6) with $\gamma=\hat{\gamma}$.

**$e = 23.45°$

***$\tilde{\Omega}_r \equiv \tan^{-1}[-1/(\tan\hat{\gamma}\ ce)]$; $-90° \leq \tilde{\Omega}_r \leq 90°$.

Plots indicating the form of the β envelope for the four ranges of inclination (A,B,C,D) in Table 4-1 and two special cases (i=0°,180°) are shown in Fig.(4-3). The upper and lower boundaries are inverted images of each other about γ=0° or 180°. For ranges A and D the upper and lower boundaries are separated by a constant angle, 2i and 360°-2i respectively, as may be deduced from Eq.(4-7). For ranges B and C this is true only for the values of γ between successive peaks of opposite sign. The The minimum boundary separation in ranges B and C is (180°-2e) which occurs at γ=90° and 270°.

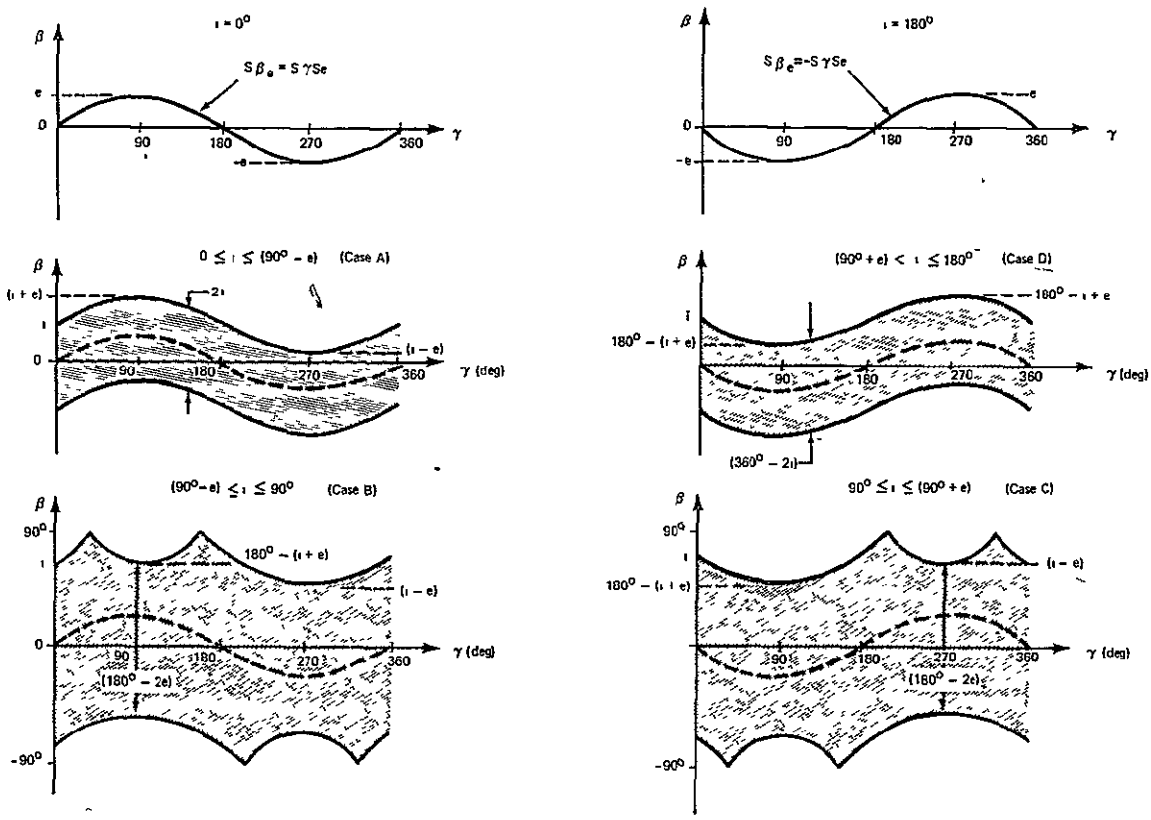

Figure (4 - 3) - Effect of Orbital Inclination on β Envelope.

4.2 $|\dot{\beta}|_{max}$

The angle β varies harmonically within the β envelope except for i=0°,180° when the envelope collapses to a median curve defined by

$$\beta_e = \sin^{-1}(s\gamma\ se) \qquad (i=0°) \qquad (4-12)$$

$$\beta_e = \sin^{-1}(-s\gamma\ se) \qquad (i=180°) \qquad (4-13)$$

which is the sun declination profile relative to the equatorial plane. Unless i=0°,180° or a particular inclination (i_{ss}) corresponding to a sun-synchronous orbit*, β crosses the median curve between successive intersections with the upper and lower boundaries as illustrated in Fig.(4-4) for ranges A and B of Table 4-1.

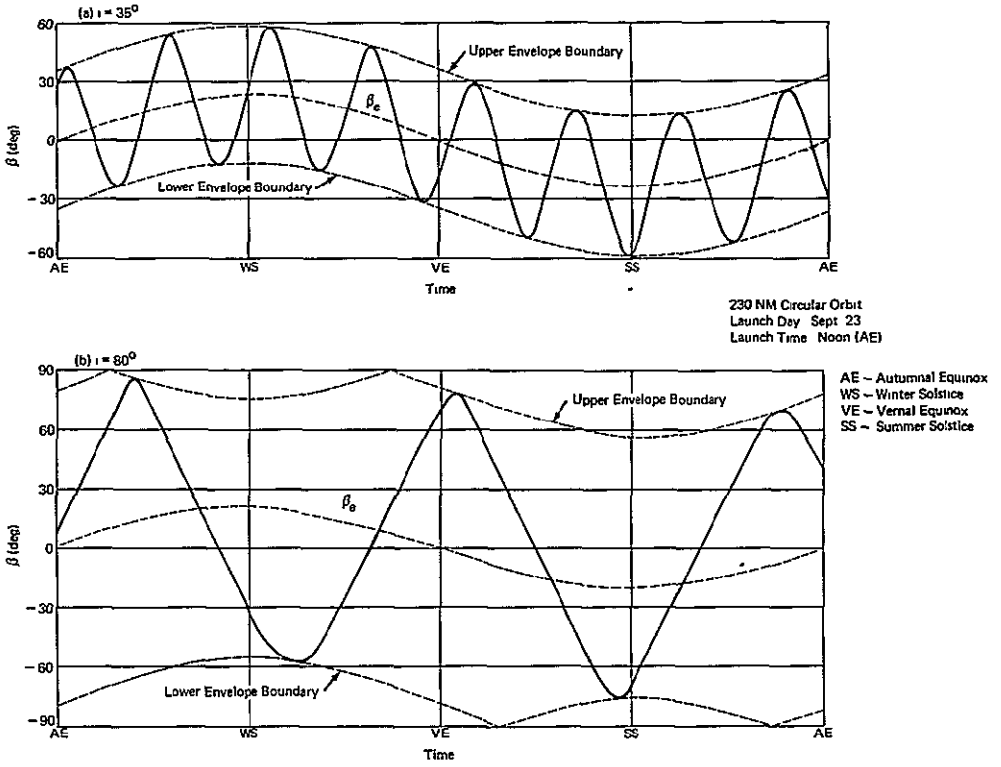

Figure (4 - 4) - Typical β Variation for Orbital Inclination in Ranges A and B.

The time rate of change of β can be calculated by differentiating Eq.(3-5) which yields

$$\frac{d(s\beta)}{dt} = c\beta\,\dot{\beta} = \left(\frac{\partial\, s\beta}{\partial\, \Omega_r}\right)\dot{\Omega}_r + \left(\frac{\partial\, s\beta}{\partial \gamma}\right)\dot{\gamma} \qquad (4\text{-}14)$$

or

$$\dot{\beta} = \frac{K_1\dot{\Omega}_r + K_2\dot{\gamma}}{c\beta} \qquad (4\text{-}15)$$

*See Section 4.4.

where

$$K_1 = -si(s\gamma\ ce\ s\Omega_r + c\gamma\ c\Omega_r) \tag{4-16}$$

$$K_2 = c\gamma(si\ ce\ c\Omega_r + ci\ se) + s\gamma\ s\Omega_r\ si \tag{4-17}$$

The β variation shown in Fig. (4-4a) suggests that $|\dot{\beta}|$ reaches a local maximum as β crosses the median curve. A formal solution for all $|\dot{\beta}|_{max}$ obtained by differentiating $\dot{\beta}$ with respect to γ and Ω_r in Eq. (4-15) is a tedious exercise. One solution is

$$|\hat{\dot{\beta}}| \equiv |(-\dot{\Omega}_r)si + \dot{\gamma}s(i+e)| = |\dot{\Omega}_{rm}si\ ci + \dot{\gamma}s(i+e)| \tag{4-18}$$

and the corresponding γ and Ω_r are

$$\Omega_r = 0°; \quad \gamma = 0°, 180° \qquad 0° \leq i \leq 90° \tag{4-19}$$

$$\Omega_r = 180°; \quad \gamma = 0°, 180° \qquad 90° < i \leq 180° \tag{4-20}$$

In Fig. (4-5) the dashed curve represents $|\hat{\dot{\beta}}|$ plotted versus inclination. The solid curve is a numerical solution for $|\dot{\beta}|_{max}$

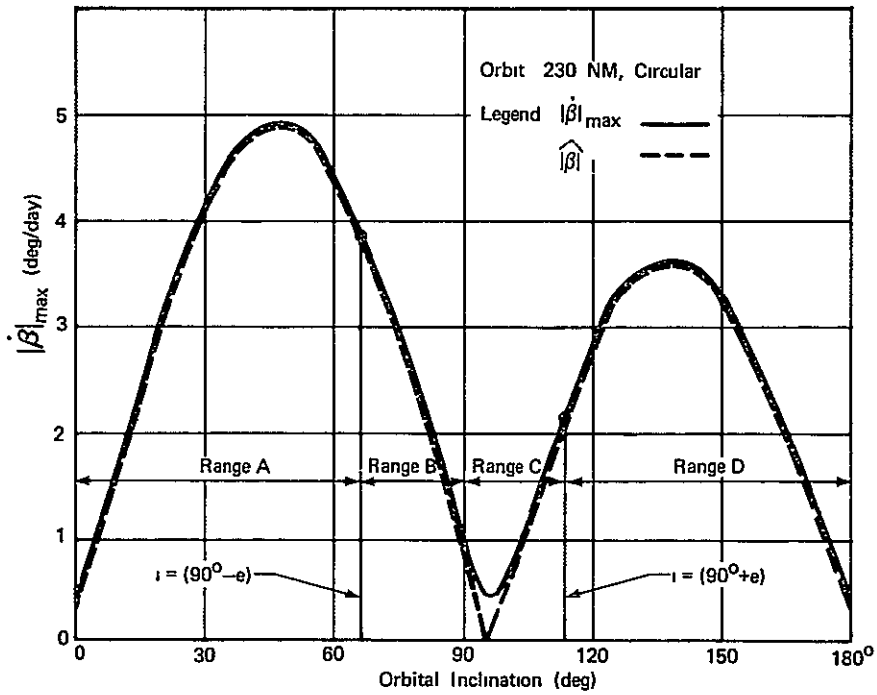

Figure (4 - 5) - $|\dot{\beta}|_{max}$ vs. Orbital Inclination

obtained by scanning all γ, Ω_r. From the figure it is evident that $|\hat{\dot{\beta}}|$ is indeed the upper limit of $|\dot{\beta}|$ when i is in the range A or D of Fig.(4-3). For i in the range B or C, $|\hat{\dot{\beta}}|$ is also the upper limit of $|\dot{\beta}|$ except in the vicinity of the inclination, i_{ss}.

The upper limit on $|\dot{\beta}|_{max}$ occurs at an inclination in range A. Differentiating $|\hat{\dot{\beta}}|$ with respect to i leads to the equation

$$c2i = (-\dot{\gamma}/\dot{\Omega}_{rm})\,c(i+e) \qquad (4\text{-}21)$$

Applicable solutions for i lie in the range $45°<i<(90°-e)$ and depend on $\dot{\Omega}_{rm}$*. A plot of the corresponding upper limit on $|\dot{\beta}|_{max}$ is shown in Fig.(4-6) as a function of altitude for circular orbits. For 230 NM the absolute upper limit is $|\dot{\beta}|_{max,max}$ = 4.90 deg/day at an inclination of 46.3°. This compares with $|\dot{\beta}|_{max}$ = 4.60 deg/day for i=35° at 230 NM as shown in Fig.(4-5).

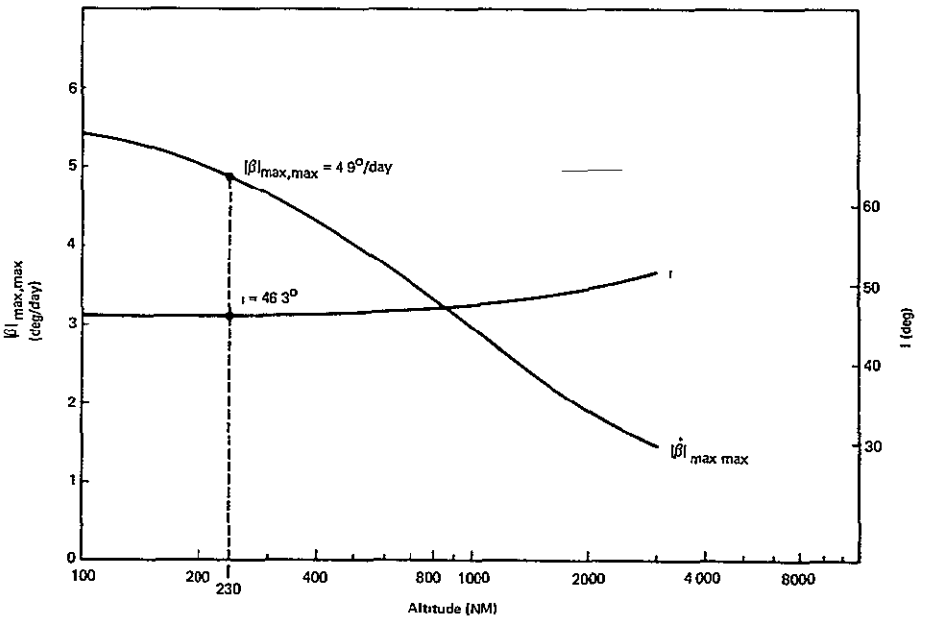

Figure (4 - 6) - Upper Limits of $|\dot{\beta}|_{max}$ and Corresponding Orbital Inclination vs Altitude (Circular Orbits).

*$\dot{\Omega}_{rm}$ is a function of the orbit semi-major axis and eccentricity in elliptical orbits and a function of orbital altitude alone in circular orbits. See Eq.(2-14).

4.3 Properties of ψ

The monotonic variation of ψ for the case shown in Fig.(4-1) indicates that $\dot{\psi}$ remains positive and fluctuates about some average rate, $\dot{\psi}_{ave}$. General conditions under which these properties hold can be determined from an expression for $\dot{\psi}$. Differentiating tan ψ in Eq.(3-6) with respect to time yields

$$\frac{d}{dt}(\tan\psi) = \dot{\psi}\sec^2\psi = \frac{\dot{S}_1 S_3 - S_1 \dot{S}_3}{S_3^2} \tag{4-22}$$

where S_1 and S_3 are defined by Eq.(3-4). Substituting for S_1, S_3, $\dot{S}_1$, and $\dot{S}_3$ and using Eq.(2-12) yields

$$\dot{\psi} = \frac{F\,\dot{\Omega}_{rm} + G\,\dot{\gamma}}{c^2\beta} \equiv \frac{g}{c^2\beta} \tag{4-23}$$

where

$$F \equiv ci(ci - s\gamma\ se\ s\beta) \tag{4-24}$$

$$G \equiv (ci\ ce - c\Omega_r\ si\ se) \tag{4-25}$$

The coefficient F is positive for all (γ,Ω_r) when the orbital inclination i is in ranges A and D defined in Table (4-1) and Fig.(4-3)*. In range A the coefficient G is positive for all Ω_r, but in range D it is negative for all Ω_r.** Since $\dot{\Omega}_{rm}$ and $\dot{\gamma}$ are positive, $\dot{\psi}$ is always positive in range A and will be positive for all i in range D provided that $\dot{\Omega}_{rm}$ is sufficiently large. For circular orbits this is the case for orbital

---

*Since the extreme value of $s\gamma s\beta$ is s(i+e) in range A and -s(i-e) in range D, it follows that F_{min}=cicec(i+e)>0 in range A and F_{min}=cicec(i-e)>0 in range D.

**Extreme values of G occur for Ω_r=0° in range A where G_{min}=c(i+e)>0 and for Ω_r=180° in range D where G_{max}=c(i-e)<0.

altitudes less than 690 NM.* Since coefficients F and G may be positive or negative for i in ranges B and C, the monotonic variation of ψ will not prevail, but may occur at intervals.

4.3a $\dot{\psi}_{ave}$

Although $\dot{\psi}$ is positive for i in ranges A and D it fluctuates about an average rate $\dot{\psi}_{ave}$, as observed previously. This average rate can be calculated by observing the number of revolutions of ψ over a particular time interval. Revolutions of ψ can be referenced to a point where $\psi=\pi/2$, which occurs when $S_3=0$ in Eq.(3-6) and implies that

$$\tan\Omega_r = -1/(\tan\gamma \; ce) \tag{4-26}$$

the same condition, Eq.(4-5), for β to intersect the β envelope.** Let Ω_r', γ' and ψ_o be values of Ω_r, γ and ψ at time, t=0. Suppose the ratio $|\dot{\Omega}_r|/\dot{\gamma}$ is rational; then at some time $t\equiv\tau=2\pi k/\dot{\gamma}$, Ω_r and γ become

$$\begin{aligned} \Omega_r &= \Omega_r' + \dot{\Omega}_r\tau = \Omega_r' \mp 2\pi m \\ \gamma &= \gamma' + \dot{\gamma}\tau = \gamma' + 2\pi k \quad (m,k \text{ integers}) \end{aligned} \tag{4-27}$$

where $(\mp)$ signs account for the sign of $\dot{\Omega}_r$.*** Inspection of solutions to Eq.(4-26) reveals that in the same interval τ, ψ makes exactly $m\pm k$ revolutions so that

$$\psi(\tau) = 2\pi(m\pm k) + \psi_o \tag{4-28}$$

Thus,

$$\dot{\psi}_{ave} \equiv \frac{\psi(\tau)-\psi_o}{\tau} = \frac{2\pi(m\pm k)}{2\pi k/\dot{\gamma}} = \dot{\gamma}\left(\frac{m}{k}\pm 1\right) \tag{4-29}$$

---

*The altitude limit for $\dot{\psi}>0$ is a minimum at i=90°+e. At inclinations above 90°+e the altitude range for $\dot{\psi}>0$ expands considerably (e.g., altitude limits at i=90°+2e and i=180° are 2206 NM and 3075 NM). This limit is found from Eq.(2-14) after minimizing g in Eq.(4-23) with respect to γ and Ω_r and evaluating $\dot{\Omega}_{rm}$ such that $g_{min}=0$.

**Hence, revolutions of ψ (relative to $n\pi/2$, n=1,3,...) are synonymous with successive intersections of β with either the upper or lower envelope boundary.

***In what follows, the upper sign in $(\pm)$ or $(\mp)$ applies to range A and the lower sign to range D.

But $m/k = \mp \dot{\Omega}_r/\dot{\gamma}$ from Eq. (4-27) so that*

$$\dot{\psi}_{ave} = (\mp \dot{\Omega}_r \pm \dot{\gamma}) = \begin{cases} (\dot{\Omega}_{rm}\, ci + \dot{\gamma}), & \text{Range A} \\ -(\dot{\Omega}_{rm}\, ci + \dot{\gamma}), & \text{Range D} \end{cases} \tag{4-30}$$

Although based on a rational ratio for $|\dot{\Omega}_r|/\dot{\gamma}$, this result is approached in general for τ sufficiently large. To show this, let

$$\begin{aligned} \Omega_r &= \Omega_r' + \dot{\Omega}_r \tau = \Omega_r' + \Omega_{re} \mp 2m\pi \\ \gamma &= \gamma' + \dot{\gamma}\,\tau = \gamma' + 2k\pi \end{aligned} \tag{4-31}$$

at time τ, so that

$$\psi(\tau) = 2\pi(m \pm k) + \psi_e + \psi_o \tag{4-32}$$

where $-\pi < (\Omega_{re}, \psi_e) < \pi$ represent the residue in Ω_r and ψ for $|\dot{\Omega}_r|/\dot{\gamma}$ not rational. Thus

$$\dot{\psi}_{ave} = \frac{\psi(\tau) - \psi_o}{\tau} = \dot{\gamma}\left(\frac{m}{k} \pm 1\right) + \frac{\dot{\gamma}}{k}\frac{\psi_e}{2\pi} \tag{4-33}$$

Solving for m/k from Eq. (4-31) and substituting into Eq. (4-33) yields

$$\dot{\psi}_{ave} = (\mp \dot{\Omega}_r \pm \dot{\gamma}) + \frac{\dot{\gamma}}{k}\left(\frac{\psi_e \pm \Omega_{re}}{2\pi}\right) \tag{4-34}$$

which approaches the result in Eq. (4-30) as k (i.e., τ) increases.

A plot of $\dot{\psi}_{ave}$ for a 230 NM circular orbit and orbital inclination in ranges A and D is shown in Fig. (4-7). Since $\dot{\psi}$ may be either positive or negative for i in ranges B and C, $|\dot{\psi}_{ave}|$ generally will be less than the result given in Eq. (4-30). Extrapolation of the $\dot{\psi}_{ave}$ curves for ranges A and D into ranges B and C is also shown in Fig. (4-7) for comparison.

---

*Hence, successive intersections of β with either the upper or lower envelope boundary occur at intervals of $2\pi/\dot{\psi}_{ave}$, on the average.

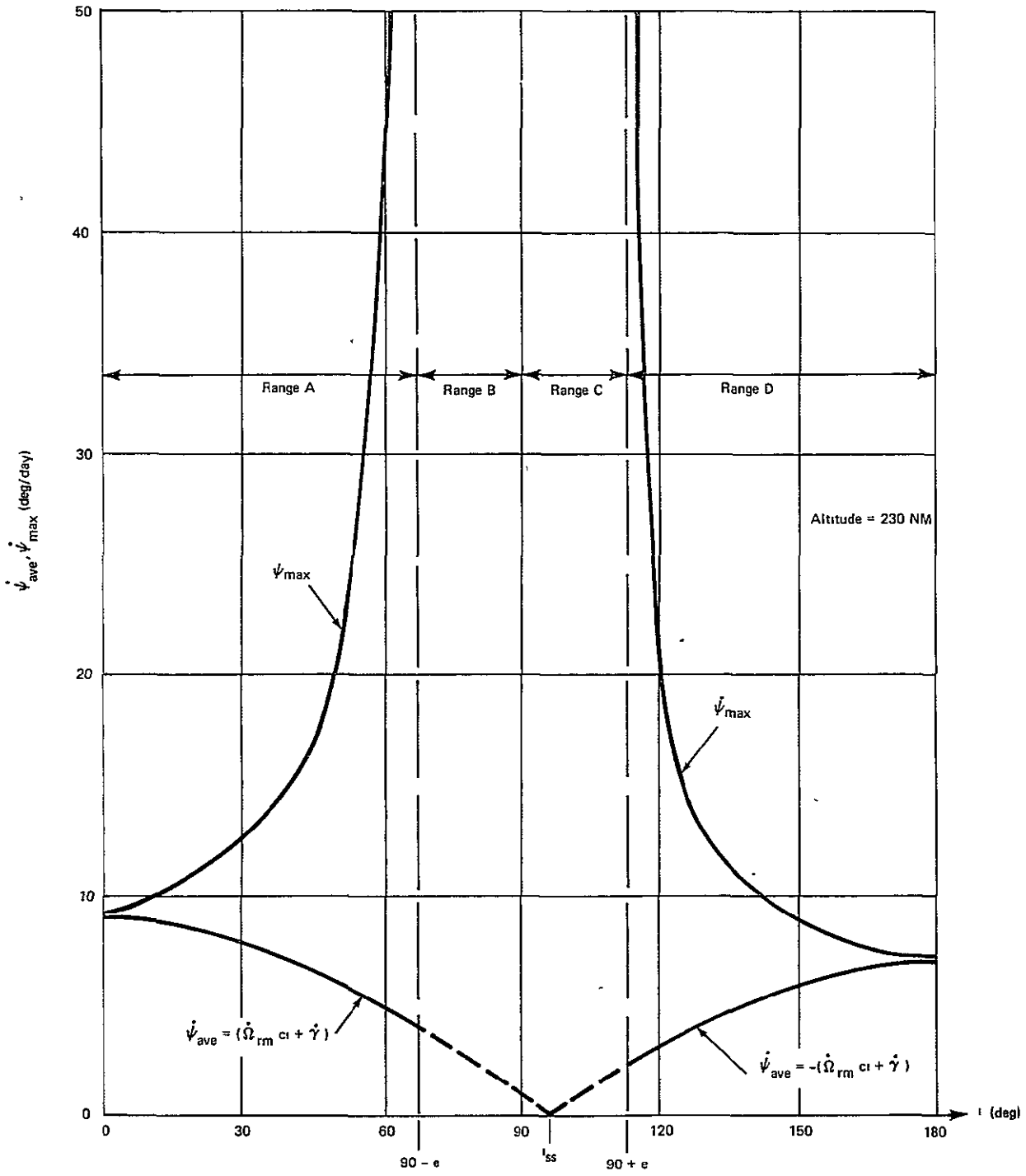

Figure (4 - 7) - $\dot{\psi}_{ave}$ and $\dot{\psi}_{max}$ vs. Orbit Inclination (Circular Orbits).

4.3b $\dot{\psi}_{max}$

The ripple on the curve of $\dot{\psi}$ vs t shown in Fig.(4-1) reflects the fluctuation of $\dot{\psi}$ about $\dot{\psi}_{ave}$. At orbital inclinations where β may approach 90°, $\dot{\psi}$ can be large at times, in fact infinite when β=90°. These aspects are illustrated in Fig.(4-8) where typical β and ψ variations are plotted versus time for two orbital inclinations: one in range B and one in range A near (90°-e).*

As is apparent from Fig.(4-8) local maxima of $\dot{\psi}$ occur as β reaches the β envelope. The upper bounds on $\dot{\psi}$ can be shown to be

$$\dot{\psi}_{max} = \begin{cases} \dfrac{\dot{\Omega}_{rm}\ ci\ ce + \dot{\gamma}}{c(i \pm e)} & (+)\ \text{Range A, } (-)\ \text{Range D} \\ \pm\ \infty & \text{Ranges B and C} \end{cases} \qquad (4\text{-}34)$$

The corresponding γ and Ω_r for each range of inclination are as given in Table(4-1). For comparison with $\dot{\psi}_{ave}$ these results are plotted versus i in Fig.(4-7) for a 230 NM circular orbit.

*Having $\dot{\psi} \to \infty$ is not a serious problem since it merely represents an instantaneous condition for satisfying the solar pointing requirement as the orbital plane passes through an orientation where it is normal to the sun line (β=90°). As a practical matter, the "jump" in ψ can be accomplished in finite time with spacecraft maneuvers or experiment gimbaling without significant time interruption of a solar pointing mode.

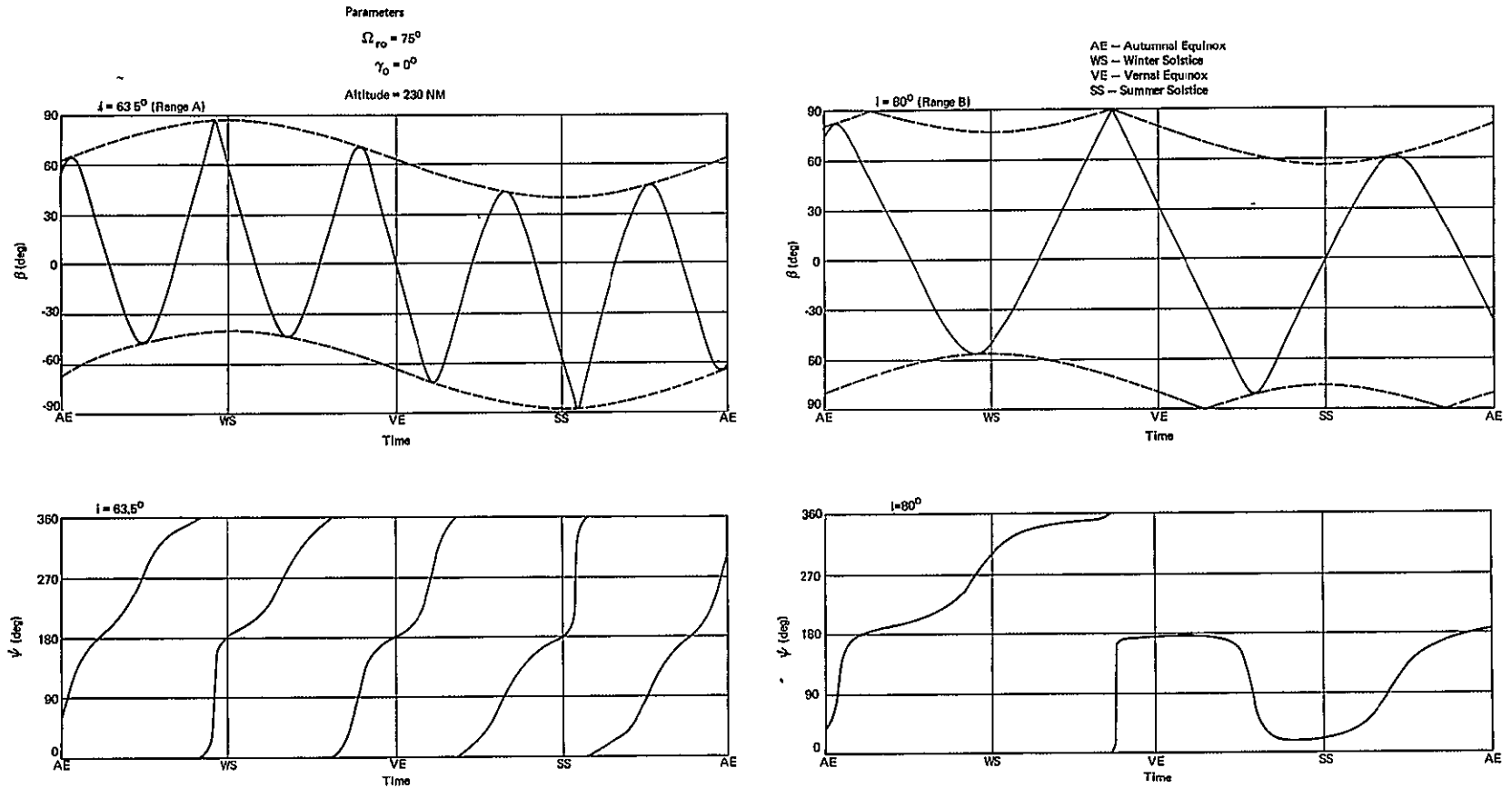

Figure (4 - 8) - Typical β and ψ Variations for Orbit Inclinations where β Approaches 90^0.

4.4 β Variation in Sun-Synchronous Orbits

A sun-synchronous orbit has been defined[7] as "an earth orbit whose plane rotates about the earth's axis just one revolution per year and remains in step with the earth's rotation about the sun."* This implies that $\dot{\Omega}_r = \dot{\gamma}$ or in view of Eq.(2-12) that

$$ci = -\dot{\gamma}/\dot{\Omega}_{rm} \equiv ci_{ss} \tag{4-35}$$

Since $\dot{\gamma}$ and $\dot{\Omega}_{rm}$ are positive, sun-synchronous orbits are necessarily retrograde orbits ($90° < i_{ss} \leq 180°$). The relationship between orbital inclination and altitude for attaining sun-synchronous circular orbits based on Eqs.(2-14) and (4-35) is plotted in Fig.(4-9). For a 230 NM circular orbit the required inclination is 97.13°.

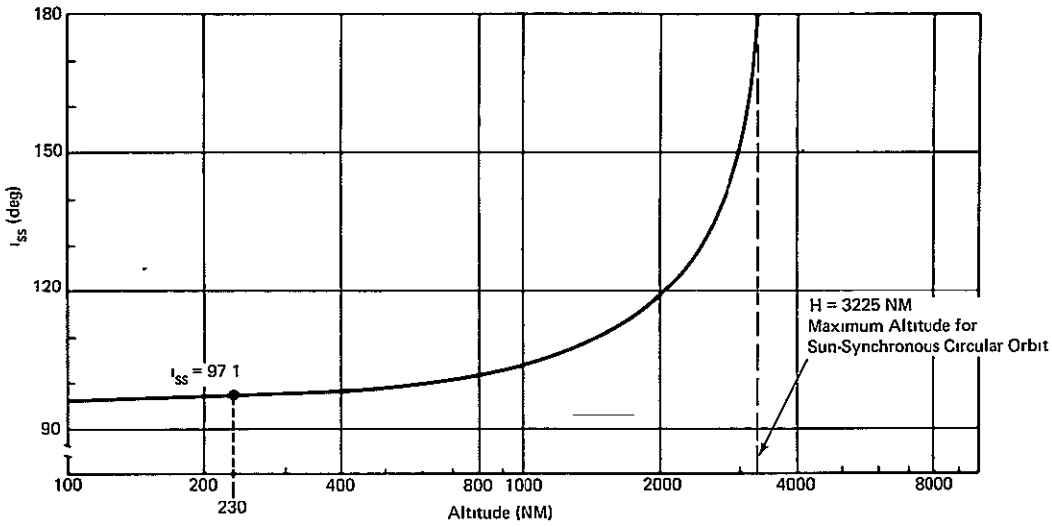

Figure (4 - 9) - Orbital Inclination and Altitude Requirements for Sun-Synchronous Circular Orbits.

The β variation in a sun-synchronous orbit can be determined from Eqs.(2-7), (2-10) and (3-7) where the nodal rotation is given by

$$\Omega_r = \Omega_{ro} + \dot{\gamma}t \pm \gamma_o = \bar{\Omega}_r + \gamma \tag{4-36}$$

and

$$\bar{\Omega}_r \equiv \Omega_{ro} - \gamma_o \tag{4-37}$$

is a constant depending upon initial conditions. From Eqs.(3-7) and (4-36) it follows that

$$s\beta = f + g\, s\gamma + h\, s(2\gamma + \bar{\Omega}_r) \tag{4-38}$$

*Since the earth's orbit is slightly elliptical, "remains in step" is not true exactly, only on the average. However, the deviation is small.

where

$$f \equiv -si\left(\frac{1+ce}{2}\right)s\bar{\Omega}_r \tag{4-39}$$

$$g \equiv ci\ se \tag{4-40}$$

$$h \equiv -si\left(\frac{1-ce}{2}\right) \tag{4-41}$$

Hence, in sun-synchronous orbits β varies about a constant, $\beta_s=\sin^{-1}(-sis\Omega_r)$, with two dominant frequency components, $\dot{\gamma}$ and $2\dot{\gamma}$. Curves of β vs t are plotted in Fig.(4-10) for various values of $\bar{\Omega}_r$.

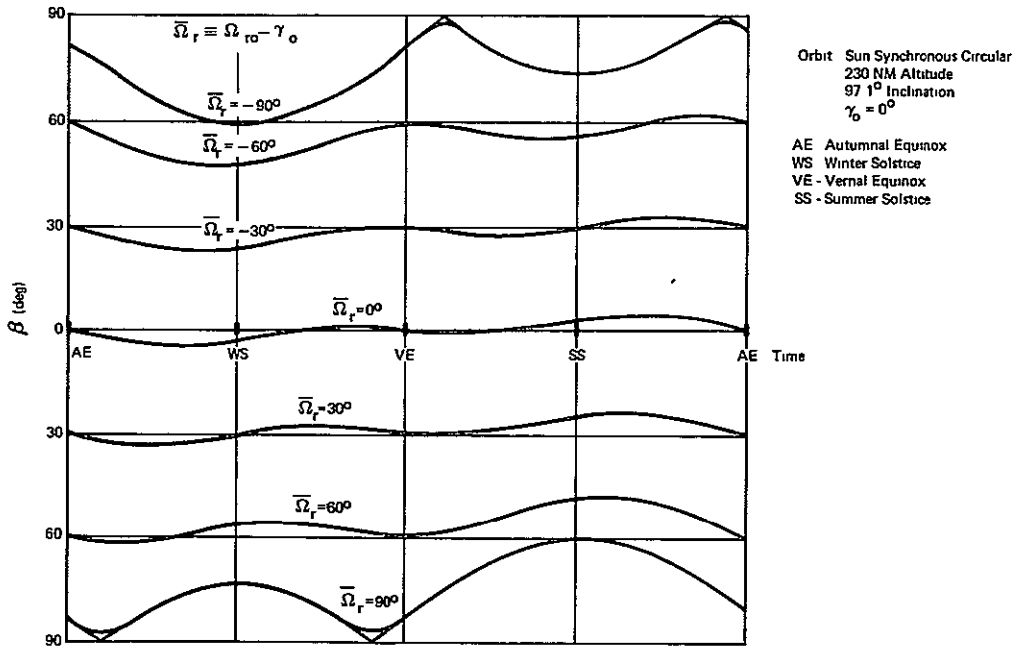

Figure (4 - 10) - β Profiles in Sun-Synchronous Orbits.

These results indicate that β does not make successive intersections with the β envelope as in non-sun-synchronous orbits. Since the constants g and h in Eq.(4-38) are small, β remains in the vicinity of $-\bar{\Omega}_r$ except near $\bar{\Omega}_r=\pm 90°$ where it follows the envelope variation.* The results are similar

*For $\bar{\Omega}_r=\pm 90°$, it follows from Eqs.(3-5) and (4-6) that

$$s\beta = ci(s\gamma se) \mp si[1-s^2\gamma(1-ce)]$$

which is nearly equivalent to the β envelope equations. The first term in this equation and that in Eq.(4-7) are equal and the second terms are identical through the first two terms of a series expansion in e.

for $90° < |\bar{\Omega}_r| \leq 180°$ with β varying about zero for $\bar{\Omega}_r = \pm 180°$. Sun-synchronous orbits may be of particular interest for long duration missions where a relatively flat β profile is of importance in certain photographic or earth viewing experiments.

4.5 Summary of β, ψ Properties

General properties of the solar pointing angles (β, ψ) have been evaluated as a function of time of year (sun line location, γ), ascending node location (Ω_r), orbital inclination (i) and the sun line and nodal rotation rates $(\dot{\gamma}, \dot{\Omega}_r)$. Specific properties depend on the range of orbital inclination (A,B,C, or D) defined in Table(4-1). In general β varies harmonically within an envelope which depends on both γ and i. Upper limits for the envelope are given in Table(4-1). Limits on $|\dot{\beta}|_{max}$ within the β envelope are shown in Figs.(4-5) and (4-6) and may be evaluated from Eq.(4-18).

The angle ψ increases monotonically for i in ranges A and D, but not necessarily in ranges C and D where the orbital plane may pass through an orientation normal to the sun line $(|\beta| = 90°)$. In all cases where $|\beta|$ approaches 90°, $|\dot{\psi}|$ increases sharply with $|\dot{\psi}|_{max} = \infty$, theoretically. A summary of properties of (β, ψ) for typical AAP Workshop missions is given in Table(4-2).

TABLE (4-2) Summary of (β, ψ) Properties for Two 230 NM Circular Orbits)

i	$\dot{\Omega}_r$	$\dot{\Omega}_a$	$\lvert\beta\rvert$ max	$\lvert\beta\rvert$ max	$\dot{\psi}_{ave}$	$\dot{\psi}_{max}$
35°	-6.5° / day	9.3° /day	58.45°	4.57° / day	7.5° / day	13.2° / day
50°	-5.1° / day	4.2° /day	73.45°	4.86° / day	6.1° / day	19.9° / day

As noted in Section 4.3a, β intersects the β envelope when $\psi = n\pi/2$ $(n = 1, 3, \ldots)$. Although this does not occur uniformly in time, successive intersections with either the upper or lower envelope boundary occur at intervals of $360°/\dot{\psi}_{ave}$, on the average. Hence, the "average period" of the β variation is 48 days in a 35°, 230 NM orbit and 59 days in a 50°, 230 NM orbit.

In sun-synchronous orbits ($\dot{\Omega}_r = \dot{\gamma}$), β does not make successive intersections with the β envelope, but varies slightly about a constant, $\beta_s = -\sin^{-1}[s_i s(\Omega_{ro}-\gamma_o)]$ as shown in Fig.(4-10). Since β_s can be selected by appropriate choice of launch conditions (Ω_{ro}, γ_o), sun-synchronous orbits may be of interest where a relatively flat β profile is of importance for photographic and earth-viewing experiments, electrical power from solar arrays and spacecraft thermal control considerations.

Physically, ψ represents the angle between orbital noon and the ascending node as shown in Fig.(1-1). Hence, noon may advance relative to the ascending node by as much as 13.2°/day in a 35°, 230 NM orbit and 19.9°/day in a 50°, 230 NM orbit. This is of interest in the Saturn-V Workshop (SVWS) mission where the ascending node will be located by ground tracking and orbital noon by calculating ψ.

In maintaining the solar-inertial mode spacecraft motion can be described in terms of azimuth and elevation maneuvers relative to the nodal coordinate system (x_n,y_n,z_n) in Fig.(1-1). The elevation maneuver rate ($\dot{\beta}_a$) is simply $\dot{\beta}$, but because of orbital plane motion ($\dot{\Omega}_a$)*, the azimuth maneuver rate ($\dot{\psi}_a$) is

$$\dot{\psi}_a = \dot{\psi} - \dot{\Omega}_a \qquad (4\text{-}42)$$

Hence, the maximum azimuth maneuver rate, $(\dot{\psi}_a)_{max}$, is 3.9°/day in a 35°, 230 NM orbit and 15.7°/day in a 50°, 230 NM orbit. The maximum required angular momentum of the SVWS (including the effect of $\dot{\Omega}_r$ with $\dot{\beta}_a$ and $\dot{\psi}_a$) can be shown to be** $\sim$3.0 ft lb sec in the 35° orbit and $\sim$10.0 ft lb sec in the 50° orbit, which is well within the angular momentum capacity of the CMG system.

Pointing angles for maintaining solar arrays and experiments in a solar orientation with spacecraft in orbit-oriented modes are related to β. This relationship is developed in Appendix D for spacecraft in LV, LH and POP modes.

---

*See Footnote **, p. 9.

**Calculations are based on mass data in Reference 8.

5.0 EVALUATION OF SYSTEM PERFORMANCE FACTORS FOR CIRCULAR ORBITS*

Earth orbital mission design is influenced by a variety of conflicting constraints, some due to mission objectives and others due to orbit environmental aspects. Of importance in the latter category, for example, are the effects on attitude control, electrical power and thermal control system performance requirements imposed by motion of the orbital plane due to earth oblateness and motion of the earth about the sun. These effects on system performance can be related to the solar pointing angles, β and ψ, although in circular orbits only β may be involved.

The objective of this section is to examine various system performance factors which are related to β. Specifically, this includes evaluation of:

(1) the bias gravity gradient torque-impulse on spacecraft in a solar-inertial mode,

(2) the orbital sunlight-interval,

(3) the electrical energy per orbit available from solar arrays in LV, LH and POP attitude modes** with incrementally articulated solar arrays, and

(4) The incident thermal energy per orbit on spacecraft in LV, LH and POP modes** and on a flat solar panel in sun-oriented modes.

In this work spacecraft and solar array models are chosen primarily to illustrate general properties and the influence of the β variation. All results are given in normalized form which permits simple application or approximation to particular spacecraft configurations or changes in orbital altitude.

---

*Results in this section for circular orbits are essentially the same for slightly elliptical orbits of equal period. (See Footnote *, p. 4)

**See Footnote **, p. 1.

5.1 Gravity Gradient Torque-Impulse in Solar-Inertial Mode

An asymmetric* spacecraft in orbit experiences a torque due to the earth's gravitational field unless one principal axis remains parallel to the local vertical. In the solar inertial mode the orientation of the spacecraft geometric axes (x_{sc}, y_{sc}, z_{sc}) relative to the sun line and the orbital plane is defined by the solar pointing angles (β, ψ) as illustrated previously in Fig.(1-1). For the Saturn-V Workshop (SVWS) model shown in Fig.(5-1) the spacecraft principal axes are assumed to be displaced from the geometrical axes by a single rotation $(\hat{\phi})$ about the roll axis (x_{sc}).**

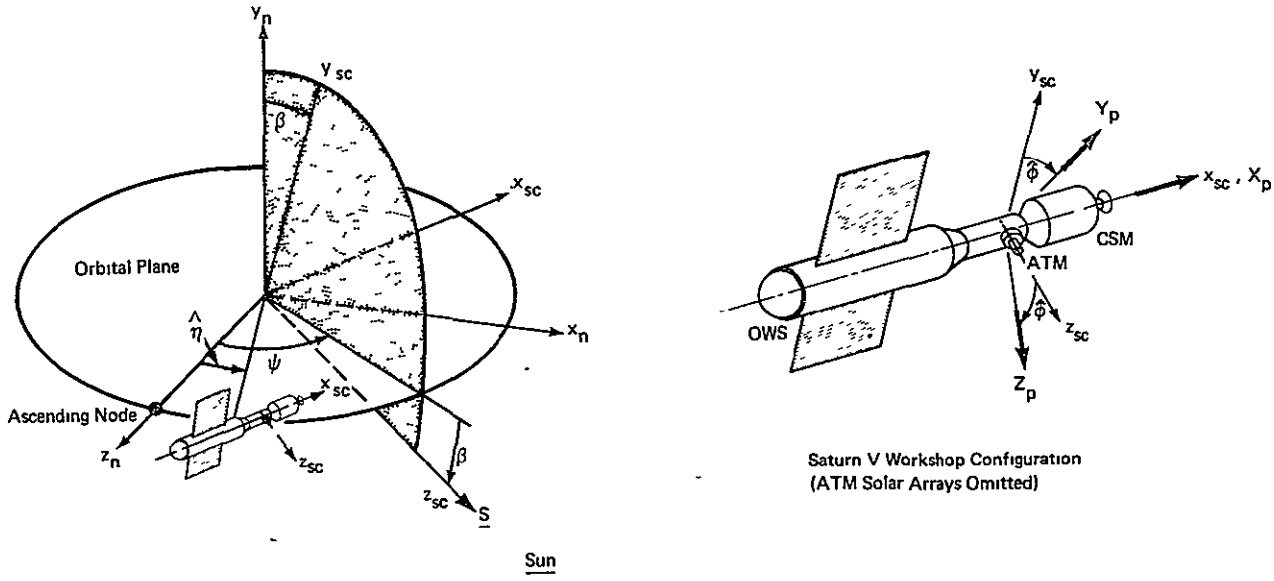

Figure (5 - 1) - Spacecraft Orientation in Solar - Inertial Mode .

*Here asymmetry implies unequal principal moments of inertia (i.e. $I_{xp} \neq I_{yp} \neq I_{zp}$).

**Coincidence of the principal axis of minimum moment of inertia (X_p) and the roll axis (x_{sc}) is a reasonable assumption for this analysis. In a current dry-workshop configuration[8] the actual displacement is only 3.6°. However, the rotation of transverse principal axes is 23°.

As given in Eq.(B-5) of Appendix B the gravity gradient torque for this orientation is

$$\underline{T}_{g_p} = \begin{pmatrix} T_{gx} \\ T_{gy} \\ T_{gz} \end{pmatrix} = \begin{pmatrix} T_{gmx}\ s2(\beta+\hat{\phi})c^2(\psi-\hat{\eta}) \\ T_{gmy}\ c(\beta+\hat{\phi})s2(\psi-\hat{\eta}) \\ T_{gmz}\ s(\beta+\hat{\phi})s2(\psi-\hat{\eta}) \end{pmatrix} \qquad (5\text{-}1)$$

where T_{gmx}, T_{gmy}, T_{gmz} represent the maximum values of torque along the respective spacecraft principal axes and $\hat{\eta}$ is the angle between local vertical and the nodal axis, z_n. The torque components T_{gy} and T_{gz} are purely periodic whereas T_{gx} is periodic about a bias value of*

$$(T_{gx})_{bias} = 1/2\ T_{gmx}\ s2(\beta+\hat{\phi}) \qquad (5\text{-}2)$$

Consequently, the magnitude of the gravity gradient torque-impulse (or bias momentum) over an orbit is*

$$|\underline{\Delta H}| = \left|\int_0^T \underline{T}_g dt\right| = \left|\frac{T_{gmx}\ T}{2}\right| |s2(\beta+\hat{\phi})| = \Delta H_{max} |s2(\beta+\hat{\phi})| \qquad (5\text{-}3)$$

where T is the orbital period. This result applies for both circular and elliptical orbits. Over a mission $|\underline{\Delta H}|$ will vary depending on β. In Fig.(5-2) a typical variation of $|\underline{\Delta H}|/\Delta H_{max} = |s2(\beta+\hat{\phi})|$ is shown for $\hat{\phi}=0°$ and 23° with the same orbit and launch conditions given previously in Fig.(4-1).

With momentum storage devices such as control moment gyros (CMGs) employed for attitude control, the periodic component of the gravity gradient torque-impulse is easily removed. However, the bias component of the torque-impulse causes an accumulation of angular momentum. In order to avoid eventual saturation, this bias momentum must be removed periodically. Three approaches for momentum dumping are based on:

---

*This result is based on keeping β and ψ constant which is a reasonable approximation over an orbital period.

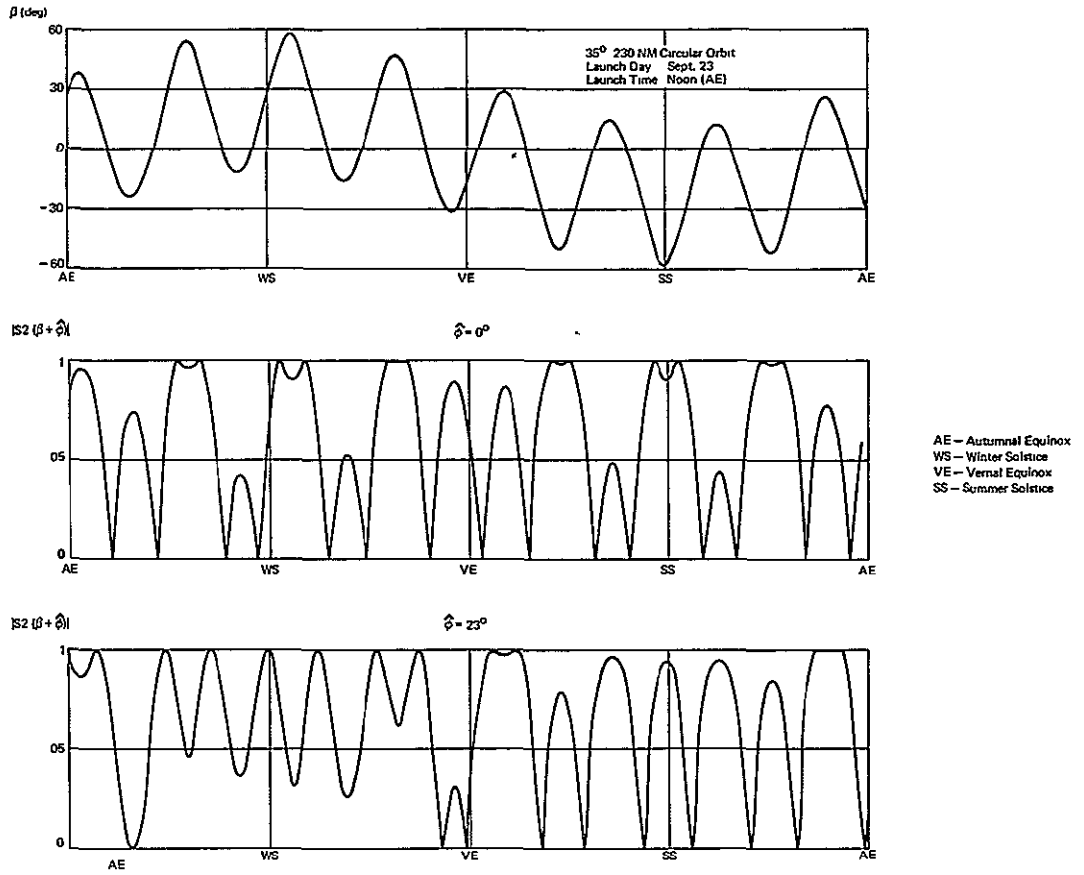

Figure (5 - 2) - Typical Variation of β and Normalized Bias Momentum.

1. reaction thrust - large torques produced by reaction jets provide rapid desaturation;

2. magnetic control[9] - interaction of a control magnetic dipole and the earth's magnetic field produces a bias torque for continuous gravity gradient bias torque cancellation or short period momentum desaturation;

3. gravity field[10,11] - orbit dark-side maneuver and attitude hold operations produce gravity gradient torques which reverse angular momentum accumulation.

In the first two approaches $|\underline{\Delta H}|$ given in Eq.(5-3) is the bias momentum dump requirement. In the third approach the dumping requirement will vary between $|\underline{\Delta H}|/2$ and $|\underline{\Delta H}|$, since the spacecraft is not held fixed in the solar-inertial mode during part of the orbit dark-side interval. For the first SVWS mission the gravity gradient dump procedure is superior. However, the other methods are useful alternatives when operating, for example, with only two CMGs or during high β phases of a mission in which the dark-side time interval is small or non-existent.* Momentum dumping with magnetic control is also an attractive possibility for the second workshop and in future space stations where orbit dark-side maneuvers or reaction jet firings might upset critical telescope alignment during stellar astronomy experiments.

5.2 Orbital Sunlight Interval

The period during an orbit in which the sun is unocculted by the earth is referred to as the earth sunlight interval. In general, this interval depends on the proximity of the orbit path to the earth and its orientation with respect to the earth and sun line. Geometry for determining the shadow interval in circular orbits is shown in Fig.(5-3) where R is the earth's radius and H is the orbital altitude. Points P_1 and P_2 are the locations in orbit where an observer's line-of-sight to the sun's center just becomes occulted by the earth.** The earth shadow terminator corresponds to the great circle $\overline{ABC}$ which is normal to the sun line for a given β.

The orbit angle corresponding to the shadow interval is defined as $2\sigma_1$. The corresponding angle for the sunlight interval is $2\eta_{es}$ where

$$\eta_{es} = 180° - \sigma_1 \qquad (5\text{-}4)$$

---

*Spacecraft maneuvers during sunlight periods may interfere with solar experiments. As shown in Fig.(5-4) for circular orbits, the dark-side interval vanishes for $\beta \geq \sigma = \sin^{-1}(R/R+H)$ where R is the earth's radius and H the orbital altitude.

**Umbra and penumbra effects of the earth-sun geometry are not included in this analysis. See footnote in Appendix E, p.E-3.

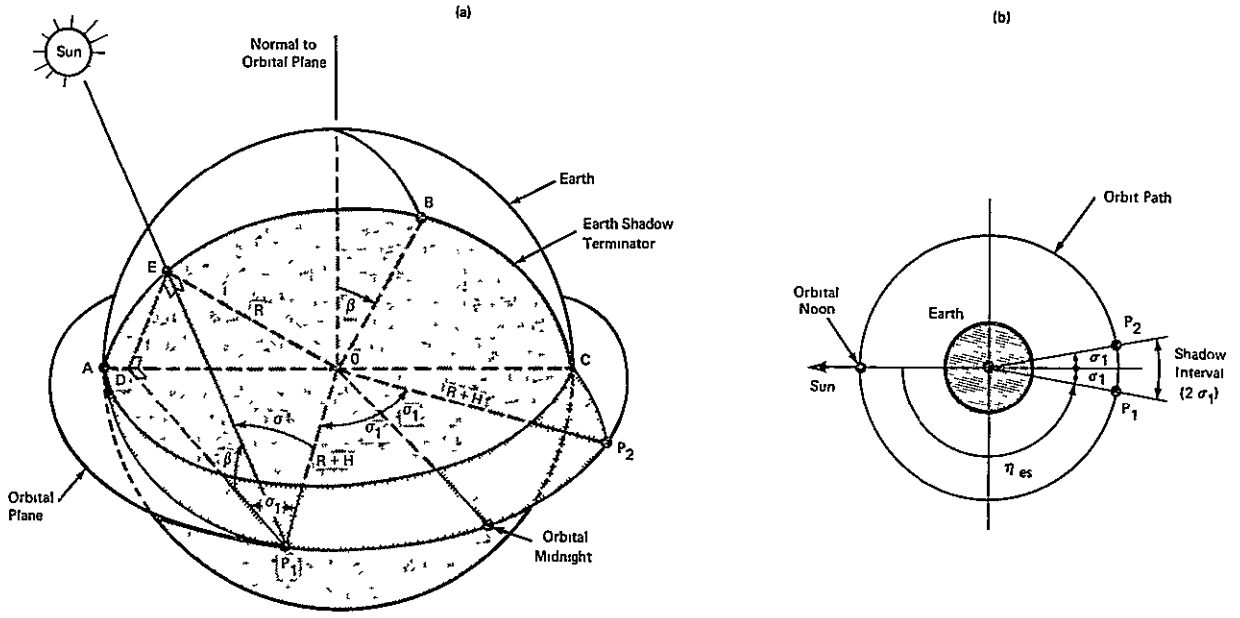

Figure (5 - 3) - Geometry for Determining Earth Shadow Interval.

as shown in Fig.(5-3b). The relation between σ_1 and β is obtained from a solution of the tetrahedron $DEOP_1$ in Fig.(5-3a).

This yields*

$$c\sigma_1 = c\sigma/c\beta \qquad (\beta \leq \sigma) \qquad (5\text{-}5)$$

where

$$s\sigma = R/(R+H) \qquad (5\text{-}6)$$

Hence, η_{es} is given by

$$\eta_{es} = \begin{cases} \cos^{-1}(-c\sigma/c\beta) & \beta < \sigma \\ 180° & \beta \geq \sigma \end{cases} \qquad (5\text{-}7)$$

*In circular orbits $c\sigma_1$ is only a function of β, which is assumed constant over an orbit. In elliptical orbits the shadow interval is a function of both β and ψ. Analytical results for this case are derived in Reference 13 and summarized in Appendix E.

Since the orbital angular velocity is constant in a circular orbit the fraction of an orbit in sunlight is

$$T_{SL} = (2\eta_{es}/360°) = \eta_{es}/180° \qquad (5\text{-}8)$$

A plot of T_{SL} as a function of β is shown in Fig.(5-4) for various orbital altitudes. When $\beta \geq \sigma$, the orbit is in total sunlight. For a 230 NM circular orbit this occurs for $\beta \geq 69.6°$.

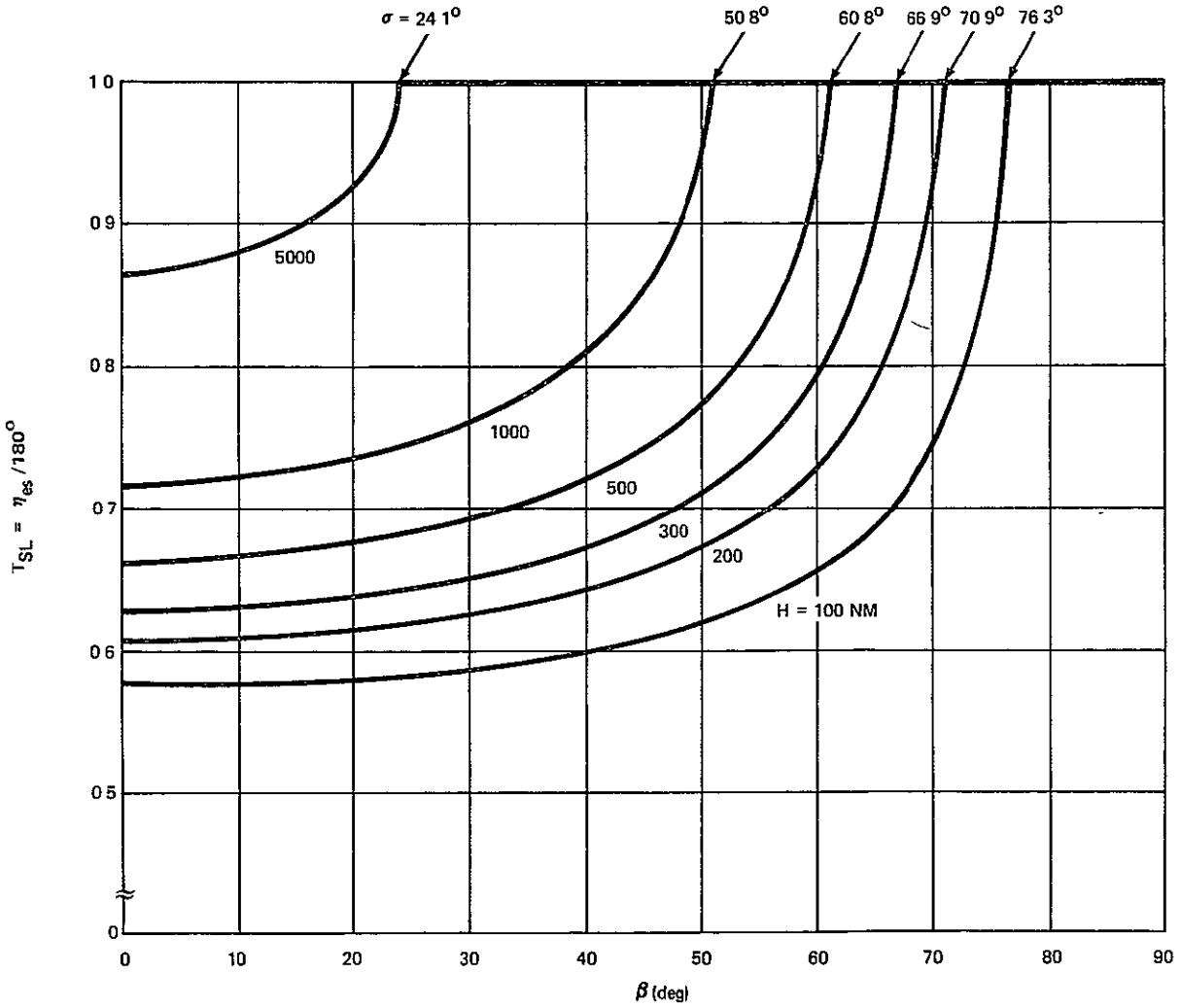

Figure (5 - 4) - Fraction of a Circular Orbit in Sunlight vs. β

5.3 Electrical Energy from Solar Arrays

Electrical energy from solar arrays is a function of the array orientation relative to the sun line and the duration of the sunlight interval. In a solar orientation, such as the solar-inertial mode illustrated in Fig.(1-1), the incident solar energy on the arrays is a maximum. In orbit-oriented modes, such as LV, LH and POP,* the maximum is obtainable only with an independent array pointing capability. This may be achieved by two-degree-of-freedom (TDOF) articulation of the array or by combining single-degree-of-freedom (SDOF) array articulation with spacecraft rotation about the roll axis. However, continuous articulation of large solar arrays at orbital rates in long duration missions may be undesirable from a reliability standpoint. Nevertheless, an improvement over fixed arrays can still be achieved with SDOF arrays which need only be articulated intermittently to account for the relatively slow (daily) variation in β.

In the following subsections the effect of β on the electrical energy available from fixed and incrementally articulated (SDOF) solar arrays is examined for LV, LH and POP attitude modes and various spacecraft roll profiles. In each case optimum panel articulation for maximum utilization of the incident solar energy is evaluated as a function of β. The subsequent analysis is based on the following assumptions:

(1) secondary effects on array output such as fluctuations in panel temperature and loss of incident energy due to cover glass reflection[14] are ignored,

(2) the solar panels are mounted such that shadowing by the spacecraft is negligible,

(3) the panel articulation axis is normal to the spacecraft roll axis, and

(4) the solar panels may be rotated only intermittently (e.g. daily).

---

*LV, LH and POP modes are defined in Footnote **, p. 1.

5.3.1 Evaluation of Electrical Energy

The electrical power (P) generated by a planar solar array for an arbitrary array orientation is expressed as a fraction of the maximum electrical power (P_M) which is generated when the array is pointed directly at the sun. This relationship is given by

$$P = P_M c\lambda \qquad |\lambda| \leq 90° \qquad (5\text{-}9)$$

where $c\lambda$ is the cosine of the angle between the sun line and the outward normal to the active side of the solar array. Generally, $c\lambda$ is a function of four angles: β, η, ϕ, and α_p. As illustrated in Fig.(5-5), η is the current location in orbit relative to noon, ϕ is the spacecraft roll angle and α_p is the array articulation angle.*

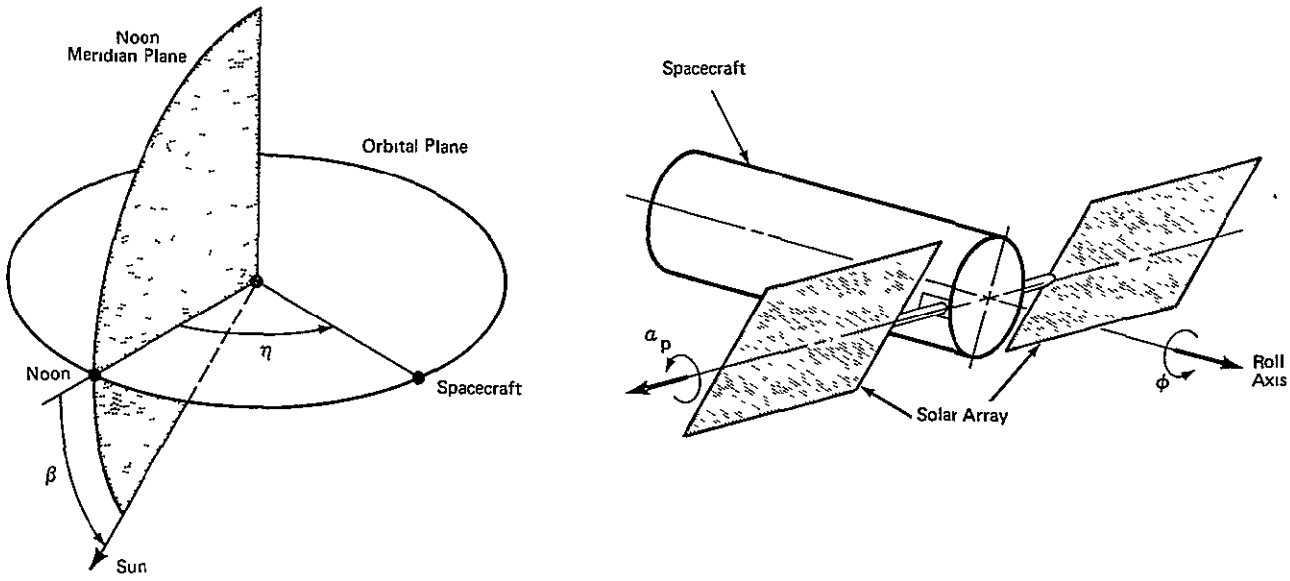

Figure (5 - 5) - Spacecraft Location and Solar Array Orientation Angles.

*The reference for α_p=0° and ϕ=0° will be defined subsequently for each attitude mode.

The array power output is zero whenever the spacecraft is within the earth shadow interval $|\eta| > \eta_{es}$* or whenever $c\lambda \leq 0$, which represents panel self-shadowing. The respective points in the orbit ($\eta=\eta_{ss2}$, $\eta=\eta_{ss1}$) corresponding to entry into and exit from the self-shadow region can be obtained by solving the equation, $c\lambda=0$, for η. Array self-shadowing is of interest whenever $\eta_{ss2} < \eta_{es}$ and/or $\eta_{ss1} > -\eta_{es}$.** In that event the self-shadow region includes part of the sunlight region, as shown in Fig. (5-6) for two possible cases, and thus reduces the total electrical energy obtainable from the solar array.

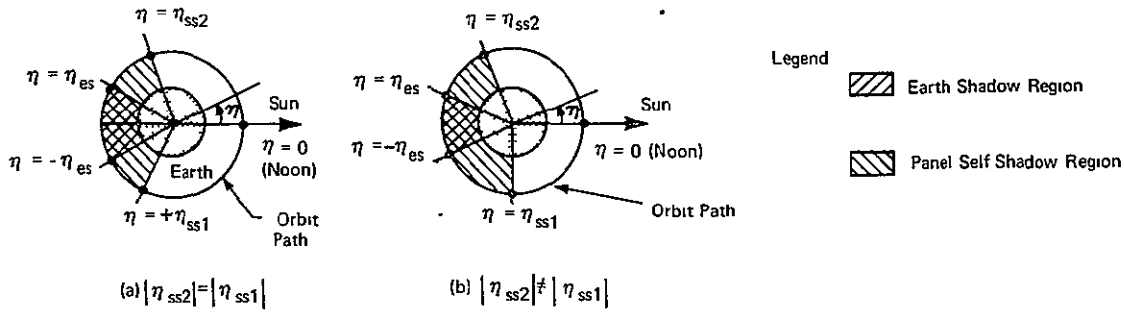

Figure (5 - 6) - Earth Shadow and Array Self-Shadow Regions in Circular Orbits

The electrical energy (E) available per orbit from the solar array is equal to the integral of the output power (P) over the period in the orbit when the panels are exposed to sunlight. This integral can be written as

$$E = \int_{t_1}^{t_2} P dt = \int_{\eta_1}^{\eta_2} P d\eta/\dot{\eta} \qquad (5\text{-}10)$$

where (η_2, t_2) correspond to the point of array entry into shadow, (η_1, t_1) corresponds to the point of exit from shadow and $\dot{\eta}$ is

---

*See Section 5-2 and Fig. (5-3).

**In general, $|\eta_{ss2}| \neq |\eta_{ss1}|$, since the solutions of $c\lambda=0$ for η are not necessarily symmetric about $\eta=0°$. However, for many cases considered in subsequent work, $\eta_{ss2} = -\eta_{ss1} \equiv \eta_{ss}$.

the instantaneous angular velocity in orbit. The average power supplied during the period (t_2-t_1) is simply

$$P_{ave} = \frac{1}{t_2-t_1} \int_{t_1}^{t_2} P dt = \frac{E}{t_2-t_1} \tag{5-11}$$

For circular orbits, $\dot{\eta} \equiv \omega_o$ is constant and $\omega_o(t_2-t_1) = (\eta_2-\eta_1)$, so that the expressions for the electrical energy and average power become

$$E = \frac{1}{\omega_o} \int_{\eta_1}^{\eta_2} P d\eta = \frac{P_M}{\omega_o} \int_{\eta_1}^{\eta_2} c\lambda d\eta \tag{5-12}$$

and

$$P_{ave} = \frac{\omega_o}{(\eta_2-\eta_1)} E = \frac{P_M}{(\eta_2-\eta_1)} \int_{\eta_1}^{\eta_2} c\lambda d\eta \tag{5-13}$$

where Eq.(5-9) has been substituted into Eq.(5-12) for P.

The maximum electrical energy (E_s) is obtained with the panels pointed continuously at the sun, which means that $c\lambda=1$. Since panel self-shadowing is precluded in that case, $\eta_2=\eta_{es}$, $\eta_1= -\eta_{es}$ and Eq.(5-12) yields

$$E_s \equiv \frac{P_M}{\omega_o} (\eta_2-\eta_1) = \frac{P_M}{\omega_o} (2\eta_{es}) \tag{5-14}$$

Hence, the maximum electrical energy obtainable from solar arrays varies with β and orbital altitude as shown by the curves in Fig.(5-4) for η_{es}.

For an arbitrary panel orientation the available electrical energy given by Eq.(5-12) can be expressed in terms of the sun-oriented array energy output (E_s) by substituting for P_M/ω_o from Eq.(5-14). This yields

$$E = \frac{E_s}{2\eta_{es}} \int_{\eta_1}^{\eta_2} c\lambda d\eta \tag{5-15}$$

or in normalized form

$$\hat{E} \equiv (E/E_s) = \frac{1}{2\eta_{es}} \int_{\eta_1}^{\eta_2} c\lambda d\eta \qquad (5\text{-}16)$$

Thus, $\hat{E}$ represents the fraction of E_s obtainable for a given attitude mode and array orientation.*

In view of Eq.(5-13) the maximum average power obtainable with the array pointed continuously at the sun is just P_M. Consequently the normalized average power is given by

$$\hat{P} = (P_{ave}/P_M) = \frac{1}{(\eta_2-\eta_1)} \int_{\eta_1}^{\eta_2} c\lambda d\eta = \frac{2\eta_{es}}{(\eta_2-\eta_1)} \hat{E} \qquad (5\text{-}17)$$

This indicates that the normalized electrical energy, $\hat{E}$ and the normalized average power $\hat{P}$ are identical, if self-shadowing occurs only during the earth shadow region (i.e., $\eta_2-\eta_1=2\eta_{es}$).

---

*An alternate normalization of the array energy output (E) could be made relative to the sun-oriented array output (E_{so}) at $\beta=0°$. In view of Eq.(5-14) it follows that $E_{so}=(P_m/\omega_o)2\eta_{eso}$ where $2\eta_{eso}$ corresponds to the sunlight interval at $\beta=0°$. Accordingly η_{es} in Eqs.(5-15) and (5-16) is replaced by η_{eso} and the normalized array output is designated $\hat{E}_o$. Also, if E_s in Eq.(5-14) is normalized to E_{so}, the sun-oriented array output can be expressed as

$$\hat{E}_s \equiv E_s/E_{so} = \eta_{es}/\eta_{eso}$$

which varies with β analogous to the curves for $\eta_{es}/180°$ in Fig.(4-4). Normalization relative to E_s is preferred in this section however, since this approach will indicate directly the array output relative to the sun-oriented array for all β. Nevertheless, the two approaches are simply related, since $\hat{E}_o=\hat{E}_s\hat{E}$.

5.3.2 Electrical Energy in Local Vertical Modes*

The solar array orientation in the LV mode is illustrated in Fig.(5-7), where the panel coordinate axes, y_p and z_p, define the articulation axis and the normal to the active side of the array. When the panel angle (α_p) and the spacecraft roll angle (ϕ) are zero, the array lies in the orbital plane with x_p parallel to the spacecraft roll axis (x_{po}). For arbitrary α_p and ϕ the expression for $c\lambda$ given in Eq.(D-19) of Appendix D is

$$c\lambda_{LV} = c\alpha_p \, s\beta \, c\phi + s\alpha_p \, c\beta \, c\eta - c\alpha_p \, c\beta \, s\phi \, s\eta \qquad (5\text{-}18)$$

In the following subsections $\hat{E}$ is evaluated as a function of β from Eqs.(5-16) and (5-18) for various panel angles and several spacecraft roll profiles.**

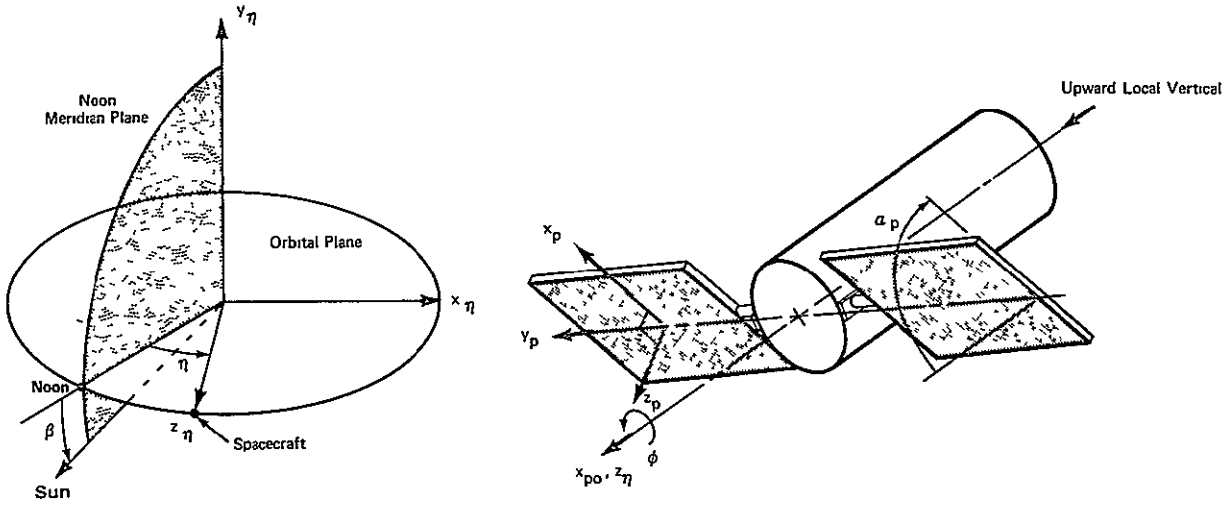

Figure (5 - 7) - Solar Array Orientation in Local Vertical Mode

*The results in this section were contributed previously to Reference 15.

**As may be surmised from Fig.(5-7) it is really only necessary to consider $0° \leq \beta \leq 90°$, since redefining the spacecraft roll such that $\phi \to 180° - \phi$, when $-90° \leq \beta \leq 0°$, yields exactly the same expression for $c\lambda_{LV}$ in Eq.(5-18). Also, in view of Fig.(5-7) it is sufficient to consider $0° \leq \alpha_p \leq 90°$, since α_p in the range, $-90° \leq \alpha_p \leq 0°$, serves only to orient the outward normal to the array (z_p) further away from the sun line.

5.3.2.1 Solar Arrays Operated with Spacecraft Roll ($\dot{\phi}\neq 0$)

The angles α_p and ϕ corresponding to a solar oriented array ($c\lambda_{LV}=1$) are defined by Eqs.(D-11) and (D-12), namely

$$s\alpha_p = c\eta\, c\beta \tag{5-19}$$

$$\tan\phi = -s\eta/\tan\beta \tag{5-20}$$

Although variation of α_p at orbital rates is precluded by assumption, the variation of ϕ according to Eq.(5-20) represents the optimum spacecraft roll in the sense that this maximizes the instantaneous array power output.* A plot of ϕ_{opt} as a function of η is illustrated by the solid curves in Fig.(5-8a) for various values of β.

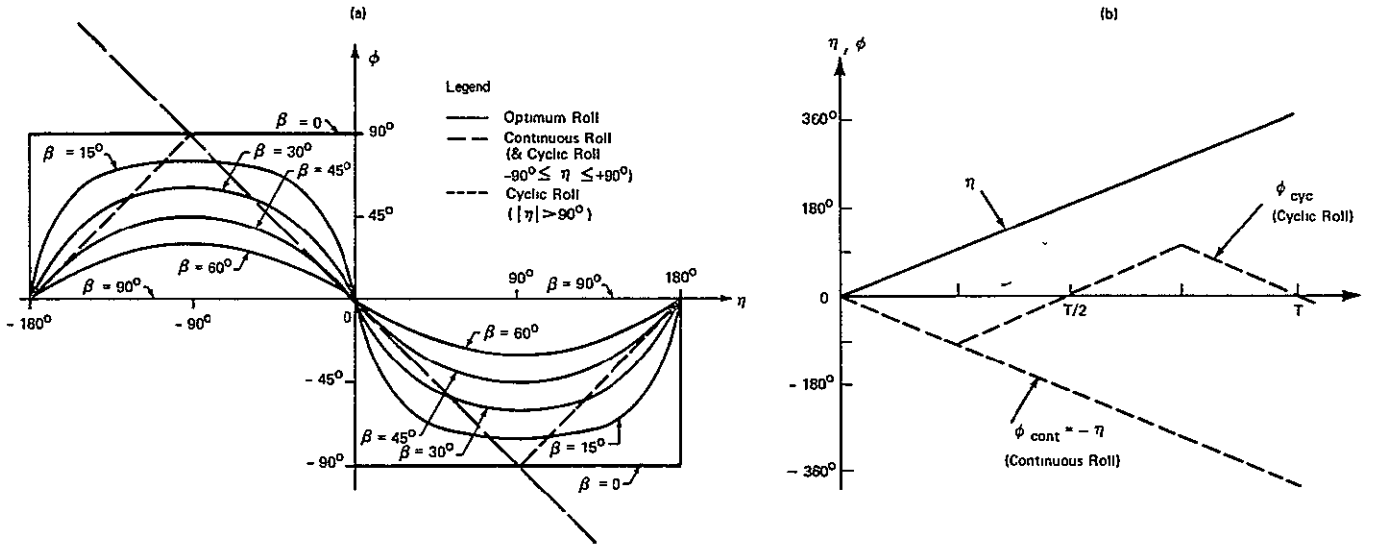

Figure (5 - 8) - Spacecraft Roll Angle vs Orbital Position Angle for Three Roll Modes.

Although theoretically possible, the variation of ϕ according to Eq.(5-20) imposes some adverse conditions on the spacecraft attitude control system. One practical aspect is that the spacecraft must follow a rather complex roll command, which varies with β. The primary disadvantage, however, is that the spacecraft must execute an abrupt roll maneuver twice per orbit, when β is small.*

---

*Since $P=P_m c\lambda$, it follows that $\partial/\partial\phi(c\lambda_{LV})=0$ yields Eq.(5-20).

*In view of Figure (5-8a) the theoretical maximum roll rate, $|\dot{\phi}|_{max}$, which occurs at $\eta=0°$ and $\pm 180°$ approaches infinity as $\beta\to 0°$, since $|\dot{\phi}|_{max}=\omega_o/\tan\beta$.

Two easily implemented suboptimal alternatives to the optimum roll are represented by the dashed curves in Fig.(5-8a). In one case the roll motion (ϕ_{cont}) is continuous with $\dot{\phi}_{cont}=-\omega_o$. In the other case the roll motion (ϕ_{cyc}) is cyclic about zero such that

$$\phi_{cyc} = \begin{cases} \eta+180° & -180° \leq \eta \leq -90° \\ -\eta & -90° \leq \eta \leq 90° \\ \eta-180° & 90° \leq \eta \leq 180° \end{cases} \qquad (5\text{-}21)$$

As is evident from Fig.(5-8a) both cases closely approximate ϕ_{opt} near $\eta=0°$ and $\beta=45°$.

These two alternatives will be compared with the optimum roll case in terms of the electrical energy ($\hat{E}$) available from the array as expressed in Eq.(5-16). The boundaries of the array sunlight interval ($\eta_1 \leq \eta \leq \eta_2$) needed for evaluating $\hat{E}$ can be determined by comparing the earth shadow boundary ($\pm\eta_{es}$) with the panel self-shadow boundary (η_{ss1}, η_{ss2}) described previously. In Appendix C the self-shadow boundary is shown to be symmetrical about $\eta=0°$ for all three cases so that $\eta_{ss2} = -\eta_{ss1} \equiv \eta_{ss}$. Consequently the array sunlight interval is determined by

$$\eta_2 = -\eta_1 \equiv \eta_{s\ell} = \begin{cases} \eta_{es} & \text{if} \quad \eta_{es} \leq \eta_{ss} \\ \eta_{ss} & \text{if} \quad \eta_{ss} < \eta_{es} \end{cases} \qquad (5\text{-}22)$$

The relationship between η_{es} and η_{ss} for various values of α_p and β is shown by the curves in Fig.(C-1), (C-2) and (C-3) in Appendix C for the optimum roll, continuous roll and cyclic roll cases respectively.

With these data the normalized electrical energy ($\hat{E}$) can be evaluated after integration of Eq.(5-16) with Eq.(5-18) substituted for $c\lambda$. The normalized average power ($\hat{P}$) available during the sunlight interval is then obtained by using Eq.(5-17). The expressions for $\hat{E}$ as given in Eqs.(C-12), (C-19) and (C-30) are listed below.

Optimum Roll*

$$\hat{E} = \frac{1}{\eta_{es}} \left\{ s\alpha_p \, c\beta \, s\eta_{s\ell} + c\alpha_p [E(k) + E(k,\theta)] \right\} \tag{5-23}$$

$$\hat{P} = \left(\eta_{es}/\eta_{s\ell}\right)\hat{E} \tag{5-24}$$

where

$$k = c\beta \tag{5-25}$$

and

$$\theta = \eta_{s\ell} - 90° \tag{5-26}$$

Continuous Roll

$$\hat{E} = \frac{1}{2\eta_{es}} \left[2s(\alpha_p+\beta) s\eta_{s\ell} + \frac{c\alpha_p c\beta}{2} (2\eta_{s\ell} - s2\eta_{s\ell}) \right] \tag{5-27}$$

$$\hat{P} = \left(\eta_{es}/\eta_{s\ell}\right)\hat{E} \tag{5-28}$$

Cyclic Roll

$$\hat{E} = \frac{1}{2\eta_{es}} \left[4c\alpha_p s\beta + 2s(\alpha_p-\beta) s\eta_{s\ell} + \frac{c\alpha_p c\beta}{2} (2\eta_{s\ell} - s2\eta_{s\ell}) \right] \tag{5-29}$$

$$\hat{P} = \left(\eta_{es}/\eta_{s\ell}\right)\hat{E} \tag{5-30}$$

In Figs. (5-9), (5-10) and (5-11), $\hat{E}$ is plotted as a function of β and the panel angle (α_p) for the various roll modes. The corresponding results for $\hat{P}$ differ significantly from those of $\hat{E}$ only in the continuous roll mode. The curves of $\hat{P}$ vs β for this case are shown in Fig. (5-12). The knee in the curves of $\hat{E}$ vs β near $\beta=70°$ is due to the rapid decrease in the earth shadow interval.** In each case the upper envelope boundary on the curves for $\hat{E}$ represents the maximum electrical energy ($\hat{E}_{max}$) available from the array with optimum variation of α_p with β. A comparison of optimum results for these cases and optimum results in other attitude modes are given in Section 5.3.5.

*The function $E(k,\theta)$ in Eq. (5-23) is an elliptic integral of the second kind which is available in tabulated form[16] as a function of the modulus k and argument θ. The function E(k) is the complete elliptic integral of the second kind ($\theta=90°$).

**See Fig. (5-4).

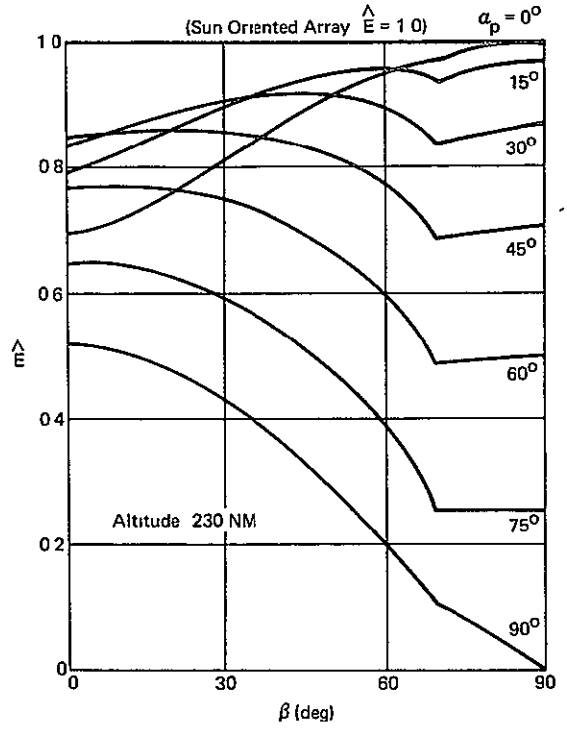

Figure (5 - 9) - Normalized Electrical Energy from Solar Array as a Function of α_p and β (LV - Optimum Roll Mode).

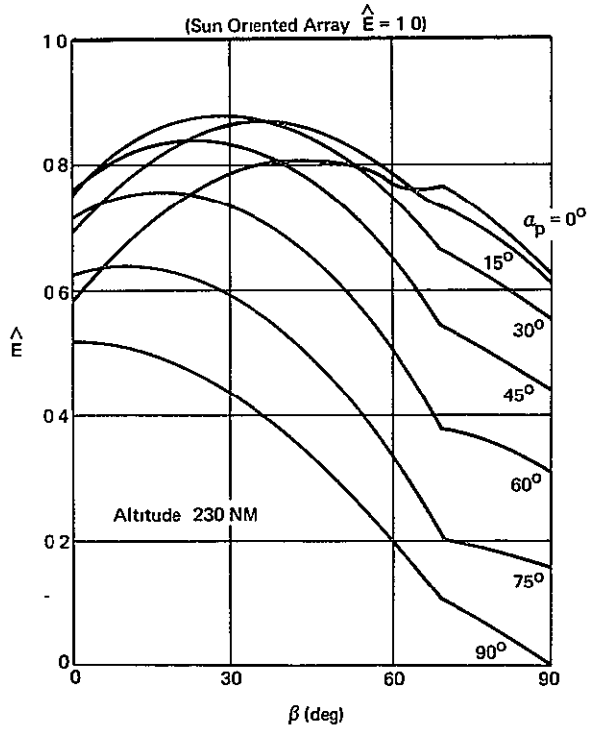

Figure (5 - 10) - Normalized Electrical Energy from Solar Array as a Function of α_p and β (LV - Cyclic Roll Mode).

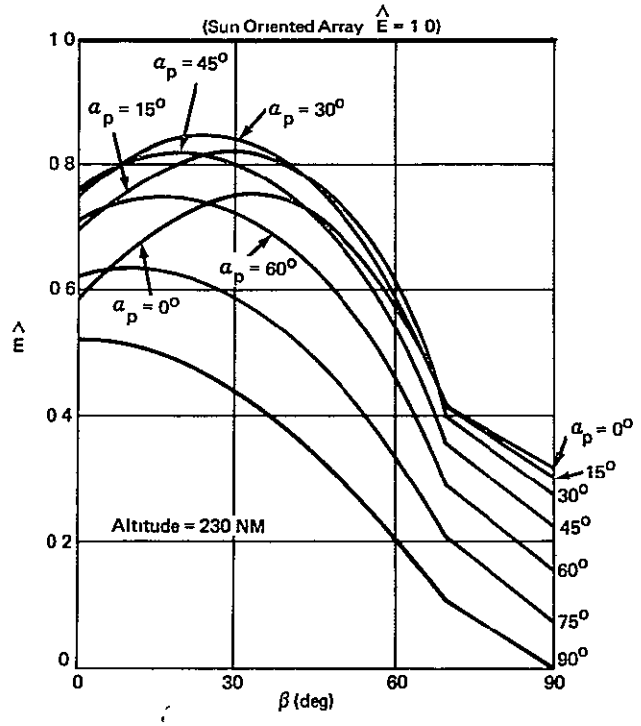

Figure (5 - 11) - Normalized Electrical Energy From Solar Array as a Function of α_p and β (LV - Continuous Roll Mode).

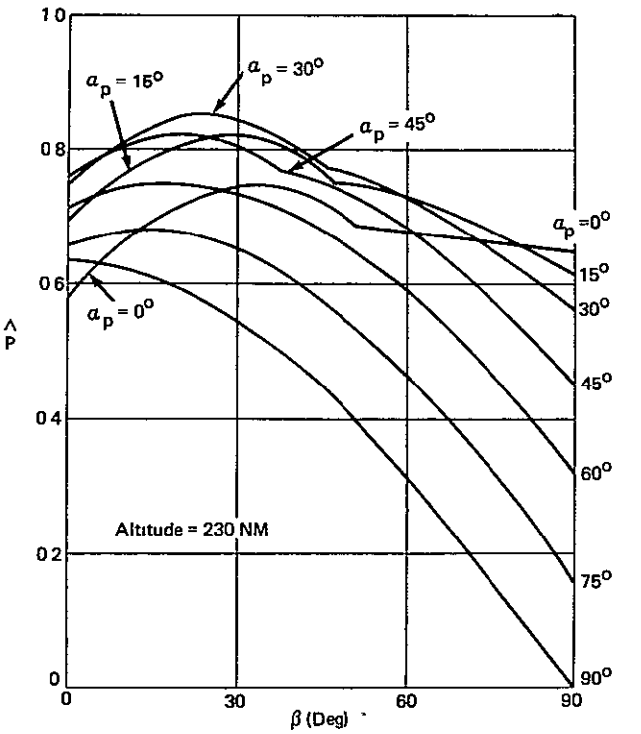

Figure (5 - 12) - Normalized Average Power from Solar Array as a Function of α_p and β (LV - Continuous Roll Mode).

5.3.2.2 Solar Arrays Operated with Fixed Spacecraft Roll ($\dot{\phi}=0$)

If the spacecraft is roll stabilized, the roll degree-of-freedom for pointing the solar array is not available on a continuous basis. Unless otherwise constrained however, the spacecraft roll angle is arbitrary and can be fixed at some desired value (ϕ=constant).* It is of interest therefore to evaluate the electrical energy ($\hat{E}$) available from the array for various fixed values of ϕ and to determine as a function of β the optimum combination of fixed roll angle (ϕ) and panel angle (α_p) which maximizes $\hat{E}$.

As in previous work the sunlight interval must be determined in order to evaluate $\hat{E}$ according to Eq.(5-16). In the fixed roll mode the panel self-shadow boundaries (η_{ss1}, η_{ss2}) are not symmetrical about $\eta=0°$ except when $\phi=0°$. Consequently, the self-shadow and earth shadow intervals may assume any one of four possible arrangements, as shown in Fig.(5-13).

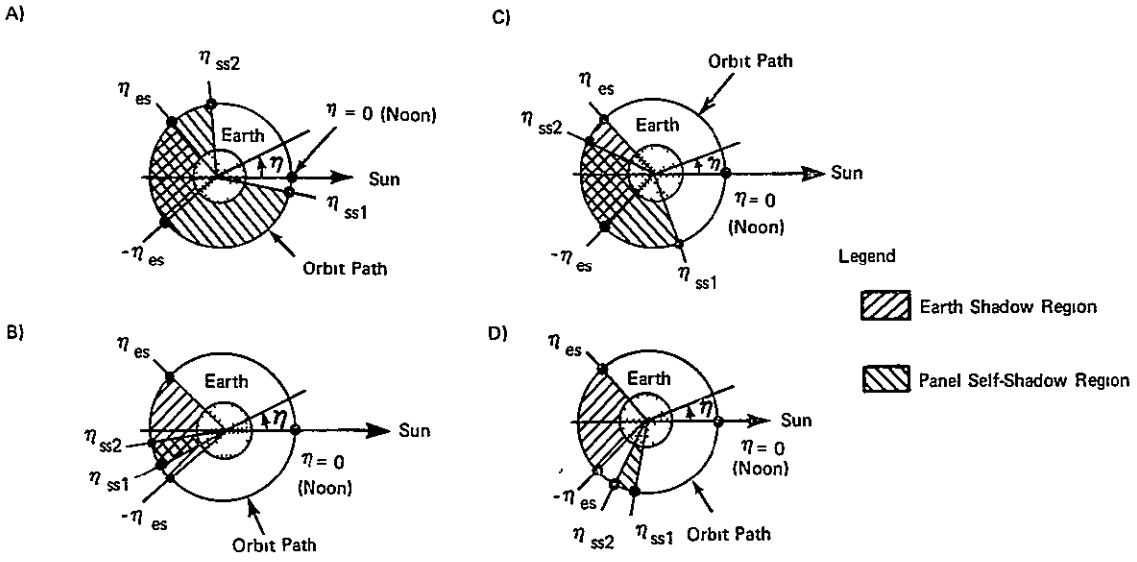

Figure (5 - 13) - Possible Earth Shadow and Solar Panel Self-Shadow Regions (LV - Fixed Roll Mode).

*If the spacecraft is roll stabilized by reaction thrust methods, ϕ will normally drift within a limit cycle deadband. If the deadband is sufficiently small however, ϕ can be considered essentially constant. If momentum exchange devices are used for control, a precisely fixed value of ϕ can be maintained.

In general the self-shadow boundaries (η_{ss1}, η_{ss2}) vary with β. In Figs.(C-5), (C-6a) and (C-6b) of Appendix C.4 the variation of η_{ss1} and η_{ss2} as a function of β and α_p is shown for ϕ=-45°, 0° and -90° respectively. Also shown are the earth shadow boundaries ($\pm\eta_{es}$) corresponding to a 230 NM circular orbit. The various shaded regions (A, B, C or D) in Figs.(C-5) and (C-6) correspond to the respective shadow boundary arrangements in Fig.(5-13).

With this information the electrical energy ($\hat{E}$) can be evaluated after integration of Eq.(5-16). In order to include the effect of distinct earth shadow and panel self-shadow intervals as in Fig.(5-13d), it is necessary to modify this expression so that

$$\hat{E} = \frac{1}{2\eta_{es}} \left\{ \int_{\eta_1}^{\eta_2} c\lambda_{LV} d\eta - \int_{\eta_1'}^{\eta_2'} c\lambda_{LV} d\eta \right\} \qquad (5\text{-}31)$$

where the limits ($\eta_2, \eta_1; \eta_2', \eta_1'$) corresponding to the various cases in Fig.(5-13) are defined as

$$\eta_2 = \begin{cases} \eta_{ss2} & \text{Case: A} \\ \eta_{es} & \text{Case: B,C,D} \end{cases} \qquad (5\text{-}32a)$$

$$\eta_1 = \begin{cases} \eta_{ss1} & \text{Case: A,C} \\ -\eta_{es} & \text{Case: B,D} \end{cases} \qquad (5\text{-}32b)$$

$$\eta_2' = \begin{cases} \eta_{ss1} & \text{Case: D} \\ 0° & \text{Case: A,B,C} \end{cases} \qquad (5\text{-}33a)$$

$$\eta_1' = \begin{cases} \eta_{ss2}-360° & \text{Case: D} \\ 0° & \text{Case: A,B,C} \end{cases} \qquad (5\text{-}33b)$$

Substitution for $c\lambda$ from Eq.(5-18) and integration of Eq.(5-31) yields

$$\hat{E} = \frac{1}{2\eta_{es}} [A(\eta_2-\eta_1) + B(s\eta_2-s\eta_1) + C(c\eta_2-c\eta_1)]$$

$$- [A(\eta_2'-\eta_1') + B(s\eta_2'-s\eta_2') + C(c\eta_2'-c\eta_1'] \quad (5-34)$$

where

$$A = c\alpha_p \; c\phi \; s\beta \quad (5-35)$$

$$B = s\alpha_p \; c\beta \quad (5-36)$$

and

$$C = +c\alpha_p \; c\beta \; s\phi \quad (5-37)$$

In Fig.(5-15a,b,c) $\hat{E}$ is plotted as a function of β and the panel angle (α_p) for three different roll angles: $\phi=0°$*, $\phi= -45°$ and $\phi= -90°$.

Three particular cases are of interest, since they represent possible orientations of a spacecraft in a local vertical storage mode. The three panel orientations and the associated α_p and ϕ are shown in Fig.(5-14). The corresponding shadow boundaries for each case are given in Fig.(C-6) in Appendix C.4. Consequently, the respective expressions for $\hat{E}$ obtained from Eq.(5-34) are as follows:

1) $\underline{\alpha_p=0°, \; \phi=0° \; (\eta_2= -\eta_1=\eta_{es})}$:

$$\hat{E} = \frac{1}{2\eta_{es}}[s\beta(\eta_2-\eta_1)] = s\beta \quad (5-38)$$

2) $\underline{\alpha_p=0°, \; \phi= -90° \; (\eta_2= +\eta_{es}, \eta_1=0°)}$:

$$\hat{E} = \frac{1}{2\eta_{es}}[-c\beta(c\eta_2-c\eta_1)] = (c\beta/\eta_{es})(1-c\eta_{es})/2 \quad (5-39)$$

*This case was studied in Reference 17.

3) $\alpha_p=90°$, $\phi=0°$ $(\eta_2=-\eta_1=90°)$:

$$\hat{E} = \frac{1}{2\eta_{es}}[c\beta(s\eta_2-s\eta_1)] = c\beta/\eta_{es} \qquad (5\text{-}40)$$

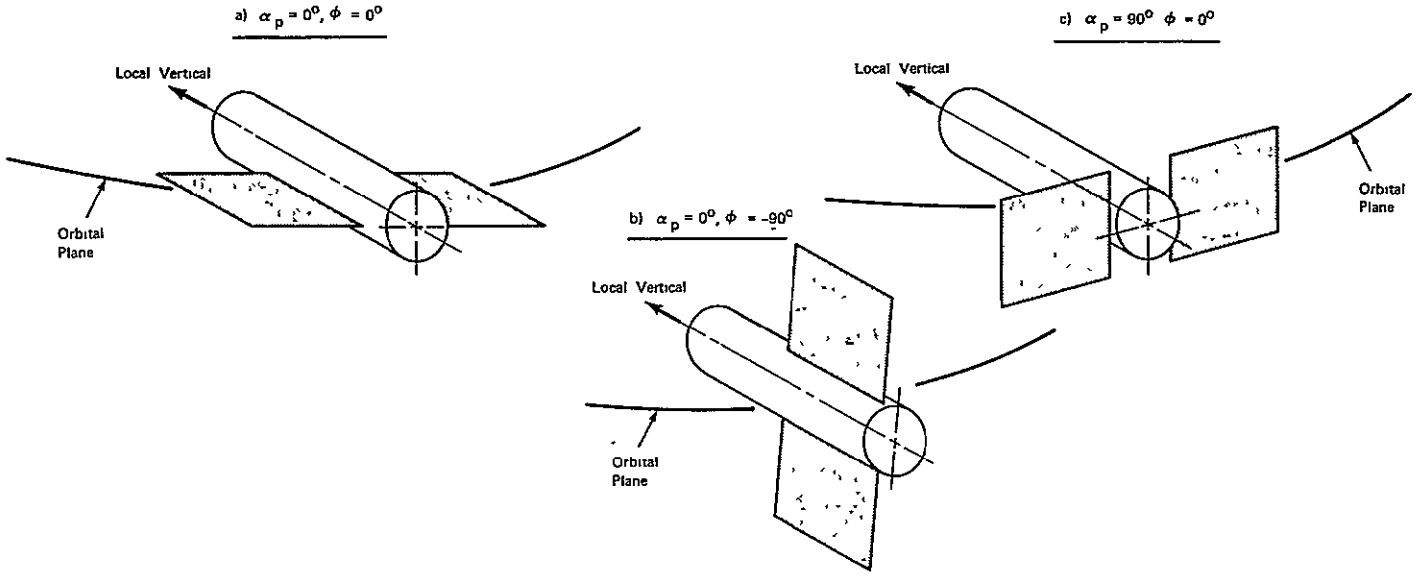

Figure (5 - 14) - Three Possible Panel Orientations for Spacecraft in a Local Vertical Storage Mode.

The curves in Fig.(5-15) indicate the electrical energy ($\hat{E}$) available for other panel orientations as a function of β. The upper envelope boundary on each family of curves represents the maximum electrical energy ($\hat{E}_{max}$) available from the array with optimum variation of α_p with β. Plots of $\hat{E}_{max}$ and $\alpha_{p(opt)}$ vs β obtained numerically for several fixed roll angles (ϕ) are shown in Figs.(5-16) and (5-17) respectively. These results indicate that $\phi=0°$ apparently yields the largest $\hat{E}_{max}$ for all β. As discussed in Appendix C.4, however, other combinations of α_p and ϕ exist, which yield the same $\hat{E}_{max}$ as with $\phi=0°$ for β in the range $0° \leq \beta \lesssim 23°$. Bounds on $\alpha_{p(opt)}$ for other possible values of ϕ are shown in Fig.(C-8) in Appendix C.4. From an attitude control standpoint however, the simplest scheme would be to use $\phi_{opt}=0°$ for all β.

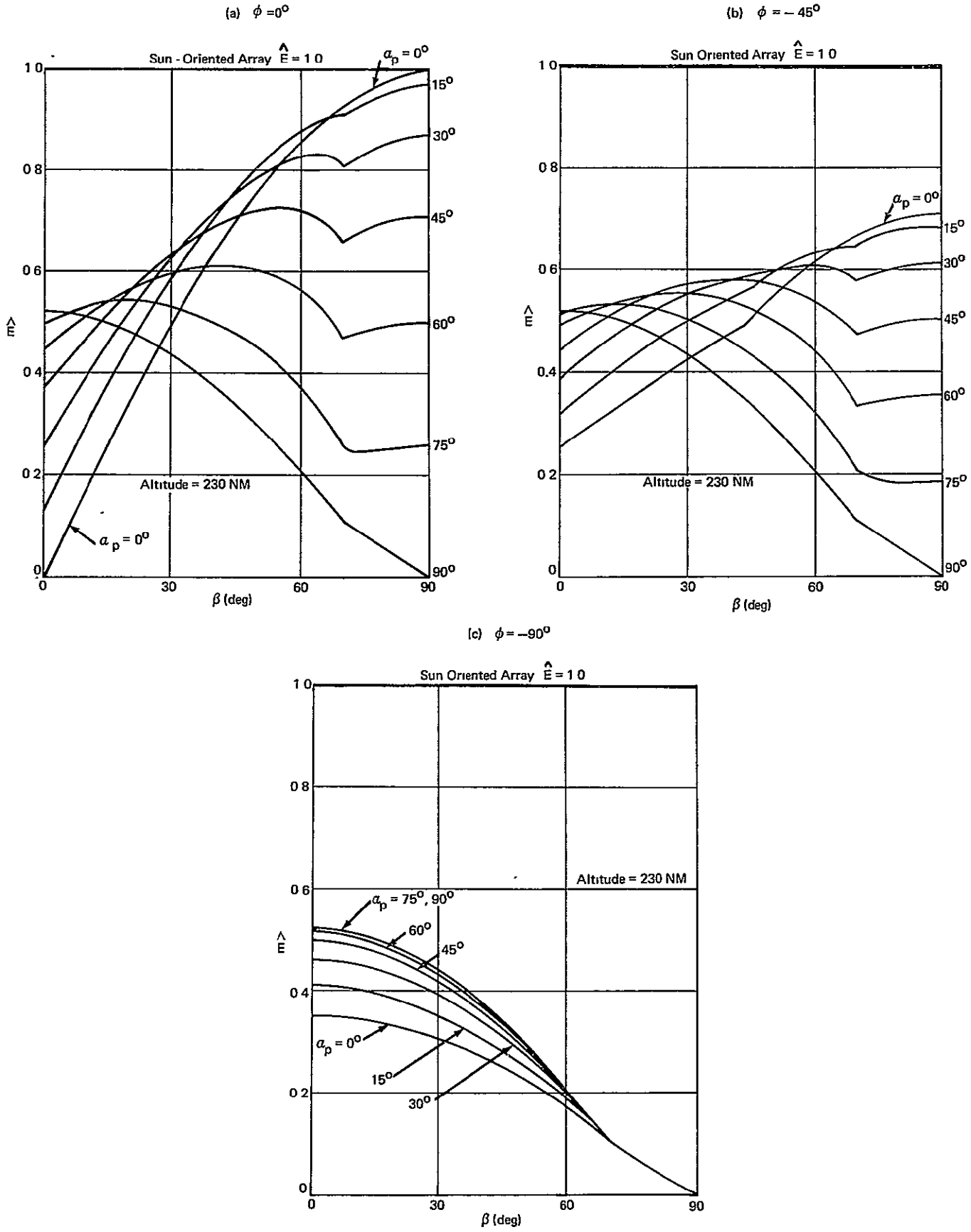

Figure (5 - 15) - Normalized Electrical Energy from Solar Array as a Function of α_p and β (LV - Fixed Roll Mode)

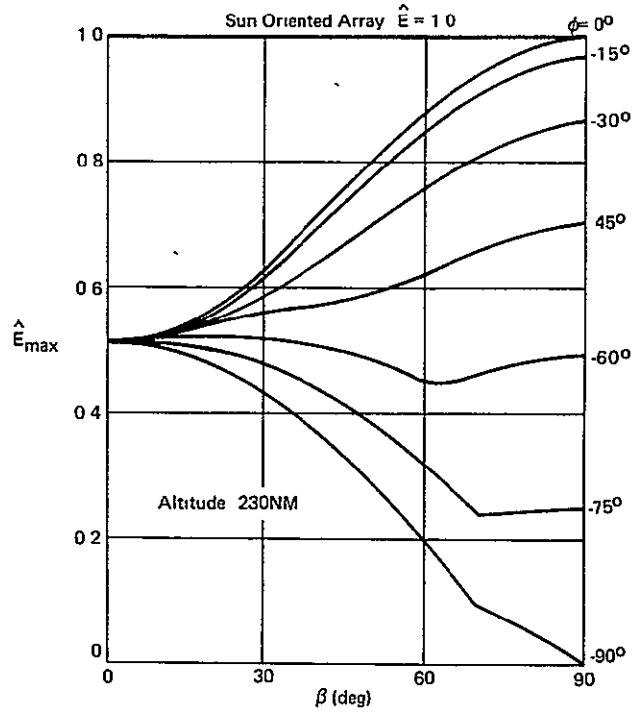

Figure (5 - 16) - Maximum Electrical Energy from Solar Array as a Function of β. ($a_p = a_{p\,(opt)}$; LV - Fixed Roll Mode).

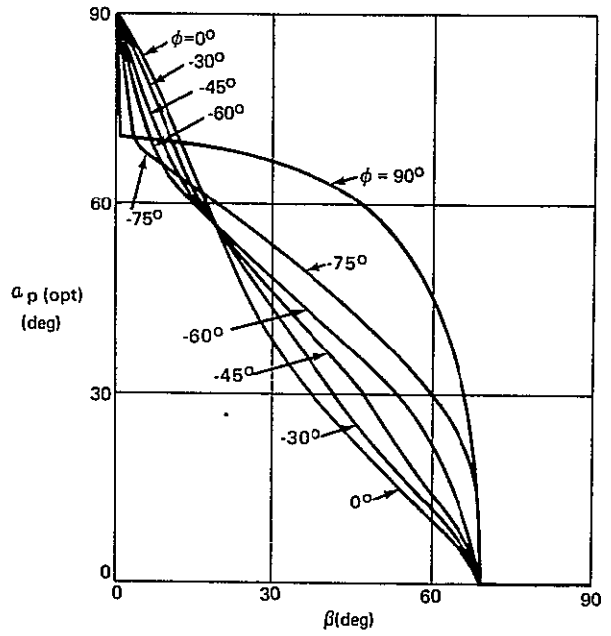

Figure (5 - 17) - Optimum Panel Angle vs β (LV - Fixed Roll Mode).

5.3.3 Electrical Energy in Local Horizontal Modes

The solar array orientation in the LH mode is illustrated in Fig.(5-18) with the same panel coordinates (x_p, y_p, z_p) as used in the LV mode. When the panel angle (α_p) and the spacecraft roll angle (ϕ) are zero, the array lies in the orbital plane with y_p, the articulation axis, directed along the upward local vertical (z_η). For arbitrary α_p and ϕ the expression for $c\lambda$ given in Eq.(D-20) of Appendix D is

$$c\lambda_{LH} = c\alpha_p \, s\beta \, c\phi - s\alpha_p \, c\beta \, s\eta - c\alpha_p c\beta \, s\phi \, c\eta \qquad (5\text{-}41)$$

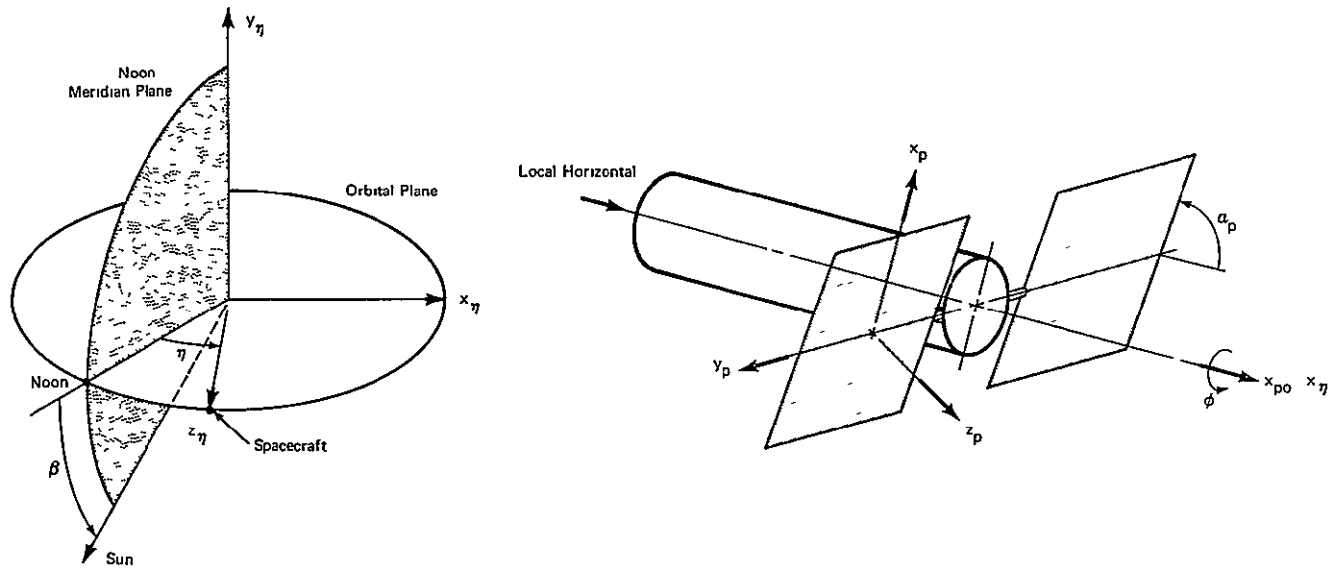

Figure (5 - 18) - Solar Array Orientation in Local Horizontal Mode

In the following subsections $\hat{E}$ is evaluated as a function of β from Eqs.(5-16) and (5-41) for various panel angles and several spacecraft roll profiles.*

*As in the LV mode it is only necessary to consider $0 \leq \beta \leq 90°$ and $0 \leq \alpha_p \leq 90°$. See Footnote**, p.45.

5.3.3.1 Solar Arrays Operated With Spacecraft Roll ($\dot{\phi}\neq 0$)

The angles α_p and ϕ corresponding to a solar oriented array ($c\lambda_{LH}=1$) are defined by Eqs.(D-13) and (D-14), namely,

$$s\alpha_p = -s\eta\ c\beta \tag{5-42}$$

$$\tan\ \phi = -c\eta/\tan\ \beta \tag{5-43}$$

Although α_p is restricted to incremental variation, spacecraft roll according to Eq.(5-43) is optimum in the sense of maximizing instantaneous array power output.* A plot of ϕ_{opt} as a function of η is illustrated by the solid curves in Fig.(5-19) for various β.

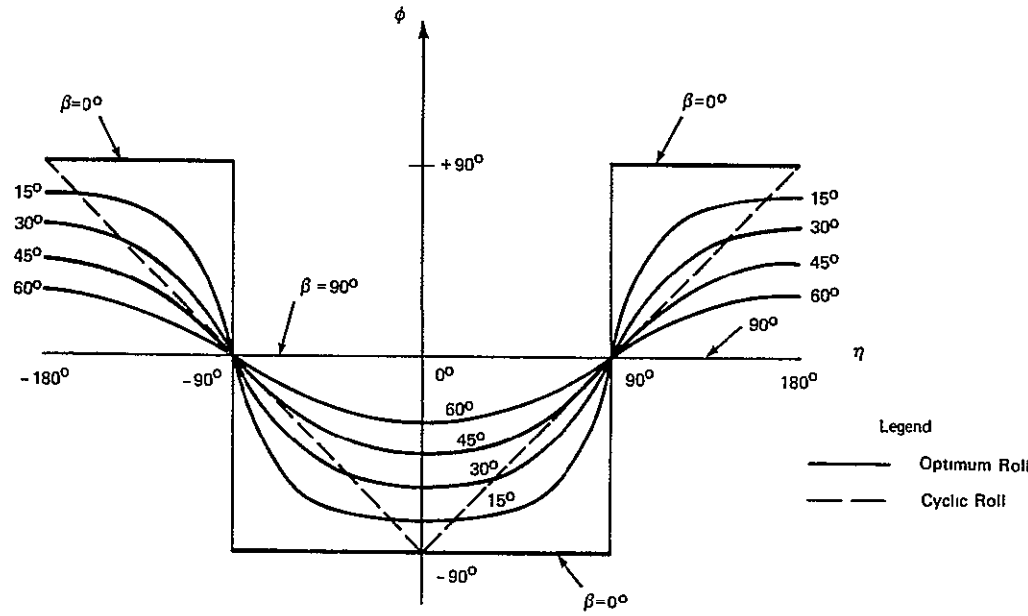

Figure (5 - 19) - Spacecraft Roll Angle vs Orbital Position Angle for Two Roll Modes.

*Analogous to the local vertical case $\partial/\partial\phi(c\lambda_{LH})=0$ yields Eq.(5-43).

The variation of ϕ according Eq.(5-43) leads to abrupt roll maneuvers twice per orbit when β is small, just as in the LV mode. A practical suboptimal alternative* to optimum roll is the cyclic roll profile shown in Fig.(5-19) and defined by

$$\phi_{cyc} = \begin{cases} -90°-\eta & -180° \leq \eta \leq 0° \\ -90°+\eta & 0° \leq \eta \leq 180° \end{cases} \qquad (5\text{-}44)$$

This approximates ϕ_{opt} closely near $\eta=\pm 90°$ and $\beta=45°$.

As found in Appendices C.5 and C.6 for the LH optimum and cyclic roll modes, the panel self-shadow boundaries (η_{ss1}, η_{ss2}) are symmetrical about $\eta=+90°$ rather than $\eta=180°$. Consequently Eq.(5-16) for evaluating $\hat{E}$ must be modified slightly to accommodate the possibility of distinct earth shadow and self-shadow regions as illustrated in Fig.(5-20). Thus,

$$\hat{E} = \frac{1}{2\eta_{es}} \left\{ \int_{-\eta_{es}}^{\eta_{es}} c\lambda_{LH} d\eta - \int_{\eta_{ss2}}^{\eta_2''} c\lambda_{LH} d\eta \right\} \qquad (5\text{-}45)$$

where

$$\eta_2'' = \begin{cases} \eta_{es} & \eta_{es} \leq \eta_{ss1} \quad \text{(Case C)} \\ \eta_{ss1} = (180° - \eta_{ss2}) & \eta_{es} > \eta_{ss1} \quad \text{(Case D)} \end{cases} \qquad (5\text{-}46)$$

The relationship between η_{es} and η_{ss2} for various values of α_p and β is shown by the curves in Figs.(C-9) and (C-10) for the optimum roll and cyclic roll cases.

---

*In the LH mode a continuous roll profile analogous to that used for the LV mode does not yield a sufficiently close approximation to ϕ_{opt} and is therefore not considered.

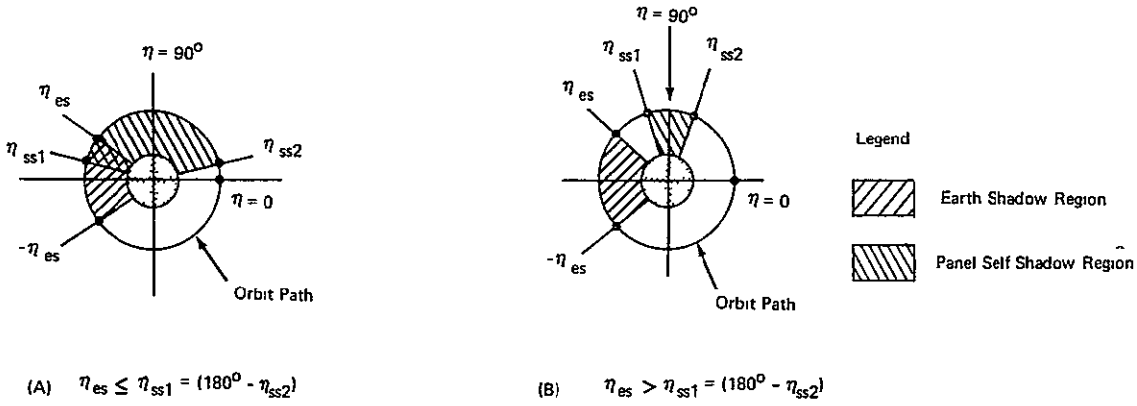

(A) $\eta_{es} \leq \eta_{ss1} = (180^o - \eta_{ss2})$ (B) $\eta_{es} > \eta_{ss1} = (180^o - \eta_{ss2})$

Figure (5 - 20) - Possible Earth Shadow and Panel Self-Shadow Regions in Local Horizontal Optimum and Cyclic Roll Modes.

The corresponding evaluation of $\hat{E}$ for cases C and D as given by Eqs.(C-93) and (C-100) of Appendix C yields

Optimum Roll*

$$C)\quad \hat{E} = \frac{1}{2\eta_{es}} \left\{ c\alpha_p [E(k,\eta_{es}) + E(k,\eta_{ss2})] + s\alpha_p c\beta (c\eta_{ss2} - c\eta_{es}) \right\} \tag{5-47}$$

$$D)\quad \hat{E} = \frac{1}{\eta_{es}} \left\{ c\alpha_p [E(k) + E(k,\eta_{es}) - E(k,\eta_{ss2})] + s\alpha_p c\beta c\eta_{ss2} \right\}$$

where $k=c\beta$,

Cyclic Roll

$$C)\quad \hat{E} = \frac{1}{2\eta_{es}} \left\{ 2c\alpha_p s\beta - s(\alpha_p+\beta) c\eta_{es} + s(\alpha_p-\beta) c\eta_{ss2} + \frac{c\alpha_p c\beta}{4} [2(\eta_{es}+\eta_{ss2}) + (s2\eta_{es}+s2\eta_{ss2})] \right\} \tag{5-48}$$

$$D)\quad \hat{E} = \frac{1}{\eta_{es}} \left\{ c\alpha_p s\beta (1-c\eta_{es}) + s(\alpha_p-\beta) c\eta_{ss2} + \frac{c\alpha_p c\beta}{4} [2(\eta_{es}+\eta_{ss2}-\pi/2) + (s2\eta_{es}+s2\eta_{ss2})] \right\}$$

*See Footnote *, p.48.

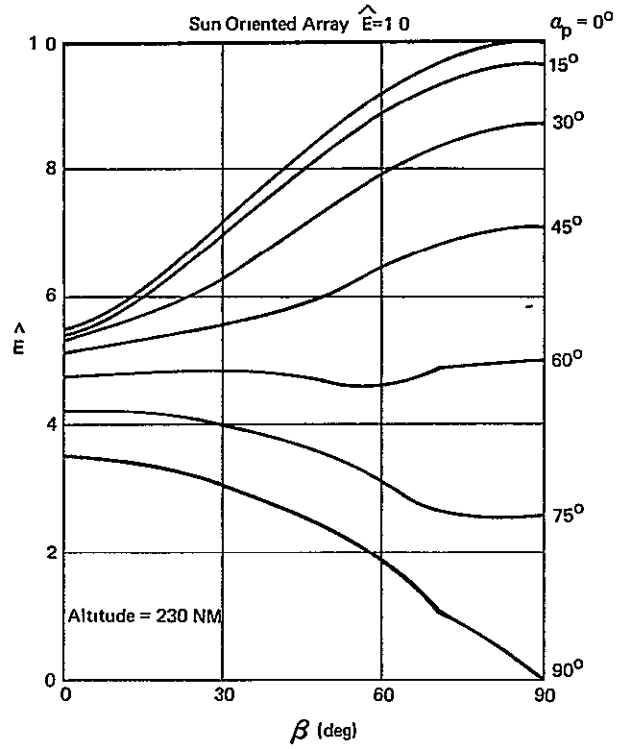

Figure (5 - 21) - Normalized Electrical Energy from Solar Array as a Function of α_p and β (LH - Optimum Roll Mode).

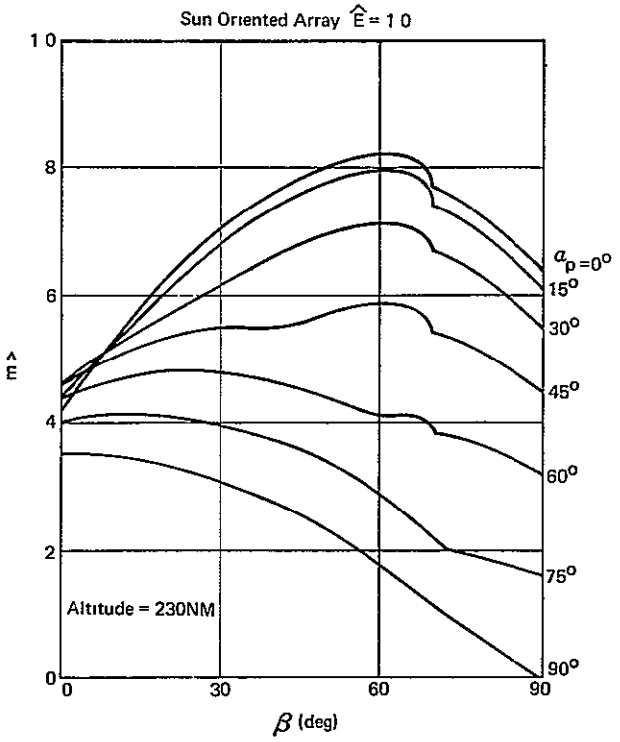

Figure (5 - 22) - Normalized Electrical Energy from Solar Array as a Function of α_p and β (LH - Cyclic Roll Mode)

In Figs.(5-21) and (5-22), $\hat{E}$ is plotted as a function of β and α_p for the optimum roll and cyclic roll modes. In each case the upper envelope boundary on the curves for $\hat{E}$ represents the maximum electrical energy ($\hat{E}_{max}$) available from the array with optimum variation of α_p with β. A comparison of the optimum results is given in Section 5.3.5.

5.3.3.2 Solar Arrays Operated with Fixed Spacecraft Roll ($\dot{\phi}=0$)

The local horizontal fixed roll mode is of importance because it is suitable for earth pointing experiments, it is easily acquired from the solar-inertial mode and external disturbance torques acting on the spacecraft tend to be small. It is of interest therefore to evaluate the electrical energy ($\hat{E}$) available from a solar array for various panel and fixed roll angles (α_p, ϕ) and to determine a combination which maximizes $\hat{E}$.

As in previous work the array sunlight interval must be determined in order to evaluate $\hat{E}$. Analogous to the local vertical fixed roll mode the array self-shadow boundaries (η_{ss1}, η_{ss2}) are not symmetrical about $\eta=180°$. Consequently, the self-shadow and earth shadow interval may assume any one of four possible arrangements shown in Fig.(5-23). In Figs.(C-11), (C-12a) and (C-12b) of Appendix C the variation of η_{ss1} and η_{ss2} with β and α_p is shown for $\phi= -45°$, $0°$ and $-90°$ respectively.* Also shown are the earth shadow boundaries corresponding to a 230 NM orbit. The various shaded regions (A,B,C or D) in Figs.(C-11) and (C-12) correspond to the respective shadow boundary arrangements in Fig.(5-23).

---

*For a given ϕ, α_p and β the self-shadow boundaries in the LH mode are rotated 90° back (clockwise) toward noon ($\eta=0°$) from corresponding boundaries in the LV mode. This follows because substituting $\eta=\eta-90°$ into Eq.(5-41) for $c\lambda_{LH}$ yields $c\lambda_{LV}$ in Eq.(5-18).

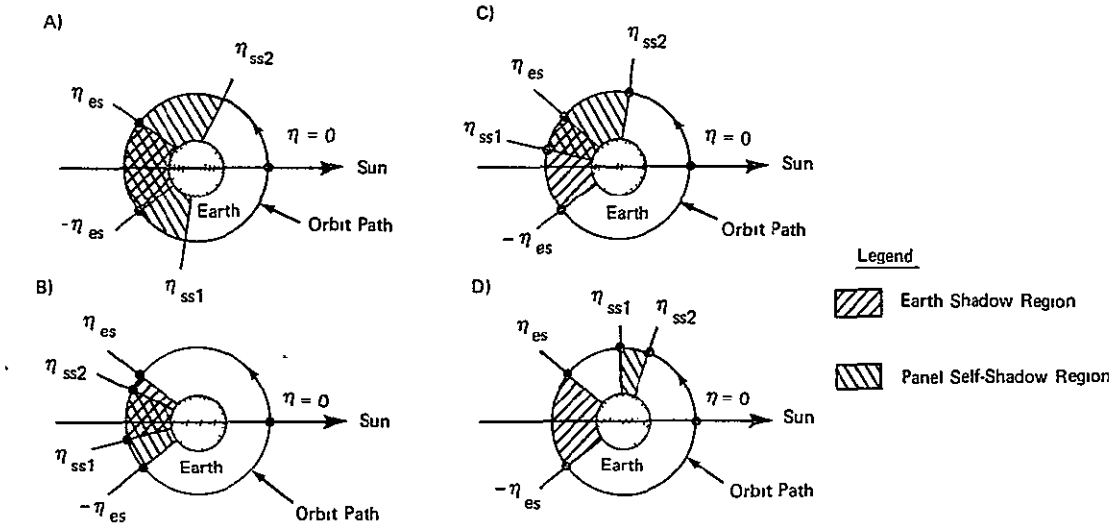

Figure (5 - 23) - Possible Earth Shadow and Array Self-Shadow Regions (LH - Fixed Roll Mode)

In order to include the effect of distinct earth shadow and self-shadow intervals it is again necessary to modify Eq. (5-16) for $\hat{E}$ so that

$$\hat{E} = \frac{1}{2\eta_{es}} \left\{ \int_{\eta_1}^{\eta_2} c\lambda_{LH} d\eta - \int_{\eta_1'}^{\eta_2'} c\lambda_{LH} d\eta \right\} \qquad (5\text{-}49)$$

where

$$\eta_2 = \begin{cases} \eta_{ss2} & \text{Case: A,C} \\ \eta_{es} & \text{Case: B,D} \end{cases} \qquad (5\text{-}50a)$$

$$\eta_1 = \begin{cases} \eta_{ss1} & \text{Case: A} \\ -\eta_{es} & \text{Case: B,C,D} \end{cases} \qquad (5\text{-}50b)$$

$$\eta_2' = \begin{cases} \eta_{ss1} & \text{Case: D} \\ 0° & \text{Case: A,B,C} \end{cases} \qquad (5\text{-}50c)$$

$$\eta_1' = \begin{cases} \eta_{ss2} & \text{Case: D} \\ 0° & \text{Case: A,B,C} \end{cases} \qquad (5\text{-}50d)$$

Substitutions for $c\lambda_{LH}$ from Eq.(5-41) and integration of Eq.(5-49) yields

$$\hat{E} = \frac{1}{2\eta_{es}} \left[A(\eta_2-\eta_1) + B(c\eta_2-c\eta_1) - C(s\eta_2-s\eta_1)\right] - \left[A(\eta_2'-\eta_1') + B(c\eta_2'-c\eta_1') - C(s\eta_2'-s\eta_1')\right] \qquad (5\text{-}51)$$

where A, B and C are as defined in Eqs.(5-35), (5-36) and (5-37) for the local vertical mode. In Fig.(5-24a,b,c) $\hat{E}$ is plotted vs β for various panel angles (α_p) and three different roll angles: $\phi=0°$, $\phi= -45°$ and $\phi= -90°$. The upper envelope boundary on each family of curves represents the maximum electrical energy ($\hat{E}_{max}$) available from the array with optimum variation of α_p with β. Plots of $\hat{E}_{max}$ and $\alpha_{p(opt)}$ vs β for several fixed roll angles are shown in Figs.(5-25) and (5-26).

The upper boundary on the curves in Fig.(5-25) represents the largest $\hat{E}_{max}$ obtainable with optimum variation of both α_p and ϕ. As discussed in Appendix C.7 this can be achieved with $\alpha_p=0°$ and $\phi= -\alpha_{p(opt)}$ for the LV-Fixed Roll mode as shown in Fig.(5-26). As in the local vertical case however, the optimum combination of α_p and ϕ is not unique for $0 \leq \beta \lesssim 23°$. Bounds on $\alpha_{p(opt)}$ and ϕ_{opt} which yield the same $\hat{E}_{max}$ are shown in Fig.(C-13). From an array design standpoint the simplest scheme would be to use a fixed array ($\alpha_p=0°$).

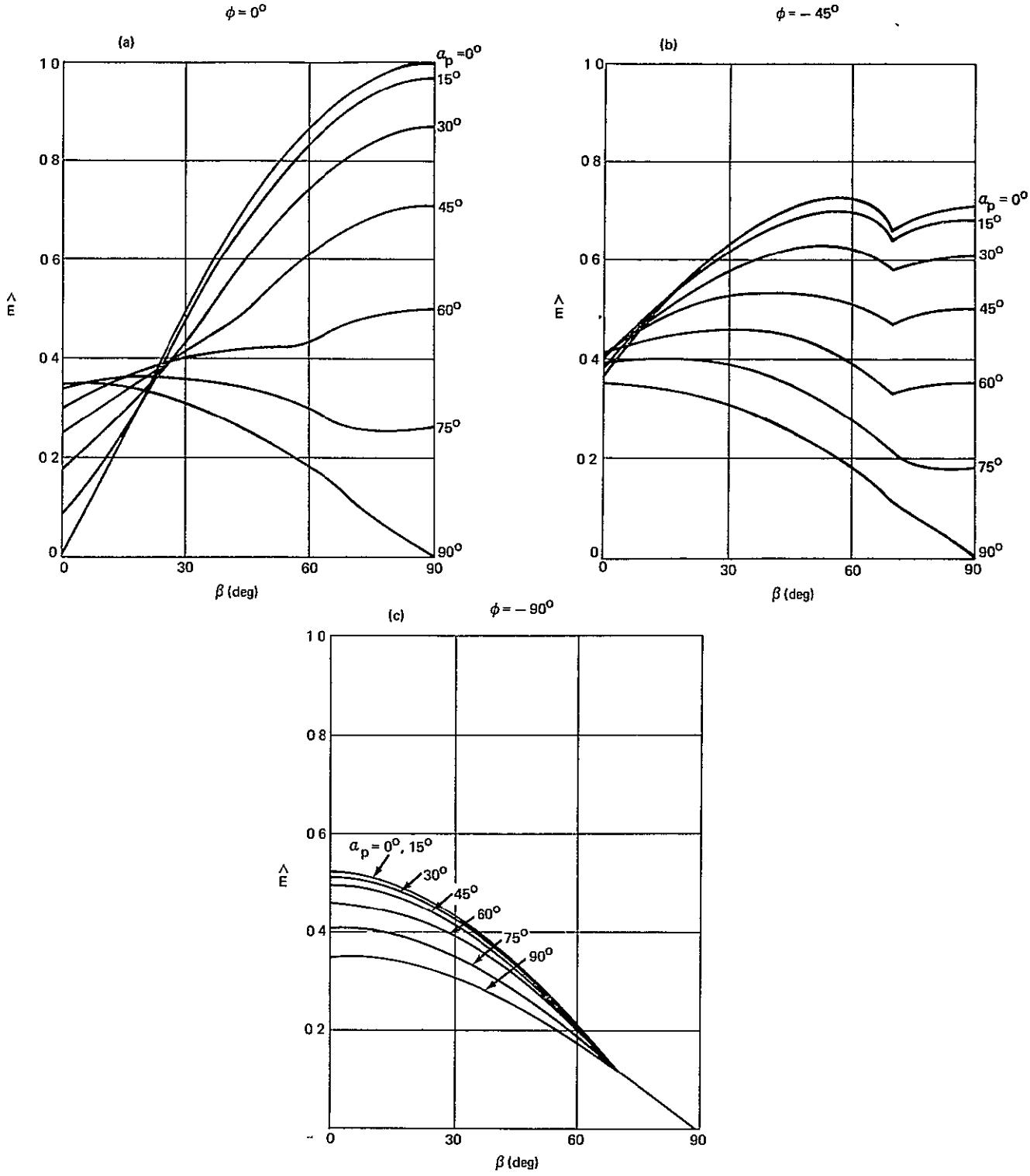

Figure (5 - 24) - Normalized Electrical Energy from Solar Array as a Function of α_p and β (LH - Fixed Roll Modes)

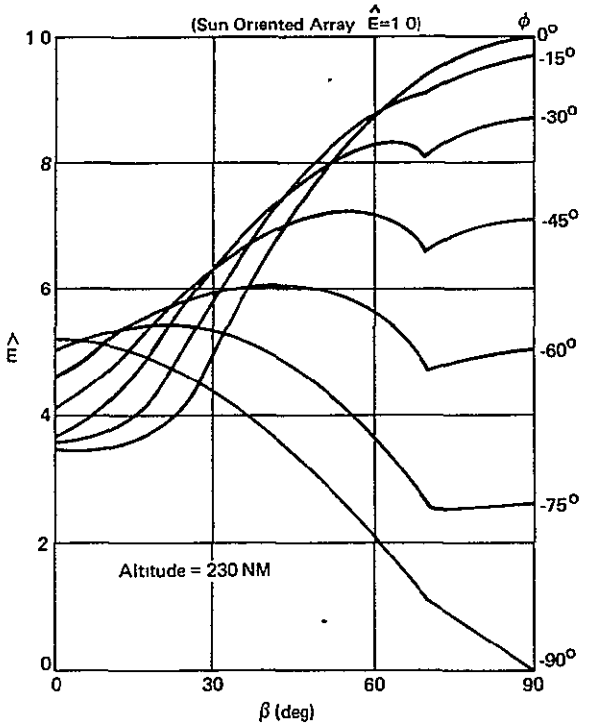

Figure (5 - 25) - Maximum Electrical Energy from Solar Array as a Function of β ($\alpha_p = \alpha_{p(opt)}$, LH- Fixed Roll Mode) .

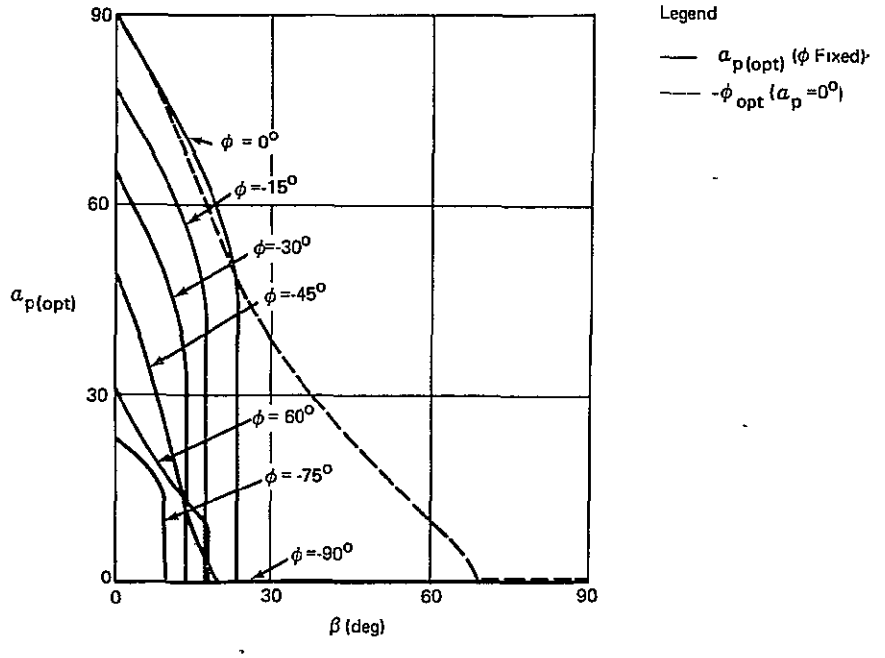

Figure (5 - 26) - Optimum Panel Angle vs β (LH - Fixed Roll Mode).

5.3.4 Electrical Energy in Perpendicular-to-Orbital-Plane Modes

The solar array orientation in the POP mode is illustrated in Fig. (5-27) with the panel coordinates (x_p, y_p, z_p) defined as in the LV and POP modes. When the panel angle (α_p) and the spacecraft roll angle (ϕ) are zero, the array is normal to the orbital plane with z_p directed along the upward local vertical.

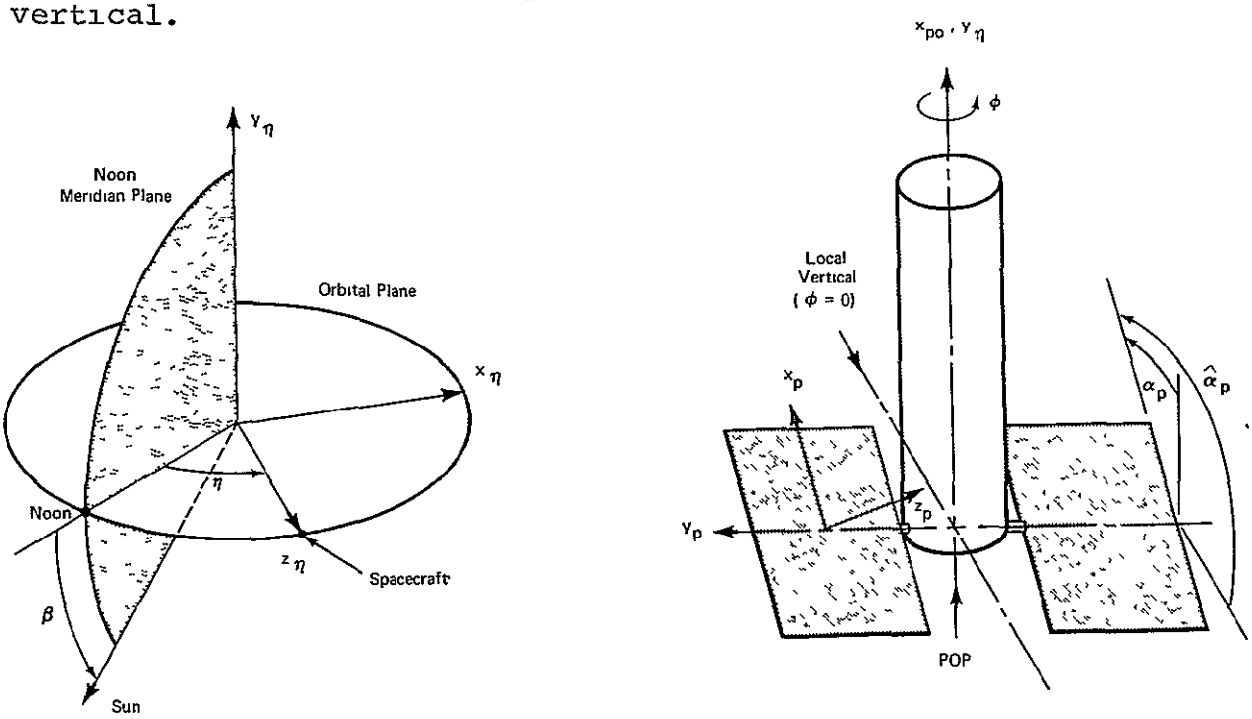

Figure (5 - 27) - Solar Array Orientation in POP Mode

For arbitrary α_p and ϕ the expression for $c\lambda$ given in Eq. (D-21) of Appendix D is

$$c\lambda_{POP} = c\alpha_p \; c\beta \; c(\phi+\eta) - s\alpha_p \; s\beta \qquad (5\text{-}52)$$

Two POP modes of interest are based on a solar oriented array (S/POP) and a local vertical oriented spacecraft (LV/POP) for accommodating earth pointing experiments.

S/POP Mode

The angles α_p and ϕ corresponding to a solar oriented array ($c\lambda_{POP}=1$) are simply

$$\alpha_p = -\beta \qquad (5\text{-}53)$$

$$\phi = -\eta \qquad (5\text{-}54)$$

so that $\hat{E}$ in Eq.(5-16) is just $\hat{E}=1.0$. This mode was to be used for AAP-1/AAP-2/AAP-3A missions with the "Wet Workshop" configuration.

LV/POP Mode

In a LV/POP mode $\phi=0°$ is the spacecraft roll angle for accommodating earth pointing experiments with a line-of-sight normal to the array articulation axis (y_p). Hence,

$$c\lambda_{POP} = c\alpha_p \, c\beta \, c\eta - s\alpha_p \, s\beta = s\hat{\alpha}_p \, c\beta \, c\eta + c\hat{\alpha}_p \, s\beta \quad (5\text{-}55)$$

which is equivalent to $c\lambda_{LV}$ in Eq.(5-18) for $\phi=0°$, if the angle $\hat{\alpha}_p=90°+\alpha_p$ shown in Fig.(5-27) is interpreted as the panel angle. Thus, all results in Section 5.3.2.2 for the LV-Fixed Roll mode ($\phi=0°$) are applicable to the LV/POP mode. Specifically this includes curves for $\hat{E}$, $\hat{E}_{max}$ and $\alpha_{p(opt)}$ vs β given in Figs.(5-15a), (5-16) and (5-17).

5.3.5 Summary and Comparison of Optimum Solar Array Performance

Solar array energy output ($\hat{E}$) normalized to the output from a sun-oriented array at the same β has been evaluated for LV, LH and POP spacecraft attitudes and various roll profiles. In each case $\hat{E}$ is formulated as a function of β and the panel angle (α_p). For 230 NM orbits $\hat{E}$ is plotted vs β for various values of α_p in Figs. (5-9,10,11,15,21,22 and 24). The upper envelope boundary on these curves represents the maximum electrical energy ($\hat{E}_{max}$) available from the array with optimum variation of α_p with β. Plots of $\hat{E}_{max}$ and the corresponding optimum panel angle and roll angle (fixed roll modes) are shown in Figs.(5-28)-(5-31). Analytical expressions for $\hat{E}_{max}$, $\alpha_p(opt)$ and ϕ_{opt} (fixed roll modes) are given in Appendix C. For comparison, the maximum electrical energy ($\hat{E}_{o\ max}$) normalized to the sun-oriented array output at $\beta=0°$* is shown in Fig.(5-32).

Solar array performance in the LV-Optimum Roll mode is up to 50% higher than in the LH-Optimum Roll mode and at worst is only 15% less than the sun-oriented array performance. In the LV and LH-Cyclic Roll modes performance approaches 85% of that for the sun-oriented array in the intermediate range of β ($30°<\beta<60°$) with the LV-Cyclic Roll mode significantly better than the LH-Cyclic Roll mode for $\beta<30°$.

---

*See Footnote *, p. 44.

In fixed roll cases optimum array performance is the same in all three attitude modes: LV, LH and POP. The results indicate that the maximum array output is only 52% of the sun-oriented array output at $\beta=0°$, but increases steadily with increasing β. Maximum output is achieved in LV and POP modes with array articulation only ($\phi_{opt}=0°$, $\alpha_{p(opt)}=\underline{+}\alpha_{opt}$)* whereas in the LH mode, only incremental spacecraft roll is necessary ($\phi_{opt}=-\underline{+}\alpha_{opt}$, $\alpha_{p(opt)}=0°$).

These results represent the maximum which can be achieved with array pointing using only spacecraft roll and/or incremental SDOF array articulation.** The curves of $\hat{E}_{max}$ vs β permit a direct assessment of the minimum possible performance degradation in several orbit-oriented modes from the performance of solar-oriented arrays.*** Additional degradation for particular configurations where spacecraft shadowing of arrays is a significant factor must be evaluated separately. Changes in orbital altitude of perhaps ±30 NM from the 230 NM altitude used in this analysis will tend to have only slight effect. Altitude affects η_{es}, which in view of Fig.(5-4) varies only slightly with a ±30 NM altitude change. For larger altitude changes the analytical results in previous sections and in Appendix C can be used to evaluate $\hat{E}$ and $\hat{E}_{max}$ vs β.

---

*See Appendices C.4 and C.7 for derivation of $\underline{+}\alpha_{opt}$ and evaluation of ϕ_{opt} and $\alpha_{p(opt)}$.

**Results in Section 4 for $|\beta|_{max}$ and $|\dot{\beta}|_{max}$ may be used with curves of $\alpha_{p(opt)}$ vs β in assessing maximum articulation and articulation rate requirements.

***The solar array model used in this analysis, Eq.(5-9), includes the primary effect ($c\lambda$) on array output. When the sun incidence angle (λ) is large (e.g. $\lambda>70°$), temperature fluctuations and cover glass reflection[14] may have a significant effect on the instantaneous power output. However, unless λ is large over an appreciable portion of the array sunlight interval, the impact of these effects on energy output per orbit is relatively small.

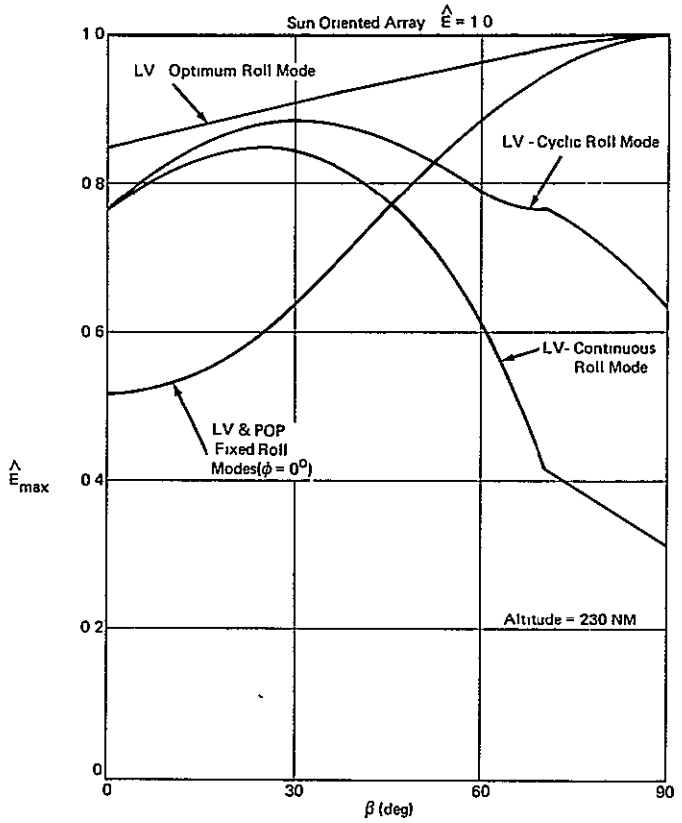

Figure (5 - 28) - Maximum Electrical Energy from Solar Array vs β (LV and POP Modes).

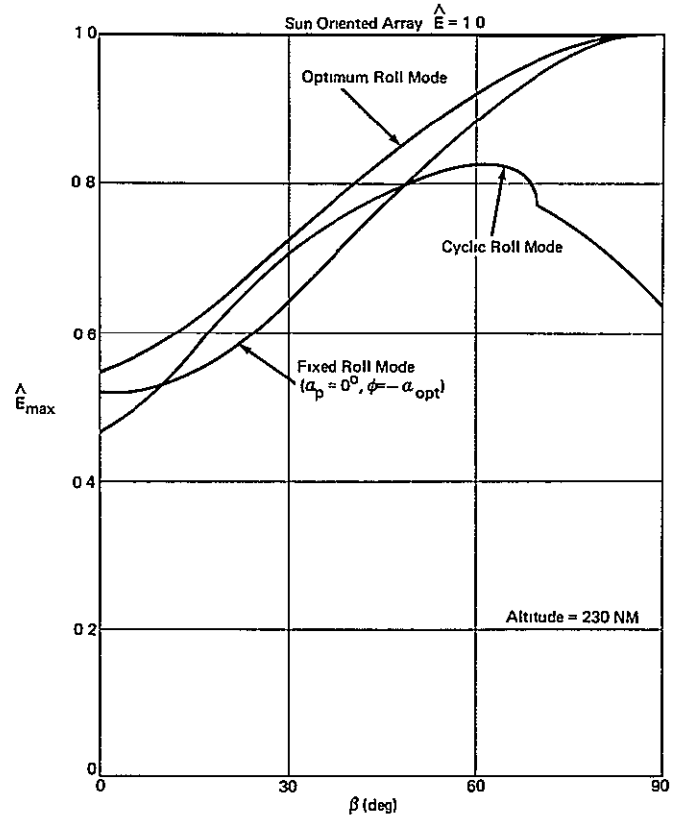

Figure (5 - 29) - Maximum Electrical Energy from Solar Array vs β (LH Modes).

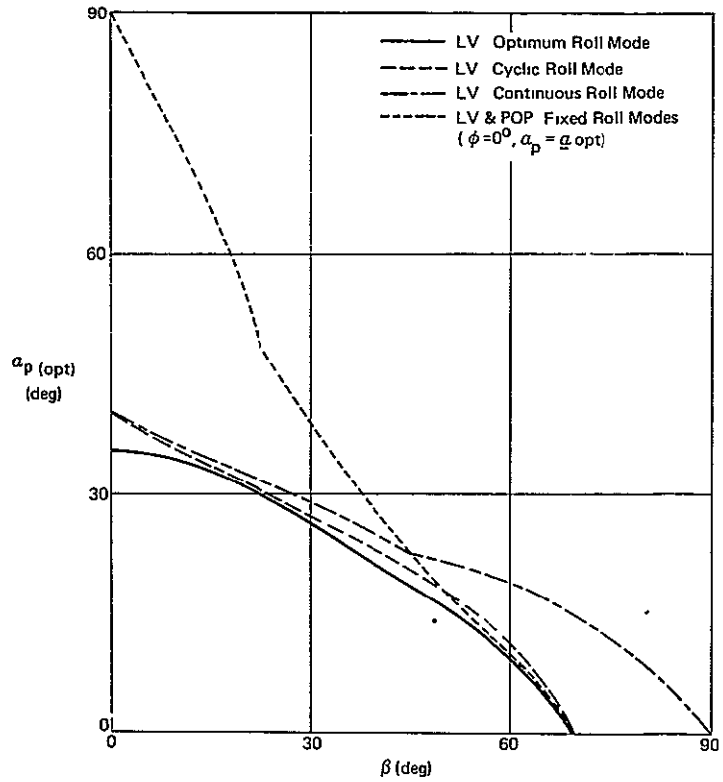

Figure (5 - 30) - Optimum Panel Angle vs β (LV and POP Modes)

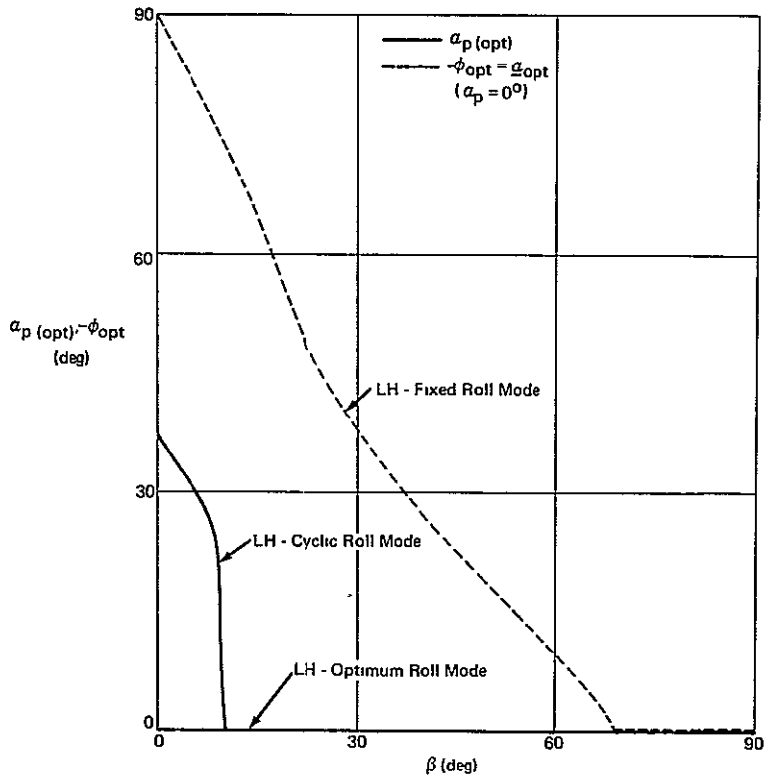

Figure (5 - 31) - Optimum Panel Angle vs β (LH - Optimum & Cyclic Roll Modes), Optimum Spacecraft Roll Angle vs β (LH - Fixed Roll Mode).

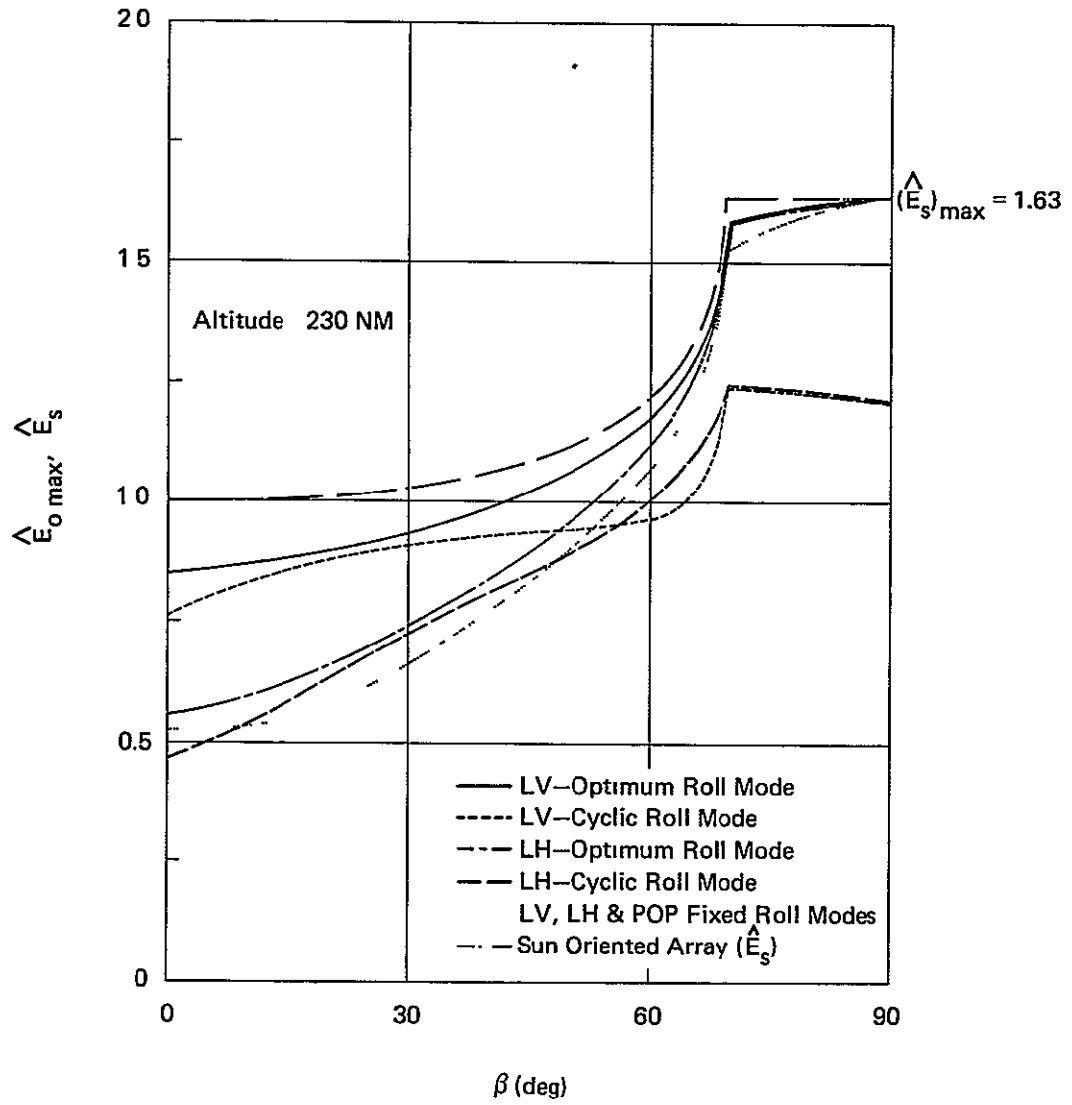

Figure (5 - 32) - Maximum Electrical Energy from Solar Array vs. β (Normalized to Sun-Oriented Array Output at $\beta = 0^{o}$).

5.4 Incident Thermal Energy on Spacecraft

Thermal energy incident on spacecraft surfaces in earth orbit is derived primarily from three external sources: direct solar radiation, earth reflected solar radiation and earth-emitted thermal radiation. In solar-oriented attitudes the direct solar component is constant during sunlight intervals whereas the reflected solar and earth thermal components vary with location in orbit and β. In earth-oriented attitudes the direct and reflected solar components vary with location in orbit and β while the earth thermal component is constant for circular orbits and varies only with altitude for elliptical orbits.

The incident radiation from each energy source can be evaluated in terms of view factors which account for the surface configuration and other parameters such as orbit altitude and the orientation of the surface with respect to the sun and the earth. View factors are normally derived on the basis of the following assumptions:

1. direct solar radiation impinges with parallel rays,
2. earth emitted radiation is diffuse and constant for all points on the earth (earth assumed in state of thermal equilibrium),
3. earth is a diffuse reflector with constant albedo over the entire surface, and
4. atmospheric scattering effects of direct solar radiation on spacecraft surfaces are negligible.

In terms of view factors the incident thermal radiation from each energy source can be expressed as

$$Q_D = SA \cdot F_{DS} \qquad \text{(Direct Solar)} \qquad (5\text{-}56)$$

$$Q_R = SA \cdot \bar{a} F_{RS} \qquad \text{(Reflected Solar)} \qquad (5\text{-}57)$$

$$Q_{ET} = SA \cdot \frac{(1-\bar{a})}{4} F_{ET} \qquad \text{(Earth Thermal)} \qquad (5\text{-}58)$$

Here S represents the solar constant (443 Btu/hr/ft^2)[12], A is the maximum projected surface and $\bar{a}$ is the earth albedo constant (0.36).[12] The various view factors are represented by

F_{DS}, F_{RS} and F_{ET}.* Since the spectral content of earth thermal radiation is wide, it normally is treated separately whereas direct and reflected solar radiation frequently are combined.**

The incident thermal energy per orbit upon a surface is obtained by integrating each component of the incident thermal radiation over an orbital period (T):

$$W_i \equiv \int_{-T/2}^{T/2} Q_i dt = \int_{-\pi}^{\pi} Q_i d\eta/\dot{\eta} \qquad (i = DS,RS \text{ or } ET) \tag{5-59}$$

where $\dot{\eta}$ is the instantaneous orbital angular velocity. In the following work only circular orbits are considered so that $\dot{\eta} \equiv \omega_o = 2\pi/T$. It is convenient to normalize W_i with respect to the direct solar component for $\beta=0°$ with the area A normal to the sun line (i.e., $F_{DS}=1.0$ during the sunlight interval $-\eta_{eso}<\eta<\eta_{eso}$).*** In normalized form

$$\hat{W}_i \equiv W_i/W_n = \frac{1}{2\eta_{eso}} \int_{-\pi}^{\pi} \frac{Q_i}{SA} d\eta \qquad (i = DS,RS \text{ or } ET) \tag{5-60}$$

---

*As a consequence of the parallel ray assumption for direct solar radiation, F_{DS} is merely the direction cosine between the sun line and the positive normal to area A. Evaluation of F_{RS} and F_{ET} entails integration over the surface of the earth which can reflect or radiate thermal energy to area A. Heretofore, F_{RS} and F_{ET} have been evaluated numerically[18,19,20] and tabulated for certain ranges of parameters.[18] Recent analytical results[21] have led to closed form expressions which cover several geometrical shapes and a wide range of parameters exactly and approximate well the exact case in other ranges.

**An equivalent view factor corresponding to the sum of direct and reflected solar radiation is given by

$$F_S = F_{DS} + \bar{a}F_{RS} \equiv Q_s/SA$$

***Here $\pm\eta_{eso}$ represents the orbital terminator at $\beta=0°$. See Fig. (5-3b).

where

$$W_n \equiv \frac{1}{\omega_o}\int_{-\pi}^{\pi} Q_{DS}\,d\eta = \frac{1}{\omega_o}\int_{-\eta_{eso}}^{\eta_{eso}} SA\,d\eta = \frac{SA}{\omega_o}\left(2\eta_{eso}\right) \quad (5\text{-}61)$$

Specification of a particular attitude mode and surface configuration leads to particular expressions for the view factors F_{DS}, F_{RS} and F_{ET} which are functions of β, orbital position η and orbital altitude H.[21] Integration of Eq.(5-60) for each radiation component yields the normalized incident thermal energy.

5.4.1 Cylindrical Surface Configurations in Earth-Oriented Modes

The incident thermal energy is evaluated first for LV, LH and POP attitude modes* and a cylindrical spacecraft model with hemispherical ends shown in Fig.(5-33a). View factors F_{DS}, F_{RS}, F_{ET} and the corresponding components of the incident thermal energy per orbit are given in Table 5-1. The first term in each block of Table 5-1a corresponds to the lateral surface of the cylinder, while the second term is

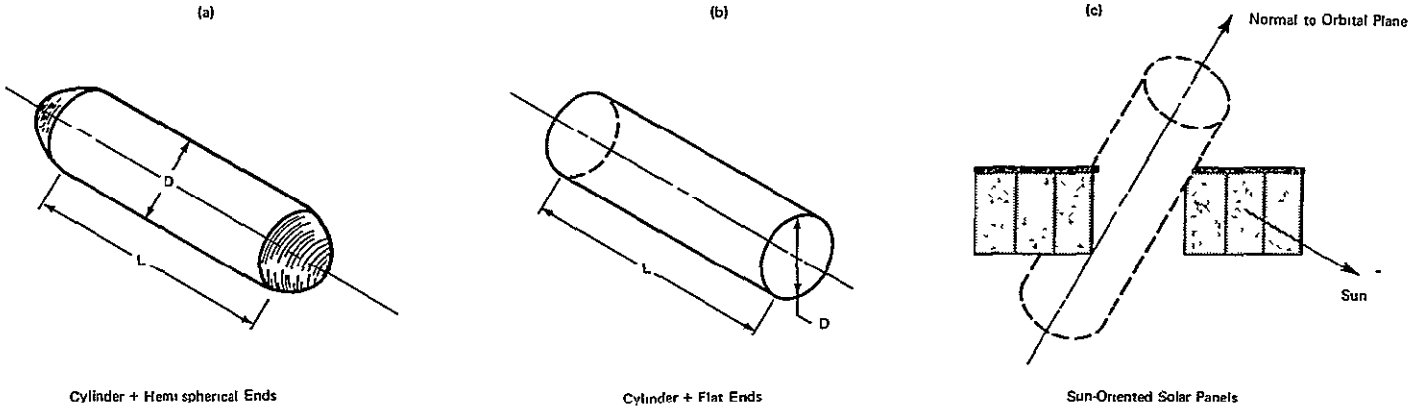

Figure (5 - 33) - Flat, Hemispherical and Cylindrical Spacecraft Surface Configurations.

*See Footnote **, p.1.

TABLE 5 - 1

(a) View Factors and Normalized Incident Thermal Energy Per Orbit For a Cylinder/Hemispherical-End Spacecraft Configuration

Attitude Mode \ View Factor	F_{DS}	F_{RS}*		F_{ET}
	$-\eta_{es} < \eta < \eta_{es}$	$0 \leq \theta_s \leq 90° - \theta_o$	$\theta_s = 90°$	$-180° \leq \eta \leq 180°$
LV	$\sqrt{1 - c^2\beta c^2\eta} + \underline{\lambda}$	$I_{cc}\ c\theta_s + \underline{\lambda} I_{cs}\ c\theta_s$	$I_{sc} + \underline{\lambda} I_{ss}$	$F_{co} + \underline{\lambda} F_s$
LH	$\sqrt{1 - c^2\beta s^2\eta} + \underline{\lambda}$	$J_{cc}\ c\theta_s + \underline{\lambda} I_{cs}\ c\theta_s$	$2J_{s90} + \underline{\lambda} I_{ss}$	$F_{c90} + \underline{\lambda} F_s$
POP	$c\beta + \underline{\lambda}$	$J_{cc}\ c\theta_s + \underline{\lambda} I_{cs}\ c\theta_s$	$J_{so} + \underline{\lambda} I_{ss}$	$F_{c90} + \underline{\lambda} F_s$
Attitude Mode \ $\hat{W}$	$\hat{W}_{DS}(2\eta_{eso})$ **	$\hat{W}_{RS}(2\eta_{eso}/\bar{a})$		$\hat{W}_{ET}\left(\frac{8\eta_{eso}}{1-\bar{a}}\right)$
		$0 \leq \beta < 90°$	$\beta = 90°$	
LV	$2[E(k) + E(\Theta, k)] + \underline{\lambda}(2\eta_{es})$	$2I_{cc}c\beta + \underline{\lambda}(2I_{cs}\ c\beta)$	$2\pi I_{sc} + \underline{\lambda}(2\pi I_{ss})$	$2\pi F_{co} + \underline{\lambda}(2\pi F_s)$
LH	$2E(k, \eta_{es}) + \underline{\lambda}(2\eta_{es})$	$2J_{cc}c\beta + \underline{\lambda}(2I_{cs}\ c\beta)$	$2\pi J_{s90} + \underline{\lambda}(2\pi I_{ss})$	$2\pi F_{c90} + \underline{\lambda}(2\pi F_s)$
POP	$2\eta_{es}\ c\beta + \underline{\lambda}(2\eta_{es})$	$2J_{cc}c\beta + \underline{\lambda}(2I_{cs}\ c\beta)$	$2\pi J_{so} + \underline{\lambda}(2\pi I_{ss})$	$2\pi F_{c90} + \underline{\lambda}(2\pi F_s)$

Definitions $\theta_s = \cos^{-1}(c\beta\, c\eta)$, $0 \leq \theta_s \leq 180°$

$r = c\theta_o = R/(R+H)$, R = earth radius; H = local altitude

$k = c\beta$

$\eta_{eso} = 90° + \theta_o$; $\eta_{es} = 180° - \cos^{-1}(s\theta_o/c\beta)$; $\Theta = \eta_{es} - 90°$

(b) View Factor Coefficients **

Coefficient	H Arbitrary	H= 230 NM
F_s	$2(1-\sqrt{1-r^2})$	0.326
F_{co}	$(\sin^{-1} r - r\sqrt{1-r^2})$	0 889
$F_{c\,90}$	$[\sin^{-1} r + \sqrt{1-r^2}/(1+r+r^2/2) - (2/\pi)\sqrt{1-r^2}\,E(r)]$	1.113
I_{cs}	$(2/3r)\,[(2+r^3) - (2+r^2)\sqrt{1-r^2}]$	1.295
I_{ss}	$(2/3r\pi)\{(2+r^2)(1-r)[K(k_r) - F(\phi_r, k_r)] - (2-r^2)(1+r)[E(k_r) - E(\phi_r, k_r)] - 2r(1-r^2)\}$; $k_r = 4r/(1+r)^2$, $\phi_r = \sin^{-1}(\sqrt{1+r}/2)$	0 038
I_{cc}	$\pi r^3/8 + (3/4r)[\sin^{-1} r - r(1+2r^2/3)\sqrt{1-r^2}]$	0 881
I_{sc}	$(1/4\pi)\{(1/2r)(3+r^2)(1-r^2)\ln[(1+r)/(1-r)] - (3-r^2-2r^3)\}$	0 031
J_{cc}	$(r/4)[1-r(1-\sqrt{1-r^2})] + [(1+r^2)/2r]\sin^{-1} r + (\sqrt{1-r^2}/4r)[2.5(1+r+r^2) + (r/2) - (1/\pi)(4r^2+7)E(r) + (2/\pi)(1-r^2)K(r)]$	1.104
J_{so}	———	0.028***
J_{s90}	———	0.033***

*The expressions given for F_R are exact for the range of θ_s stated. Except for values of η and β approaching 90° however, the expressions for $0° \leq \theta_s \leq 90° - \theta_o$ also approximate well the exact case when $90° - \theta_o < \theta_s < 90°$. When $\theta_s > 90°$, F_R is negligibly small. For typical low earth orbits, $180 \leq H \leq 240$ NM, note also that $18.13° \leq \theta_o \leq 20\,80°$.

**Complete Elliptic Integrals are designated by. K(k), K(r) (1st kind); E(k), E(k_r) or E(r) (2nd kind) Incomplete Elliptic Integrals are designated by· $F(\phi_r, k_r)$ (1st kind); $E(\Theta, k)$ or $E(\phi_r, k_r)$ (2nd kind)

***Data obtained numerically, no analytical expression available

associated with the hemispherical ends.* Since the cylinder lateral cross-sectional area (DL) is used as the reference area (A), the factor, $\underline{\lambda} = \pi D/4L$, accounts for the maximum projected area ratio between the ends and the lateral surface. In Table 5-1b coefficients of the view factors in Table 5-1a are tabulated: (a) as functions of the altitude parameter, r=R/(R+H), and (b) for a specific altitude, H=230 NM.

The variation in incident thermal radiation ($F_S=Q_S/SA$** and $F_{ET}=Q_{ET}/SA$) is shown in Fig.(5-34a) as a function of β and orbital position η for the POP mode at an orbital altitude of 230 NM and D/L=0.2. The relationship between incident radiation in LV, LH and POP attitude modes is shown in Figs.(5-34b) and (5-34c) for $\beta=0°$ and 60°. The corresponding incident thermal energy per orbit ($\hat{W}_S$ and $\hat{W}_{ET}$) is shown in Fig.(5-35a) as a function of β for all three modes. These results show that the incident energy obtained in POP exceeds that in LV and LH for $|\beta| \lesssim 36°$. However, the incident energy obtained in LV and LH increases markedly as the earth shadow interval disappears ($\beta \gtrsim 69.6°$).

The effect of the hemispherical-end surfaces can be assessed by comparing the incident thermal energy data with that shown in Fig.(5-35b) for a cylinder/flat-end configuration. See Fig.(5-33b).*** Although the incident thermal energy level is somewhat higher due to the larger surface area of the hemispherical ends, the basic trend is the same for all three attitude modes. Results for other end surface configurations lying inside the hemispheric volume should fall within the data for hemispherical and flat-end cylinders.

---

*In this example only the total incident thermal energy on the configuration is considered. Consequently, the hemispherical ends are equivalent to a single sphere of the same diameter insofar as evaluation of view factors is concerned. In other analyses, because of different surface coatings for heat load modification, the incident radiation on elemental areas of the spacecraft may be of interest. This can be achieved by approximating the actual surface with an appropriate number of flat plates for which the view factors and incident thermal energy can be evaluated separately.[21]

**See Footnote ** on page 74.

***View factors F_{DS}, F_{RS} and F_{ET} for this configuration are given in Ref. 21.

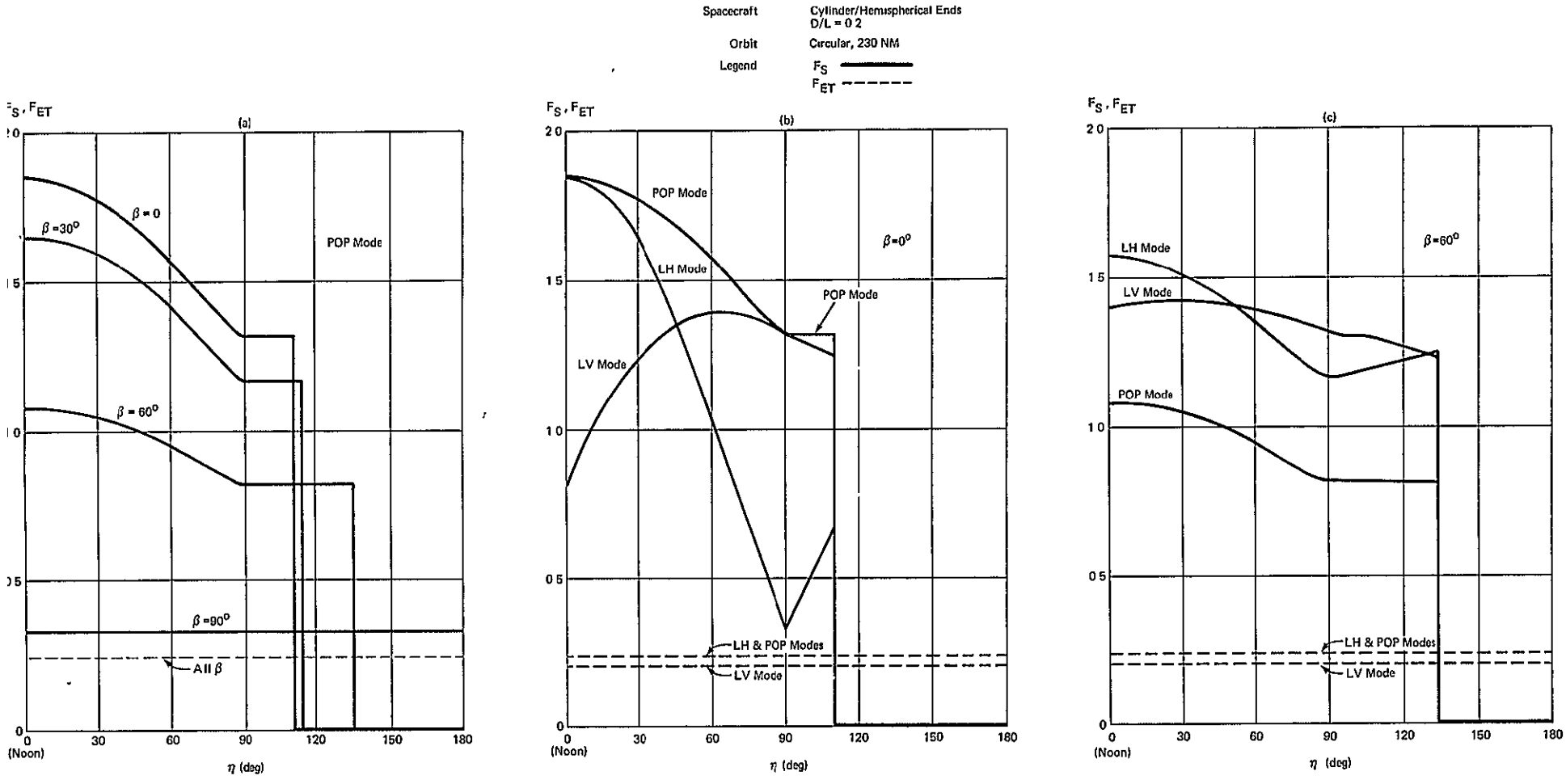

Figure (5 - 34) - Normalized Incident Thermal Radiation vs Location in Orbit (η) (LV, LH and POP Modes).

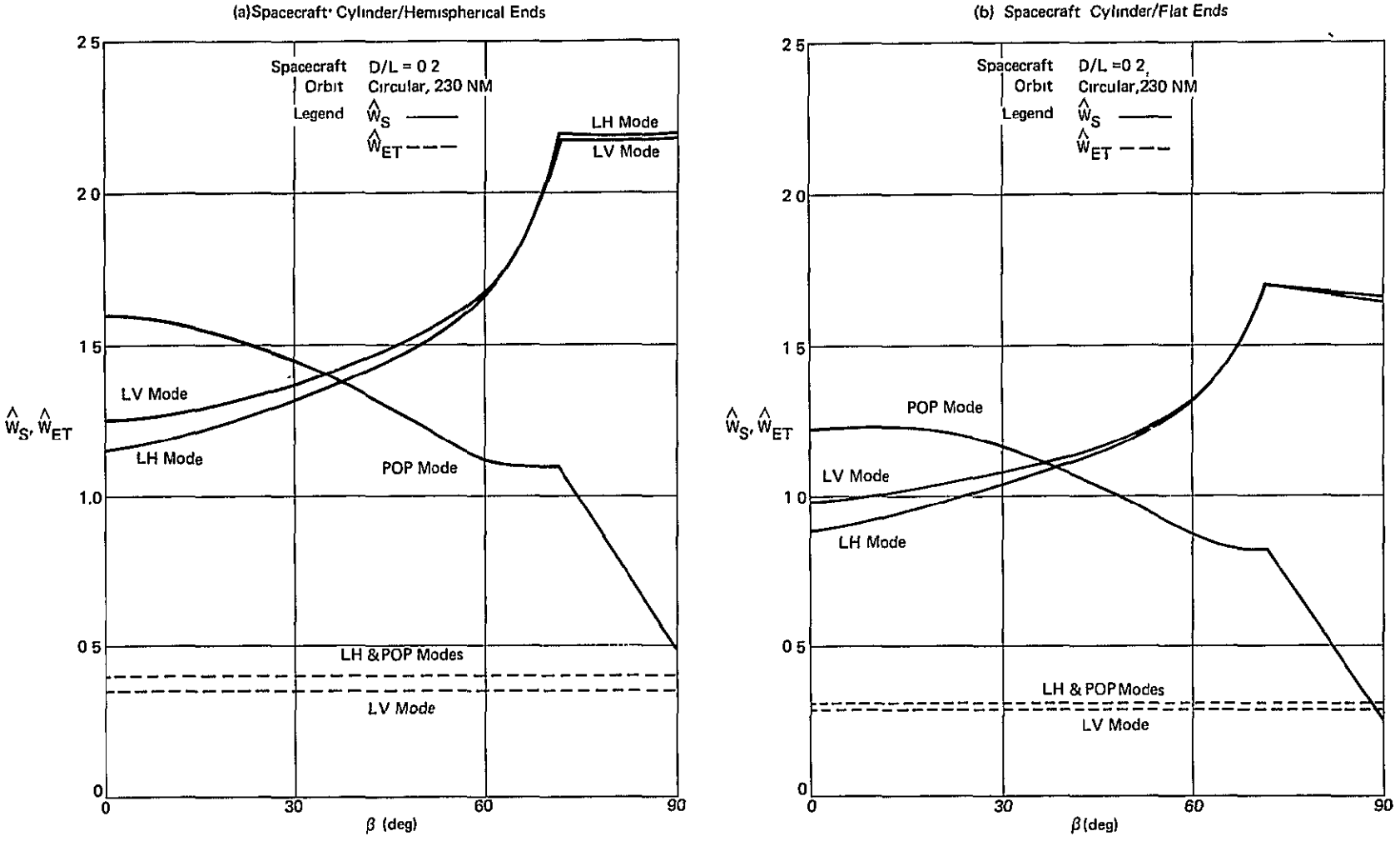

Figure (5 - 35) - Normalized Incident Thermal Energy Per Orbit vs β
(LV, LH and POP Modes)

5.4.2 Flat Surface Configuration in Solar Oriented Attitude Mode

An attitude mode and flat surface configuration of interest is one with a sun-oriented solar panel as encountered, for example, in the solar-inertial mode and in the POP mode shown in Fig.(5-33c). Here direct solar radiation impinges only on one side whereas reflected solar and earth thermal radiation may impinge on both sides, but varies with β and η. The normalized incident radiation for the sun-oriented panel is shown in Fig.(5-36) as a function of β and η.* The incident thermal energy per orbit vs. β is given in Fig.(5-37).

*View factors F_{DS}, F_{RS} and F_{ET} for this configuration are given in Ref. 21.

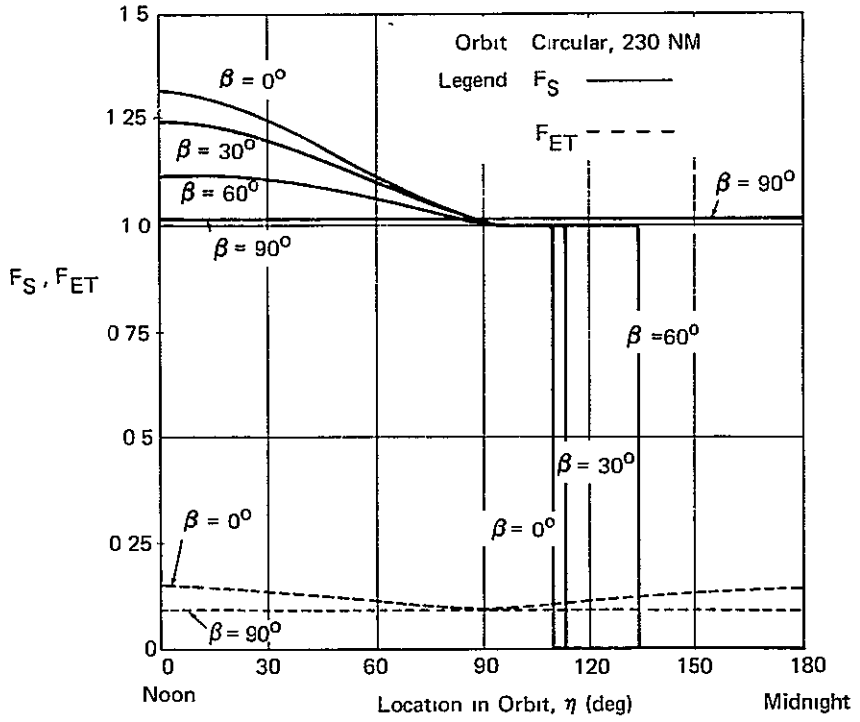

Figure (5 - 36) - Normalized Incident Thermal Radiation vs Location in Orbit (Sun-Oriented Solar Panel)

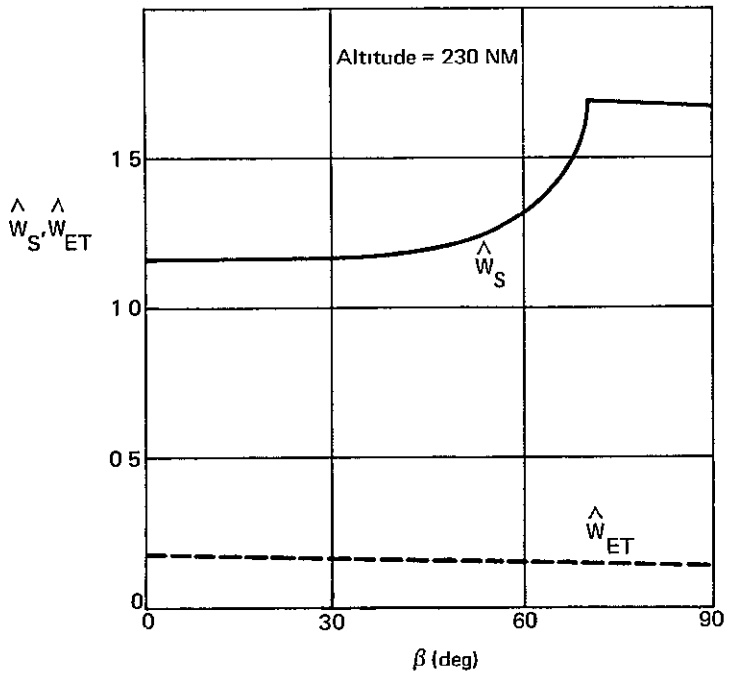

Figure (5 - 37) - Normalized Incident Thermal Energy per Orbit vs β (Sun-Oriented Solar Panel)

6.0 AVERAGE EFFECTS OF THE β VARIATION

For a particular mission the β profile in circular orbits is influenced by five parameters: time (t), time of day of launch (t_L), launch date (D_L)*, orbit inclination (i) and orbit altitude (H). In previous sections a number of system performance factors have been described and related to β. From a mission design standpoint it is of interest to examine mission averages of these factors** and the effect of mission duration (T_M), launch time uncertainty (t_L,D_L) and orbit inclination and altitude. Before discussing averages of specific performance factors, mission averages are defined in general and several properties are described.

6.1 Mission Averages

The mission average of a function f(β) can be expressed as

$$f_{av} = f_{av}(T_M, t_L, D_L, i, H)$$

$$\equiv \frac{1}{T_M}\int_0^{T_M} f(\beta)dt = \frac{1}{T_M}\int_0^{T_M} f(t, t_L, D_L, i, H)dt \qquad (6\text{-}1)$$

where T_M is the mission duration. The extremes on f_{av} with respect to launch conditions (t_L,D_L) are defined as

$$\langle\langle f_{av}\rangle\rangle \equiv \underset{t_L, D_L}{\text{Max}}\ f_{av} = \underset{t_L, D_L}{\text{Max}}\ \frac{1}{T_M}\int_0^{T_M} f(t, t_L, D_L, i, H)dt \qquad (6\text{-}2)$$

$$\langle f_{av}\rangle \equiv \underset{t_L, D_L}{\text{Min}}\ f_{av} = \underset{t_L, D_L}{\text{Min}}\ \frac{1}{T_M}\int_0^{T_M} f(t, t_L, D_L, i, H)dt \qquad (6\text{-}3)$$

---

*See Section 4.0 or Appendix A.1 for discussion of launch time.

**The relevance of mission averages to mission design is discussed in Section 6.2.

Frequently launch time and date are uncertain at early stages of mission planning. If t_L and D_L are regarded as independent, uniformly distributed random variables, the mean of f_{av} is given by

$$\overline{f_{av}} \equiv \underset{t_L, D_L}{\text{Mean}} \; f_{av} = \frac{1}{D_{LM}\, t_{LM}} \int_0^{D_{LM}} \int_0^{t_{LM}} f_{av}\left(T_M, t_L, D_L, i, H\right) dt_{LM} dD_{LM} \tag{6-4}$$

where

$$t_{LM} \equiv 24 \text{ hours} \tag{6-5}$$

and

$$D_{LM} = 365 \text{ days} \tag{6-6}$$

A particular function of interest is $f(\beta) = |\beta|$. In Fig. (6-1a) the mean and limits of $|\beta|_{av}$ obtained numerically by scanning t_L and D_L are shown for a 35°, 230 NM circular orbit and mission durations up to one year. The mission average of $|\beta|$ for all possible launch times and dates lies within the envelope formed by $\ll|\beta|_{av}\gg$ and $\langle|\beta|_{av}\rangle$. The $|\beta|_{av}$ envelope converges to $\overline{|\beta|_{av}}$=23.53° which is independent of mission duration and altitude.* Oscillatory behavior of the envelope is due to the multiperiodic nature of β. The rate of envelope convergence to $\overline{|\beta|_{av}}$ is a function of altitude, although the effect is only slight in low altitude orbits. Hence, mission average characteristics for $|\beta|_{av}$, as in Fig. (6-1) will apply in near earth orbits even with altitude decay.

---

*In calculating $|\beta|_{av}$ all possible β for a given orbit inclination are weighted equally, since t_L and D_L are assumed to be uniformly distributed. Consequently only orbit inclination, which determines the maximum range of β, has any effect on $\overline{|\beta|_{av}}$. (See section 4.1 for discussion on the β envelope.)

The variation of the mean and limits of $|\beta|_{av}$ with orbit inclination is shown in Fig.(6-1b)* for a 28 day mission. As mission duration increases, the $|\beta|_{av}$ envelope converges to $\overline{|\beta|_{av}}$, although the rate of convergence decreases continuously as i approaches i_{ss}, the inclination for a sun-synchronous orbit. (See Section 4.4). At $i=i_{ss}$ the $|\beta|_{av}$ envelope does not converge to $\overline{|\beta|_{av}}$, since β no longer oscillates between the upper and lower boundaries of the β envelope, as shown in Fig.(4-10).

*The curves are plotted for $0° \leq i \leq 180°$, although only certain inclinations are achievable with a direct launch from a given latitude and launch corridor (azimuth constraint) without yaw steering during launch or subsequent plane change maneuvers. See Eq.(2-9).

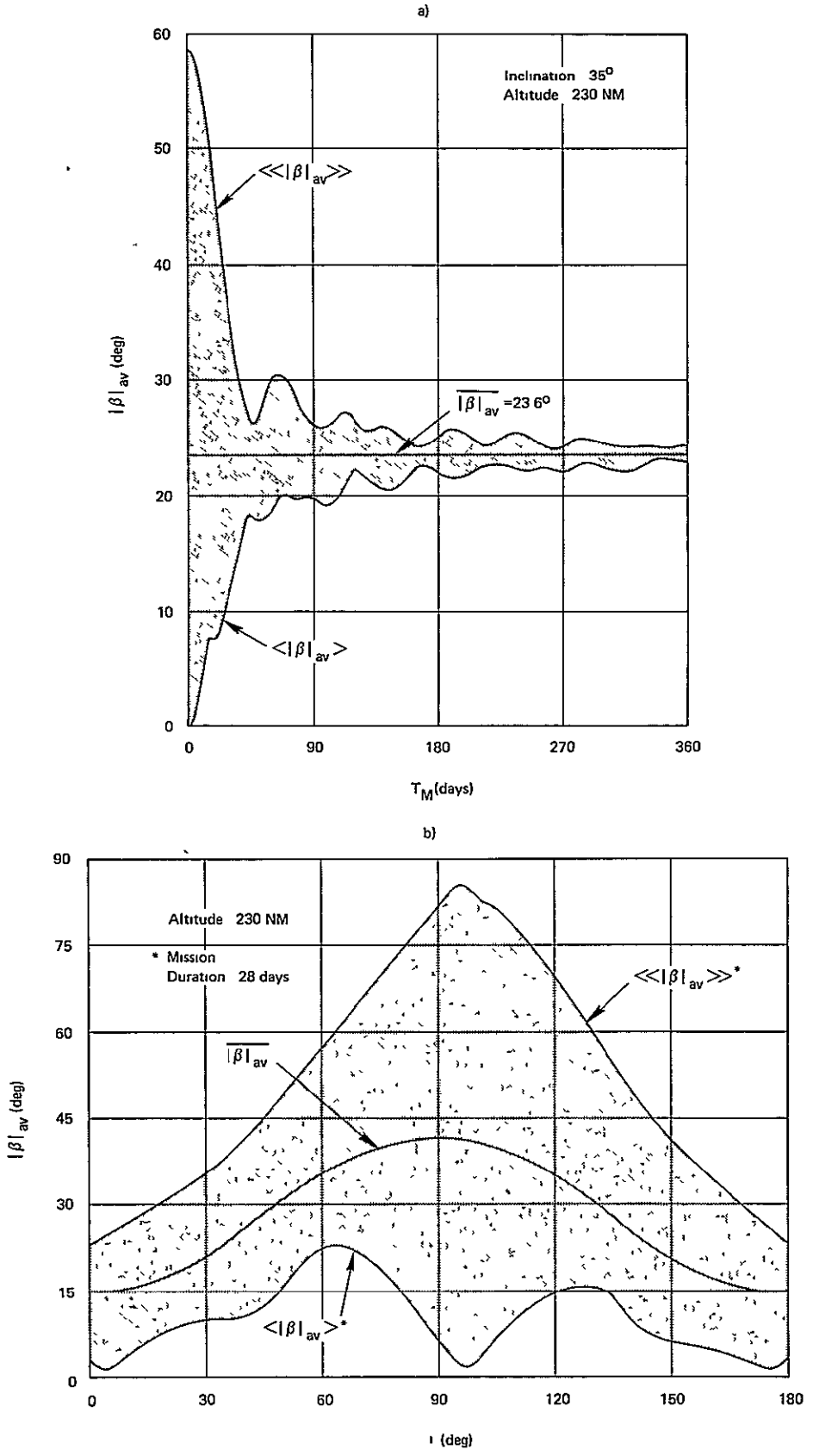

Figure (6 - 1) - Mean and Limits of $|\beta|_{av}$ vs Mission Duration (T_M) and Orbit Inclination (i)

6.2 Mission Average of System Performance Factors

Mission averages of system performance factors are often relevant to mission planning, since system designs based solely on worst case β conditions, which occur only at discrete times, may impose excessive requirements or may not utilize available performance margins. The system performance factors evaluated in Section 5 included:

1. $|\Delta\underline{H}|/\Delta H_{max}$ - the normalized bias gravity gradient torque-impulse on spacecraft in a solar-inertial mode (Section 5.1),
2. T_{SL} - the fraction of an orbit in sunlight (Section 5.2),
3. $\hat{E}_{max}$* - the normalized maximum electrical energy available from a planar solar array, optimally articulated (SDOF) with β, in LV and LH optimum roll modes, LV and LH cyclic roll modes and LV, LH and POP fixed roll modes (Section 5.3),
4. $\hat{W}_s$** - the normalized direct and reflected solar component of incident thermal energy per orbit on a cylindrical/hemispherical-end spacecraft configuration in LV, LH and POP attitude modes (Section 5.4).

---

*The normalization inherent in $\hat{E}_{max}$ represents the maximum array energy output (E_{max}) available in a particular attitude mode relative to the output from a sun-oriented array (E_s). Since E_s varies with β, it is more appropriate in evaluating mission averages of the array energy output to normalize relative to the sun-oriented array output at some particular β, say β=0°. In view of Footnote *, p.44,

$$\hat{E}_{o\ max} \equiv E_{max}/E_{so} = \hat{E}_s\ \hat{E}_{max}$$

Curves of $\hat{E}_{o\ max}$ vs β are shown in Fig.(5-32).

**$\hat{W}_{ET}$, the earth thermal component, is not considered here since it is constant for all β in these attitude modes.

The results obtained from evaluating the mean and limits of mission averages of these functions, $f(\beta)$, are presented in Figs. (6-2) through (6-7). These results are based on a 230 NM circular orbit, although altitude changes of ±30 NM or more (in many cases) have only slight effect. The various averages are plotted versus mission duration for i=35° and versus orbit inclination* for a 28 day mission. As was the case for $|\beta|_{av}$, the envelope on the functions (f_{av}) converges to the mean ($\overline{f_{av}}$), which is independent of mission duration, although not necessarily independent of orbit altitude.**

Mission averages of system performance factors are relevant to mission design in assessing certain systems requirements and/or performance margins, as will now be discussed for the performance factors described above.

$\underline{|\Delta H|/\Delta H_{max}}$

For bias momentum dumping via reaction thrust, $\overline{|s2(\beta+\hat{\phi})|}_{av}$ is directly proportional to the propellant requirement,

$$W_p = W_{pm}(T_M/T)\cdot\overline{|s2(\beta+\hat{\phi})|}_{av}$$

where W_{pm} is the maximum propellant consumption per orbit,*** T is the orbital period and T_M is the mission duration. The

---

*See Footnote *, p. 84.

**Generally $\overline{f_{av}}$ is a function of altitude, if $f(\beta)$ depends on altitude (H) explicitly, e.g., $f(\beta)=\eta_{es}$ depends on H explicitly whereas $f(\beta)=|s2(\beta+\hat{\phi})|$ does not.

***Since the maximum reaction thrust impulse requirement per orbit for dumping $|\underline{\Delta H}|$ is ΔH_{max},

$$W_{pm} = (2\Delta H_{max})/I_{sp}\ L = T_{gmx}\ T/I_{sp}\ L$$

where I_{sp} is the propellant specific impulse, L is the distance between a pair of thrusters fired as a couple and ΔH_{max} is defined in Eq. (5-3).

limits on $|s2(\beta+\hat{\phi})|_{av}$ shown in Fig. (6-2) indicate the possible variation in the propellant requirement due to launch time uncertainty for short duration missions (e.g. T_M<90 days) and in early phases of long duration missions. Angular displacement ($\hat{\phi}$=23°) of the spacecraft principal and geometric axes has relatively little effect on $\overline{|s2(\beta+\hat{\phi})|_{av}}$ vs i except at low or high inclinations where $\overline{|s2(\beta+\hat{\phi})|_{av}}$ is up to 40% more for $\hat{\phi}$=23° than for $\hat{\phi}$=0°.

T_{SL}

For solar observation experiments $\overline{(T_{SL})_{av}}$ is of interest, since it is proportional to the total-solar-viewing-time (TSVT)[3,13] for long duration missions (T_M>90 days, say). In fact*

$$TSVT = \overline{(T_{SL})_{av}} \cdot T_M \qquad (6-8)$$

The limits on $(T_{SL})_{av}$ shown in Fig. (6-3) indicate the possible variation in TSVT due to launch time uncertainty for short missions.

$\hat{E}_{o\ max}$

Solar array sizing is usually based on a worst-case analysis to insure that basic system power requirements are always accommodated. In the absence of constraints a designer may be able to afford the luxury of adding all subsystems to the basic system requirement without regard to intermittent operating requirements of many accessory systems (e.g. experiments, centrifuge operations, etc.). Since the worst-case condition corresponding to certain β angles exists only at discrete times however, some margin is available at other times to accommodate accessory systems on a scheduling basis. From a power availability standpoint the best on-time for accessory systems could be selected during a mission by an on-board scheduler monitoring the β profile and electrical power margins or prior to launch by time-line analysis, when system design

*The viewing time for experiments affected by earth's atmosphere is less. Atmospheric effects on solar viewing time are considered in References 13 and 22.

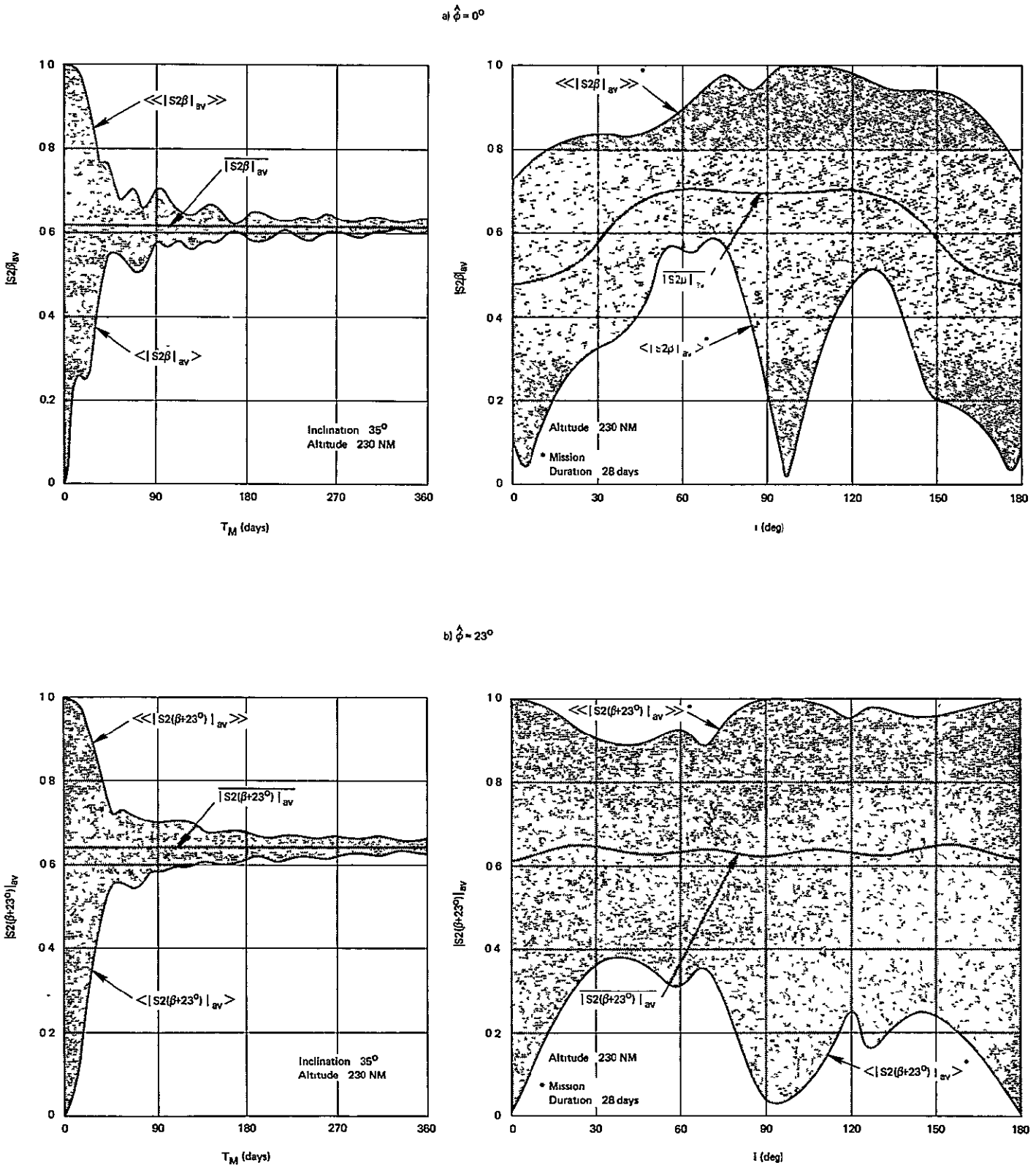

Figure (6 - 2) - Mean and Limits of $|s2(\beta + \hat{\phi})|_{av}$ vs Mission Duration and Orbit Inclination.

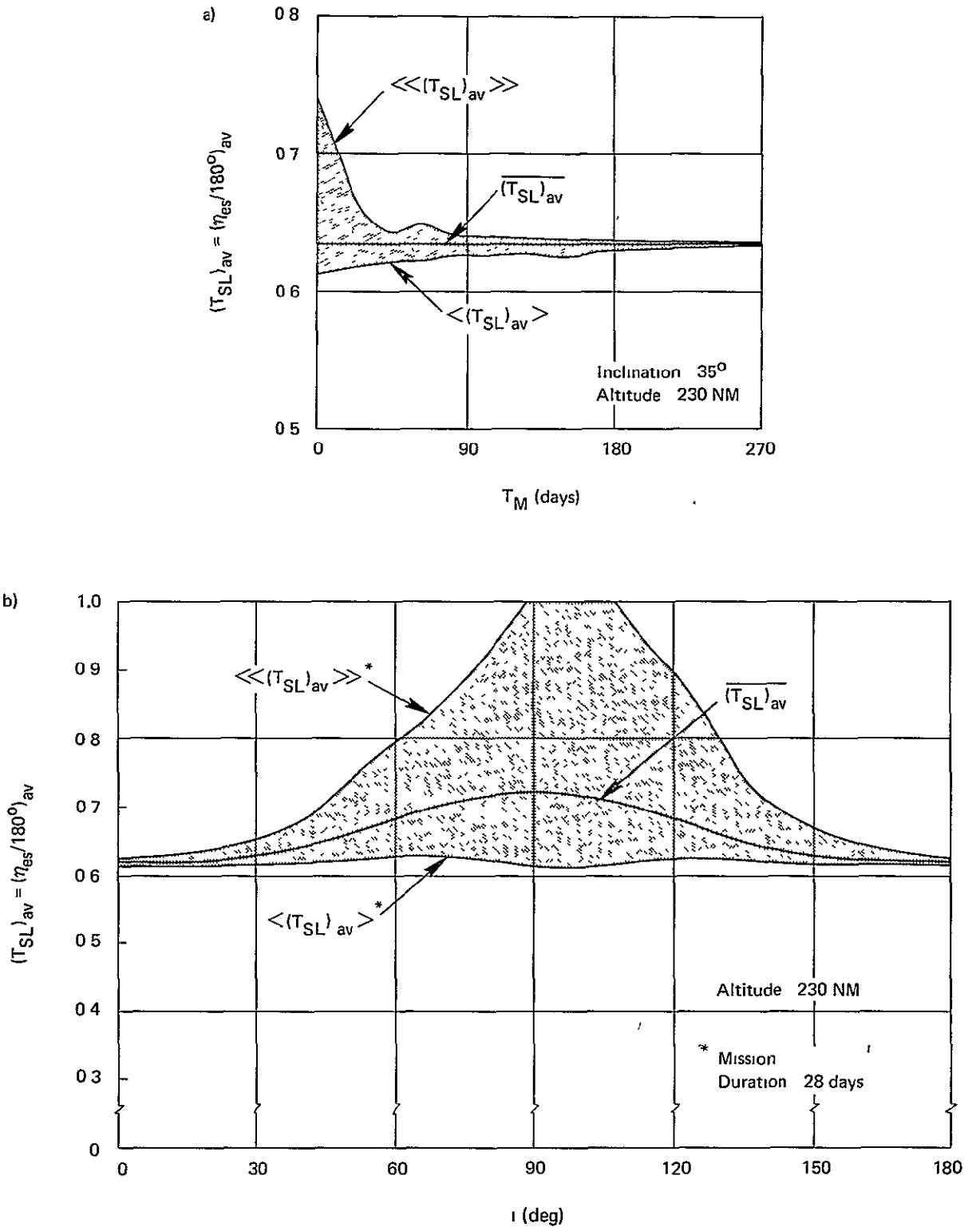

Figure (6 - 3) - Mean and Limits of T_{SL} vs Mission Duration and Orbit Inclination

and launch time are firm. In the interest of utilizing this additional capacity a question for mission designers is: What is the mean margin available during a mission for accommodating accessory system requirements and the effect on array size? If this margin exceeds these requirements, on-time scheduling of all accessory systems is a possible design option. If not, certain accessory system requirements must be added to basic system requirements and array size correspondingly increased.

The curves in Fig. (5-32) indicate that the worst-case condition for all modes considered is $\beta=0°$, where $\hat{E}_{o\ max}$ is a minimum. To obtain the same energy output at $\beta=0°$ in a particular mode, the required array size relative to the sun-oriented array size is given by the factor*

$$\rho \equiv (\hat{E}_s)_{min}/(\hat{E}_{o\ max})_{min} = 1/(\hat{E}_{o\ max})_{min} \qquad (6\text{-}9)$$

Thus, in Figs. (6-4) and (6-5) the corresponding mean and limits of $(\hat{E}_{o\ max})_{av}$ can be scaled by ρ so that the mean energy margin $(\overline{E}_{mar})$ in each mode becomes

$$\overline{E}_{mar} \equiv \rho[\overline{(\hat{E}_{o\ max})_{av}} - (\hat{E}_{o\ max})_{min}]$$

$$= \rho\,\overline{(\hat{E}_{o\ max})_{av}} - 1.0 \qquad (6\text{-}10)$$

This expresses the margin available for accessory systems as a fraction of the array energy output at $\beta=0°$. Similarly for the sun-oriented array the mean energy margin $(\overline{E}_s)_{mar}$, is

$$(\overline{E}_s)_{mar} = \overline{(\hat{E}_s)_{av}} - (\hat{E}_s)_{min} = \overline{(\hat{E}_s)_{av}} - 1.0 \qquad (6\text{-}11)$$

Mean energy margins and array size factors for the various modes are given in Table (6-1) for 35° and 50°, 230 NM orbits.

---

*As defined in Footnote *, p. 44: $\hat{E}_s = \eta_{es}/\eta_{eso}$.

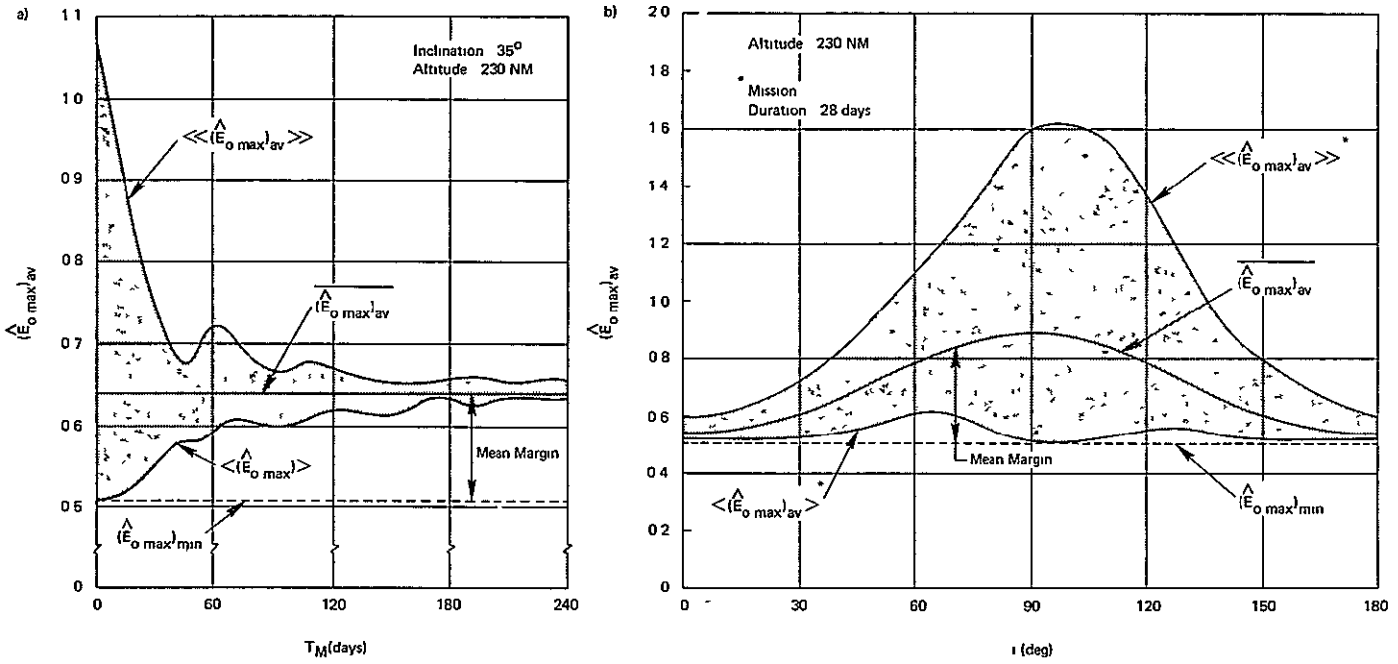

Figure (6 - 4) - Mean and Limits of $(\hat{E}_{o\ max})_{av}$ vs. Mission Duration and Orbit Inclination (LV, LH & POP Fixed Roll Modes)

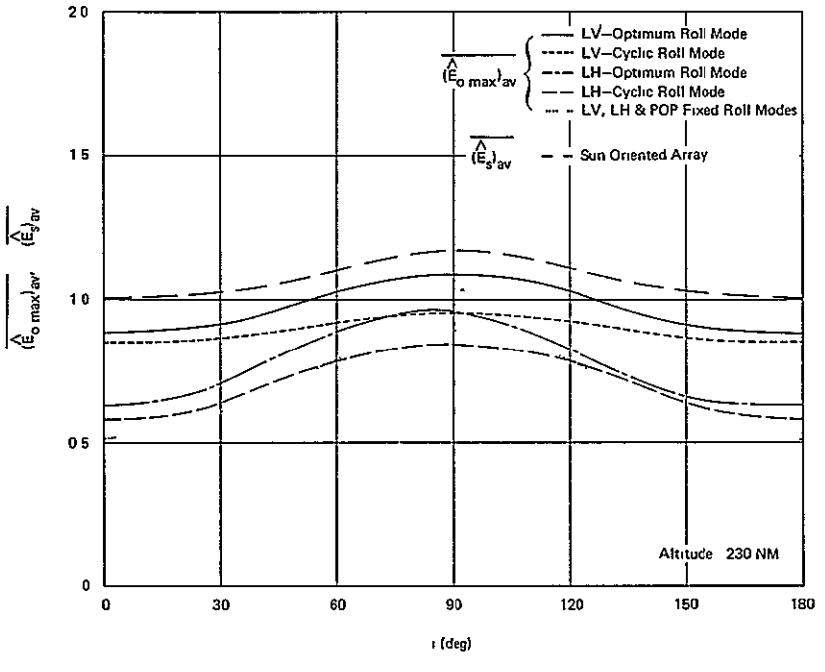

Figure (6 - 5) - $(\hat{E}_{o\ max})_{av}$ and $(\hat{E}_s)_{av}$ vs Orbit Inclination

Table 6-1 Mean Electrical Energy Margins and Array Size Factors in 35^o and 50^o, 230 NM Orbits

Mode	$(\hat{E}_{o\ max})_{min}$	$\bar{E}_{mar}$		ρ	ρ_r	
		i=35°	i=50°		i=35°	i=50°
LV-Optimum Roll	0.85	0.08	0.15	1.17	1.11	1.08
LV-Cyclic Roll	0.76	0 15	0 19	1.31	1.18	1.18
LH- Optimum Roll	0.55	0.28	0 44	1.81	1.45	1.33
LH-Cyclic Roll	0.46	0.42	0.58	2.16	1 56	1.43
LV, LH & POP Fixed Roll	0.52	0.22	0 39	1.93	1.63	1.47
Sun-Oriented Array	$(\hat{E}_s)_{min}$	$(\bar{E}_s)_{mar}$				
		i = 35°	i=50°			
	1.0	0.03	0 08			

While the array size is minimum for the sun-oriented array, the energy margin is also the least. Hence, comparison of other modes with a sun-oriented mode solely on the basis of array size* is misleading since the mean array output over a mission is higher in the other modes. To obtain array capacity comparable to that of any particular mode, the sun-oriented array size should be increased by the factor

$$\rho_s = 1.0 + \left(\bar{E}_{mar} - (\bar{E}_s)_{mar}\right) \qquad (6\text{-}12)$$

Therefore, the array size for that mode relative to the sun-oriented array size is

$$\rho_r \equiv \rho/\rho_s \qquad (6\text{-}13)$$

Values of ρ_r for the various modes are given in Table (6-1).

---

*i.e., array size as determined by array output at $\beta=0°$ (worst case).

In short duration missions and early phases of long missions, launch time has an effect on the energy margins. This can be observed in Fig. (6-4a) as the difference between the limits of $(\hat{E}_{o\ max})_{av}$ and $(\hat{E}_{o\ max})_{min}$. As mission duration increases, however, these converge to the mean. The effect of orbit inclination on the mean margin is shown in Fig. (6-4b).

$\hat{W}_s$

Thermal control system design for spacecraft is frequently based on a worst-case analysis in which the incident thermal energy per orbit is either a minimum (cold case) or a maximum (hot case). This establishes maximum internal heating or cooling requirements for maintaining spacecraft modules at desired temperature levels. Since the worst-case condition corresponding to certain β angles occurs only at discrete times, some margin on heating or cooling requirements exists at other times. Because thermal control requirements are directly related to electrical energy requirements, any incident thermal energy margins are translatable into electrical energy margins, which may assist in accommodating accessory system requirements on an on-time scheduling basis as described previously.

As an example, the relative thermal energy margins obtainable in LV, LH and POP attitude modes will be compared on the basis of a cold-case design for the cylinder/hemispherical-end spacecraft configuration shown in Fig. (5-33a). The curves in Fig. (5-35a) indicate that $\hat{W}_s$ is a minimum at $\beta=0°$ for the LV and LH modes, but in the POP mode the minimum for $\hat{W}_s$ depends on $|\beta|_{max}$, which varies with orbital inclination.* In Fig. (6-6) $(\hat{W}_s)_{min}$ is plotted along with the mean and limits of $(\hat{W}_s)_{av}$ for the LV mode. The mean incident energy margin is defined as

$$(\overline{W}_s)_{mar} \equiv \overline{(\hat{W}_s)_{av}} - (\hat{W}_s)_{min} \qquad (6\text{-}14)$$

Due to the normalization inherent in $\hat{W}_s$, Eq. (6-14) expresses the mean energy margin as a fraction of the direct solar component of incident thermal energy per orbit on the lateral

*See Section 4.1.

surface of a solar-oriented cylinder.* Mean margins for the three attitude modes are given in Table (6-2) for 35° and 50°, 230 NM orbits.** The maximum margin is obtained in the POP mode where $(\hat{W}_s)_{mar}$ is 29% and 34% of $(\hat{W}_s)_{min}$ for the 35° and 50° orbits.

Table 6-2 Mean Incident Thermal Energy Margins in 30° and 50°, 230 NM Orbits *

Attitude Mode	$(\hat{W}_s)_{min}$		$(\hat{W}_s)_{av}$		$(\overline{W_s})_{mar}$	
	i=35°	i=50°	i=35°	i=50°	i=35°	i=50°
LV	1 26	1.26	1.35	1.42	0.09	0.16
LH	1.15	1.15	1.28	1.36	0.13	0 21
POP	1.15	1.06	1.48	1.42	0.33	0.36

* (Cylinder/Hemispherical–End Spacecraft: D/L=0 2)

The effect of launch time on incident thermal energy margins in short duration missions or early phases of long missions is observable in Fig. (6-6) by the difference between the limits of $(\hat{W}_s)_{av}$ and $(\hat{W}_s)_{min}$. As mission duration increases, this difference converges to $(\overline{W}_s)_{mar}$. The effect of orbit inclination on $\overline{(\hat{W}_s)_{av}}$ is shown in Fig. (6-7).

6.3 Approximate Evaluation of Mission Averages of System Performance Factors

Because of the number of parameters involved, evaluation of mission averages (f_{av}) and subsequent determination of the mean and limits is generally a lengthy, although straightforward, numerical process. In the course of this work it was

---

*When solar-oriented, the cylinder axis is assumed normal to the sun line.

**Since the curves of $\hat{W}_s$ vs β in Fig. (5-35) for the cylinder/flat-end and cylinder/hemispherical-end spacecraft configurations are similar, results for $(\overline{W}_s)_{mar}$ will also be comparable.

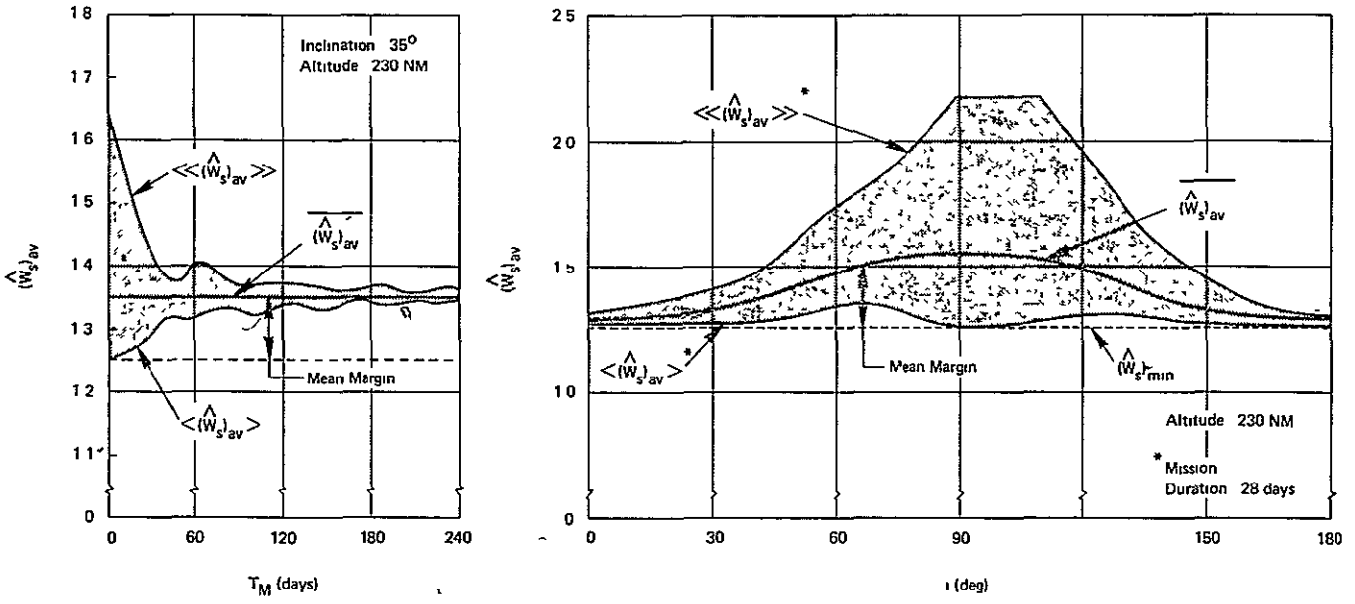

Figure (6 - 6) - Mean and Limits of $\hat{(W_s)}_{av}$ vs Mission Duration and Orbit Inclination (LV Mode)

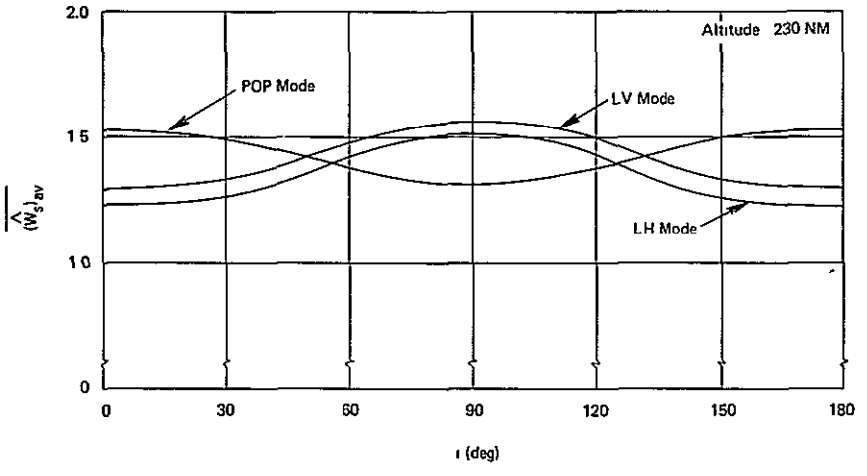

Figure (6 - 7) - $\overline{\hat{(W_s)}_{av}}$ vs Orbit Inclination .

observed that the mean and limits of f_{av} could also be approximated with good accuracy in most cases by evaluating $f(\beta)$ with the mean and limits of $|\beta|_{av}$, that is,

$$\overline{f_{av}} \approx f(\overline{|\beta|_{av}}) \equiv \overline{f}_{\beta} \qquad (6\text{-}15)$$

$$\langle f_{av} \rangle \approx f(\langle |\beta|_{av} \rangle) \equiv \langle f_{\beta} \rangle \qquad (6\text{-}16)$$

and

$$\langle\langle f_{av} \rangle\rangle \approx f(\langle\langle |\beta|_{av} \rangle\rangle) \equiv \langle\langle f_{\beta} \rangle\rangle \qquad (6\text{-}17)$$

For comparison, mission averages of several performance factors evaluated both ways, are tabulated in Table 6-3.

Table 6-3 Comparison of Exact and Approximate Evaluation of Mission Averages of Typical Performance Factors

Inclination	$\langle\|\beta\|_{av}\rangle$	$\overline{\|\beta\|_{av}}$	$\ll\|\beta\|_{av}\gg$	$f(\beta)$	Exact			Approximate		
					$\langle f_{av} \rangle$	$\overline{f_{av}}$	$\ll f_{av} \gg$	$\langle f_{\beta} \rangle$	$\overline{f_{\beta}}$	$\ll f_{\beta} \gg$
i=35°	10 40°	23 56°	38 07°	$\hat{E}_{o\,max}$*	0 83	0 87	0 91	0 83	0 89	0 92
				$\hat{E}_{o\,max}$**	0 52	0 63	0 77	0 51	0 60	0 75
				$\hat{W}_s$***	1 28	1 35	1.44	1 28	1 34	1 42
				T_{SL}	0 62	0 63	0 66	0 62	0 62	0 65
				$\|s2\beta\|$	0 34	0 62	0 84	0 35	0 73	0 97
i=50°	15 01°	30 77°	48 63°	$\hat{E}_{o\,max}$*	0 85	0 90	0 99	0 85	0 91	0 94
				$\hat{E}_{o\,max}$**	0 55	0 72	0 97	0 54	0 67	0 88
				$\hat{W}_s$***	1 30	1 42	1 62	1 30	1 38	1 51
				T_{SL}	0 62	0 66	0 74	0 62	0 63	0 68
				$\|s2\beta\|$	0 48	0 69	0 85	0 50	0 88	0 99

*LV-Cyclic Roll Mode **LV,LH & POP Fixed Roll Modes ***LV Mode

The approximate method was found to be reasonably accurate when $f(\beta)$ was a weakly nonlinear function of β. The approximation is less accurate when $f(\beta)$ is highly nonlinear in the range of β encountered (e.g., $f(\beta)=|s2\beta|$ where $|\beta|_{max}>45°$). Since $\overline{|\beta|}_{av}$ has been obtained once and for all as a function of orbit inclination* in Fig.(6-1b), approximate evaluation of $\overline{f}_{av}$ for other orbit altitudes or for performance factors other than those studied here, is simple, once $f(\beta)$ is obtained, either analytically or numerically. Convergence of the limits on $|\beta|_{av}$ to $\overline{|\beta|}_{av}$ is altitude dependent in general, although not significantly different from the curves in Fig.(6-1) for altitudes in the range, 230 ±30 NM. Hence, approximate evaluation of the limits on f_{av} based on these curves is also reasonable for altitudes in this range.

*As noted previously, $\overline{|\beta|}_{av}$ is independent of orbit altitude.

7.0 SUMMARY AND CONCLUSIONS

Orientation of the solar vector relative to an earth orbit has been defined in terms of two pointing angles: β, the minimum angle between the solar vector and the orbital plane, and ψ, the location of orbital noon relative to the ascending node. Analytical expressions for evaluating β and ψ have been derived as a function of four angles, two that are constant:

- i - the orbit inclination relative to the equatorial plane*,
- e - the angle between the equatorial and ecliptic planes (23.45°),

and two that vary with time:

- γ - which describes the earths' motion about the sun, and
- Ω_r - which describes motion of the orbit ascending node in the equatorial plane due to earth oblateness effects.

In general, β varies harmonically within an envelope which depends on both γ and i as shown in Fig.(4-3) for both posigrade ($0° \leq i < 90°$) and retrograde ($90° < i \leq 180°$) orbits. The angle ψ increases monotonically with time except for orbit inclinations ($90°-e<i<90°+e$) where the orbital plane may pass through an orientation normal to the sunline and the monotonic variation occurs only at intervals. Various characteristics of the solar pointing angles are described in Section 4 and typical time variations are shown in Figs.(4-1), (4-2, (4-4) and (4-8). A general summary of properties is given in Section 4.5 together with specific results for 35° and 50°, 230 NM circular orbits, which have been considered for AAP Workshop missions.

The relationship between a number of system performance factors and the solar vector orientation relative to the orbital plane has been evaluated for circular orbits. Specific performance factors considered were:

1) the bias gravity-gradient torque-impulse on spacecraft in a solar-inertial mode (Section 5.1),
2) the orbit sunlight interval (Section 5.2),

---

*Periodic variation of orbit inclination due to earth oblateness is a relatively small effect[6] and is neglected in this work.

3) the electrical energy per orbit available from solar arrays in LV, LH and POP modes with incrementally articulated* solar arrays and various spacecraft roll profiles (Section 5.3),

4) the incident thermal energy per orbit on a cylindrical spacecraft in LV, LH and POP modes. (Section 5.4)

While possible options are virtually endless, spacecraft and solar array models and these attitude modes have been chosen to illustrate typical properties and effects of the β variation, as they may effect AAP and future space station missions. All results are given in normalized form to facilitate application or approximation to particular spacecraft configurations or changes in orbit altitude where appropriate**. In addition to the analytical formulation these relationships are plotted vs β for 230 NM orbits and other parameters relative to each case.

Included in Section 5.3 are curves showing the maximum array energy output relative to a sun-oriented array for each mode with optimum array articulation as a function of β. The highest array energy output is obtained in a LV-Optimum Roll mode where the output is always within 15% of the sun-oriented array output (worst case: $\beta=0°$). Because the spacecraft is rolled such that the array articulation axis remains normal to the plane formed by the sun line and local vertical, large roll maneuvers (up to 180°) must be executed abruptly near $\beta=0°$. An easily implemented, suboptimal alternative at low β is the LV-Cyclic Roll mode in which array output is within 23% of the sun-oriented array output up to $\beta=60°$. Array performance with comparable roll profiles in LH modes is decidedly lower than in LV modes for $|\beta|<45°$. A more detailed summary and comparison of optimum array performance in various modes is given in Section 5.3.5.

Mission averages of system performance factors are often relevant to mission planning, since system designs based solely on worst case β conditions, which occur only at discrete

---

*Solar arrays are assumed to be articulated about one axis and only intermittently (e.g., daily), not at rates comparable to the orbital angular velocity.

**Although the analysis is based on circular orbits, the results are also applicable to slightly elliptical orbits of comparable period. (See Footnote *, p.4). The equivalent circular altitude (H) is the average of apogee and perigee altitudes, $H=(h_a+h_p)/2$. For arbitrary elliptical orbits, however, system performance factors are a function of both β and ψ.

times, may impose excessive requirements or may not utilize available performance margins. Mission averages (f_{av})* of each performance factor, (1-4) above, have been evaluated as a means of assessing the effect of the β variation and arbitrary launch time and date. The mean and limits of f_{av} based on independent, uniformly distributed launch time and date are plotted vs mission duration and orbit inclination in Figs. (6-2) through (6-7). The limits of f_{av}, which asymptotically approach the mean, $(\overline{f_{av}})$, as mission duration increases, indicate the possible variation in f_{av} due to launch time uncertainty.

In evaluating whether or not a design based on worst case conditions (β_{wc}) is entirely realistic, the difference (or margin) between $f(\beta_{wc})$ and the mean or limits of f_{av} can be useful data. In one case studied in Section 6.2, $f(\beta)=|s2\beta|$ is proportional to the propellant requirement per orbit for momentum dumping of the bias gravity gradient torque-impulse by reaction thrust. Here, $f(\beta_{wc})=f(45°)=1.0$ and $\overline{f_{av}}=0.62$ for a 35° orbit. Hence propellant requirements based on the worst case over a long mission (e.g., 56 days) would be excessive. If requirements are based nevertheless on the worst case, the calculation, $f(\beta_{wc})-\overline{f_{av}}$, indicates a propellant margin up to 38%, which might be used for supporting short duration experiment pointing modes. In Section 6.2 mission averages of the performance factors, (3-4) above, are used to evaluate the margins on electrical energy per orbit from solar arrays and the incident thermal energy per orbit on spacecraft in various attitude modes.

Acknowledgement

The author gratefully acknowledges the efforts of Mrs. N. I. Kirkendall for her support in developing and executing several computer programs used in this work. The author is also grateful for additional programming support from Mrs. C. F. Mummert and Mrs. B. J. Brooks. The thorough review and criticism of this work by Messers. G. M. Anderson, J. Kranton and S. Shapiro is greatly appreciated.

B. D. Elrod

1022-BDE-cds

*The mission average (f_{av}) of a function $f(\beta)$ is defined as the time average of $f(\beta)$ over a mission.

APPENDIX A

Location of Sun Line and Ascending Node at Launch

The purpose of this appendix is to determine as a function of launch time the initial location of the sun line and the orbit-equatorial plane ascending node as represented by the angles γ_o and Ω_{ro}. Since launch time depends in general on the reference point for measuring time, some discussion with regard to this point is in order. In Fig.(A-1) a particular orientation of the ecliptic, equatorial and orbital planes is shown, similar to that shown in Fig.(2-2). In the equatorial plane, true noon is defined by the intersection with the equator of the meridian plane containing the sun line and the normal to the equatorial plane (earth's polar axis). With an analogous definition of noon

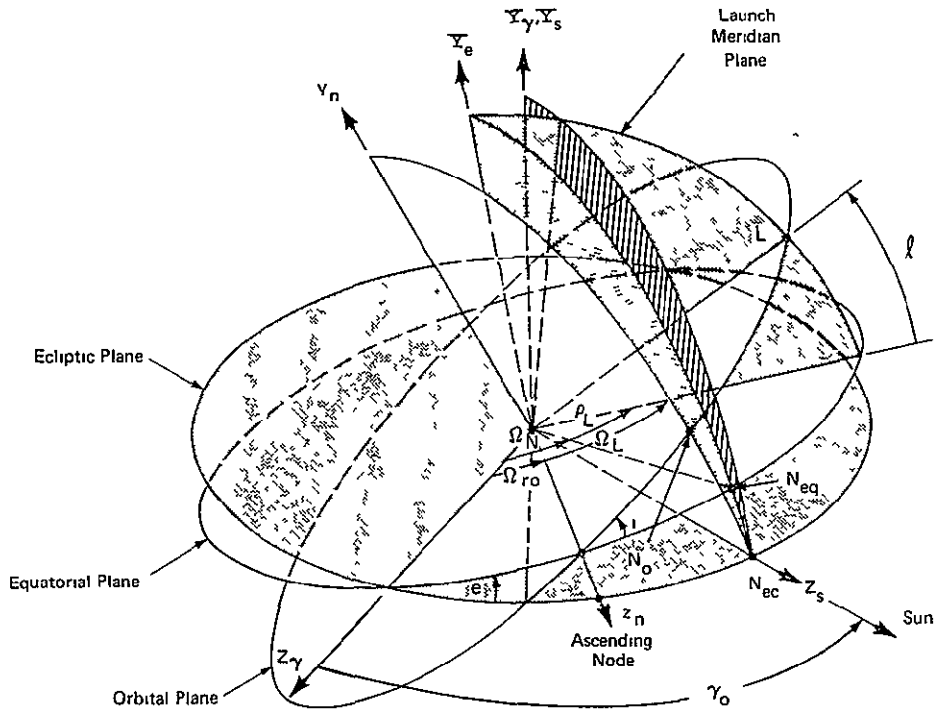

Figure (A - 1) - Orientation of the Orbital Plane Relative to the Equatorial and Ecliptic Planes at Launch

for the orbital and ecliptic planes it follows, because of the relative orbit inclinations, that true noon occurs at different points for the three planes as noted by N_o, N_{eq} and N_{ec} in Fig. (A-1). During orbital flight, the logical reference would be N_o. For launch purposes, however, N_{eq} is appropriate.

A.1 Location of Sun Line

In Fig. (A-2) launch time is measured from two reference points, one based on autumnal equinox and the other on midnight (00^h:00) of September 23. The various time intervals are related by

$$t_{ae} + 24d_L = 24D_L + t_L \qquad \text{(A-1)}$$

so that

$$d_L = D_L + (t_L - t_{ae})/24 \qquad \text{(A-2)}$$

where

d_L = launch time measured from autumnal equinox in days (non-integer)

D_L = number of calendar days (integer) at launch since September 23 (00^h:00 U.T.*)

t_L = launch site Universal Time* at launch ($0<t_L<24.0$ hours)

t_{ae} = launch site Universal Time* at autumnal equinox ($0<t_{ae}\leq 24.0$ hours)**

---

*Here Universal Time (U.T.) is defined as Greenwich Mean Time corrected for the longitudinal location of the launch site. For KSC, located at 80.5° W. Longitude, the launch site correction is -80.5/15 = -5.37 hours.

**Generally t_{ae} is obtained from emphemeris data.[23] However, the maximum error incurred in γ_o by ignoring t_L and t_{ae} is less than 1°.

Upon evaluating d_L, the sun line location at launch (γ_o) can be determined exactly from ephemeris tables[23] or approximately from*

$$\gamma_o = \dot{\gamma}\, d_L \qquad (A-3)$$

where $\dot{\gamma}$ is the mean sun line rotation rate as given in Eq.(2-8).

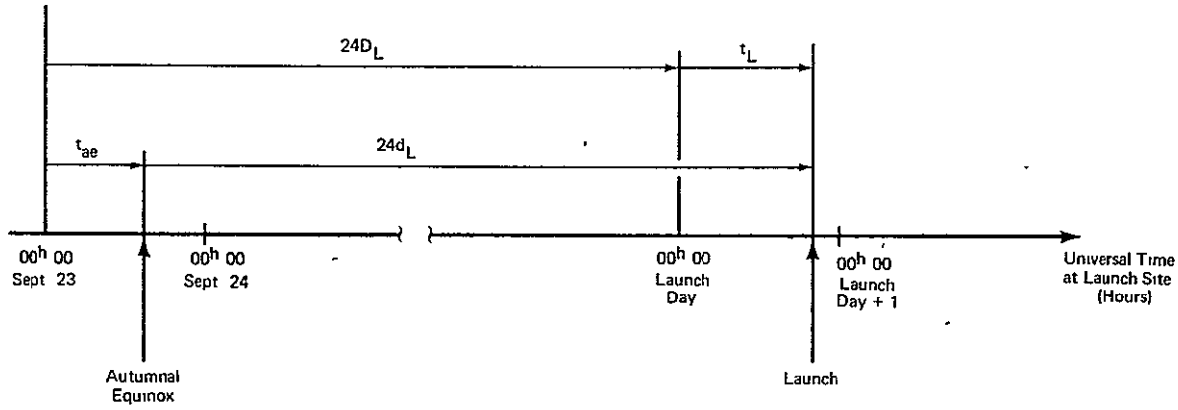

Figure (A - 2) - Relationship of Launch Time to Autumnal Equinox

A.2 Location of Ascending Node

In Fig.(A-1), the point L is considered to be immediately above the launch site. The longitude of the launch site with respect to the noon meridian (through N_{eq}) can be specified by the angle ρ_L where

$$\rho_L = [15(t_L+t_N) - 180°] \qquad (A-4)$$

t_L is launch site Universal Time as defined in Section A.1, and t_N is the difference between the true noon and apparent (clock) noon at Greenwich.** As is evident from Fig.(A-1), the longitude of the launch site can also be specified with respect to the autumnal equinox reference (Z_γ) by either of the angles,

---

*See Section 2.2 and Footnote *, p. 7.

**True noon represents $(t_L+t_N)=12.0$. The variation in t_N is available from ephemeris data.[23] Since $|t_N|_{max}<0.27$ hours, the maximum error incurred in ρ_L (and Ω_{ro}) by ignoring t_N is 4°.

$(\Omega_{ro}+\Omega_L)$ or $(\Omega_N+\tilde{\Omega}_L)$. Consequently, the initial location of the ascending node is given by

$$\Omega_{ro} = \rho_L + \Omega_N - \Omega_L \tag{A-5}$$

where Ω_N and Ω_L are defined in Fig.(A-1) and derived in Sections A.3 and A.4 respectively. Substituting Eqs.(A-4), (A-9) and (A-15) into Eq.(A-5) yields

$$\Omega_{ro} = [15(t_L+t_N)-180°] + \tan^{-1}(\tan\gamma_o ce) - \tan^{-1}(\tan\alpha_L s\ell) \tag{A-6}$$

where γ_o is the sun line location at launch, e = 23.45°, α_L is the launch azimuth and ℓ is the latitude of the launch site.

A.2.1 Determination of Ω_N

As shown in Fig.(A-1), Ω_N is the angle between the noon meridian plane (through N_{eq}) and the autumnal equinox reference (Z_γ). Consider a coordinate system (x_N,y_N,z_N) defined such that y_N is parallel to Y_e (the normal to the equatorial plane), z_N lies in the equatorial plane along the line of intersection with the noon meridian plane and x_N completes the right hand system. The transformation relating (x_N,y_N,z_N) and (X_s,Y_s,Z_s) for a given launch time (γ_o) is:

$$\underline{\mu}_N = A\underline{\mu}_s = T^Y_{\Omega_N}\ T^Z_e\ T^Y_{-\gamma_o}\ \underline{\mu}_s \tag{A-7}$$

Since x_N is normal to the noon meridian plane, it follows that the element a_{13}, which is the direction cosine between x_N and Z_s (the sun line) must be zero. This yields

$$a_{13} = \left(T^Y_{\Omega_N}\ T^Z_e\ T^Y_{-\gamma_o}\right)_{13} = c\Omega_N s\gamma_o ce - s\Omega_N c\gamma_o = 0 \tag{A-8}$$

so that

$$\tan\Omega_N = \tan\gamma_o \cdot ce \tag{A-9}$$

A.2.2 Determination of Launch Parameters (Ω_L, i)

The relationship between various launch parameters can be described in terms of the diagram in Fig.(A-3).

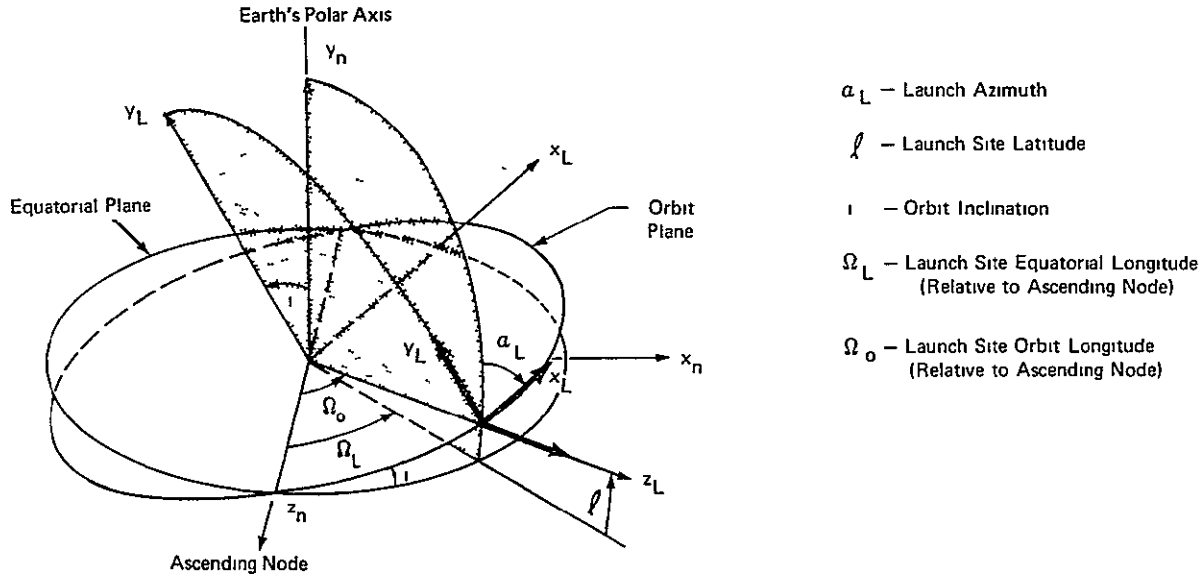

Figure (A - 3) - Launch Site Coordinates and Parameters

The coordinate system (x_n, y_n, z_n) is the nodal system used previously. The coordinate system (x_L, y_L, z_L) is defined such that z_L corresponds to the launch site local vertical, x_L is parallel to the launch heading and y_L completes the right hand system and is normal to the orbital plane.

The launch azimuth α_L is defined positive with respect to geographical north with $\alpha_L = 90°$ corresponding to a due east launch. The transformation relating (x_L, y_L, z_L) and (x_n, y_n, z_n) coordinates can be expressed in either of two elementary Euler angle sequences: $(\Omega_L, -\ell, 90°-\alpha_L)$ or (i, Ω_o) so that

$$\underline{\mu}_L = \begin{pmatrix} x_L \\ y_L \\ z_L \end{pmatrix} = B\underline{\mu}_n = C\underline{\mu}_n \qquad \text{(A-10)}$$

where

$$B = T^{Z}_{90°-\alpha_L} T^{X}_{-\ell} T^{Y}_{\Omega_L} \tag{A-11}$$

$$= \begin{bmatrix} (s\alpha_L c\Omega_L - c\alpha_L s\ell s\Omega_L) & c\alpha_L c\ell & (-s\alpha_L s\Omega_L - c\alpha_L s\ell c\Omega_L) \\ -(c\alpha_L c\Omega_L + s\alpha_L s\ell s\Omega_L) & s\alpha_L c\ell & (c\alpha_L s\Omega_L - s\alpha_L s\ell c\Omega_L) \\ c\ell s\Omega_L & s\ell & c\ell c\Omega_L \end{bmatrix}$$

and

$$C = T^{Y}_{\Omega_O} T^{Z}_{i} \tag{A-12}$$

$$= \begin{bmatrix} c\Omega_O ci & c\Omega_O si & -s\Omega_O \\ -si & ci & o \\ s\Omega_O ci & s\Omega_O si & c\Omega_O \end{bmatrix}$$

Of the many possible relations obtainable from equating elements of B and C the two of interest here are $b_{22}=c_{22}$ and $b_{23}=c_{23}$ so that

$$ci = s\alpha_L c\ell \tag{A-13}$$

and

$$0 = c\alpha_L s\Omega_L - s\alpha_L c\Omega_L s\ell \tag{A-14}$$

or

$$\tan \Omega_L = \tan \alpha_L s\ell \tag{A-15}$$

A.3 Initial Solar Vector Orientation (β_o, ψ_o)

The pointing angles, β_o and ψ_o, represent the solar vector orientation relative to an earth orbit at launch. These may be evaluated in terms of launch parameters (α_L, ℓ, ρ_L) and the equatorial sun declination ($-\alpha_d$) at launch. From Eqs. (3-5) and (3-6) the expressions for β_o and ψ_o are

$$s\beta_o = si(s\gamma_o \; ce \; c\Omega_{ro} - c\gamma_o \; s\Omega_{ro}) + ci \; s\gamma_o \; se \qquad \text{(A-16)}$$

$$\tan \psi_o = \frac{ci(s\gamma_o \; ce \; c\Omega_{ro} - c\gamma_o \; s\Omega_{ro}) - si \; s\gamma_o \; se}{c\gamma_o \; c\Omega_{ro} + s\gamma_o \; ce \; s\Omega_{ro}} \qquad \text{(A-17)}$$

where

$$\Omega_{ro} = \rho_L + (\Omega_N - \Omega_L) \qquad \text{(A-18)}$$

and (ρ_L, Ω_N, Ω_L) are defined in Section A.2. As given in Eq. (4-8),

$$s\alpha_d = s\gamma_o \; se \qquad \text{(A-19)}$$

so that

$$c\alpha_d = \sqrt{c^2\gamma_o + s^2\gamma_o \; c^2 e} \qquad \text{(A-20)}$$

which means, in view of Eq. (A-9), that

$$s\Omega_N = s\gamma_o \; ce/c\alpha_d \qquad \text{(A-21)}$$

$$c\Omega_N = c\gamma_o/c\alpha_d \qquad \text{(A-22)}$$

Substituting these equations into Eqs.(A-16) and (A-17) yields after some manipulation

$$s\beta_o = s\alpha_d \; ci + s(\Omega_L - \rho_L) \; c\alpha_d \; si \tag{A-23}$$

$$\tan \psi_o = \frac{c\alpha_d \; ci \; s(\Omega_L - \rho_L) - s\alpha_d \; si}{c\alpha_d \; c(\Omega_L - \rho_L)} \tag{A-24}$$

The orbit inclination (i) and the launch site longitude (Ω_L) relative to the orbit ascending node are related to launch azimuth (α_L) and launch site latitude (ℓ) in Eqs.(A-13) and (A-15). The launch site longitude (ρ_L) relative to true noon (N_{eq}) is obtained from Eq.(A-4).

Certain special cases are of interest. For true noon (ρ_L=0°) and true midnight (ρ_L=180°) launches, it follows, in general, that

$$\begin{aligned} s\beta_o &= s\alpha_d \; ci \pm s\Omega_L \; si \; c\alpha_d \\ &= s\alpha_L \; s(\alpha_d \pm \ell) \end{aligned} \qquad \text{Noon (+), Midnight (−)} \tag{A-25}$$

and

$$\tan \psi_o = \frac{c\alpha_d \; ci \; s\Omega_L \pm s\alpha_d \; si}{c\alpha_d \; c\Omega_L} \qquad \text{Noon (+), Midnight (−)}$$

$$= \frac{s^2\alpha_L \; c\ell \; s(\alpha_d + \ell) - s\alpha_d}{c\alpha_d \; c\alpha_L} \qquad \text{(Noon)} \tag{A-26a}$$

$$= \frac{-s^2\alpha_L \; c\ell \; s(\alpha_d - \ell) + s\alpha_d}{c\alpha_d \; c\alpha_L} \qquad \text{(Midnight)} \tag{A-26b}$$

where the latter forms in each case result from substituting for α_L from Eq.(A-15).

Appendix A

As indicated by Fig. (A-1), the angle $(\Omega_L - \rho_L)$ locates the equatorial noon meridian plane relative to the orbit ascending node. Hence, whenever $(\Omega_L - \rho_L) = \pm 90°$, it follows that

$$s\beta_o = s(\alpha_d \pm i) \tag{A-27}$$

$$\psi_o = \pm 90° \tag{A-28}$$

which implies that β_o is at the upper or lower β envelope boundary.* The corresponding launch time (t_L) at the launch site is determined from Eqs. (A-4) and (A-15) which yield

$$\rho_L = 15(t_L + t_N) - 180° = \Omega_L - (\pm 90°)$$

or

$$t_L = -t_N + \frac{1}{15}\left[\tan^{-1}(\tan \alpha_L \, s\ell) \pm 90°\right] \tag{A-29}$$

*See Section 4.1. Algebraic signs ($\pm$) are associated with upper (+) and lower (-) envelope boundaries.

APPENDIX B

Gravity Gradient Torque in Solar-Inertial Mode

In the solar-inertial mode the orientation of the spacecraft geometric axes (x_{sc}, y_{sc}, z_{sc}) relative to the orbital plane is specified by the solar pointing angles (β, ψ) shown in Fig. (B-1). The coordinate axes (X_p, Y_p, Z_p) are principal axes where X_p is parallel to the roll axis (x_{sc}) with (Y_p, Z_p) displaced by a fixed angle $\hat{\phi}$ from (y_{sc}, z_{sc}).*

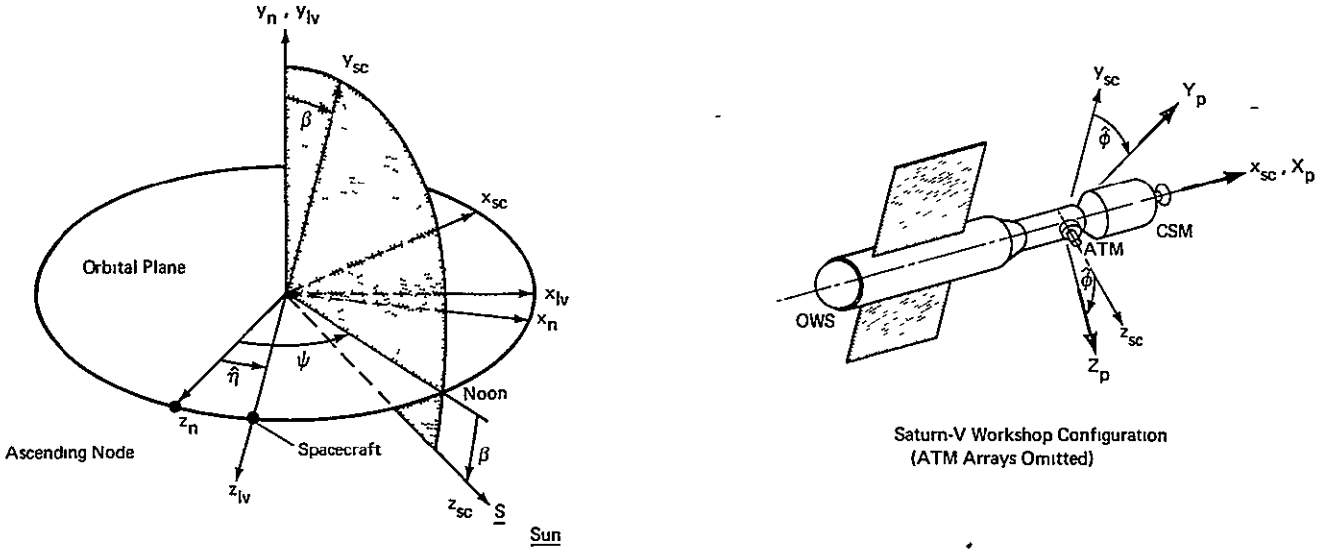

Figure (B - 1) - Spacecraft Orientation in Solar Pointing Mode

The transformation relating (X_p, Y_p, Z_p) and (x_n, y_n, z_n) is given by

$$\underline{\mu}_p = T^x_{\hat{\phi}}\, T^x_{\beta}\, T^y_{\psi}\, \underline{\mu}_n = T^x_{(\beta+\hat{\phi})} T^y_{\psi}\, \underline{\mu}_n \qquad \text{(B-1)}$$

---

* See Footnote ** on p. 34.

Appendix B

The gravity gradient torque expressed in general form is[12]

$$\underline{T_g} = 3\mu_o(\underline{\rho}\times I\cdot\underline{\rho}) \tag{B-2}$$

where $\sqrt{\mu_o} = \sqrt{\mu/R_h^3}$ is the instantaneous orbit angular velocity, μ is the earth's gravitational parameter, R_h is the local geocentric altitude, $\underline{\rho}$ is a unit vector directed along the local vertical and I is the spacecraft inertia tensor. In Fig.(B-1) the coordinates $(x_{\ell v}, y_{\ell v}, x_{\ell v})$ represent the local vertical system so that $\underline{\rho}_{\ell v} = (0,0,1)^{\dagger}$. The transformation relating $(x_{\ell v}, y_{\ell v}, z_{\ell v})$ and (x_n, y_n, z_n) coordinates is

$$\underline{\mu}_{\ell v} = T^{Y}_{\hat{\eta}} \quad \underline{\mu}_n \tag{B-3}$$

In view of Eqs.(B-1) and (B-3) the unit vector $\underline{\rho}$ in Eq.(B-2) may be expressed in principal axis coordinates as

$$\begin{aligned}\underline{\rho}_{sc} = \begin{pmatrix}\rho_1\\ \rho_2\\ \rho_3\end{pmatrix} &= T^{X}_{\beta+\hat{\phi}}\, T^{Y}_{\psi}\, T^{Y}_{-\hat{\eta}}\, \underline{\rho}_{\ell v}\\ &= T^{X}_{\beta+\hat{\phi}} T^{Y}_{\psi-\hat{\eta}} \begin{pmatrix}0\\0\\1\end{pmatrix} = \begin{pmatrix}-s(\psi-\hat{\eta})\\ s(\beta+\hat{\phi})c(\psi-\hat{\eta})\\ c(\beta+\hat{\phi})c(\psi-\hat{\eta})\end{pmatrix}\end{aligned} \tag{B-4}$$

Substitution of Eq.(B-4) into Eq.(B-2) yields

$$\underline{T_g}_p = 3\mu_o \begin{Bmatrix}(I_z-I_y)\rho_2\rho_3\\ (I_x-I_z)\rho_1\rho_3\\ (I_y-I_x)\rho_1\rho_2\end{Bmatrix} \tag{B-5}$$

$$= \frac{3\mu_o}{2} \begin{Bmatrix} (I_z-I_y)s2(\beta+\hat{\phi})c^2(\psi-\hat{\eta}) \\ (I_z-I_x)c(\beta+\hat{\phi})s2(\psi-\hat{\eta}) \\ -(I_y-I_x)s(\beta+\hat{\phi})s2(\psi-\hat{\eta}) \end{Bmatrix} = \begin{Bmatrix} T_{gmx}s2(\beta+\hat{\phi})c^2(\psi-\hat{\eta}) \\ T_{gmy}c(\beta+\hat{\phi})s2(\psi-\hat{\eta}) \\ T_{gmz}s(\beta+\hat{\phi})s2(\psi-\hat{\eta}) \end{Bmatrix}$$

For a circular orbit, $\mu_o \equiv \omega_o^2$ is constant and $\hat{\eta} = \omega_o t$ where ω_o represents the orbital angular velocity.

APPENDIX C

Evaluation of Electrical Energy Available from a Solar Array on Spacecraft in LV, LH and POP Attitude Modes

The purpose of this appendix is to obtain analytical expressions for the electrical energy available from the solar array configuration described in Section 5.3 for LV, LH and POP spacecraft attitude modes and various roll profiles.

The profiles include optimum roll, continuous roll, cyclic roll, and fixed roll. In each case, it is first necessary to determine the array sunlight interval by comparing the earth shadow boundary ($\pm\eta_{es}$) with the panel self-shadow boundary (η_{ss1}, η_{ss2}) defined in Section (5.3). With this information, the normalized electrical energy ($\hat{E}$)* is then evaluated after integration of Eq.(5-16).

C.1 LV-Optimum Roll Mode

In the optimum roll case, the panel self-shadow boundary is obtained after setting $c\lambda_{LV}=0$ in Eq.(5-18) with ϕ defined in Eq.(5-20) by

$$\tan\phi = -s\eta/\tan\beta \tag{C-1}$$

From this it follows that

$$c\phi = \frac{\tan\beta}{\sqrt{\tan^2\beta + s^2\eta}} \tag{C-2}$$

Rewriting Eq.(5-18) and substituting $\tan\phi$ and $c\phi$ above yields

$$c\lambda_{LV} = s\alpha_p c\beta c\eta + c\alpha_p c\phi s\beta[1+\tan\phi(-s\eta/\tan\beta)] \tag{C-3}$$

$$= s\alpha_p c\beta c\eta + c\alpha_p s\beta/c\phi = c\beta\left[s\alpha_p c\eta + c\alpha_p \sqrt{\tan^2\beta + s^2\eta}\right]$$

---

*Hereafter, the term electrical energy in this appendix will imply normalized electrical energy ($\hat{E}$).

Appendix C

Equating the bracketed term to zero, transposing terms and squaring yields

$$s^2\alpha_p c^2\eta = c^2\alpha_p[\tan^2\beta + s^2\eta]$$

$$= c^2\alpha_p \tan^2\beta + c^2\alpha_p(1-c^2\eta) \qquad \text{(C-4)}$$

or

$$c^2\eta = c^2\alpha_p(1+\tan^2\beta) = c^2\alpha_p/c^2\beta \qquad \text{(C-5)}$$

Since $c\eta$ is an even function, the values of η obtained from Eq.(C-5) are symmetrical about $\eta=0°$. Consequently, the self-shadow boundary is also symmetrical about $\eta=180°$, so that *

$$\eta_{ss2} = -\eta_{ss1} \equiv \eta_{ss} = \begin{cases} 180° - \cos^{-1}(c\alpha_p/c\beta) & \beta \leq \alpha_p \\ \\ \text{no self-shadow} & \beta > \alpha_p \end{cases} \qquad \text{(C-6)}$$

A plot of η_{ss} vs. β obtained from Eq.(C-6) for various values of α_p is shown in Fig.(C-1). The dashed curve represents the earth shadow boundary (η_{es}), as obtained from Eqs.(5-6) and (5-7) for a 230 NM circular orbit.** The sunlight interval is then determined by noting for specific α_p and β, whether self-shadowing occurs first ($\eta_{ss}<\eta_{es}$) or whether earth shadow occurs first ($\eta_{es}<\eta_{ss}$). Since the self-shadow boundary is symmetrical about $\eta=0$, the sunlight interval ($\eta_1 \leq \eta \leq \eta_2$) is

---

* Of the two solutions to Eq.(C-5), namely $c\eta=c\alpha_p/c\beta$ and $c\eta=-c\alpha_p/c\beta$, only the latter is of interest, since the other solution does not satisfy Eq.(C-3) for $c\lambda_{LV}=0$ with a positive radical.

** For orbit altitudes other than 230 NM the curves of η_{es} vs. β are similar as indicated by Fig.(5-4).

given by

$$\eta_2 = -\eta_1 \equiv \eta_{s\ell} = \begin{cases} \eta_{es} & \text{if } \begin{cases} \eta_{es} \leq \eta_{ss} \text{ or} \\ \text{no self-shadow} \end{cases} \\ \eta_{ss} & \text{if } \eta_{es} > \eta_{ss} \end{cases} \quad \text{(C-7)}$$

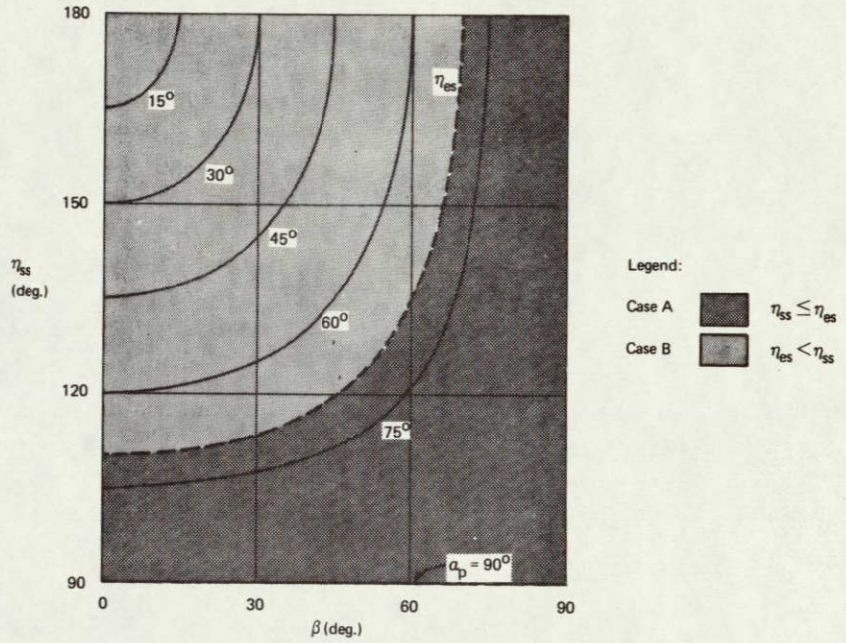

Figure (C - 1) - Variation in Panel Self-Shadow Boundary with α_p and β (LV - Optimum Roll Mode).

In view of Fig.(C-1), it follows that $\eta_{s\ell}=\eta_{es}$ in region B whereas $\eta_{s\ell}=\eta_{ss}$ in region A.

The electrical energy ($\hat{E}$) available from the array can be evaluated after integration of Eq.(5-16). Upon substituting Eq.(C-3) for $c\lambda$ the integration yields

Appendix C

$$\hat{E} = \frac{1}{2\eta_{es}} \int_{\eta_1}^{\eta_2} c\lambda_{LV} d\eta = \frac{1}{2\eta_{es}} \int_{-\eta_{s\ell}}^{\eta_{s\ell}} c\lambda_{LV} d\eta$$

$$= \frac{c\beta}{2\eta_{es}} \left\{ 2s\alpha_p s\eta_{s\ell} + 2 \frac{c\alpha_p}{c\beta} \int_0^{\eta_{s\ell}} \sqrt{s^2\beta + c^2\beta s^2\eta} \; d\eta \right\} \quad \text{(C-8)}$$

$$= \frac{1}{\eta_{es}} \left\{ c\beta s\alpha_p s\eta_{s\ell} + c\alpha_p \int_0^{\eta_{s\ell}} \sqrt{1-c^2\beta c^2\eta} \; d\eta \right\}$$

The last term can be recognized as a form of an elliptic integral of the second kind, which can be converted to standard form by the substitution, $\eta=\theta-90°$, so that *

$$\int_0^{\eta_{s\ell}} \sqrt{1-c^2\beta c^2\eta} \; d\eta = \int_{90°}^{\eta_{s\ell}+90°} \sqrt{1-c^2\beta s^2\theta} \; d\theta = \int_{90°}^{\theta+180°} \sqrt{1-k^2 s^2\theta} \; d\theta$$

$$= E(k,\theta+180°)-E(k) \quad \text{(C-9)}$$

$$= E(k,\theta) + E(k)$$

where

$$k=c\beta \quad \text{(C-10)}$$

and

$$\theta=\eta_{s\ell}-90° \quad \text{(C-11)}$$

---

* The incomplete elliptic integral of the second kind, $E(k,\theta)$, is available in tabulated form[16] as a function of the modulus k and argument θ. The second function $E(k)$ is the complete elliptic integral of the second kind ($\theta=90°$). The last step in Eq.(C-9) follows from the property that

$$E(k,n\pi+\theta) = 2nE(k)+E(k,\theta)$$

Appendix C

The expression for $\hat{E}$ can then be written as

$$\hat{E} = \frac{1}{\eta_{es}} \left\{ s\alpha_p c\beta s\eta_{s\ell} + c\alpha_p [E(k,\Theta)+E(k)] \right\} \qquad (C\text{-}12)$$

In Fig.(5-9) $\hat{E}$ vs. β is plotted for various panel angles (α_p). The upper envelope boundary on the curves represents the maximum electrical energy ($\hat{E}_{max}$) available from the array in the LV-Optimum Roll mode with optimum variation in panel angle as a function of β. Plots of $\hat{E}_{max}$ and $\alpha_{p(opt)}$ obtained numerically are shown in Figs.(5-28) and (5-30). In general, an analytical expression for $\alpha_{p(opt)}$ can be determined by setting $\partial\hat{E}/\partial\alpha_p=0$, although the result may not be amenable to closed form solution if $\eta_{s\ell}=\eta_{ss}$, since η_{ss} is a function of α_p. In view of Figs.(5-30) and (C-1) however, it follows that $\eta_{s\ell}=\eta_{es}$ for all β in the vicinity of $\alpha_p=\alpha_{p(opt)}$ in the optimum roll case. Consequently, $\eta_{s\ell}$ in Eq.(C-12) is not a function of α_p in that region, so that $\partial\hat{E}/\partial\alpha_p=0$ is simply

$$\frac{\partial\hat{E}}{\partial\alpha_p} = \frac{1}{\eta_{es}} \left\{ c\alpha_p c\beta s\eta_{es} - s\alpha_p [E(k,\Theta)+E(k)] \right\} = 0 \qquad (C\text{-}13)$$

The optimum panel angle is then given by

$$\tan\alpha_{p(opt)} = \frac{c\beta s\eta_{es}}{E(k)+E(k,\eta_{es}-90°)} \qquad (C\text{-}14)$$

which is in agreement with the curve of $\alpha_{p(opt)}$ determined numerically in Fig.(5-30). Since

$$c\alpha_{p(opt)} = \frac{[E(k) + E(k,\eta_{es}-90°)]}{\sqrt{[E(k) + E(k,\eta_{es}-90°)]^2 + c^2\beta s^2\eta_{es}}} \qquad (C\text{-}15)$$

it follows from Eq.(C-12) that $\hat{E}_{max}$ is given by

$$\hat{E}_{max} = c\alpha_{p(opt)}[E(k)+E(k,\eta_{es}-90°)]\cdot[1+\tan^2\alpha_{p(opt)}]/\eta_{es}$$

$$= [E(k)+E(k,\eta_{es}-90°)]/\eta_{es}c\alpha_{p(opt)} \qquad (C-16)$$

$$= \frac{1}{\eta_{es}}\sqrt{[E(k)+E(k,\eta_{es}-90°)]^2 + c^2\beta s^2\eta_{es}}$$

which agrees with the results in Fig.(5-28).

C.2 LV-Continuous Roll Mode

In the continuous roll case, the panel self-shadow boundary is obtained after setting $c\lambda_{LV}=0$ in Eq.(5-18) with $\phi= -\eta$. The expression for $c\lambda_{LV}$ with $\phi= -\eta$ is

$$c\lambda_{LV} = s(\alpha_p+\beta)c\eta + c\alpha_p c\beta s^2\eta$$

$$= -[c\alpha_p c\beta c^2\eta - s(\alpha_p+\beta)c\eta - c\alpha_p c\beta] \qquad (C-17)$$

The solution of Eq.(C-17) for $c\lambda_{LV}=0$, which satisfies the constraint, $0\leq|c\eta|\leq 1$, is given by

$$c\eta = \frac{s(\alpha_p+\beta) - \sqrt{s^2(\alpha_p+\beta) + 4c^2\alpha_p c^2\beta}}{2c\alpha_p c\beta} \qquad (C-18)$$

Since the cosine function is even, the two values of η resulting from Eq.(C-18), which specify the self-shadow boundary (η_{ss1} and η_{ss2}), are symmetric about $\eta=0°$ so that $\eta_{ss2}=-\eta_{ss1}\equiv\eta_{ss}$. A plot of η_{ss} vs. β obtained from Eq.(C-18) for various values of α_p is shown in Fig.(C-2). The dashed curve represents the

earth shadow boundary as obtained from Eqs.(5-6) and (5-7) for a 230 NM circular orbit.

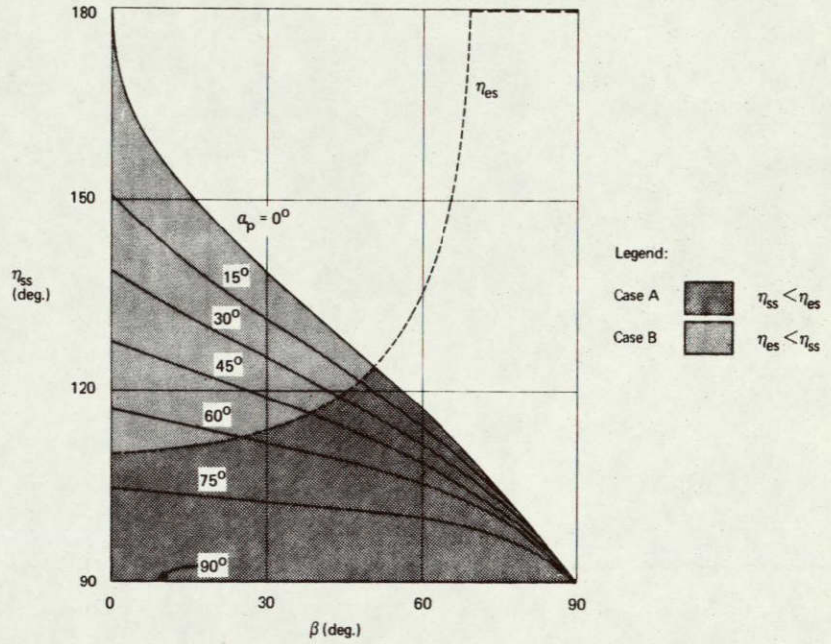

Figure (C - 2) - Variation in Panel Self-Shadow Boundary with α_p and β (LV - Continuous Roll Mode).

Since the self-shadow boundary is symmetrical about $\eta=0°$, the sunlight interval $(-\eta_{s\ell} < \eta < \eta_{s\ell})$ is also determined as in Eq.(C-7). In view of Fig.(C-2) it follows that $\eta_{s\ell}=\eta_{es}$ in region B whereas $\eta_{s\ell}=\eta_{ss}$ in region A.

The electrical energy $(\hat{E})$ available from the array can be evaluated after integration of Eq.(5-16). Substitution of Eq.(C-17) for $c\lambda$ and integration yields

$$\hat{E} = \frac{1}{2\eta_{es}} \int_{-\eta_{s\ell}}^{\eta_{s\ell}} c\lambda_{LV} d\eta \qquad (C\text{-}19)$$

$$= \frac{1}{2\eta_{es}} \left[2s(\alpha_p+\beta) s\eta_{s\ell} + \frac{c\alpha_p c\beta}{2} (2\eta_{s\ell} - s2\eta_{s\ell}) \right]$$

Appendix C

In Fig.(5-11) $\hat{E}$ vs β is plotted for various panel angles (α_p). The upper envelope boundary represents the maximum electrical energy ($\hat{E}_{max}$) available from the array in the continuous roll mode with optimum variation of α_p with β. Plots of $\hat{E}_{max}$ and $\alpha_{p(opt)}$ obtained numerically are shown in Figs.(5-28) and (5-30). The slight bend in the curve of $\alpha_{p(opt)}$ vs. β at $\beta \equiv \beta_\tau \approx 47°$ signifies the transition point for calculating $\hat{E}_{max}$, since $\eta_{s\ell}=\eta_{es}$ when $\beta \leq \beta_\tau$. For $\beta > \beta_\tau$, setting $\partial\hat{E}/\partial\alpha_p=0$ to obtain $\alpha_{p(opt)}$ leads to an unwieldy transcendental equation, since $\eta_{s\ell}=\eta_{ss}$ is a function of α_p. The result is not amenable to closed form solution. For $\beta < \beta_\tau$, determination of $\alpha_{p(opt)}$ is relatively simple since $\eta_{s\ell}=\eta_{es}$ is not a function of α_p. As a result

$$\frac{\partial\hat{E}}{\partial\alpha_p} = \frac{1}{2\eta_{es}} \left\{ (2c\beta s\eta_{es}) c\alpha_p - s\alpha_p [2s\beta s\eta_{es} + \frac{c\beta}{2}(2\eta_{es} - s2\eta_{es})] \right\} \tag{C-20}$$

Setting $\partial\hat{E}/\partial\alpha_p = 0$ yields

$$\tan\alpha_{p(opt)} = \frac{1}{\tan\beta + K(\beta)} \qquad \beta \leq \beta_\tau \tag{C-21}$$

where

$$K(\beta) = (2\eta_{es} - s2\eta_{es})/4s\eta_{es} \tag{C-22}$$

and

$$c\alpha_{p(opt)} = \frac{\tan\beta + K(\beta)}{\sqrt{1 + [\tan\beta + K(\beta)]^2}} \tag{C-23}$$

It follows from Eqs.(C-21), (C-23) and (C-19) with $\eta_{s\ell}=\eta_{es}$ that $\hat{E}_{max}$ is given by

Appendix C

$$\hat{E}_{max} = \frac{1}{2\eta_{es}} \left\{ 2c\beta s\eta_{es} s\alpha_{p(opt)} + c\alpha_{p(opt)} [2s\beta s\eta_{es} + \frac{c\beta}{2}(2\eta_{es} - s2\eta_{es})] \right\}$$

$$= \frac{c\beta s\eta_{es}}{\eta_{es}} \; c\alpha_{p(opt)} [\tan\beta + K(\beta)][\tan^2\alpha_{p(opt)} + 1]$$

$$= \frac{c\beta s\eta_{es}}{\eta_{es}} \left\{ [\tan\beta + K(\beta)]/c\alpha_{p(opt)} \right\}$$

$$= \frac{c\beta s\eta_{es}}{\eta_{es}} \sqrt{1 + [\tan\beta + K(\beta)]^2} \qquad \beta \leq \beta_\tau \qquad \text{(C-24)}$$

The results in Eqs. (C-24) and (C-21) for $\hat{E}_{max}$ and $\alpha_{p(opt)}$ are consistent with the numerical results in Figs. (5-28) and (5-30).

C.3 LV-Cyclic Roll Mode

In the cyclic roll case, the panel self-shadow boundary is obtained by setting $c\lambda_{LV}=0$ in Eq. (5-18) with $\phi=\phi_{cyc}$ as defined in Eq. (5-21) where

$$\phi_{cyc} = \begin{cases} \eta + 180° & -180° \leq \eta \leq -90° \\ -\eta & -90° \leq \eta \leq 90° \\ \eta - 180° & 90° \leq \eta \leq 180° \end{cases} \qquad \text{(C-25)}$$

The expressions for $c\lambda_{LV}$ with $\phi=\phi_{cyc}$ are then

$$(c\lambda_{LV})_1 = s(\alpha_p+\beta)c\eta + c\alpha_p c\beta s^2\eta \qquad |\eta| < 90° \qquad \text{(C-26)}$$

and

$$(c\lambda_{LV})_2 = s(\alpha_p-\beta)c\eta + c\alpha_p c\beta s^2\eta$$

$$= -[c\alpha_p c\beta c^2\eta - s(\alpha_p-\beta)c\eta - c\alpha_p c\beta]$$

$$90° \leq |\eta| \leq 180° \qquad \text{(C-27)}$$

However, in determining the self-shadow boundary, only the latter expression is significant.* The solution of Eq.(C-27) for $(c\lambda_{LV})_2=0$, which satisfies the constraint $0\leq|c\eta|\leq 1$, is given by

$$c\eta = \frac{s(\alpha_p-\beta) - \sqrt{s^2(\alpha_p-\beta) + 4c^2\alpha_p c^2\beta}}{2c\alpha_p c\beta} \qquad \beta\leq\alpha_p \qquad \text{(C-28)}$$

As before the self-shadow boundary is symmetrical about $\eta=0°$ so that

$$\eta_{ss2}=-\eta_{ss1}\equiv\eta_{ss} = \begin{cases} 180°-\cos^{-1}\left[\dfrac{-s(\alpha_p-\beta)+\sqrt{s^2(\alpha_p-\beta)+4c^2\alpha_p c^2\beta}}{2c\alpha_p c\beta}\right] & \beta\leq\alpha_p \\ \text{no self-shadow} & \beta>\alpha_p \end{cases} \qquad \text{(C-29)}$$

A plot of η_{ss} vs. β obtained from Eq.(C-29) for various values of α_p is shown in Fig.(C-3). As in previous cases, the dashed curve represents the earth shadow boundary for a 230 NM circular orbit.

---

* Since $(c\lambda_{LV})_1=0$ has no real roots of $c\eta$ which satisfy the constraints $0\leq|c\eta|<1$ and $0°\leq\alpha_p,\beta\leq 90°$, it follows that only $(c\lambda_{LV})_2$ need be considered in determining the self-shadow boundary.

Appendix C

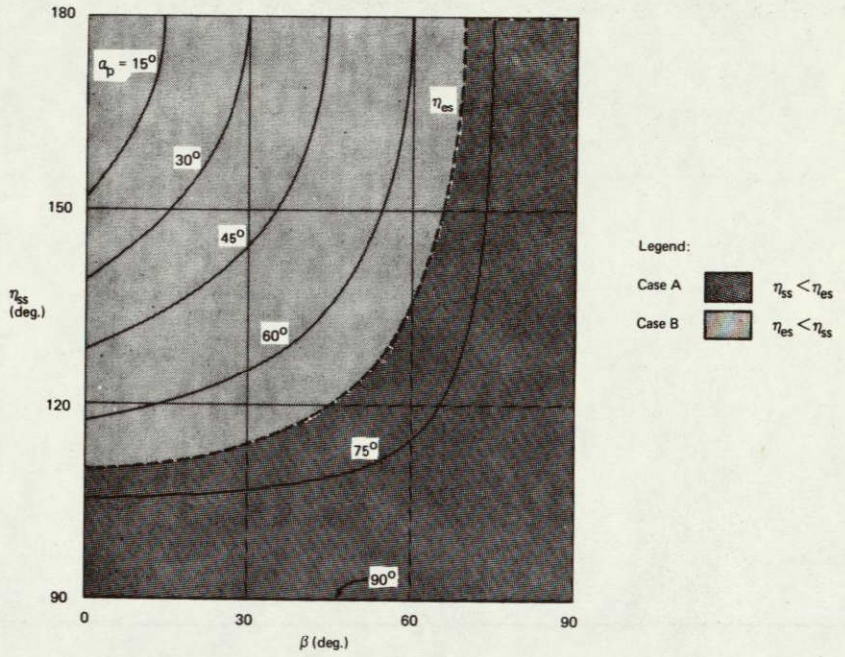

Figure (C - 3) - Variation in Panel Self-Shadow Boundary with α_p and β (LV - Cyclic Roll Mode).

Since the self-shadow boundary is symmetrical about $\eta=0$; the sunlight interval $(-\eta_{s\ell} \leq \eta \leq \eta_{s\ell})$ is also determined as in Eq.(C-7). In view of Fig.(C-3), it follows that $\eta_{s\ell}=\eta_{es}$ in region B whereas $\eta_{s\ell}=\eta_{ss}$ in region A.

The electrical energy $(\hat{E})$ available from the array can be evaluated after integration of Eq.(5-16). Substitution of Eqs.(C-26) and (C-27) for $c\lambda$ in the appropriate integration intervals yields

Appendix C

$$\hat{E} = \frac{1}{2\eta_{es}} \int_{-\eta_{s\ell}}^{\eta_{s\ell}} c\lambda_{LV} d\eta = \frac{1}{2\eta_{es}} \left\{ \int_{-\eta_{s\ell}}^{-90^\circ} (c\lambda_{LV})_2 d\eta + \int_{-90^\circ}^{90^\circ} (c\lambda_{LV})_1 d\eta \right.$$

$$\left. + \int_{90^\circ}^{\eta_{s\ell}} (c\lambda_{LV})_2 d\eta \right\} = \frac{1}{2\eta_{es}} \left\{ 2 \int_{0}^{90^\circ} (c\lambda_{LV})_1 d\eta + 2 \int_{90^\circ}^{\eta_{s\ell}} (c\lambda_{LV})_2 d\eta \right\}$$

$$= \frac{1}{2\eta_{es}} \left[4c\alpha_p s\beta + 2s(\alpha_p - \beta) s\eta_{s\ell} + \frac{c\alpha_p c\beta}{2} (2\eta_{s\ell} - s2\eta_{s\ell}) \right] \qquad (C-30)$$

In Fig. (5-10) $\hat{E}$ vs. β is plotted for various panel angles (α_p). The upper envelope boundary represents the maximum electrical energy ($\hat{E}_{max}$) available from the array in the continuous roll mode with optimum variation of α_p with β. Plots of $\hat{E}_{max}$ and $\alpha_{p(opt)}$ obtained numerically are shown in Figs. (5-28) and (5-30).

In view of Figs. (5-30) and (C-3), it is evident that $\eta_{s\ell} = \eta_{es}$ for all β, when $\alpha_p = \alpha_{p(opt)}$ in the cyclic roll case. Consequently, an analytical solution for $\alpha_{p(opt)}$ obtained by setting $\partial\hat{E}/\partial\alpha_p = 0$ with $\eta_{s\ell} = \eta_{es}$ will hold for all β. This procedure yields

$$\frac{\partial \hat{E}}{\partial \alpha_p} = \frac{1}{2\eta_{es}} \left\{ (2c\beta s\eta_{es}) c\alpha_p - s\alpha_p \left[4s\beta - 2s\beta s\eta_{es} + \frac{c\beta}{2} (2\eta_{es} - s2\eta_{es}) \right] \right\} = 0 \qquad (C-31)$$

so that

$$\tan\alpha_{p(opt)} = \frac{1}{G(\beta)\tan\beta + K(\beta)} \qquad (C-32)$$

Appendix C

where

$$G(\beta) = \frac{2 - s\eta_{es}}{4\eta_{es}} \tag{C-33}$$

$$K(\beta) = \frac{2\eta_{es} - s2\eta_{es}}{4s\eta_{es}} \tag{C-34}$$

and

$$c\alpha_{p(opt)} = \frac{G(\beta)\tan\beta + K(\beta)}{\sqrt{1 + [G(\beta)\tan\beta + K(\beta)]^2}} \tag{C-35}$$

It follows from Eqs.(C-32), (C-35) and (C-30) with $\eta_{s\ell}=\eta_{es}$ that $\hat{E}_{max}$ is given by

$$\hat{E}_{max} = \frac{1}{2\eta_{es}} \left\{ 2c\beta s\eta_{es} s\alpha_{p(opt)} + c\alpha_{p(opt)} [4s\beta - 2s\beta s\eta_{es} + \frac{s\beta}{2}(2\eta_{es} - s2\eta_{es})] \right\}$$

$$= \frac{c\beta s\eta_{es}}{\eta_{es}} c\alpha_{p(opt)} [G(\beta)\tan\beta + K(\beta)][\tan^2\alpha_{p(opt)} + 1]$$

$$= \frac{c\beta s\eta_{es}}{\eta_{es}} \sqrt{1 + [G(\beta)\tan\beta + K(\beta)]^2} \tag{C-36}$$

The results in Eqs.(C-36) and (C-32) for $\hat{E}_{max}$ and $\alpha_{p(opt)}$ are in agreement with the numerical results in Figs.(5-28) and (5-30) respectively.

C.4 Fixed Roll Mode

In the fixed roll mode the panel self shadow boundary (η_{ss1}, η_{ss2}) is obtained by solving Eq.(5-18) for η with $c\lambda_{LV}=0$ and ϕ=constant. The general form of this equation is

$$c\lambda_{LV} = A + Bc\eta - Cs\eta = 0 \tag{C-37}$$

Appendix C

where

$$A = c\alpha_p \; c\phi \; s\beta \tag{C-38}$$

$$B = s\alpha_p \; c\beta \tag{C-39}$$

and

$$C = c\alpha_p \; c\beta \; s\phi \tag{C-40}$$

In contrast to previous cases, the solutions of Eq.(C-37) for η are generally not symmetrical about $\eta=0°$. The two solutions can be expressed in terms of $s\eta$ and $c\eta$ after alternately eliminating $c\eta$ and $s\eta$ from Eq.(C-37) and solving the resulting quadratic equation for $s\eta$ and $c\eta$ respectively. This yields

$$s\eta_{ss2} = \frac{AC + BR}{B^2 + C^2} \tag{C-41}$$

$$c\eta_{ss2} = \frac{-AB + CR}{B^2 + C^2} \tag{C-42}$$

and

$$s\eta_{ss1} = \frac{AC - BR}{B^2 + C^2} \tag{C-43}$$

$$c\eta_{ss1} = \frac{-AB - CR}{B^2 + C^2} \tag{C-44}$$

where

$$R \equiv \sqrt{B^2 + C^2 - A^2} = \sqrt{c^2\beta - c^2\alpha_p c^2\phi} \tag{C-45}$$

Appendix C

If $0 \leq (\alpha_p, \beta) \leq 90°$* and $-90° \leq \phi \leq 0$,** then A and B are always positive and C is always negative. In view of Eqs.(C-42) and (C-43) it follows that $c\eta_{ss2} \leq 0$ and $s\eta_{ss1} \leq 0$ so that $90° \leq \eta_{ss2} \leq 270°$ and $-180° \leq \eta_{ss1} \leq 0°$.*** As a result, the self-shadow interval is not necessarily symmetrical about $\eta=0°$, as is the earth shadow interval ($\pm\eta_{es}$). Consequently the self-shadow and earth shadow intervals may assume any one of four possible relationships, as shown in Figure (C-4).

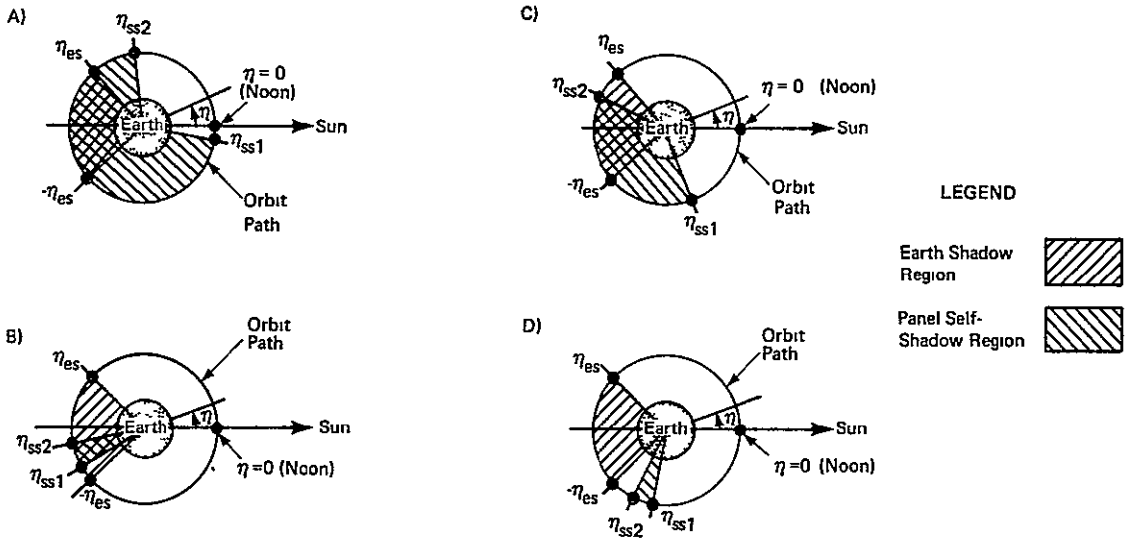

Figure (C - 4) - Possible Earth Shadow and Solar Panel Self-Shadow Regions (LV - Fixed Roll Mode)

---

*See Footnote ** on page 45.

**While the useful range on ϕ for $\beta>0$ is $-90° \leq \phi \leq 90°$, it is only necessary in evaluating η_{ss1} and η_{ss2}, to consider either $-90° \leq \phi \leq 0$ or $0 \leq \phi \leq 90°$. This follows from Eqs.(C-41) - (C-44), which indicate that the extent of the self-shadow interval is the same, whether $C>0$ or $C<0$. The only difference is that for $C<0$ the self-shadow interval lies within the range $90° \leq \eta \leq 360°$ whereas this range is $0° \leq \eta \leq 270°$ for $C>0$. Consequently only $-90° \leq \phi \leq 0°$ is considered.

***The convention adopted here is that η_{ss2} is always a positive angle whereas η_{ss1} is always a negative angle.

Appendix C

The terminal point (η_{sst}) at which the self-shadow region reduces to zero, occurs when $\eta_{ss1}=(\eta_{ss2}-360°)$. This condition results when the radical in Eqs.(C-41) - (C-44) becomes zero or in view of Eq.(C-45), when $c\beta=c\alpha_p c\phi$.

The self-shadow boundary is then specified by

$$\eta_{ss2} = \begin{cases} 180° + \tan^{-1}\left(\frac{AC + BR}{-AB + CR}\right) & \beta \leq \cos^{-1}(c\alpha_p c\phi) \\ \text{no self-shadow} & \beta > \cos^{-1}(c\alpha_p c\phi) \end{cases} \quad \text{(C-46)}$$

and*

$$\eta_{ss1} = \begin{cases} -90° - \tan^{-1}\left(\frac{-AB - CR}{AC - BR}\right) & \beta \leq \cos^{-1}(c\alpha_p c\phi) \\ \text{no self-shadow} & \beta > \cos^{-1}(c\alpha_p c\phi) \end{cases} \quad \text{(C-47)}$$

and when $\beta=\cos^{-1}(c\alpha_p c\phi)$, it follows from the preceding equations and Eqs.(C-39) and (C-40) that

$$\eta_{sst} \equiv \eta_{ss1} = (\eta_{ss2}-360°) = -180° - \tan^{-1}(-C/B)$$

$$= -180° - \tan^{-1}\left(\frac{c\beta s\phi}{-\sqrt{c^2\phi - c^2\beta}}\right) \quad \beta \geq |\phi| \quad \text{(C-48)}$$

In Fig.(C-5) curves illustrating the behavior of η_{ss1} and η_{ss2} as a function of β and α_p are shown for $\phi= -45°$. The terminator curve corresponding to η_{sst} is represented by the heavy dotted line. The earth shadow boundaries ($\pm\eta_{es}$) corresponding to a 230 NM circular orbit are represented by the dashed curves. The various shaded regions in Fig.(C-5) denoted by A, B, C and D, correspond to the location of the self-shadow

---

*This particular form for η_{ss1} follows from the fact that $\tan\eta_{ss1}=\tan[-90°-\tan^{-1}(c\eta_{ss1}/s\eta_{ss1})]$.

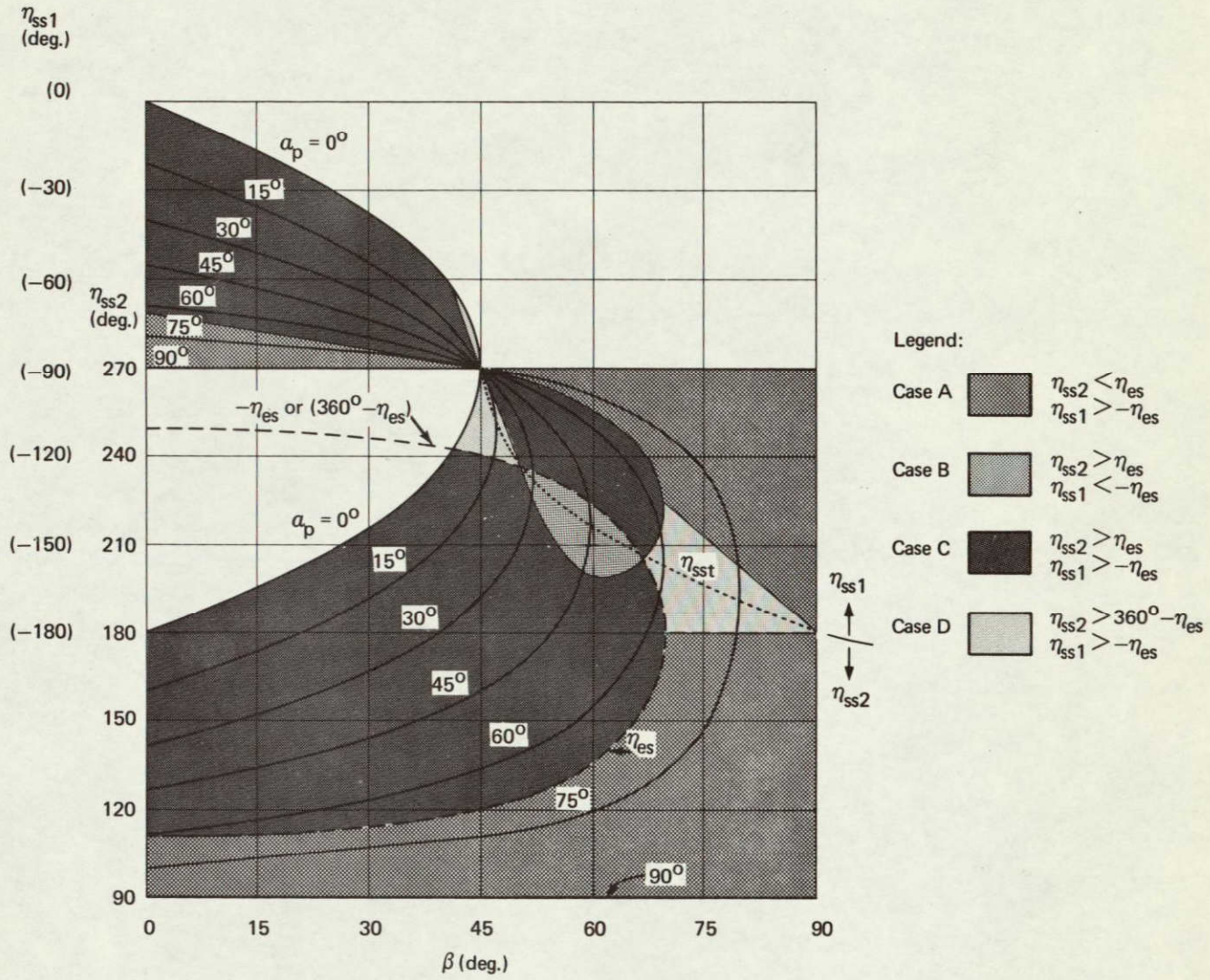

Figure (C - 5) - Variation in Panel Self-Shadow Boundary with α_p and β (LV - Fixed Roll Mode: $\phi = -45^o$).

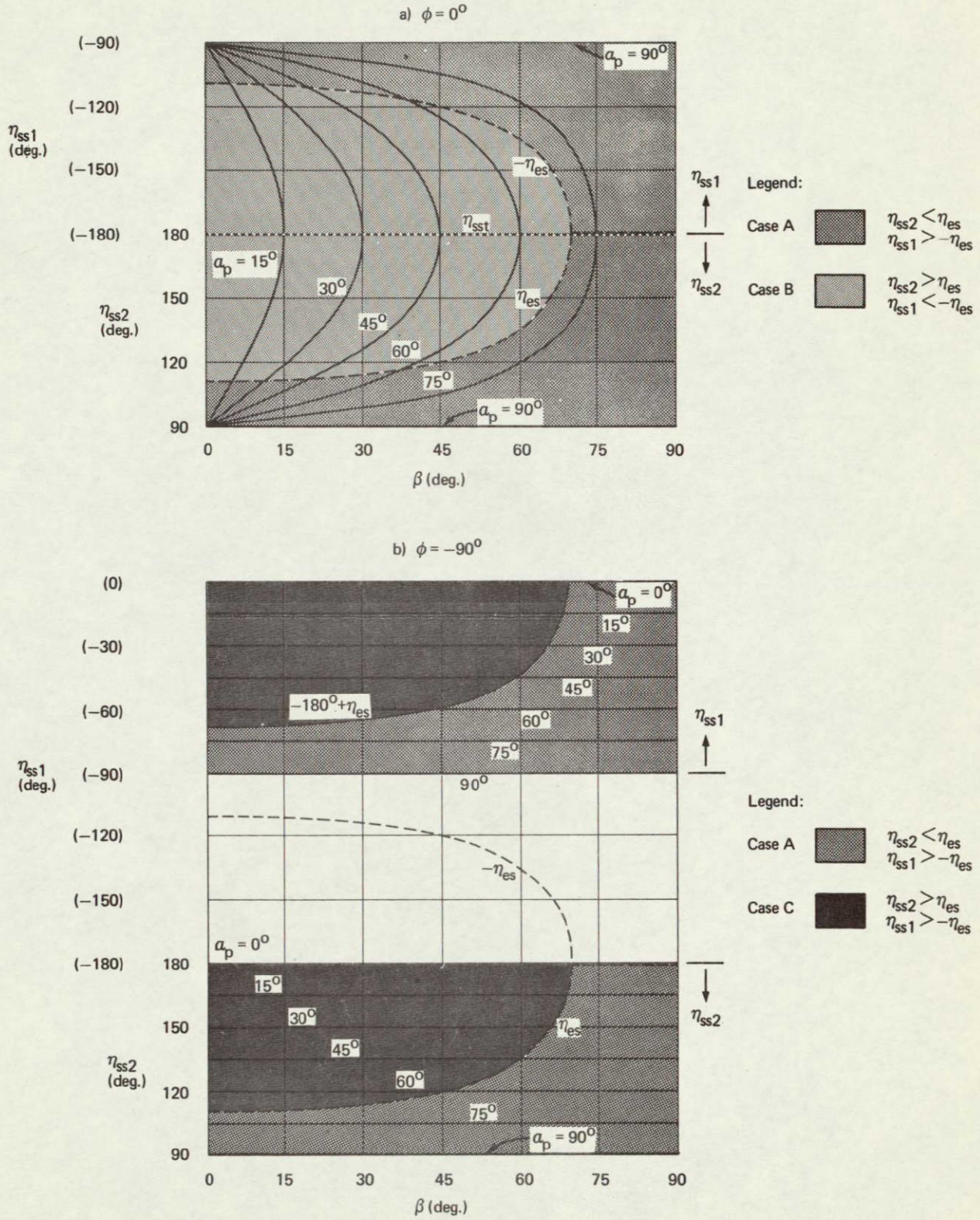

Figure (C - 6) - Variation in Panel Self-Shadow Boundary with α_p and β (LV - Fixed Roll Mode).

boundaries for the four cases illustrated in Fig.(C-4). The relative size of these areas varies with ϕ and some vanish as $\phi \to 0°$ or $\phi \to -90°$. The curves for η_{ss1} and η_{ss2} and the corresponding shaded areas, when $\phi=0°$ and $\phi=-90°$, are shown in Figs.(C-6a) and (C-6b) respectively. When $\phi=0°$, the self-shadow interval is symmetrical about $\eta=180°$, as shown in Fig.(C-6a) where $\eta_{ss2} = -\eta_{ss1}$ and $\eta_{sst} = -180°$ for all β and α_p.

Evaluation of $\hat{E}$

The electrical energy ($\hat{E}$) available from the solar array according to Eq.(5-16) is given by

$$\hat{E} = \frac{1}{2\eta_{es}} \int_{\eta_1}^{\eta_2} c\lambda_{LV} d\eta \qquad \text{(C-49)}$$

where $\eta_1 \leq \eta \leq \eta_2$ represents the array sunlight interval. In order to include the effect of distinct earth shadow and self-shadow intervals as shown in Fig.(C-4d), it is convenient to modify this expression so that

$$\hat{E} = \frac{1}{2\eta_{es}} \left\{ \int_{\eta_1}^{\eta_2} c\lambda_{LV} d\eta - \int_{\eta_1'}^{\eta_2'} c\lambda_{LV} d\eta \right\} \qquad \text{(C-50)}$$

where

$$\eta_2 = \begin{cases} \eta_{ss2} & \eta_{ss2} < \eta_{es} \quad \text{(Case: A)} \\ \eta_{es} & \eta_{es} \leq \eta_{ss2}^* \quad \text{(Case: B,C,D)} \end{cases} \qquad \text{(C-51a)}$$

$$\eta_1 = \begin{cases} \eta_{ss1} & |\eta_{ss1}| < \eta_{es} \quad \text{(Case: A,C,D)} \\ -\eta_{es} & \eta_{es} \leq |\eta_{ss1}|^* \quad \text{(Case: B)} \end{cases} \qquad \text{(C-51b)}$$

---

*or if no self-shadowing occurs, i.e., $(\beta > \cos^{-1}[c\alpha_p c\phi])$.

and

$$\eta_2' = \begin{cases} \eta_{ss1} & |\eta_{ss2}-360°| < \eta_{es} \quad \text{(Case: D)} \\ 0 & \text{otherwise*} \quad \text{(Case: A,B,C)} \end{cases} \tag{C-52a}$$

$$\eta_1' = \begin{cases} (\eta_{ss2}-360°) & |\eta_{ss2}-360°| < \eta_{es} \quad \text{(Case: D)} \\ 0 & \text{otherwise*} \quad \text{(Case: A,B,C)} \end{cases} \tag{C-52b}$$

After substitution for $c\lambda$ from Eq.(C-37) and integration of Eq.(C-50) the expression for $\hat{E}$ becomes

$$\hat{E} = \frac{1}{2\eta_{es}} \left\{ [A(\eta_2-\eta_1) + B(s\eta_2-s\eta_1) + C(c\eta_2-c\eta_1] - [A(\eta_2'-\eta_1') + B(s\eta_2'-s\eta_1') + C(c\eta_2'-c\eta_1')] \right\} \tag{C-53}$$

where A, B and C are defined by Eqs.(C-38), (C-39) and (C-40). In Fig.(5-15) $\hat{E}$ vs. β is plotted as a function of the panel angle (α_p) for three cases: $\phi=0$, $\phi=-45°$ and $\phi=-90°$. In each case the upper envelope boundary on the curves corresponds to the maximum electrical energy ($\hat{E}_{max}$) available from the array (for a specific ϕ) with optimum variation of α_p with β. Plots of $\hat{E}_{max}$ and $\alpha_{p(opt)}$ vs. β obtained numerically for several values of ϕ are shown in Figs.(5-16) and (5-17) respectively. These results indicate that making $\phi=0°$ evidently yields the largest $\hat{E}_{max}$ for all β. Of theoretical interest perhaps, is the fact that in the region $0 \leq \beta \lesssim 23°$ other combinations of α_p and ϕ also exist which yield the same $\hat{E}_{max}$ as with $\phi=0°$, as will now be shown.

---

*or if no self-shadowing occurs, i.e., ($\beta > \cos^{-1}[c\alpha_p c\phi]$).

Appendix C

Analytical Determination of $\alpha_{p(opt)}$ and ϕ_{opt}

It is convenient at this point to introduce a change of variables for the terms involving α_p and ϕ in the expression for $c\lambda_{LV}$ in Eq.(5-9). Specifically, let

$$s\phi c\alpha_p = s\underline{\phi}\ s\underline{\alpha} \tag{C-54}$$

and

$$s\alpha_p = c\underline{\phi}\ s\underline{\alpha} \tag{C-55}$$

where $-90° \leq \underline{\phi} \leq 0°$ and $0° \leq \underline{\alpha} \leq 90°$. Since

$$c\alpha_p c\phi = \sqrt{c^2\alpha_p - s^2\phi c^2\alpha_p} = \sqrt{c^2\alpha_p - s^2\underline{\phi}s^2\underline{\alpha}}$$

$$= \sqrt{c^2\alpha_p + c^2\underline{\phi}s^2\underline{\alpha} - s^2\underline{\alpha}} = c\underline{\alpha} \tag{C-56}$$

it follows that $c\lambda_{LV}$ in Eq.(5-9) can be written as

$$c\lambda_{LV} = c\alpha_p c\phi s\beta + s\alpha_p c\beta c\eta - s\phi c\alpha_p c\beta s\eta$$

$$= c\underline{\alpha}s\beta + s\underline{\alpha}c\beta c(\underline{\phi}+\eta) \tag{C-57}$$

The procedure here will be to express the electrical energy $\hat{E}$ in terms of $\underline{\alpha}$ and $\underline{\phi}$, next to determine the $\underline{\alpha}$ and $\underline{\phi}$ which maximize $\hat{E}$ and finally to infer from the relationships in Eqs.(C-54), (C-55) and (C-56), the corresponding optimum values of α_p and ϕ. In evaluating $\hat{E}$ the panel self-shadow boundary is first expressed in terms of β, $\underline{\alpha}$ and $\underline{\phi}$ from Eq.(C-57) after setting $c\lambda=0$. This yields

$$c(\underline{\phi}+\eta) = -\tan\beta/\tan\underline{\alpha} \qquad \beta \leq \underline{\alpha} \tag{C-58}$$

so that

$$\eta_{ss2} = \xi - \underline{\phi} \tag{C-59}$$

and

$$\eta_{ss1} = -\xi - \underline{\phi} \tag{C-60}$$

where

$$\xi \equiv \begin{cases} 180° - \cos^{-1}(\tan\beta/\tan\underline{\alpha}) & \beta \leq \underline{\alpha} \\ 180° & \beta > \underline{\alpha} \end{cases}$$

For $\underline{\phi}=0$, the self-shadow boundaries are symmetrical about $\eta=180°$. Since $\underline{\phi}=0°$ implies from Eqs.(C-54) and (C-55) that $\phi=0°$ and $\alpha_p=\underline{\alpha}$, the curves in Fig.(C-6a) for η_{ss1} and η_{ss2} correspond directly to $\eta_{ss1}=-\xi$ and $\eta_{ss2}=+\xi$ respectively. The effect of making $-90° \leq \underline{\phi} < 0$ is to shift these curves upwards, thereby creating four possible shadow boundary arrangements as described earlier in Fig.(C-4).

Expressions for the electrical energy ($\hat{E}$) corresponding to each of the four shadow boundary arrangements in Fig.(C-4) can be obtained after integrating Eq.(C-50). Upon substituting, Eq.(C-57) for $c\lambda$ and appropriate values for the limits η_2, η_1, η_2' and η_1' from Eqs.(C-51), (C-52) and (C-60) the results are

Case A:

$$\hat{E} = \frac{1}{2\eta_{es}} \int_{\eta_{ss1}}^{\eta_{ss2}} [c\underline{\alpha}s\beta + s\underline{\alpha}c\beta c(\underline{\phi}+\eta)]d\eta = \frac{1}{\eta_{es}}(c\underline{\alpha}s\beta \cdot \xi + s\underline{\alpha}c\beta s\xi) \tag{C-62}$$

Case B:

$$\hat{E} = \frac{1}{2\eta_{es}} \int_{-\eta_{es}}^{\eta_{es}} [c\underline{\alpha}s\beta + s\underline{\alpha}c\beta c(\underline{\phi}+\eta)]d\eta = \frac{1}{\eta_{es}}(c\underline{\alpha}s\beta \cdot \eta_{es} + s\underline{\alpha}c\beta s\eta_{es}c\phi) \tag{C-63}$$

Case C:

$$\hat{E} = \frac{1}{2\eta_{es}} \int_{\eta_{ss1}}^{\eta_{es}} [c\underline{\alpha}s\beta + s\underline{\alpha}c\beta c(\underline{\phi}+\eta)]d\eta$$

$$= \frac{1}{2\eta_{es}} \left\{c\underline{\alpha}s\beta(\eta_{es}+\phi+\xi) + s\underline{\alpha}c\beta[s(\eta_{es}+\underline{\phi}) + s\xi]\right\} \tag{C-64}$$

Case D:

$$\hat{E} = \frac{1}{2\eta_{es}} \left[\int_{-\eta_{es}}^{\eta_{es}} c\lambda_{LV}d\eta - \int_{(\eta_{ss2}-2\pi)}^{\eta_{ss1}} c\lambda_{LV}d\eta \right]$$

$$= \frac{1}{\eta_{es}} \left\{[c\underline{\alpha}s\beta \cdot \eta_{es} + s\underline{\alpha}c\beta s\eta_{es}c\underline{\phi}] - [c\underline{\alpha}s\beta(2\pi-\xi) - s\underline{\alpha}c\beta s\xi]\right\} \tag{C-65}$$

The optimum $\underline{\alpha}$ and $\underline{\phi}$ can be obtained in each case by setting $\partial\hat{E}/\partial\underline{\alpha}=0$ and $\partial\hat{E}/\partial\underline{\phi}=0$ respectively. In evaluating the results however, only those solutions for $\underline{\alpha}_{opt}$ and $\underline{\phi}_{opt}$ which

yield shadow boundaries consistent with the respective cases (A, B, C or D) are acceptable.*

Case B:

It follows from Eq.(C-63) that $\underline{\phi}_{opt}=0°$

and

$$\frac{\partial \hat{E}}{\partial \underline{\alpha}} = \frac{1}{\eta_{es}}(-s\underline{\alpha}s\beta\cdot\eta_{es} + c\underline{\alpha}c\beta s\eta_{es}) = 0 \qquad (C-66)$$

so that

$$\tan\underline{\alpha}_{opt} = \frac{s\eta_{es}/\eta_{es}}{\tan\beta} \qquad (C-67)$$

and

$$c\alpha_{p(opt)} = \frac{\tan\beta}{\sqrt{(s\eta_{es}/\eta_{es})^2 + \tan^2\beta}} \qquad (C-68)$$

Consequently $\hat{E}_{max}$ in case B is given by

$$\hat{E}_{max} = \frac{1}{\eta_{es}} \left\{\eta_{es}\cdot s\beta c\underline{\alpha}_{opt}\left[1 + \left(\frac{s\eta_{es}/\eta_{es}}{\tan\beta}\right)\tan\underline{\alpha}_{opt}\right]\right\}$$

$$= \left(s\beta/c\underline{\alpha}_{opt}\right) = \frac{1}{\eta_{es}}\sqrt{c^2\beta s^2\eta_{es} + s^2\beta\cdot\eta_{es}^2} \qquad (C-69)$$

---

*With regard to case D however, it follows from Eqs.(C-63) and (C-65) that $\hat{E}_{(D)} \leq \hat{E}_{(B)}$ so that no further consideration of this case is actually necessary.

It follows from Eq. (C-62) that E is independent of $\underline{\phi}$. Hence,

$$\frac{\partial \hat{E}}{\partial \underline{\alpha}} = \frac{1}{\eta_{es}}\left[-s\underline{\alpha}s\beta\cdot\xi + c\underline{\alpha}c\beta s\xi + (c\underline{\alpha}s\beta + s\underline{\alpha}c\beta c\xi)\frac{\partial \xi}{\partial \underline{\alpha}}\right] = 0 \quad (C\text{-}70)$$

so that

$$s\underline{\alpha}\ s\beta\cdot\xi = c\underline{\alpha}\ c\beta\ s\xi \quad (C\text{-}71)$$

since

$$c\xi = \tan\beta/\tan\underline{\alpha} \quad (C\text{-}72)$$

from Eq. (C-61). Since ξ is a function of $\underline{\alpha}$, it is necessary to eliminate $\underline{\alpha}$ via Eqs. (C-71) and (C-72), solve for $\xi \equiv \xi_{opt}$ as a function of β and then determine $\underline{\alpha}_{opt}$ from Eq. (C-71) where

$$\tan\underline{\alpha}_{opt} = \frac{s\xi_{opt}/\xi_{opt}}{\tan\beta} \quad (C\text{-}73)$$

Eliminating $\underline{\alpha}$ from Eqs. (C-71) and (C-72) yields the following transcendental equation

$$2\xi = -\frac{s2\xi}{\tan^2\beta} \quad (C\text{-}74)$$

As illustrated in Fig. (C-7a) two solutions for ξ exist for sufficiently small β. The limiting case corresponding to $\beta \equiv \beta_c$

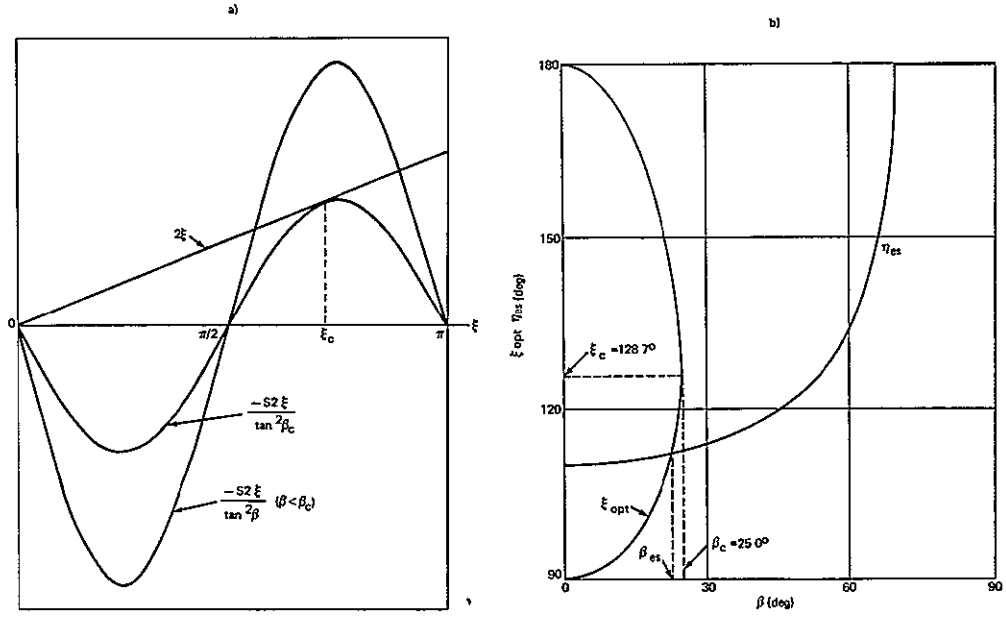

Figure (C - 7) - Relationship between Panel Self-Shadow Parameter (ξ) and β.

occurs when $c2\xi = -\tan^2\beta$ which means, in view of Eq.(C-74), that

$$2\xi_c = \tan 2\xi_c \tag{C-75}$$

Solution of Eq.(C-75) yields $\xi_c=128.7°$, which implies that $\beta_c=\tan^{-1}\left(\sqrt{-c^2 2\xi_c}\right)=25.0°$. The solutions for $\xi=\xi_{opt}$ obtained from Eq.(C-74) and a curve of the earth shadow boundary (η_{es}) are plotted in Fig.(C-7b) as a function of β. The intersection of the ξ_{opt} and η_{es} curves represents the transition point from case A to case B. In view of Fig.(C-7b) and Eq.(C-59), case A applies provided

$$\eta_{ss2} = \xi_{opt} - \underline{\phi} \leq \eta_{es} \tag{C-76}$$

or

$$\phi_{min} \equiv (-\eta_{es}+\xi_{opt}) \leq \phi \leq 0° \tag{C-77}$$

For $\beta=0°$ it follows that $\underline{\phi}_{min}=(-\eta_{es}+90°)$, since $\xi_{opt}=90°$ whereas $\underline{\phi}_{min}=0$ at $\beta=\beta_{es}$, since $\xi_{opt}=\eta_{es}$.

The optimum $\underline{\alpha}$ for case A is given by Eq.(C-73) and is similar in form to the result in Eq.(C-67) for case B. The corresponding electrical energy ($\hat{E}_{max}$) obtained from Eq.(C-62) with $\underline{\alpha}=\underline{\alpha}_{opt}$ is given by

$$\hat{E}_{max} = \frac{1}{\eta_{es}}\sqrt{c^2\beta s^2\xi_{opt} + s^2\beta\cdot\xi_{opt}^2} \tag{C-78}$$

which is identical with Eq.(C-69) when $\xi_{opt}=\eta_{es}$.

Case C:

The procedure is similar. Setting $\partial\hat{E}/\partial\underline{\phi}=0$ results in

$$\underline{\phi}_{opt} = (-\eta_{es}+\xi) \tag{C-79}$$

Substituting this result into Eq.(C-64) yields an expression for $\hat{E}$ which is identical to $\hat{E}$ for case A in Eq.(C-62). The result obtained from $\partial\hat{E}/\partial\alpha=0$ is also identical to Eq.(C-71) so that case C is really included in case A insofar as determining the optimum $\underline{\alpha}$ and $\underline{\phi}$ is concerned.

In summary then, it follows that

$\underline{0\leq\beta\leq\beta_{es}}$:

$$\hat{E}_{max} = \frac{1}{\eta_{es}}\sqrt{c^2\beta s^2\xi_{opt} + s^2\beta\cdot\xi_{opt}^2} \tag{C-80}$$

$$\tan\underline{\alpha}_{opt} = \frac{s\xi_{opt}/\xi_{opt}}{\tan\beta} \tag{C-81}$$

$$(-\eta_{es}+\xi_{opt}) \leq \underline{\phi} \leq 0° \tag{C-82}$$

$\underline{\beta_{es}\leq\beta\leq 90°}$:

$$\hat{E}_{max} = \frac{1}{\eta_{es}}\sqrt{c^2\beta s^2\eta_{es} + s^2\beta\cdot\eta_{es}^2} \tag{C-83}$$

$$\tan\underline{\alpha}_{opt} = \frac{s\eta_{es}/\eta_{es}}{\tan\beta} \tag{C-84}$$

$$\underline{\phi}_{opt} = 0° \tag{C-85}$$

Appendix C

The optimum spacecraft roll angle (ϕ) and optimum panel angle (α_p) corresponding to $\underline{\phi}_{opt}$ and $\underline{\alpha}_{opt}$ are then obtained from Eqs.(C-54), (C-55) and (C-56), which can be expressed as

$$\tan\phi = s\underline{\phi} \tan\underline{\alpha} \tag{C-86}$$

and

$$s\alpha_p = c\underline{\phi}\, s\underline{\alpha} \tag{C-87}$$

Curves for $\alpha_{p(opt)}$ and ϕ_{opt} obtained from Eqs.(C-86) and (C-87) for $\underline{\phi}_{opt}=0°$ and $\underline{\phi}_{opt}=(-\eta_{es}+\xi_{opt})$ with $\underline{\alpha}_{opt}$ given by Eqs.(C-81) and (C-83) are shown in Fig.(C-8). In the region $0\leq\beta\leq\beta_{es}=22.9°$ these curves represent the bounds on the other possible combinations of $\alpha_{p(opt)}$ and ϕ_{opt} which yield the same $\hat{E}_{max}$. For $\underline{\phi}=0°$ it follows from Eqs.(C-86), (C-87) and (C-84) that $\phi=0°$ and $\alpha_{p(opt)}=\underline{\alpha}_{opt}$.

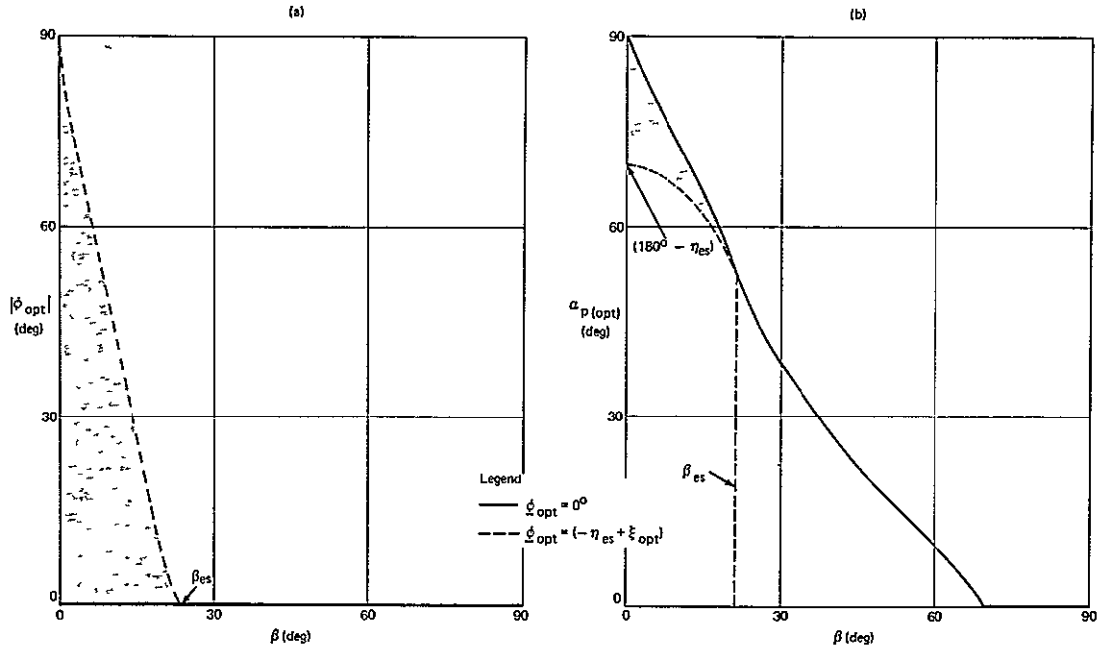

Figure (C - 8) - Optimum α_p and ϕ vs β (LV - Fixed Roll Mode).

C.5 LH-Optimum Roll Mode

Panel self-shadow boundaries in LH modes are closely related to those in corresponding LV modes. The expression for $c\lambda_{LH}$ in Eq.(5-41) with ϕ defined by Eq.(5-43) is

$$c\lambda_{LH} = c\beta\left[-s\alpha_p s\eta + c\alpha_p\sqrt{\tan^2\beta+c^2\eta}\right] \qquad \text{(C-88)}$$

If η is replaced by $(\eta-90°)$ it follows that Eq.(C-88) is identical to $c\lambda_{LV}$ in Eq.(C-3). Hence self-shadow boundaries have the same general character as in the LV-Optimum Roll mode, but are symmetrical about 90° rather than 180°. In view of Eq.(C-6) the self-shadow entry and exit points (η_{ss2},η_{ss1}) are given by

$$\eta_{ss2} = 180°-\eta_{ss1} = \begin{cases} 90° - \cos^{-1}(c\alpha_p/c\beta) & \beta \le \alpha_p \\ \text{no self-shadow} & \beta > \alpha_p \end{cases} \qquad \text{(C-89)}$$

A plot of (η_{ss2},η_{ss1}) vs. β is shown in Fig.(C-9) where the dashed curve represents the earth shadow boundary (η_{es}).

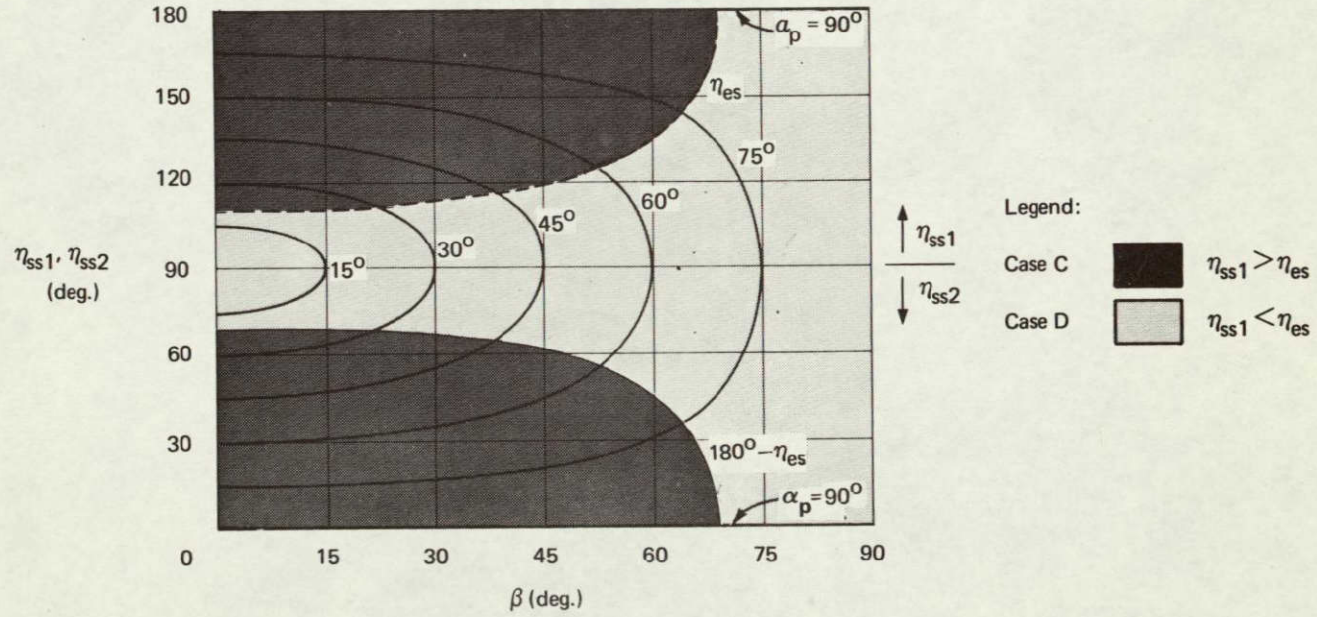

Figure (C - 9) - Variation in Panel Self-Shadow Boundary with α_p and β (LH - Optimum Roll Mode).

Appendix C

Self-shadow and earth shadow regions are distinct, whenever $\eta_{ss1} < \eta_{es}$ (Case D) and overlap partially whenever $\eta_{ss1} \geq \eta_{es}$ (Case C) as shown in Fig.(5-20). To evaluate $\hat{E}$ it is necessary to modify Eq.(5-16) such that

$$\hat{E} = \frac{1}{2\eta_{es}} \left\{ \int_{\eta_1}^{\eta_2} c\lambda_{LH} d\eta - \int_{\eta_1'}^{\eta_2'} c\lambda_{LH} d\eta \right\} \tag{C-90}$$

where

$$\eta_2 = -\eta_1 = \eta_{es} \tag{C-91a}$$

$$\eta_1' = \eta_{ss2} \tag{C-91b}$$

$$\eta_2' = \begin{cases} \eta_{es} & \text{(Case C)} \\ \eta_{ss1} & \text{(Case D)} \end{cases} \tag{C-91c}$$

Rearranging $c\lambda_{LH}$ similar to the procedure in Eq.(C-8) and subsequent integration of Eq.(C-90) yields*

(Case C):

$$\hat{E} = \frac{1}{2\eta_{es}} \left\{ c\alpha_p [E(k,\eta_{es}) + E(k,\eta_{ss2})] + s\alpha_p c\beta (c\eta_{ss2} - c\eta_{es}) \right\} \tag{C-93a}$$

(Case D):

$$\hat{E} = \frac{1}{\eta_{es}} \left\{ c\alpha_p [E(k) + E(k,\eta_{es}) - E(k,\eta_{ss2})] + s\alpha_p c\beta c\eta_{ss2} \right\} \tag{C-93b}$$

where

$$k = c\beta \tag{C-94}$$

*See Footnote *, p. C-4.

Appendix C

Formal analytical evaluation of $\hat{E}_{max}$ with respect to α_p, as in the LV modes, is not amenable to closed form solution, since $\hat{E}$ is a more complex function of α_p in both case C and case D. Nevertheless, $\hat{E}_{max}$ and the corresponding $\alpha_{p(opt)}$ were obtained numerically as shown in Figs.(5-29) and (5-30). Since $\alpha_{p(opt)}=0°$ for all β, it follows from Fig.(C-9) that case D applies and $\eta_{ss2}=90°$. Hence, Eq.(C-93b) yields

$$\hat{E}_{max} = E(k,\eta_{es})/\eta_{es} \qquad \text{(C-95)}$$

C.6 LH-Cyclic Roll Mode

In the cyclic roll case, the expression for $c\lambda_{LH}$ in Eq.(5-41) with ϕ defined by Eq.(5-44) is

$$(c\lambda_{LH})_1 = -s\eta s(\alpha_p+\beta) + c\alpha_p c\beta c^2\eta \qquad -180° \leq \eta < 0° \qquad \text{(C-95)}$$

$$(c\lambda_{LH})_2 = -s\eta s(\alpha_p-\beta) + c\alpha_p c\beta c^2\eta \qquad 0° \leq \eta \leq 180° \qquad \text{(C-96)}$$

If η is replaced by $(\eta-90°)$ it follows that Eqs.(C-95) and (C-96) are identical to $c\lambda_{LV}$ in Eqs.(C-26) and (C-27). Hence self-shadow boundaries have the same character as in the LV-Cyclic Roll mode, but are symmetrical about 90° rather than 180°. In view of Eq.(C-29) the self-shadow entry and exit points (η_{ss2},η_{ss1}) are given by

$$\eta_{ss2}=180°-\eta_{ss1}=\begin{cases} 90°-\cos^{-1}\left[\dfrac{-s(\alpha_p-\beta) + \sqrt{s^2(\alpha_p-\beta)+4c^2\alpha_p c^2\beta}}{2c\alpha_p c\beta}\right] & \beta \leq \alpha_p \\ \text{no self-shadow} & \beta > \alpha_p \end{cases} \qquad \text{(C-97)}$$

Appendix C

A plot of (η_{ss2}, η_{ss1}) vs. β is shown in Fig.(C-10) where the dashed curve represents the earth shadow boundary (η_{es}).

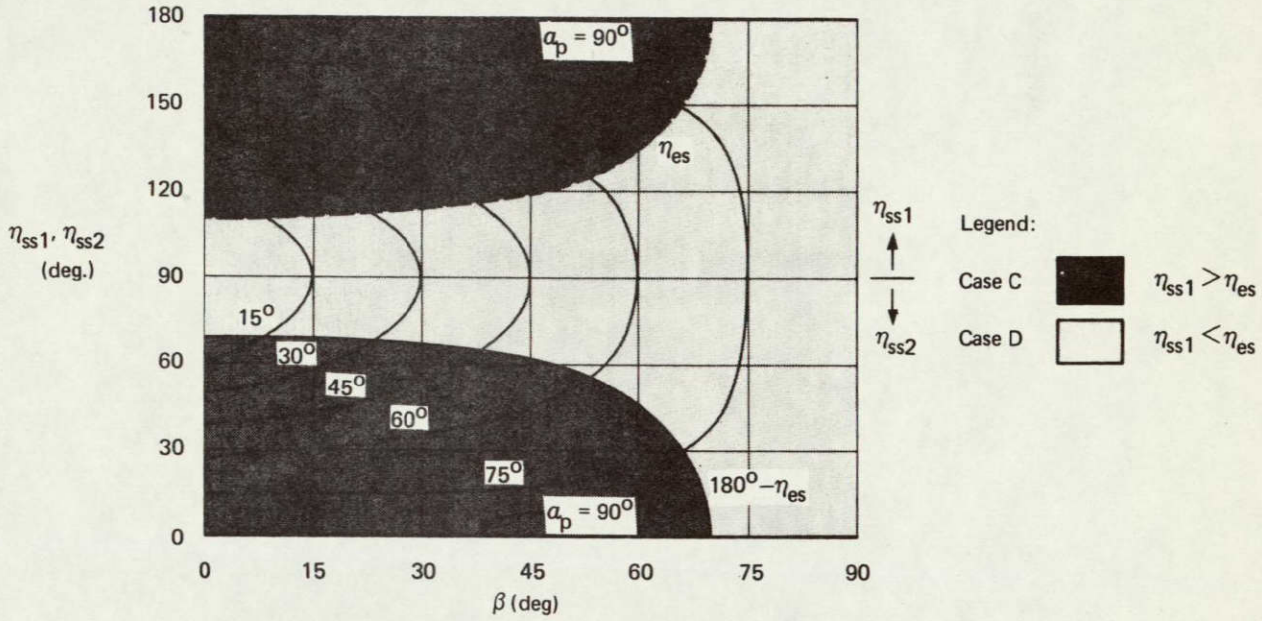

Figure (C - 10) - Variation in Panel Self-Shadow Boundary with α_p and β (LH - Cyclic Roll Mode).

Self-shadow and earth shadow regions are distinct, whenever $\eta_{ss1} < \eta_{es}$ (Case D) and overlap partially whenever $\eta_{ss1} > \eta_{es}$ (Case C) as shown in Fig.(5-20). The modification of Eq.(5-16) to evaluate $\hat{E}$ is

$$\hat{E} = \frac{1}{2\eta_{es}} \left\{ \int_{\eta_1}^{0} (c\lambda_{LH})_1 \, d\eta + \int_{0}^{\eta_2} (c\lambda_{LH})_2 \, d\eta - \int_{\eta_1'}^{\eta_2'} (c\lambda_{LH})_2 \, d\eta \right\}$$

(C-98)

where

$$\eta_2 = -\eta_1 = \eta_{es} \tag{C-99a}$$

$$\eta_1' = \eta_{ss2} \tag{C-99b}$$

$$\eta_2' = \begin{cases} \eta_{es} & \text{Case C} \\ \eta_{ss1} & \text{Case D} \end{cases} \tag{C-99c}$$

Integration of Eq.(C-98) after substitution for $(c\lambda_{LH})_1$ and $(c\lambda_{LH})_2$ yields

(Case C):

$$\hat{E} = \frac{1}{2\eta_{es}} \left\{ 2c\alpha_p s\beta - s(\alpha_p+\beta)c\eta_{es} + s(\alpha_p-\beta)c\eta_{ss2} + \frac{c\alpha_p c\beta}{4}\left[2(\eta_{es}+\eta_{ss2}) + (s2\eta_{es}+s2\eta_{ss2})\right]\right\} \tag{C-100a}$$

(Case D):

$$\hat{E} = \frac{1}{\eta_{es}} \left\{ c\alpha_p s\beta(1-c\eta_{es}) + s(\alpha_p-\beta)c\eta_{ss2} + \frac{c\alpha_p c\beta}{4}\left[2(\eta_{es}+\eta_{ss2}-\pi/2) + (s2\eta_{es}+s2\eta_{ss2})\right]\right\} \tag{C-100b}$$

Again formal analytical evaluation of $\hat{E}_{max}$ with respect to α_p is not amenable to closed form solution. Numerical results for $\hat{E}_{max}$ and $\alpha_{p(opt)}$ in Figs.(5-29) and (5-30) indicate that except for $\beta<\beta_{cyc}\approx 10°$, $\hat{E}_{max}$ is obtained for $\alpha_{p(opt)}=0°$. From Fig.(5-22) it is clear that for $\alpha_p=0°$, $\hat{E}$ is also close to the optimum for small β. For $\alpha_p=0°$ case D applies and $\eta_{ss2}=90°$ as

indicated by Fig.(C-10). Hence, Eq.(C-100b) yields

$$\hat{E}_{max} = \left[s\beta(1-c\eta_{es}) + c\beta(2\eta_{es}+s2\eta_{es})/4\right]/\eta_{es} \qquad \beta \geq \beta_{cyc} \simeq 10° \tag{C-101}$$

For $\beta<\beta_{cyc}\simeq 10°$, this result is also a reasonable approximation to the optimum.

C.7 LH-Fixed Roll Mode

In the fixed roll case ϕ is constant in Eq.(5-41), which can be written as

$$c\lambda_{LH} = A - Bs\eta - Cc\eta \tag{C-102}$$

where A, B and C are as defined in Eqs.(C-38), (C-39) and (C-40). If η is replaced by $(\eta-90°)$, this expression is identical to $c\lambda_{LV}$ in Eq.(C-37). Hence for a given ϕ, α_p and β, the self-shadow boundary points, η_{ss1} and η_{ss2} are merely rotated by 90°, clockwise in Fig.(C-4). This yields the four possible shadow arrangements, cases A-D, shown previously in Fig.(5-23). In view of Eqs.(C-46), (C-47) and (C-48), the corresponding expressions for η_{ss1}, η_{ss2} and η_{sst}, the self-shadow terminal point, are given by*

$$\eta_{ss2} = \begin{cases} 90° + \tan^{-1}\left(\dfrac{AC + BR}{-AB + CR}\right) & \beta \leq \cos^{-1}(c\alpha_p c\phi) \\ \text{no self-shadow} & \beta > \cos^{-1}(c\alpha_p c\phi) \end{cases} \tag{C-103}$$

$$\eta_{ss1} = \begin{cases} -180° - \tan^{-1}\left(\dfrac{-AB - CR}{AC - BR}\right) & \beta \leq \cos^{-1}(c\alpha_p c\phi) \\ \text{no self-shadow} & \beta > \cos^{-1}(c\alpha_p c\phi) \end{cases} \tag{C-104}$$

*See Footnote ***, p. C-15.

Appendix C

and*

$$\eta_{sst} = 90° - \tan^{-1}\left(c\beta s\phi / \sqrt{c^2\phi - c^2\beta}\right) \quad |\beta| \geq |\phi| \qquad \text{(C-105)}$$

In Fig. (C-11) curves of η_{ss1}, η_{ss2} and η_{sst} and the four possible regions corresponding to self-shadow cases A-D, are shown for $\phi = -45°$. The relative shape and size of these regions differ from the LV-Fixed Roll mode, but also vary with ϕ with some vanishing as $\phi \to 0°$ or $\phi \to -90°$. The curves for η_{ss1} and η_{ss2} with $\phi = 0°$ and $\phi = -90°$ are shown in Fig. (C-12).

Evaluation of $\hat{E}$ based on modifying Eq. (5-16), as in Eq. (C-90), with Eq. (C-102) substituted for $c\lambda_{LH}$ yields

$$\hat{E} = \frac{1}{2\eta_{es}} \Big\{ [A(\eta_2 - \eta_1) + B(s\eta_2 - s\eta_1) - C(c\eta_2 - c\eta_1)] - [A(\eta_2' - \eta_1') + B(s\eta_2' - s\eta_1') - C(c\eta_2' - c\eta_1')] \Big\} \qquad \text{(C-106)}$$

---

*While $(\eta_{sst})_{LV}$ in Eq. (C-48) was defined as a negative angle, a positive convention was used in Eq. (C-105) since $90° \leq (\eta_{sst}) \leq 180°$. This represents

$$(\eta_{sst})_{LH} = [(\eta_{sst})_{LV} - 90°] + 360°$$

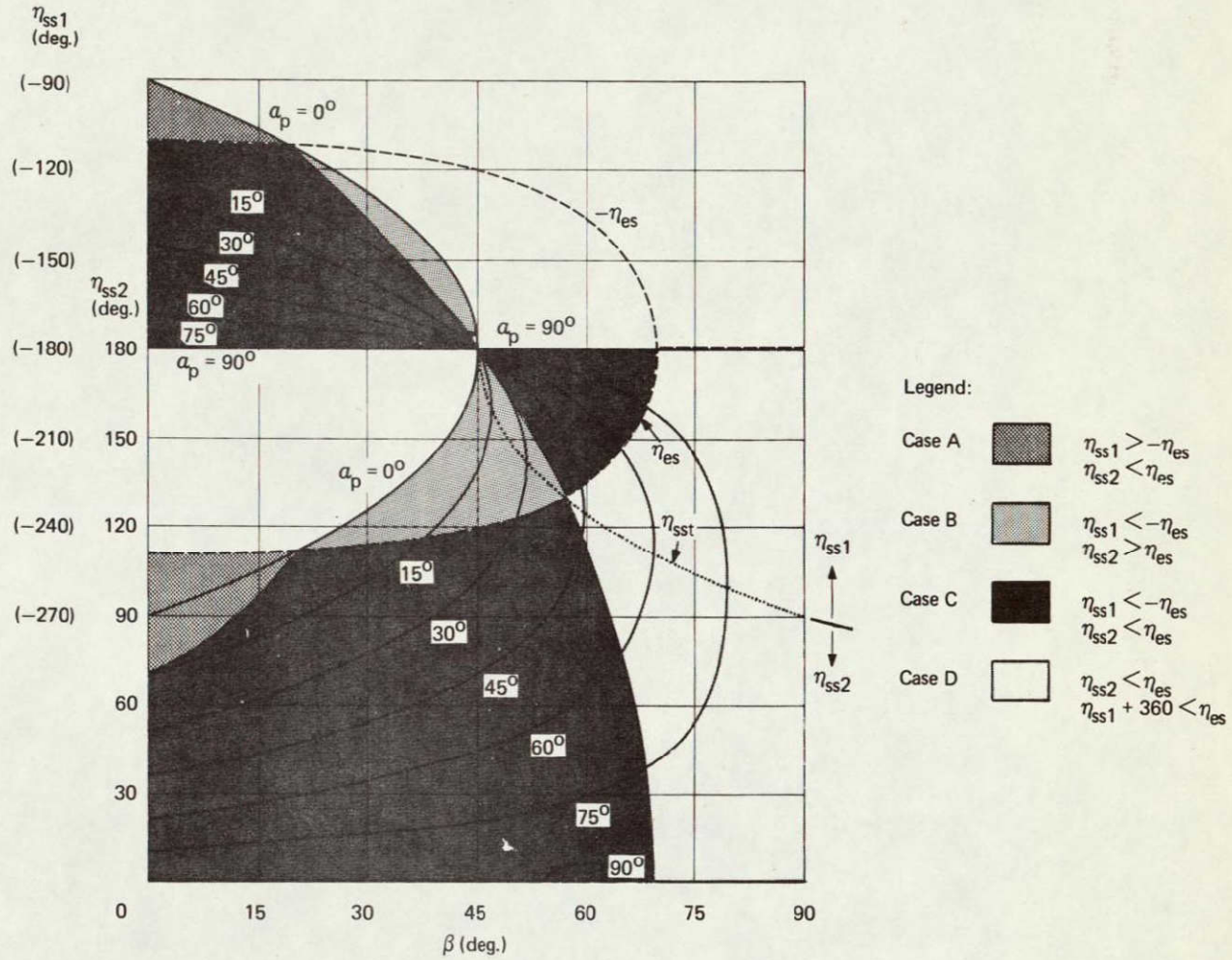

Figure (C - 11) - Variation in Panel Self-Shadow Boundary with a_p and β (LH - Fixed Roll Mode: $\phi = -45^o$).

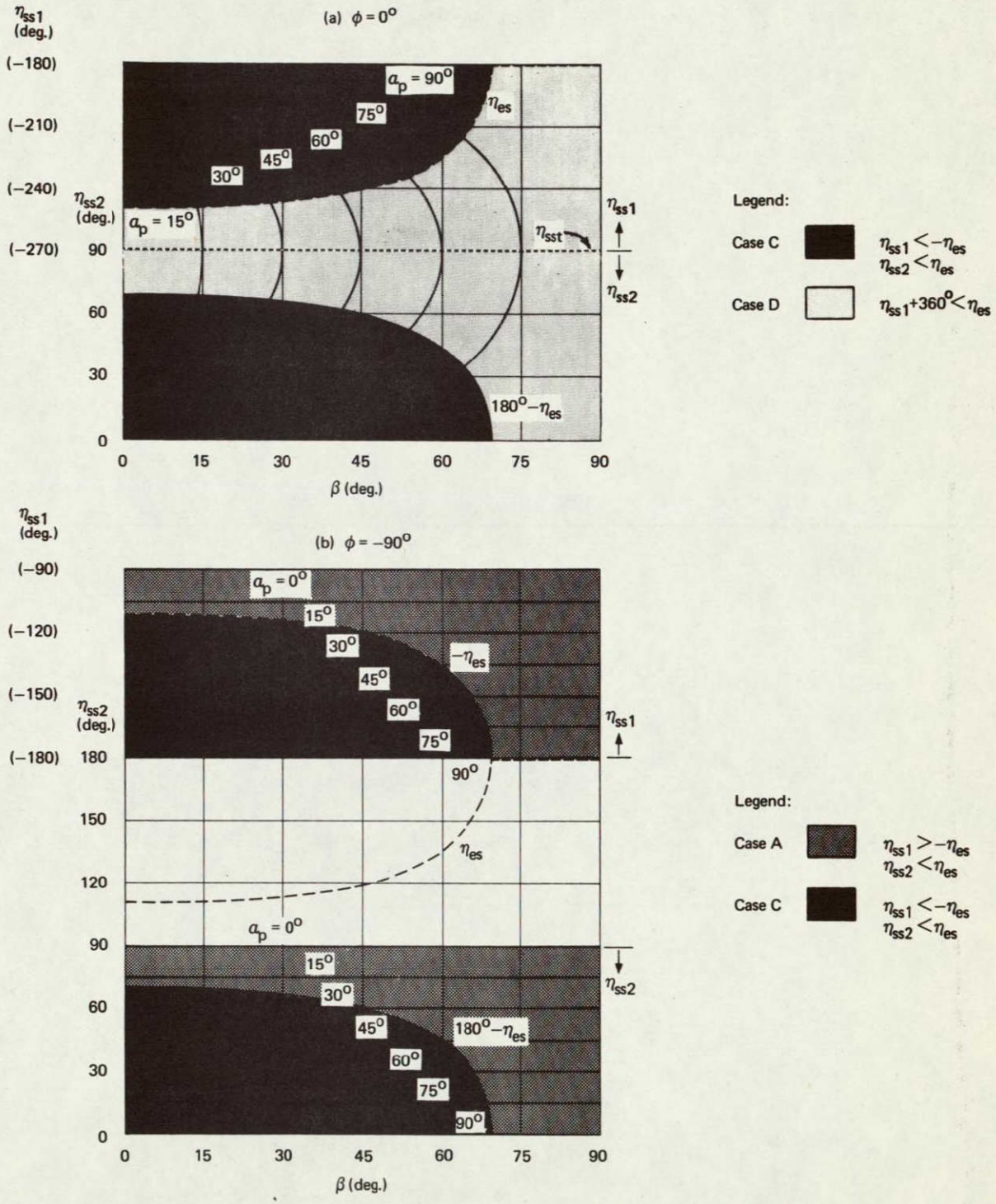

Figure (C - 12) Variation in Panel Self-Shadow Boundary with α_p and β (LH - Fixed Roll Mode: $\phi = 0^o, \phi = -90^o$)

Appendix C

where η_2, η_1, η_2' and η_1' are defined by

$$\eta_2 = \begin{cases} \eta_{ss2} & \eta_{ss2} < \eta_{es} \quad \text{(Case: A,C,D)} \\ \eta_{es} & \eta_{es} \leq \eta_{ss2}^* \quad \text{(Case: B)} \end{cases} \tag{C-107a}$$

$$\eta_1 = \begin{cases} \eta_{ss1} & |\eta_{ss1}| < \eta_{es} \quad \text{(Case: A,D)} \\ -\eta_{es} & |\eta_{ss1}| \geq \eta_{es}^* \quad \text{(Case: B,C)} \end{cases} \tag{C-107b}$$

$$\eta_2' = \begin{cases} (\eta_{ss1}+360°) & (\eta_{ss1}+360°) < \eta_{es} \quad \text{(Case: D)} \\ 0 & \text{otherwise}^* \quad \text{(Case: A,B,C)} \end{cases} \tag{C-108a}$$

$$\eta_1' = \begin{cases} \eta_{ss2} & (\eta_{ss1}+360°) < \eta_{es} \quad \text{(Case: D)} \\ 0 & \text{otherwise}^* \quad \text{(Case: A,B,C)} \end{cases} \tag{C-108b}$$

Determination of $\hat{E}_{max}$, $\alpha_{p(opt)}$ and ϕ_{opt}

The procedure and results obtained in Section C.4 for the LV-Fixed Roll mode can be used with slight modification to obtain $\hat{E}_{max}$ and the corresponding optimum α_p and ϕ. Analogous to Eqs. (C-54) and (C-55) the change of variables introduced in the LH case is

$$s\phi c\alpha_p = -c\underline{\phi}\ s\underline{\alpha} \tag{C-109}$$

$$s\alpha_p = s\underline{\phi}\ s\underline{\alpha} \tag{C-110}$$

where again $0<\underline{\alpha}<90°$, but $0<\underline{\phi}<90°$. Since

$$c\alpha_p c\phi = c\underline{\alpha} \tag{C-111}$$

*Or if no self-shadowing occurs, i.e., $(\beta > \cos^{-1}[c\alpha_p c\phi])$.

It follows that $c\lambda_{LH}$ in Eq.(5-41) can be written as

$$c\lambda_{LH} = c\underline{\alpha}\ s\beta + s\underline{\alpha}\ c\beta\ c(\underline{\phi}+\eta) \tag{C-112}$$

which is identical to Eq.(C-57). Consequently self-shadow boundaries can also be expressed as in Eqs.(C-58)-(C-61). The resulting evaluation of $\hat{E}$ for cases A and B is identical to Eqs.(C-62) and (C-63). For case B, $\underline{\phi}_{opt}=0°$ and for case A, $\hat{E}_{max}$ is independent of $\underline{\phi}$.

Determination of $\alpha_{p(opt)}$ leads to Eqs.(C-67) and (C-73) where ξ_{opt} is the solution of Eq.(C-74) shown in Fig.(C-7). The transition point from case A to case B corresponds to the intersection of the ξ_{opt} and η_{es} curves at $\beta=\beta_{es}=22.9°$ for a 230 NM orbit. In view of Fig.(C-7b) and Eqs.(C-60) and (C-107b), case A applies provided

$$\eta_{ssl} = -\xi_{opt} - \underline{\phi} > -\eta_{es} \tag{C-113}$$

or

$$0 \leq \underline{\phi} \leq \eta_{es} - \xi_{opt} \equiv \underline{\phi}_{max} \tag{C-114}$$

In summary then, the optimum results, $\hat{E}_{max}$, $\underline{\alpha}_{opt}$ and $\underline{\phi}_{opt}$ are identical to those in Eqs.(C-80)-(C-85) for the LV-Fixed Roll mode except that Eq.(C-114) replaces Eq.(C-82) for the condition on $\underline{\phi}$.

The optimum spacecraft roll angle (ϕ) and panel angle (α_p) corresponding to $\underline{\phi}_{opt}$ and $\underline{\alpha}_{opt}$ are obtained via Eqs.(C-109)-(C-111) which can be expressed as

$$\tan\phi = -c\underline{\phi}\ \tan\underline{\alpha} \tag{C-115}$$

$$s\alpha_p = s\underline{\phi}\ s\underline{\alpha} \tag{C-116}$$

Curves for $\alpha_{p(opt)}$ and ϕ_{opt} obtained from Eqs.(C-115) and (C-116) for $\underline{\phi}_{opt}=0°$ and $\underline{\phi}_{opt}=\eta_{es}-\xi_{opt}$ with $\underline{\alpha}_{opt}$ given by Eqs.(C-81) and (C-83) are shown in Fig.(C-13). In the region $0\leq\beta\leq\beta_{es}\simeq 23°$ these curves represent the bounds on the other possible combinations of $\alpha_{p(opt)}$ and ϕ_{opt} which yield the same $\hat{E}_{max}$. For $\underline{\phi}=0°$ it follows from Eqs.(C-115) and (C-116) that $\alpha_{p(opt)}=0°$ and $\phi_{opt}=-\underline{\alpha}_{opt}$. This indicates that $-\phi_{opt}$ in the LH-Fixed Roll mode is equal to $\alpha_{p(opt)}$ in the LV-Fixed Roll mode.

Appendix C

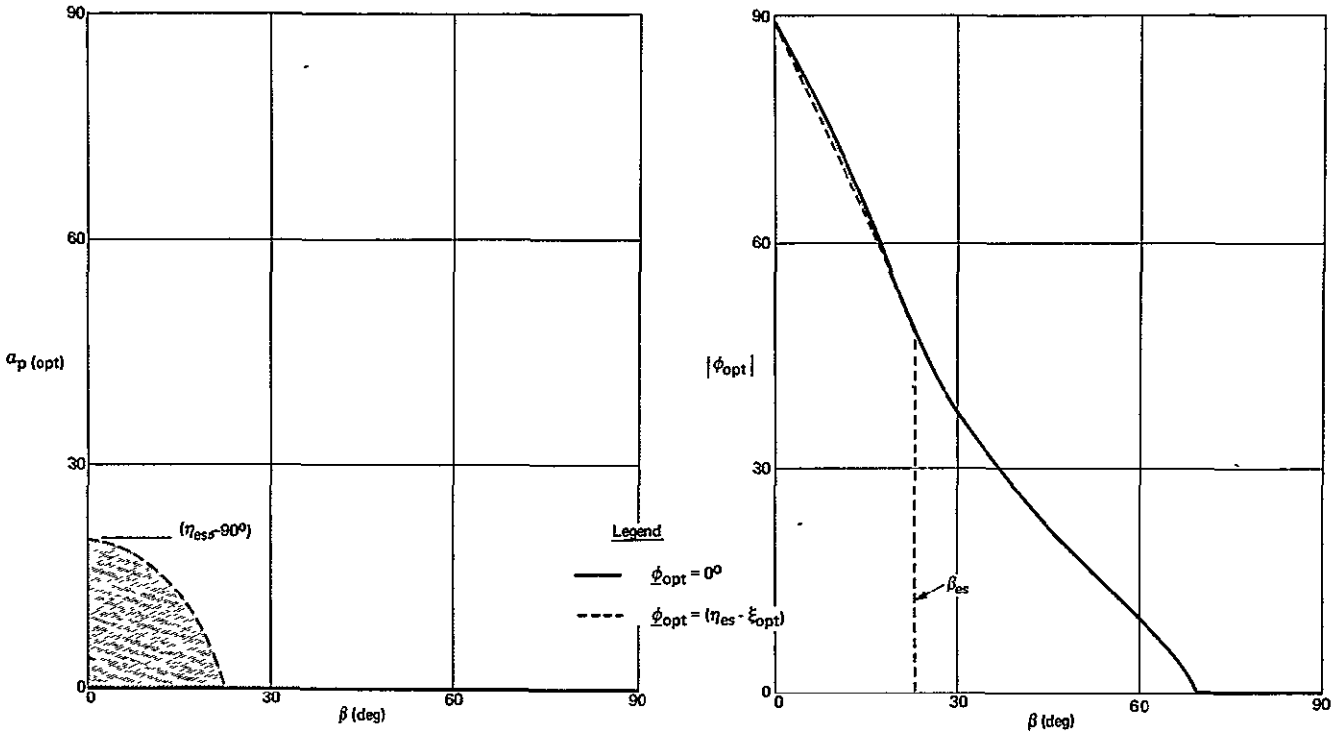

Figure (C - 13) - Optimum α_p and ϕ vs β (LH - Fixed Roll Modes).

APPENDIX D

Pointing Angles for Sun-Oriented Solar Arrays and Experiments on Spacecraft in LV, LH and POP Modes

In this appendix pointing angles for sun-oriented solar arrays and experiments on spacecraft in LV, LH and POP modes are evaluated from appropriate coordinate transformations.

D.1 Solar Array Pointing

The coordinates (x_p,y_p,z_p), (x_η,y_η,z_η) and (x_s,y_s,z_s) shown in Fig.(D-1) are defined as the solar array, orbit and sun referenced coordinate systems. From the transformation relating (x_p,y_p,z_p) and (x_s,y_s,z_s) for LV, LH and POP spacecraft attitude modes it is possible to determine:

1) the pointing angles (α_p,ϕ) for aligning the outward normal to the panels (z_p) with the sun line (z_s) and

2) the incidence angle (λ) between the sun line (z_s) and the panel outward normal (z_p) for arbitrary α_p,ϕ,η and β.

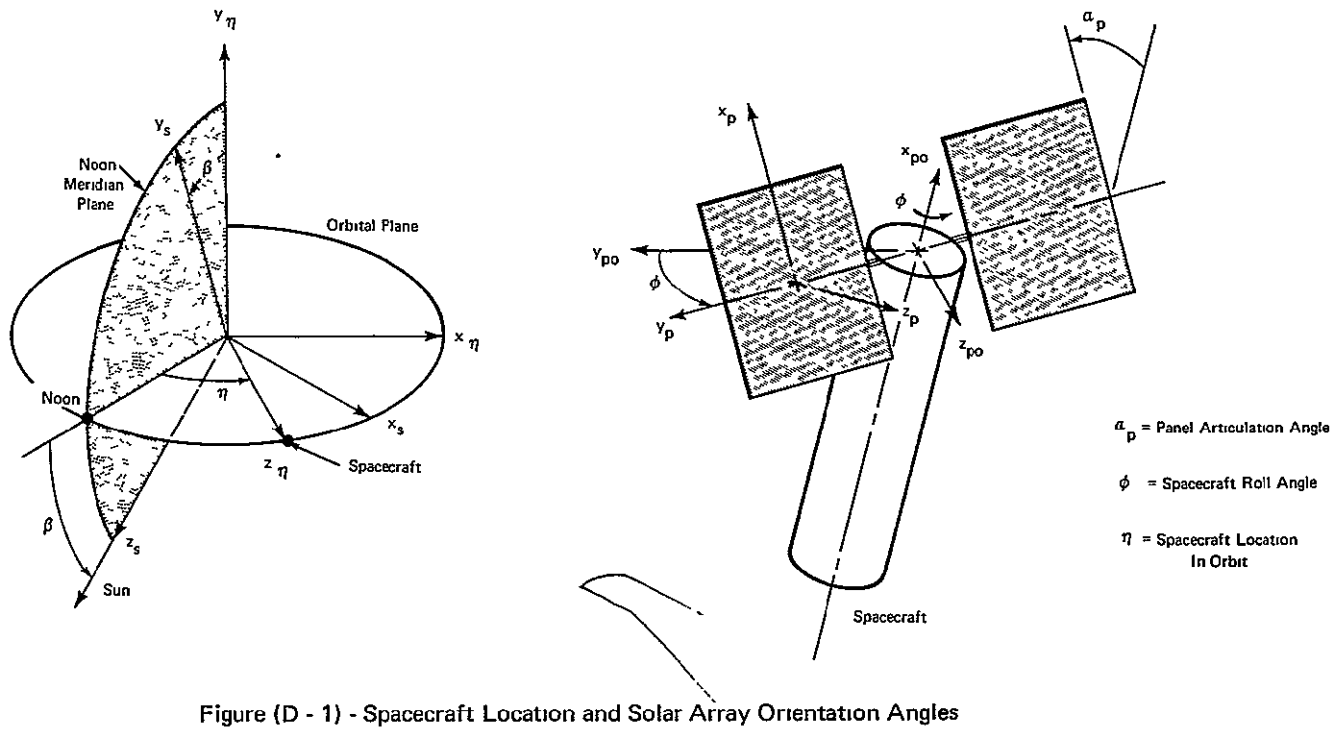

Figure (D - 1) - Spacecraft Location and Solar Array Orientation Angles

Appendix D

D.1.1 Transformations

The transformation relating (x_η, y_η, z_η) with (x_s, y_s, z_s) is

$$\underline{\mu}_\eta = T_\eta^y \; T_{-\beta}^x \; \underline{\mu}_s \tag{D-1}$$

The transformation relating (x_p, y_p, z_p) with (x_{po}, y_{po}, z_{po}), which represents the panel coordinates with $\alpha_p = \phi = 0$, is given by

$$\underline{\mu}_p = T_{\alpha_p}^y \; T_\phi^x \; \underline{\mu}_{po} \tag{D-2}$$

The transformation relating (x_{po}, y_{po}, z_{po}) with (x_η, y_η, z_η) is

$$\underline{\mu}_{po} = B_i \; \underline{\mu}_\eta \qquad (i = LV, LH, POP) \tag{D-3}$$

where B_i is to be specified for each attitude mode. From Fig. (D-2) it follows that*

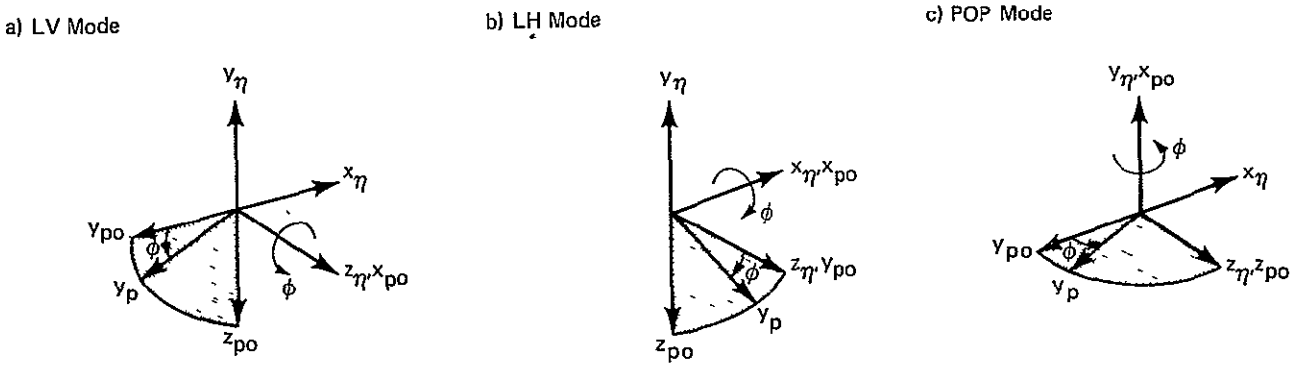

Figure (D - 2) - Orientation of Solar Array Coordinates in LV, LH and POP Attitude Modes with $\alpha_p = \phi = 0^o$.

*See also Figs. (5-7), (5-18) and (5-27).

Appendix D

$$B_{LV} = T^{x}_{90}\ T^{y}_{-90} = \begin{bmatrix} 0 & 0 & 1 \\ -1 & 0 & 0 \\ 0 & -1 & 0 \end{bmatrix} \tag{D-4}$$

$$B_{LH} = T^{x}_{90} = \begin{bmatrix} 1 & 0 & 0 \\ 0 & 0 & 1 \\ 0 & -1 & 0 \end{bmatrix}. \tag{D-5}$$

and

$$B_{POP} = T^{z}_{90} = \begin{bmatrix} 0 & 1 & 0 \\ -1 & 0 & 0 \\ 0 & 0 & 1 \end{bmatrix} \tag{D-6}$$

Consequently

$$\underline{\mu}_p = A_i\ \underline{\mu}_s \tag{D-7}$$

where

$$A_i = T^{y}_{\alpha_p}\ T^{x}_{\phi}\ B_1\ T^{y}_{\eta}\ T^{x}_{-\beta} \quad (i = LV, LH, POP) \tag{D-8}$$

D.1.2 Pointing Angles (α_p, ϕ)

With the panels pointed at the sun the solar vector is

$$\underline{S}_p = \begin{pmatrix} 0 \\ 0 \\ 1 \end{pmatrix} = A_i \underline{S}_s = A_i \begin{pmatrix} 0 \\ 0 \\ 1 \end{pmatrix} \tag{D-9}$$

or in view of Eqs.(D-7) and (D-8)

$$\left(T_{\alpha_p}^{Y}\ T_{\phi}^{X}\right)^{\dagger}\begin{pmatrix}0\\0\\1\end{pmatrix}=\begin{pmatrix}s\alpha_p\\-s\phi c\alpha_p\\c\phi c\alpha_p\end{pmatrix}=B_i\ T_{\eta}^{Y}\ T_{-\beta}^{X}\begin{pmatrix}0\\0\\1\end{pmatrix}=B_i\begin{pmatrix}-s\eta c\beta\\-s\beta\\c\eta c\beta\end{pmatrix}$$

Thus the pointing angles (α_p,ϕ) are specified by

(LV Mode)

$$s\alpha_p = c\eta c\beta \tag{D-11}$$

$$\tan\phi = -s\eta/\tan\beta \tag{D-12}$$

(LH Mode)

$$s\alpha_p = -s\eta c\beta \tag{D-13}$$

$$\tan\phi = -c\eta/\tan\beta \tag{D-14}$$

(POP Mode)

$$s\alpha_p = -s\beta \tag{D-15}$$

$$\tan\phi = -\tan\eta \tag{D-16}$$

D.1.2 Sun Incidence Angle (λ)

With the panels not pointed at the sun the solar vector expressed in (x_p,y_p,z_p) is

$$\underline{S}_p = A_i\underline{S}_s = A_i\begin{pmatrix}0\\0\\1\end{pmatrix} = \begin{pmatrix}a_{13}\\a_{23}\\a_{33}\end{pmatrix}_i \tag{D-17}$$

The incidence angle (λ_i) is then specified by

$$c\lambda_i = \underline{S}_p\cdot\underline{z}_p = (a_{33})_i \qquad (i = LV,LH,POP) \tag{D-18}$$

so that

LV Mode:

$$c\lambda_{LV} = c\alpha_p s\beta c\phi + s\alpha_p c\beta c\eta - c\alpha_p c\beta s\phi s\eta \qquad \text{(D-19)}$$

LH Mode:

$$c\lambda_{LH} = c\alpha_p s\beta c\phi - s\alpha_p c\beta s\eta - c\alpha_p c\beta s\phi c\eta \qquad \text{(D-20)}$$

POP Mode:

$$c\lambda_{POP} = c\alpha_p c\beta c(\phi+\eta) - s\alpha_p s\beta \qquad \text{(D-21)}$$

D.2 Experiment Pointing

The results in Section D.1 for solar arrays are also applicable to determining pointing angles for sun-oriented experiments on spacecraft in LV, LH and POP modes. The experiment degrees-of-freedom are assumed to be a rotation (ϕ_e) about the spacecraft roll axis and a rotation (α_e) about an axis normal to the roll axis.* With $\alpha_e = \phi_e = 0°$ and no spacecraft roll ($\phi=0°$) the experiment pointing axis is assumed parallel to the spacecraft roll axis, z_o, shown in Fig. (D-1). Hence, α_e and ϕ_e are equivalent to α_p and ϕ in Eqs.(D-11) through (D-16).** To account for cases where $\phi \neq 0°$, Eqs.(D-12), (D-14), and (D-16) are merely modified such that $\phi \rightarrow (\phi_e - \phi)$.

---

*The rotation ϕ_e could be realized partially with internal gimbaling or exactly by a spacecraft configuration[4] comprised of modules stacked along the roll axis, each with an independent roll capability.

**As a practical matter experiment occultation by the spacecraft may occur when the pointing axis is oriented nearly parallel to the roll axis unless the experiment module is located at one end of the spacecraft to permit axial pointing.

APPENDIX E

Sunlight Interval in Elliptical Orbits

The geometry for determining the sunlight interval in elliptical orbits is similar to that used for circular orbits as shown in Fig.(E-1). Here however, the orbit altitudes at P_1 and P_2 differ as given in Fig.(E-1b) where $\tilde{\eta}_1$ and $\tilde{\eta}_2$ represent the angular displacement of P_1 and P_2 from perigee and η_s is the location of midnight relative to perigee. The relationships between (σ_1,σ_2) and β are given by[13]

$$c\sigma_1 = c\rho_1/c\beta \tag{E-1}$$

$$c\sigma_2 = c\rho_2/c\beta \tag{E-2}$$

$$s\rho_1 = s\sigma[1+\varepsilon c(\eta_s-\sigma_1)] \tag{E-3}$$

$$s\rho_2 = s\sigma[1+\varepsilon c(\eta_s+\sigma_1)] \tag{E-4}$$

and

$$s\sigma = R/a(1-\varepsilon^2) \tag{E-5}$$

where R is the earth's radius, a the orbit semi-major axis and ε the orbital eccentricity. In view of Fig.(E-2), η_s is given by

$$\eta_s = \psi+180°-\Omega_a \tag{E-6}$$

where Ω_a is the location of perigee relative to the ascending node as defined in Eq.(2-11).

For a given β and η_s, solution of Eqs.(E-1) through (E-4) yields σ_1 and σ_2. The time in shadow obtained from Kepler's

Appendix E

equation in terms of the eccentric anomalies E_1 and E_2 is

$$T_{sh} = \frac{T}{2\pi} \left[(E_2 - \varepsilon sE_2) - (E_1 - \varepsilon sE_1) \right] \tag{E-7}$$

where

$$sE_1 = \frac{\sqrt{1-\varepsilon^2}\, s\tilde{\eta}_1}{1+\varepsilon c\tilde{\eta}_1} \tag{E-8}$$

$$sE_2 = \frac{\sqrt{1-\varepsilon^2}\, s\tilde{\eta}_2}{1+\varepsilon c\tilde{\eta}_2} \tag{E-9}$$

$$\tilde{\eta}_1 = \eta_s - \sigma_1 \tag{E-10}$$

$$\tilde{\eta}_2 = \eta_s + \sigma_2 \tag{E-11}$$

and T is the orbital period. The sunlight fraction of the orbit is then

$$T_{sL} = 1 - T_{sh}/T = 1 - \frac{1}{2\pi} \left[(E_2 - E_1) - \varepsilon (sE_2 - sE_1) \right] \tag{E-12}$$

For circular orbits, $\varepsilon = 0$ so that $a = R+H$, $\rho_1 = \rho_2 = \sigma$ and $\sigma_1 = \sigma_2$. Thus,

$$T_{sL} = 1 - \frac{1}{2\pi}(2\sigma_1) = \frac{\pi - \sigma_1}{\pi} \equiv \frac{\eta_{es}}{\pi} \tag{E-13}$$

where η_{es} is one-half the orbit sunlight angle in radians,

$$c\sigma_1 = c\sigma/c\beta \quad * \tag{E-14}$$

and

$$s\sigma = R/(R+H) \tag{E-15}$$

*While umbra and penumbra aspects of the earth-sun geometry have not been included here, this slight effect can be included easily. The shadow interval boundaries are based on visibility of the full solar disk for the penumbra effect and the first (or last) point of visibility of the edge of the solar disk for the umbra effect. In Eq. (E-14), for example, $c\sigma$ becomes $c(\sigma+\alpha_s)$ for the penumbra effect and $c(\sigma-\alpha_s)$ for the umbra effect where $\alpha_s \simeq 0.26°$ is half the angle subtended by the sun at earth distances (1AU). The same modification applies to $c\rho_1$ and $c\rho_2$ in Eqs. (E-1) and (E-2).

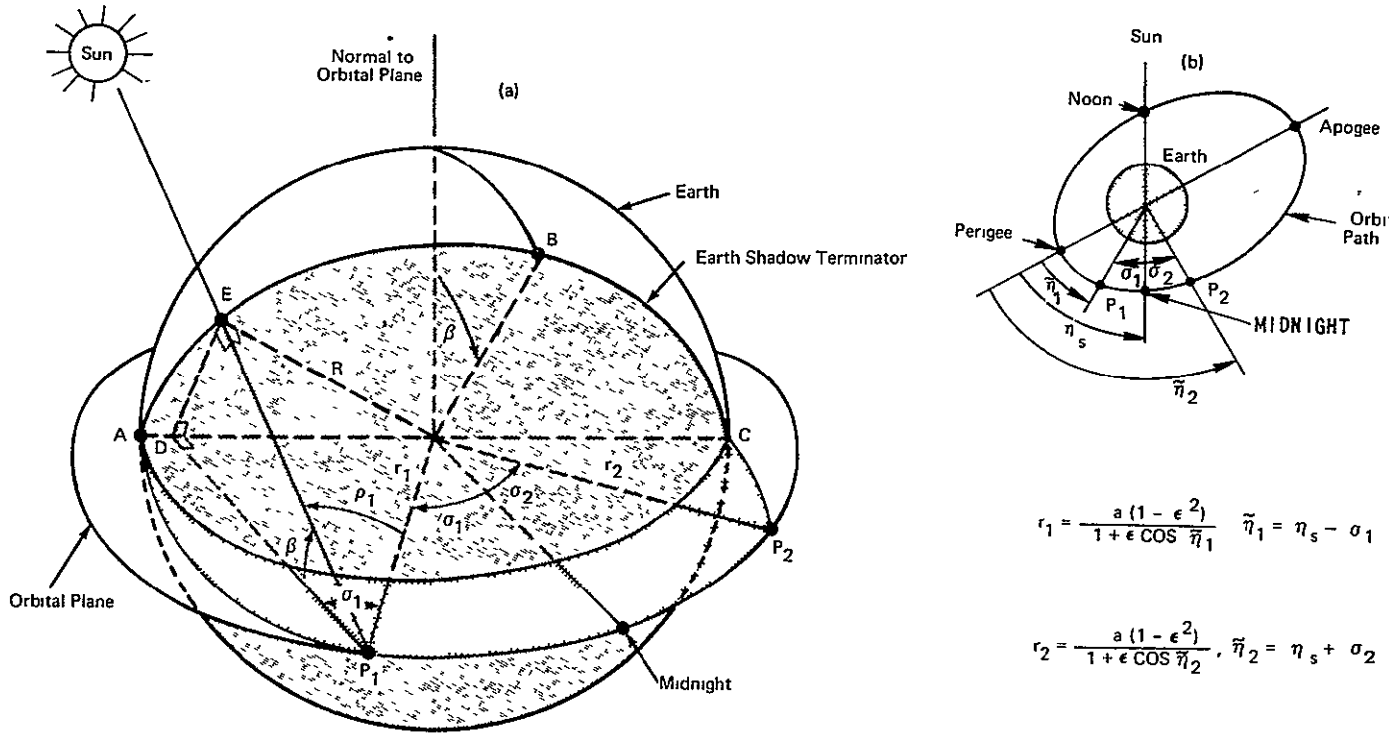

Figure (E - 1) - Geometry for Determining Earth Shadow Interval.

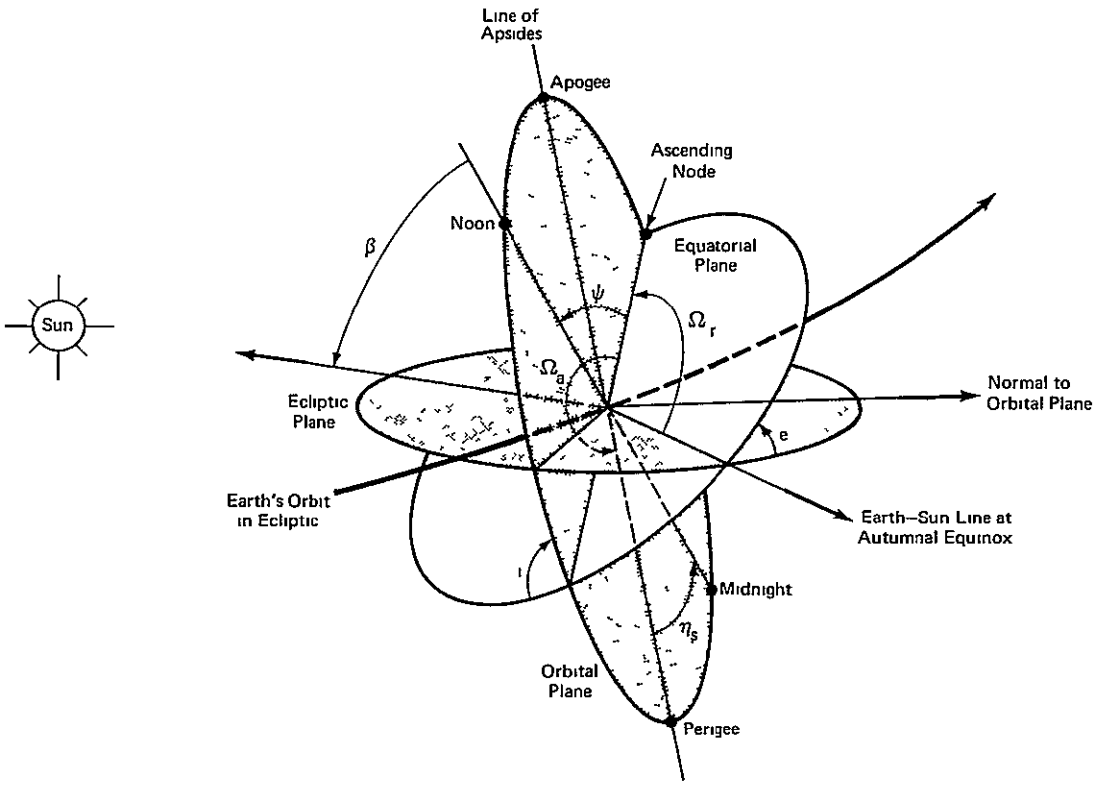

Figure (E - 2) - Location of Midnight Relative to Perigee

APPENDIX F

List of Symbols

For convenience of the reader this list contains all important symbols, a brief definition and the page location where first used. Minor symbols appearing in only one section are omitted.

Greek Symbols	Definition	First Used on Page
α_d	sun line declination relative to equatorial plane	18
α_L	launch azimuth relative to geographical north	8
α_p	solar array articulation angle	41
$\underline{\alpha}$	auxiliary variable used with $\underline{\phi}$ to define α_p in LV and LH-Fixed Roll modes	C-21
$\alpha_{p(opt)}$	optimum array articulation angle	C-5
$\underline{\alpha}_{opt}$	optimum value of $\underline{\alpha}$	C-27
β	minimum angle between sun line and orbital plane (sun line declination relative to orbital plane)	2
β_{eb}	angle denoting β envelope boundaries	17
β_s	constant angle about which β varies in sun-synchronous orbits	30
$\lvert\beta\rvert_{max}$	maximum possible $\lvert\beta\rvert$ for particular orbit inclination	3
$\dot{\beta}$	$d\beta/dt$	20
$\lvert\dot{\beta}\rvert_{max}$	maximum of $\lvert\dot{\beta}\rvert$ for particular orbit inclination and $\dot{\Omega}_{rm}$	3
$\lvert\dot{\beta}\rvert_{max,max}$	maximum of $\lvert\dot{\beta}\rvert_{max}$ with respect to orbit inclination	22
γ	angle denoting earth-sun line location in ecliptic plane relative to autumnal equinox	6

Greek Symbols	Definition	First Used on Page
γ_o	γ at time, t=0	13
$\hat{\gamma}$	γ when $\lvert\beta\rvert=\lvert\beta\rvert_{max}$	18
$\dot{\gamma}$	mean rotation rate of earth-sun line about the sun	7
ε	eccentricity of satellite orbit about earth	10
ε_s	eccentricity of earth's orbit about the sun	7
η	angle denoting spacecraft location in orbit relative to orbital noon	41
$\hat{\eta}$	angle denoting spacecraft location in orbit relative to ascending node	35
η_1	η when array exits from shadow region (earth or self-shadow, circular orbits)	42
η_2	when array enters shadow region (earth or self-shadow, circular orbits)	42
η_{es}	η when spacecraft enters earth shadow; one-half orbit sunlight interval (circular orbits)	37
η_{eso}	η_{es} at $\beta=0°$	44
η_{ss1}	η when array exits self-shadow region	42
η_{ss2}	η when array enters self-shadow region	42
$\tilde{\eta}_1$	spacecraft true anomaly when entering earth shadow	E-1
$\tilde{\eta}_2$	spacecraft true anomaly when exiting earth shadow	E-1
η_s	location of orbital midnight relative to perigee	E-1
λ	sun line incidence angle on solar array (in LV, LH and POP modes: $\lambda_{LV}, \lambda_{LH}, \lambda_{POP}$)	41
$\underline{\lambda}$	maximum projected area ratio between ends and lateral surface of cylinder/hemispherical-end spacecraft	77

Greek Symbols	Definition	First Used on Page
μ	earth's gravitational constant	10
$\underline{\mu}_i$	general unit vector expressed in coordinate system (i) with components (x_i, y_i, z_i); e.g. $\underline{\mu}_{sc}$ and $\underline{\mu}_n$ for unit vectors in spacecraft and nodal coordinate systems	5
ϕ	spacecraft roll angle	41
ϕ_{cont}	ϕ in LV-Continuous Roll Mode	47
ϕ_{cyc}	ϕ in LV and LH-Cyclic Roll Modes	47
ϕ_{opt}	optimum value of ϕ in Fixed Roll modes ($\dot{\phi}=0$)	54
$\underline{\phi}$	auxiliary variable used with $\underline{\alpha}$ to define α_p in LV and LH-Fixed Roll Modes	C-21
$\underline{\phi}_{opt}$	optimum value of $\underline{\phi}$	C-27
$\hat{\phi}$	angular displacement of spacecraft principal and geometric axes about roll axis	34
$\dot{\phi}$	$d\phi/dt$	46
ψ	angle between orbital noon and ascending node (sun line right ascension relative to ascending node)	2
$\dot{\psi}$	$d\psi/dt$	23
$\dot{\psi}_{ave}$	average of $\dot{\psi}$ over time	3
$\lvert\dot{\psi}\rvert_{max}$	maximum of $\dot{\psi}$ over time	3
ω_o	orbital angular velocity in circular orbits (constant)	43
$\lvert\underline{\Delta H}\rvert$	magnitude of bias gravity gradient torque-impulse per orbit (bias momentum)	35
Ω_a	angle between perigee and orbit ascending node	9
Ω_r	angle between orbit ascending node and autumnal equinox (measured in equatorial plane)	9

Greek Symbols	Definition	First Used on Page
Ω_{po}	Ω_a at time, t=0	9
Ω_{ro}	Ω_r at time, t=0	9
$\hat{\Omega}_r$	Ω_r when $\|\beta\|=\|\beta\|_{max}$	18
$\bar{\Omega}_r$	$(\Omega_{ro}-\gamma_o)$, a constant	29
Ω_L	launch site longitude relative to orbit ascending node (measured in equatorial plane)	14
Ω_N	longitude of equatorial noon meridian plane relative to autumnal equinox (measured in equatorial plane)	14
$\dot{\Omega}_a$	rotation rate of line-of-apsides	9
$\dot{\Omega}_r$	rotation rate of orbit ascending node	9
$\dot{\Omega}_{rm}$	$\dot{\Omega}_r$ when i=0°	10

English Symbols		
a	orbit semi-major axis	10
$\bar{a}$	earth albedo constant	73
e	fixed angle (23.45°) between equatorial and ecliptic planes	8
$f(\beta)$	functional relationship between a system performance factor and β	82
f_{av}	mission average of $f(\beta)$	82
$\overline{f_{av}}$	mean of f_{av} relative to launch time of day (t_L) and launch date (D_L)	83
$<f_{av}>$	minimum of f_{av} relative to t_L and D_L	82
$<<f_{av}>>$	maximum of f_{av} relative to t_L and D_L	82
i	orbit inclination	8

English Symbols	Definition	First Used on Page
i_{ss}	i for sun-synchronous orbits	20
ℓ	launch azimuth	8
t	current time measured from a prior event (e.g. launch, orbital noon, autumnal equinox, etc.)	7
t_L	launch time of day at launch site (U.T.)	13
t_1	orbit time corresponding to η_1	42
t_2	orbit time corresponding to η_2	42
A	maximum projected area of a geometrical surface	73
D	diameter of a cylindrical spacecraft	77
D_L	launch date at launch site (calendar days since 00^h:00 U.T. of September 23)	13
E	electrical energy per orbit generated by a solar array	42
E_s	E with the array in a sun-oriented mode	43
E_{so}	E_s when $\beta=0°$	44
$\hat{E}$	E normalized to E_s ($\hat{E}=E/E_s$)	44
$\hat{E}_o$	E normalized to E_{so} ($\hat{E}_o=E/E_{so}$)	44
$\hat{E}_{max}$	$\hat{E}$ maximized with respect to α_p	48
$\hat{E}_{o\ max}$	$\hat{E}_o$ maximized with respect to α_p ($\hat{E}_{o\ max}=\hat{E}_s\hat{E}_{max}$)	68
$\hat{E}_s$	E_s normalized to E_{so} ($\hat{E}_s=E_s/E_{so}$)	44
F_{DS}	view factor for direct solar radiation to a surface	73
F_{ET}	view factor for earth-emitted radiation to a surface	73

English Symbols	Definition	First Used on Page
F_{RS}	view factor for reflected solar radiation to a surface	73
F_S	$F_{DS} + \bar{a}F_{RS}$	74
H	circular orbit altitude	10
L	length of a cylindrical spacecraft	77
$\underline{P}_i$	unit vector specifying pointing axis to be aligned with the solar vector*	11
P	instantaneous power generated by a solar array	41
P_M	P with the array in a sun-oriented mode	41
R	earth's radius (3443.9 NM)	10
$\underline{S}_i$	solar vector, a unit vector* along the earth-sun line directed toward the sun	6
S	solar constant (443 BTU/hr/ft^2)[12]	73
T	orbital period ($2\pi/\omega_o$ in circular orbits)	35
$\underline{T}_{g_i}$	gravity gradient torque (vector*)	35
T_M	mission duration	82
T_{SL}	fraction of an orbit in sunlight	39
$T_\xi^x, T_\xi^y, T_\xi^z$	elementary coordinate transformation matrices (see definitions in Section 2.1)	5
W_n	direct solar component of incident thermal energy per orbit with A normal to the solar vector	75
$\hat{W}_{DS}$	direct solar component of incident thermal energy per orbit on a surface (normalized to W_n)	74
$\hat{W}_{ET}$	earth-emitted component of incident thermal energy per orbit on a surface (normalized to W_n)	74

*Subscript i denotes coordinate system in which the vector is expressed.

English Symbols	Definition	First Used on Page
$\hat{W}_{RS}$	reflected solar component of incident thermal energy per orbit on a surface (normalized to W_n)	74
$\hat{W}_s$	$\hat{W}_{DS} + \hat{W}_{RS}$	77

Miscellaneous Symbols		
$\| \ \|$	magnitude of a scalar or vector	3
$\dagger$	matrix transpose	5

APPENDIX G

List of Tables and Figures

REFERENCES

1. G. M. Anderson and W. W. Hough, "Hard-Docked ATM Experiment Carrier," Bellcomm Technical Memorandum TM-66-1022-1, November 18, 1966.

2. J. Kranton, "Studies of Solar Orientation for AAP-1/AAP-2," Bellcomm Memorandum for File, September 8, 1967.

3. G. M. Anderson, et. al., "ATM Alternate Mission Study," Compendium of Bellcomm Technical Memoranda and Memoranda for File, September 6, 1968.

4. G. M. Anderson, "Space Station Configuration and Flight Attitude," Bellcomm Memorandum for File, B69-08002, August 1, 1969.

5. "Hybrid Simulation Model of the Apollo Telescope Mount," MSFC Report, S&E-ASTR-SG-29-69, August 19, 1969.

6. R. W. Wolverton (ed.), "Flight Performance Handbook for Orbital Operations," John Wiley and Sons, New York, N.Y., 1961, p. 2-230.

7. F. G. Allen and R. Y. Pei, "Discussion of Sun-Synchronous Orbits and their Applications," Bellcomm Memorandum for File, September 18, 1967.

8. "Saturn V Workshop Mass Characteristics," MSFC Report, S&E-ASTN-SAE-69-74, Table VIII-Event 6, July 25, 1969.

9. L. R. Hart, et. al., "Application of Magnetic Torquing for Desaturation of Control Moment Gyros in Space Vehicle Control," U.S. Air Force Flight Dynamics Lab Report - AFFDL-TR-67-8, June, 1967.

10. H. F. Kennel, "Angular Momentum Desaturation for ATM/LM/CSM Configuration Using Gravity Gradient Torques, NASA TMX-53764, August 9, 1968.

11. D. R. Ingwerson, et. al., "Conceptual Design and Analysis of a Control System for the Apollo Telescope Mount," Lockheed Missiles and Space Co. Technical Report, LMSC-A842157, March 17, 1967.

12. J. B. Kendrick (ed.), "TRW Space Data" (Handbook), TRW Systems, Redondo Beach, California, Third Edition, 1967.

13. B. D. Elrod, "Solar Viewing Capability in High Inclination Circular and Elliptical Orbits," Bellcomm Technical Memorandum TM-68-1022-5, September 5, 1968.

14. B. W. Moss, "The Effect of Quartz Cover Slides and Radiant Energy Incident on Solar Cells," Bellcomm Memorandum for File, B69 04094, April 24, 1969.

15. W. W. Hough and B. D. Elrod, "Solar Array Performance as a Function of Orbital Parameters and Spacecraft Attitude," Transactions of the ASME, Journal of Engineering for Industry, Vol. 91, No. 1, February, 1969, pp. 13-20.

16. E. Jahnke and F. Emde, "Tables of Functions," 4th Ed., Dover Publications, New York, N.Y., 1945, pp. 52-87.

17. W. W. Hough, "The Effect of Launch Time on the Performance of a Solar Array/Battery Electrical Power System," Bellcomm Technical Memorandum, TM-67-1022-3, July 1967.

18. J. A. Stevenson and J. C. Grafton, "Radiation Heat Transfer Analysis for Space Vehicles," North American Aviation, Inc. Space and Information Systems Division Report SID 61-91, Part 1, December, 1961. (DDC No. AD 271 917)

19. F. E. Swalley, "Thermal Radiation Incident on an Earth Satellite," NASA TND-1524, December, 1962.

20. E. I. Powers, "Thermal Radiation to a Flat Surface Rotating about an Arbitrary Axis in an Elliptical Orbit," NASA TND-2147, April, 1964.

21. B. D. Elrod, "Analytical Evaluation of View Factors for Calculating Incident Thermal Radiation on Spacecraft Surfaces," Bellcomm Technical Memorandum, to be published.

22. T. C. Tweedie, "Influence of Atmospheric Absorption of Solar Ultraviolet Radiation on ATM Operation," Bellcomm Technical Memorandum TM-68-1021-1, November 12, 1968.

BELLCOMM, INC.

Subject: Solar Pointing Variations in Earth Orbit and the Impact on Mission Design

From: B. D. Elrod

Distribution List

NASA Headquarters

H. Cohen/MLR
J. H. Disher/MLD
W. B. Evans/MLO
L. K. Fero/MLV
J. P. Field, Jr./MLP
W. D. Green, Jr./MLA
W. H. Hamby/MLO
T. E. Hanes/MLA
C. Janow/REG
D. R. Lord/MTD
M. Savage/MLT
W. C. Schneider/ML

GSFC

J. T. Skladany/713

La RC

W. W. Anderson/AMPD
W. E. Howell/FID
P. R. Kurzhals/AMPD

MSC

F. M. Elam/EG25
O. K. Garriott/CB
W. J. Klinar/EG131
F. C. Littleton/KM
O. G. Smith/KF

MSFC

W. B. Chubb/S&E-ASTR-SGD
H. F. Kennel/S&E-ASTR-A
E. F. Noel/S&E-ASTR-SI
G. S. Nurre/S&E-ASTR-A
H. E. Worley/S&E-AERO-DOI

Bellcomm, Inc.

A. P. Boysen
J. O. Cappellari
C. O. Guffee
D. R. Hagner
W. G. Heffron
B. T. Howard
N. I. Kirkendall
K. E. Martersteck
J. Z. Menard
S. Shapiro
J. W. Timko
T. C. Tweedie
M. P. Wilson
Department 1022
Div. 101, 102 Supervision
Dept. 1033 Supervision
Department 1024 File
Central Files
Library

Abstract Only

I. M. Ross
R. L. Wagner
Div. 201, 203 Supervision